A tomographic exploration of the internal structure of coal and its role in single particle breakage

J. Viljoen

13037242

Thesis submitted for the degree *Doctor Philosophiae* in Chemical Engineering at the Potchefstroom Campus of the North-West University

Promoter: Prof. Q.P. Campbell

Co-promoter: Prof. M. le Roux

May 2016

Declaration

I, ***Jacob Viljoen***, hereby declare that this thesis entitled:

A tomographic exploration of the internal structure of coal and its role in single particle breakage

is my own work and has not been submitted to any other university before. Where publications involving co-authors were used, the necessary permission from these authors had been obtained in writing. The relative contributions of the different co-authors are acknowledged in their signed statements.

Signed at Potchefstroom on the 12th day of November 2015.

_____

Jacob Viljoen

Preface

Thesis format

The format of this thesis is a series of original articles as allowed for in rule 5.1.1 of the General Academic Rules 2015, approved on the 18th of November 2014. An electronic copy of the rules is available at http://www.nwu.ac.za/content/policy_rules (accessed 3rd March 2015). Other rules that are applicable to the publication of a doctoral thesis as a series of original articles are rules 5.4.2.7; 5.4.2.8 and 5.4.2.9.

Rule 5.1.1 states:

> *"The structure of a doctoral degree is prescribed by faculty rules and may be acquired through the –*
>
> *5.1.1.1 writing of a thesis; or*
>
> *5.1.1.2 writing of a series of original articles; or*
>
> *5.1.1.3 registration of an internationally examined patent; or*
>
> *5.1.1.4 performance of a concert series; or*
>
> *5.1.1.5 compilation of a composition portfolio, or*
>
> *5.1.1.6 presentation of an art exhibition,*
>
> *provided that the research product submitted for examination makes a distinct contribution to the knowledge of and insight into a subject field and produces proof of originality, either by the revelation of new facts or by the exercising of an independent critical capacity."*

Rule 5.4.2.7 states:

> *"Where a candidate is permitted to submit a thesis in the form of a published research article or articles or as an unpublished manuscript or manuscripts in article format and more than one such article or manuscript is used, the thesis must still be presented as a unit, supplemented with an inclusive problem statement, a focused literature analysis and integration and with a synoptic conclusion, and the guidelines of the journal concerned must also be included"*

Rule 5.4.2.8 states:

> *"Where any research article or manuscript and/or internationally examined patent is used for the purpose of a thesis in article format to which other authors and/or inventors than the candidate contributed, the candidate must obtain a written statement from each co-author and/or co-inventor in which it is stated that such co-author and/or co-inventor grants permission that the research article or manuscript and/or patent may be used for the stated purpose and in which it is further indicated what each co-author's and/or co-inventor's share in the relevant research article or manuscript and/or patent was."*

Rule 5.4.2.9 states:

> *"Where co-authors or co-inventors as referred to in 5.4.2.8 above were involved, the candidate must mention that fact in the preface and must include the statement of each co-author or co-inventor in the thesis immediately following the preface."*

Thesis formatting, referencing, and numbering style

Please note that, for the sake of uniformity, the formatting, referencing style, and numbering of all of the tables and figures were changed to a consistent style throughout the thesis. In addition to changing the formatting, referencing style, and numbering of tables and figures, some minor language and typographical changes to the published articles were made; however, any changes made to the content of the published articles were to correct factual inconsistencies.

A list of references cited in each chapter is given at the end of that chapter and a complete list of all of the references cited in the thesis is given at the end of the thesis.

Co-Author Statements

The following section contains all of the statements of consent of the various co-authors of the various articles, manuscripts and presentations that are contained in this thesis. These statements are in accordance to Rule 5.4.2.8 and Rule 5.4.2.9 of the General Academic Rules 2015 of the North-West University as given on Page v.

The guidelines for authors, published by the journals in which the publications listed here and in the List of publications were published, are available online at the following websites:

- http://www.sajs.co.za/guidelines-authors (accessed 2nd November 2015) for the South African Journal of Science
- http://www.tandfonline.com/action/authorSubmission?journalCode=gcop20&page=instructions#.VjcmircwiM8 (accessed 2nd November 2015) for the International Journal of Coal Preparation and Utilization

The following is a list of all of the co-authors that contributed to the various publications:

Statement of consent: Prof. Quentin P. Campbell

To whom it may concern

I, **QUENTIN PETER CAMPBELL**, hereby give **JACOB VILJOEN** consent to use the publications listed below, of which I am co-author, in the thesis entitled "***A tomographic exploration of the internal structure of coal and its role in single particle breakage***". The thesis is submitted for the degree Doctor Philosophiae in Chemical Engineering at the Potchefstroom campus of the North-West University, South Africa:

- ***Campbell, Q.P.*** & Viljoen, J. 2011. Single particle impact breakage of coal. (*In* Morsi, B., ed. 28th Annual International Pittsburgh Coal Conference organised by University of Pittsburgh, S.S.o.E., Pittsburgh, PA: International Pittsburgh Coal Conference).

- Viljoen, J., ***Campbell, Q.P.***, le Roux, M. & De Beer, F. 2015. An analysis of the slow compression breakage of coal using microfocus X-ray computed tomography. *International journal of coal preparation and utilization*, 35(1):1-13.

- Viljoen, J., ***Campbell, Q.P.***, Le Roux, M. & Hoffman, J. 2015. The qualification of coal degradation with the aid of micro-focus computed tomography: identifying invisible factors influencing coal breakage. *South African journal of science*, 111(9/10):1-10.

- Viljoen, J., ***Campbell, Q.P.***, Le Roux, M. & Hoffman, J.W. 2016? The influence of bedding plane orientation on the degradation characteristics of a Waterberg coal. *International journal of coal preparation and utilization,* (submitted for publication, Manuscript ID.: GCOP-2015-0106).

I am the promoter of the thesis, entitled "***A tomographic exploration of the internal structure of coal and its role in single particle breakage***", where these articles will be used and the initiator of the larger study on coal breakage and degradation of which this thesis forms a part of. I was also instrumental in developing the experimental concept and gave valuable insights during the development of the experimental designs used during this

thesis. I was also responsible for significant proofing and editing of the manuscripts, written by Jacob Viljoen, listed above.

This statement satisfies Rule 5.4.2.8 and Rule 5.4.2.9 of the General Academic Rules 2015 of the North-West University.

Signed at Potchefstroom on 12th day of November 2015

_____

Q.P. Campbell

Statement of consent: Prof. Marco le Roux

To whom it may concern

I, **MARCO LE ROUX**, hereby give **JACOB VILJOEN** consent to use the publications listed below, of which I am co-author, in the thesis entitled "***A tomographic exploration of the internal structure of coal and its role in single particle breakage***". The thesis is submitted for the degree Doctor Philosophiae in Chemical Engineering at the Potchefstroom campus of the North-West University, South Africa:

- Viljoen, J., Campbell, Q.P., ***le Roux, M.*** & De Beer, F. 2015. An analysis of the slow compression breakage of coal using microfocus X-ray computed tomography. *International journal of coal preparation and utilization*, 35(1):1-13.

- Viljoen, J., Campbell, Q.P., ***Le Roux, M.*** & Hoffman, J. 2015. The qualification of coal degradation with the aid of micro-focus computed tomography: identifying invisible factors influencing coal breakage. *South African journal of science*, 111(9/10):1-10.

- Viljoen, J., Campbell, Q.P., ***Le Roux, M.*** & Hoffman, J.W. 2016? The influence of bedding plane orientation on the degradation characteristics of a Waterberg coal. *International journal of coal preparation and utilization,* (submitted for publication, Manuscript ID.: GCOP-2015-0106).

I am the co-promoter of the thesis, entitled "***A tomographic exploration of the internal structure of coal and its role in single particle breakage***". I was also instrumental in developing the experimental concept and gave valuable insights during the development of the experimental designs used during this thesis. I was also responsible for significant proofing and editing of the manuscripts, written by Jacob Viljoen, listed above.

This statement satisfies Rule 5.4.2.8 and Rule 5.4.2.9 of the General Academic Rules 2015 of the North-West University.

Signed at Potchefstroom on 12th day of November 2015

_____

M. le Roux

Statement of consent: Mr Jakobus W. Hoffman

To whom it may concern

I, **JAKOBUS W. HOFFMAN**, hereby give **JACOB VILJOEN** consent to use the publications listed below, of which I am co-author, in the thesis entitled "***A tomographic exploration of the internal structure of coal and its role in single particle breakage***". The thesis is submitted for the degree Doctor Philosophiae in Chemical Engineering at the Potchefstroom campus of the North-West University, South Africa:

- Viljoen, J., Campbell, Q.P., Le Roux, M. & ***Hoffman, J.*** 2015. The qualification of coal degradation with the aid of micro-focus computed tomography: identifying invisible factors influencing coal breakage. *South African journal of science*, 111(9/10):1-10.

- Viljoen, J., Campbell, Q.P., Le Roux, M. & ***Hoffman, J.W.*** 2016? The influence of bedding plane orientation on the degradation characteristics of a Waterberg coal. *International journal of coal preparation and utilization,* (submitted for publication, Manuscript ID.: GCOP-2015-0106).

As a tomographic instrument specialist at Necsa, I was responsible for generating and reconstructing the tomograms analysed by Jacob Viljoen and used in the manuscripts listed above. I was also responsible for significant proofing and editing of the manuscripts written by Jacob Viljoen.

This statement satisfies Rule 5.4.2.8 and Rule 5.4.2.9 of the General Academic Rules 2015 of the North-West University.

Signed at Pretoria on 11th day of November 2015

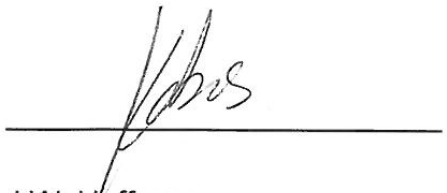

J.W. Hoffman

Statement of consent: Mr Frikkie de Beer

To whom it may concern

I, **FRIKKIE DE BEER**, hereby give **JACOB VILJOEN** consent to use the publication listed below, of which I am co-author, in the thesis entitled "***A tomographic exploration of the internal structure of coal and its role in single particle breakage***". The thesis is submitted for the degree Doctor Philosophiae in Chemical Engineering at the Potchefstroom campus of the North-West University, South Africa:

- Viljoen, J., Campbell, Q.P., le Roux, M. & ***De Beer, F.*** 2015. An analysis of the slow compression breakage of coal using microfocus X-ray computed tomography. *International journal of coal preparation and utilization*, 35(1):1-13.

As a tomographic instrument specialist at Necsa, I was responsible for generating and reconstructing the tomograms analysed by Jacob Viljoen and used in the manuscripts listed above. I was also responsible for significant proofing and editing of the manuscripts, written Jacob Viljoen, listed above.

This statement satisfies Rule 5.4.2.8 and Rule 5.4.2.9 of the General Academic Rules 2015 of the North-West University.

Signed at Pretoria on 11th day of November2015

F. de Beer

List of publications

The following papers, on work conducted for this thesis, were published in peer-reviewed journals:

- ***Viljoen, J.***, Campbell, Q.P., Le Roux, M. & Hoffman, J. 2015. The qualification of coal degradation with the aid of micro-focus computed tomography: identifying invisible factors influencing coal breakage. *South African journal of science*, 111(9/10):1-10.

- ***Viljoen, J.,*** Campbell, Q.P., le Roux, M. & De Beer, F. 2015. An analysis of the slow compression breakage of coal using microfocus X-ray computed tomography. *International journal of coal preparation and utilization*, 35(1):1-13.

The following papers, on work conducted for the thesis, were published in popular media focussed on professionals:

- Campbell, Q., ***Viljoen, J.,*** Le Roux, M. & mathews, J.P. 2014. Micro-focus X-ray computed tomography: coal processes. *Inside mining*: 22-25, February.

The following papers, on work conducted for this thesis, were presented at various conferences, and subsequently published in the conference proceedings:

- ***Viljoen, J.,*** Campbell, Q.P., Le Roux, M. & De Beer, F. 2013. An analysis of the slow compression breakage of a Waterberg coal using micro-focus X-ray computed tomography. (*In* Özbayoğlu, G. & Arol, A.I., eds. XVII International coal preparation congress, Istanbul: Aral. p. 107-113).

- Campbell, Q.P., ***Viljoen, J.,*** Le Roux, M. & Mathews, J.P. 2013. Following coal processes using micro focus X-ray computed tomography. (*In* 14th International conference on coal science and technology organised by EMS Energy Institute, State College, PA. p. 881-888).

- Campbell, Q.P. & ***Viljoen, J.*** 2011. Single particle impact breakage of coal. (*In* Morsi, B., ed. 28th Annual International Pittsburgh Coal Conference organised by University of Pittsburgh, S.S.o.E., Pittsburgh, PA: International Pittsburgh Coal Conference).

The following papers, on work conducted for this thesis, were presented at various conferences where no proceedings were published:

- ***Viljoen, J.,*** Campbell, Q.P., Le Roux, M. & De Beer, F. 2013. Qualification of cracks formation and propagation under compressive loading by micro-focus X-ray computed tomography. Paper presented at the 18th Southern African coal science and technology indaba, Parys, 14 November.

- ***Viljoen, J.,*** Campbell, Q., Le Roux, M. & Hoffman, J. 2013. The qualification of coal degradation with the aid of micro-focus computed tomography. Paper presented at the 1st Imaging with radiation conference and workshop (ImgRad-1), Pretoria, 24 September.

Abstract

The unintentional production of coal fines, or coal degradation, during coal beneficiation can lead to significant financial losses for coal producers. Coal fines in a closely sized feed can also lead to channelling, hotspots, and other hydrodynamic inefficiencies in reactors. Coal degradation occurs at any step in the beneficiation process where the coal is subjected to mechanical stresses or where the coal is subjected to a rapid increase in temperature. A number of particle and material properties influence the degradation characteristics of coal including the initial particle size, the composition of the particle, and weathering; the degradation characteristics can also be influenced by the properties of the unit processes used to beneficiate or utilise the coal, such as the breakage energy and temperature. The mechanisms that are used to describe the degradation of coal particles differ for mechanical and thermal degradation. Mechanical degradation is described by fracture and attrition, while thermal degradation is described by fragmentation and exfoliation; however, none of these mechanisms are thoroughly understood. In order to minimise the degradation that occurs across the coal mining, beneficiation, and utilisation process value chains, a better understanding of the factors that influence the degradation and the mechanisms whereby degradation occurs is necessary.

To this end, this thesis describes research that elucidates the influence of various factors on the breakage and degradation characteristics of coal, and describes attempts to model these influences using a modification of the t_{10} degradation model. The factors influencing the degradation characteristics that were considered were particle shape, the particle's orientation relative to the impact surface (impact orientation), and the particle microstructure. The influence of the microstructures was investigated using micro-focus X-ray computed tomography (µCT). The applicability of µCT as an analytical probe to identify and track the changes that occur within a particle during degradation is first confirmed for compressive breakage, and is then applied to single particles during compressive, impact, and thermal loading. The microstructures that were identified and tracked were pre-existing cracks within a particle, the orientation of the particle bedding plane relative to the applied force, the boundaries between lithotypes of varying density, and the boundaries along mineral inclusions.

The influence of particle shape and impact orientation was studied and it was found that when slab-like particles impacted onto a larger surface area more degradation products formed compared to slab-like particles that impacted onto a distinct protrusion. This was due to the protrusion disintegrating thereby dissipating the breakage energy and protecting the rest of the particle from degradation. It was also found that the t_{10} degradation model could not predict the degradation behaviour of the specific South African coals tested due to the t_{10} degradation model being unsuitable for modelling the degradation of brittle, bimodal natural resources like coal.

While studying the influence of particle shape and impact orientation, characteristic breakage patterns were observed, and the microstructure of coal suggested as a possible cause for these distinctive breakage patterns. The next phase of the investigation applied µCT to identify and track the changes that occur in a particle during degradation. Tomograms were generated before, during, and after degradation. The tomograms were compared, changes identified, and conclusions drawn regarding the influence of the microstructures on coal degradation namely:

- All of the microstructures had the potential to contribute to a particle's degradation. The microstructures either remained unchanged, acted as an initiation site for a new crack, aided the propagation of a crack, or halted the propagation of a crack. The possible influence of a specific feature on degradation could not be predicted from the tomograms generated before degradation.

- Of all of the observable microstructures considered during this study, the pre-existing cracks in a particle had the most pronounced influence on the final crack distribution within the particle.

- For both the mechanical and thermal degradation of a particle, the lower density microlithotypes present showed more new crack formation compared to the higher density microlithotypes. The lower density microlithotypes are the vitrinite rich microlithotypes which is known to be more brittle than both inertinite and carbominerite rich microlithotypes.

- The orientation of a particle's bedding plane relative to the applied mechanical force influenced the propagation of cracks in the particle by either aiding the propagation along the microlithotype boundaries when the force was applied along the bedding plane, or halting the propagation of cracks at

the microlithotype boundaries when the force was applied across the bedding plane.

It was initially hypothesised that, if the distribution of microstructures in a particle is known, then the particle size distribution of the progeny can be predicted. Due to the fact that no indication of whether a specific feature will contribute to the degradation of a particle, or what the contribution will be, the progeny size distribution of a single particle could not be predicted; however, the progeny size distribution of a population of degraded particles could be fitted using a Rosin-Rammler size distribution.

Keywords: Highveld coal; Waterberg coal; Degradation; High-speed videography; t_{10} degradation model; Micro-focus X-ray computed tomography; Coal microstructure; Single particle compressive breakage; Single particle impact breakage; Single particle thermal breakage

Acknowledgements

Although I am considered the author of this thesis, it would have been impossible to complete this project without the technical and financial aid of the following people and institutions. I am deeply in your debt.

- My two promoters, Prof. Quentin Campbell and Prof. Marco le Roux, despite your own responsibilities and cares you always guided me, motivated me when I started to doubt myself, and always found time to advise me on even the most trivial and irrelevant issues I might have had.
- Jakobus Hoffman and Frikkie de Beer at Necsa, it is thanks to your expert knowledge, training, and guidance that I was able to accomplish anything using µCT.
- The steering committee of the Southern African Coal Processing Society, for the generous funding and technical support you provided.
- The staff and students at the North-West University, especially Prof. Frans Waanders, Louis la Grange, Adrian Brock, Jan Kroeze, Ted Paarlberg, Charlotte Badenhorst, Carla Hatting, Wynand Breytenbach, and Juan Nelson. Also, a special thank you to my friends at the NWU, you are connivers in my success.
- Andre Martens at VIP Technologies, for allowing me unsupervised access to the coolest video camera I have ever operated.
- David Powell and a large number of unnamed reviewers and copyeditors, without your assistance the articles, manuscripts, and this thesis would have been a mere collection of incoherent ideas and sentences.

On a personal level, I would like to give a heartfelt thank you to my parents, my siblings, and my friends. Throughout this entire process, you all played the part of activist, cheerleader, counsellor, advisor, reverend, and teacher on more occasions than I can possibly recall.

Above all I thank and praise the Lord God.

For the Lord grants wisdom!
From his mouth come knowledge and understanding.
(Proverbs 2:6)

Table of contents

Chapter 1 - Introduction

Background

One only has to look at the number of industries where coal has been used since antiquity, and where it is still used today, to realise that coal may be one of the most important natural resources of the last two centuries. Coal was essential for steam generation during the industrial revolution, as well as for electrification and iron production during the technological revolution.[1] Today coal remains indispensible in many industries including electricity generation, liquid fuels production, steel manufacturing and cement production.[2] The biggest global market for coal is electricity production, with around 40% of the world electricity demand supplied via coal and 70% of the world steel production dependent on coal as both an energy source and reductant.[2]

South Africa is highly dependent on coal. Around 95% of South Africa's electricity generation is done via coal and accounts for 65% of South Africa's national coal consumption; around 30% of South Africa's liquid fuel production is from coal and accounts for 21% of South Africa's total consumption.[3-5] This situation is not set to change in the near future as coal is both an abundant and low cost feedstock to both processes, and there are currently no economically viable sources of alternative energy in South Africa.[4-6] All of the coal produced in South Africa is produced from six or seven of its 19 generally accepted coal fields.[7] Figure 1.1, reproduced from Hancox and Götz (2014), shows a map of all South Africa's coalfields.[7] In this study coal from the Witbank, Highveld, and Waterberg coalfields was studied and these coalfields are briefly discussed below.

The Witbank coalfield is located in the northern part of the Karoo basin, covers an area of around 5680 km^2, and produces more than half of South Africa's saleable coal as metallurgical coal, export thermal coal, and thermal coal for local markets.[4, 7] This coalfield is divided into three coal bearing units that contain its five coal seams: No. 2 seam is the basal unit, No. 4 seam is the central coal bearing unit, and No. 5 seam the topmost unit.[7, 8] The best quality coal and the majority of the Witbank coalfield's resources are contained in No. 2 seam.[4, 7, 8]

The 7000 km^2 Highveld coalfield's fill is very similar to that of its northern neighbour, the Witbank coalfield; these two coalfields are separated by the Smithfield ridge on the Highveld coalfield's northern boundary.[7, 8] The majority of the Highveld coalfield's resources are

contained in the No. 4 seam.[4, 7] The products from the Highveld coalfield are: export thermal coal, thermal coal for local markets, and feedstock for liquid fuel production.[4, 7]

The Waterberg coalfield covers an area of 3600 km^2, and is located in the Ellisras sub-basin in the Limpopo province.[7] The coalfield is divided into 11 coal bearing zones named (from the bottom upwards) Zone 1 – Zone 11; the lower zones (zones 1-4) occurs in the ±55 m thick Vryheid formation, and the upper zones (zones 5-11) occurs in the 70-90 m thick Grootegeluk formation.[4, 7, 8] The coal in the Grootegeluk formation occurs as thick interbedded seams.[4, 9] The Waterberg coalfield produces thermal coals for local markets, metallurgical coal for processes such as the COREX process, and semi-soft coking coals.[4, 7, 8] The coals from the lower zones can be used unbeneficiated, but the upper zones' coals must be beneficiated before use due to the high mineral matter content.[7]

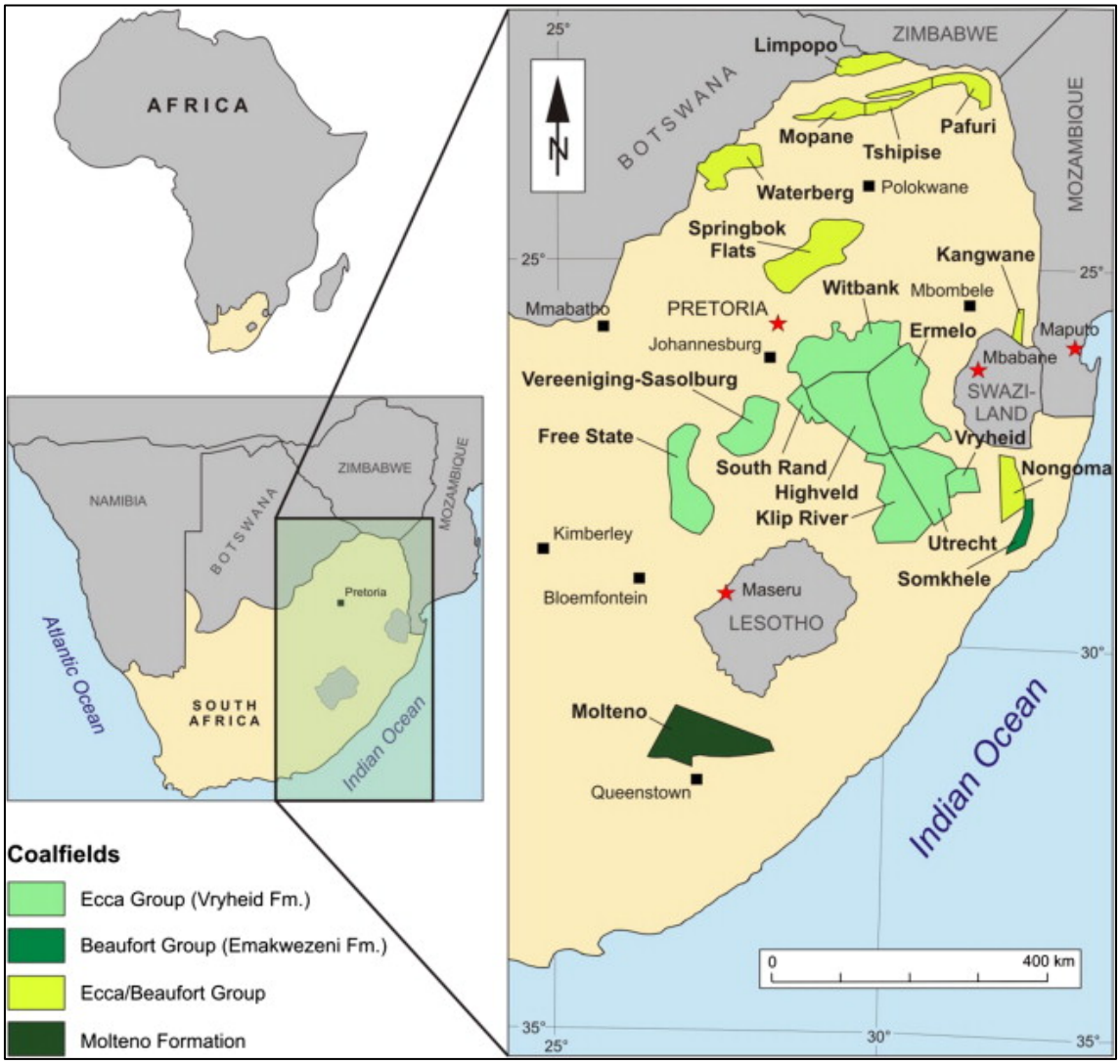

Figure 1.1: South Africa's coalfields (reproduced from Hancox and Götz (2014))[7]

Despite the fact that coal is an indispensible commodity there are a number of environmental issues involved in the mining, washing (beneficiation) and utilisation of coal. Various efforts are being made and technologies developed to reduce this impact on the environment. Most of these efforts are aimed at reducing the emissions caused by the combustion of coal, especially during electricity generation. These technologies include coal beneficiation to increase the quality of the coal feedstock and to decrease the pollutants produced, treating the effluent gasses to reduce the emitted pollutants, and capturing carbon dioxide (CO_2) for storage and sequestration. Another way to help alleviate the impact of coal use on the environment is to ensure that the mined coal is used as effectively and efficiently as possible. In the processes that are currently used to beneficiate coal a large amount of fines are produced. Annually, around 60 MT fines are produced and discarded in South Africa.[10] This unintentional, and unwanted, production of coal fines is called coal degradation. Fines, in a South African context, are defined as any particles smaller than 1 mm and ultra-fines are defined as any particle smaller than 100 µm (see Definition of fines).

Coal degradation products are the cause of downstream issues relating to the sale and utilisation of the washed coal product. Because the minimum particle size is often specified during the sale of washed thermal coal to South African users, degradation during stockpiling, handling and transport can incur penalties due to a product that is not on specification.[11] Furthermore, fine coal is significantly harder and costlier to dewater than large coal particles, hence the higher moisture content leads to increased transport costs for the wet coal.[12] Many of the processes that utilise large coal particles, such as direct reduction steel production and fixed bed gasification, are adversely affected by the presence of fine coal in the feed, where fines cause hydrodynamic effects leading to reactor inefficiencies such as hotspots and channelling.[13]

Coal degradation takes place at a number of processing steps between removing the coal from the seam to the final utilisation of the coal product. After the coal has been washed and sized it is stockpiled prior to transportation, or in some instances directly transported to the customer. When coal is transported along conveyors, degradation occurs as a result of the vertical movement over the conveyor idler-rollers; when coal is transferred from a conveyor either to another conveyor, onto a stockpile, or into a storage bin the coal can fall significant distances and undergo degradation during impact. Significant degradation also occurs where large coal particles enter heated reactor units.

The degradation mechanisms of coal are classified based on the particle size distribution of the degradation products produced. Volume breakage occurs when all the progeny produced by a single particle is smaller than the parent particle; volume breakage usually

occurs when an excessive amount of breakage energy is applied to a particle.[14-16] Surface breakage occurs when most of the progeny is significantly smaller than the parent particle while the parent particle is still recognisable; surface breakage occurs when insufficient energy is applied for the particle to undergo volume breakage, chipping and abrasion then occurs, and progeny is produced from the surface of the parent particle.[14-16]

Since the mid-1900s various authors have studied the coal degradation that occurs between the mine and the customer.[13, 15, 17-23] All of these studies used either large samples, sampling during industrial processes or double impact tests (drop weight tests, pendulum tests). The studies mentioned above clearly show the influence of many properties (composition,[17] cushioning,[13, 21, 23] weathering,[18, 23] stabilisation,[23] impact surface,[13, 23] particle size,[19, 20] breakage energy,[19, 20] and coal rank[17, 24, 25]) on the degradation of coal. Esterle et al. (1994) did test the influence of a particle's bedding plane orientation relative to the applied force for Australian coal.[24] Two of the particle properties that show an influence on the degradation of other ores, but have not been tested for South African coal, are the shape of a particle and the orientation of a particle relative to the applied load.[26] Chapter 2 and Chapter 3 focus on identifying these shortcomings, and exploring the influence of particle shape and impact orientation on coal degradation.

Another aspect of breakage that has been studied for other minerals and agglomerates such as cement clinker, but not extensively for coal, is the effect of the microstructure of the coal on degradation. One author, Esterle et al. (2002), investigated the influence of coal lithotypes on the degradation of a borehole core sample during drop shatter tests, and found that the bright-banded lithotypes (vitrinite-rich lithotypes) tended to form smaller progeny than the dull lithotypes.[17] The effect of microstructure, especially the crack and cleat network, has been studied for the sequestration of CO_2 in un-mineable coal seams, where it is important to know how the cracks and cleats are connected, and what the main direction of flow for gasses will be. In order to study the crack and cleat network in coal samples during CO_2 capture and sequestration micro-focus X-ray computed tomography (µCT) was used to identify and analyse the crack networks.

Aims of the thesis

This thesis forms part of a larger study that aims to determine fundamental coal degradation characteristics, and using these fundamental degradation characteristics, predict coal degradation during transport and storage.

The aims of this thesis were to:

- Perform a detailed review of the literature, available at the North-West University, on the degradation of coal to identify any coal properties that, although these properties influence degradation, have not been thoroughly studied for coal.

- Identify a model that can be used to predict the particle size distribution of a South African coal particle after degradation.

- Determine the influence that the shape of a coal particle, as well as the orientation of the particle during impact, has on the degradation characteristics of a single coal particle.

- Suggest micro-focus X-ray computed tomography (µCT) as a probable technology that can be used as an analytical probe to investigate the influence that the coal microstructure has on the degradation characteristics of coal.

- Perform a detailed review of the literature available on the use of µCT in the geosciences, with a specific focus on coal studies.

- Confirm the applicability of µCT as an analytical probe to study the influence of coal microstructures on the degradation of coal during compression breakage, impact breakage, and during thermal shock.

- Determine which of the microstructures, identified using µCT, had an influence on the degradation of a single coal particle during compression breakage, impact breakage and thermal treatment.

- Clarify the influence that the microstructures of a single particle have on the degradation characteristics of that coal particle.

- Predict the progeny particle size distribution of a single particle subjected to impact breakage using the knowledge gained on the influence of the various microstructures on the degradation characteristics of coal.

Number of samples

Due to the exploratory nature of the thesis and the time necessary to acquire and analyse the tomograms generated during the study, only a small number of samples (30 particles were scanned using µCT for impact, compression, and thermal breakage) were used during this investigation. This resulted in a less than optimal statistical representation. Chapter 3 shows that even a tenfold increase in the number of individual particles analysed will not increase the statistical significance of the data. To ensure statistically representative data, a prohibitively large number of individual particles would have had to be investigated. As a result the data presented is phenomenological rather than deterministic or statistical.

Definition of fines

In the South African context fines are usually defined as particles between 1 mm and 0.1 mm, while ultra-fines are defined as particles smaller than 0.1 mm. However, in this thesis, fines are defined on the basis of the parent particle from which the progeny particle was produced. If progeny particles are smaller than $^{1}/_{10}^{th}$ the size of the parent particle the particle is defined as fine. This is in line with the concept used by Shi and Kojovic (2007) when defining the t_{10}-index.[27, 28]

Hypothesis

It is hypothesised that the shape of a coal particle, the orientation of a coal particle relative to the impact surface, the orientation of the coal particle's bedding plane relative to the applied force, and the microstructure (pre-existing cracks and cleats, boundaries between coal microlithotypes of varying density, and the boundaries between coal microlithotypes and mineral inclusions) of a loaded coal particle will all influence the breakage and degradation of the coal particle. These influences will be predictable, and if the shape, orientation, and microstructure distribution of a particle are known, the progeny particle size distribution of a coal particle can be predicted using a modification of the t_{10} degradation model.

Scope and contents of the thesis

The thesis consists of two manuscripts that review coal degradation (Chapter 2) and micro-focus X-ray computed tomography (Chapter 4) respectively, three articles (Chapter 5, Chapter 6, and Chapter 7), in various stages of publication, and one published conference paper (Chapter 3). Figure 1.2 shows the flow of the thesis graphically to emphasise that the

second review manuscript (Chapter 4) was written in response to the conclusions drawn in Chapter 3, and separates the review manuscripts, conference paper, and articles into separate columns. Each of the individual manuscripts addresses a specific aspect of the hypothesis. The following section gives the scope and aims of each individual manuscript.

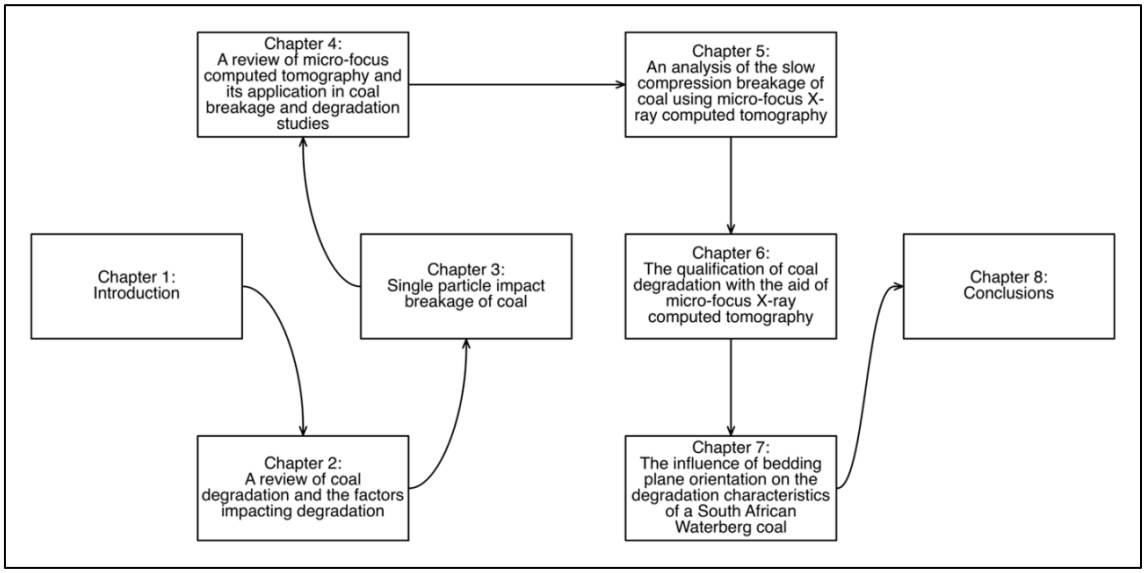

Figure 1.2: Thesis flow

Chapter 2: Breakage review

The aim of Chapter 2 is to introduce coal degradation, the properties that influence degradation, the methods used to test degradation, and the methods used to model degradation. Chapter 2 further aims to identify any shortcomings in the coal degradation literature. The comprehensive literature study identified a number of material properties, and some properties of the apparatus used to test degradation, that influences the degradation. In Chapter 2 it was concluded that there was very little literature that show the effect of the particle shape on the degradation of coal, as well as the influence that the orientation during impact has on the degradation of coal. The degradation model used by Shi and Kojovic (2007) (a modification of the JKMRC breakage model) was identified as a likely model that can be used to predict the influence of shape and impact orientation on coal degradation.[27]

Chapter 3: Single particle impact breakage of coal

Chapter 3 aims to elucidate the effect that the shape and impact orientation of coal particles has on the breakage of individual particles during single particle impact breakage as well as

to confirm the influence of particle size on the breakage of Highveld coal. It was confirmed that the size of a particle affects the degradation of coal, as the particle size increase the amount of fines produced increased. Chapter 3 shows that the particle shape and impact orientation affects the degradation: slab-like particles (a particle where one of the three orthogonal dimensions is significantly smaller than the other two) that impact onto the largest surface showed the most degradation while cubic/blocky particles (a particle where all three orthogonal dimensions are similar) that impacted on a point or protrusion showed the least degradation. Although it is clear that the particle shape and impact orientation does influence degradation, no insight could be gained into why the particle shape and impact orientation influences the degradation of coal. One possible explanation suggested during the study was that the microstructure of the parent particle will influence the degradation. The influence of the microstructure on the degradation of coal will be explored further in Chapter 4, Chapter 5, Chapter 6 and Chapter 7. From Chapter 3 it is also clear that the t_{10} degradation model cannot be used to accurately predict the degradation of a Highveld coal. The t_{10}–index (the mass percentage of progeny smaller than $^{1}/_{10}^{th}$ the parent particle's size) however, is a very convenient index to quantify degradation using a single number. In the rest of the thesis, the t_{10}–index will be used to quantify degradation as a single number.

Chapter 4: Micro-focus X-ray computed tomography review

In order to determine the effect of microstructures on coal degradation, it was first necessary to identify which structures in coal will affect the degradation, and to track the changes that occur during a loading event. Chapter 4 introduces micro-focus X-ray computed tomography (µCT) as a likely technology that has the capabilities required to identify the microstructures present in coal. Chapter 4 describes the µCT process, and relevant physics involved in the process, as well as a broad summary of the application of µCT in the geosciences, coal breakage studies and coal degradation studies.

Chapter 5: An analysis of the slow compression breakage using µCT

Chapter 5 aims to confirm that µCT can be used to identify the microstructures that will likely affect coal degradation, as well as tracking the changes that occur during the compression breakage of single coal particles. The microstructures that were identified as pertinent to coal degradation were pre-existing cracks, the boundaries between mineral inclusions and coal microlithotypes, and the boundaries between coal microlithotypes with different densities. Chapter 5 confirmed that µCT has the capability to identify and track specific features present in a coal particle. A number of changes to the experimental setup were suggested that may increase the accuracy, and significance of the data generated using

µCT. Although the focus of the study remains coal degradation during impact, degradation during compression is easier to control, and allowed the capabilities of µCT too be demonstrated without introducing to many variables.

Chapter 6: The qualification of coal degradation with the aid of µCT

Chapter 6 aims to verify the results obtained for compressive loading (Chapter 5) can be obtained for impact degradation, and to test if µCT can be used to track the changes that occurred during thermal degradation. Chapter 6 further aims to determine the efficacy of the changes to the experimental setup suggested in Chapter 5. Chapter 6 demonstrated that all of the features that contributed to the degradation during compression did contribute to degradation during impact. The thermal degradation tests showed that the features that contributed to thermal degradation could also be identified and tracked. Again a number of shortcomings in the experimental setups were identified for consideration during further studies.

Chapter 7: The influence of bedding plane orientation on the degradation characteristics of a South African Waterberg coal

Chapter 7 aims to utilise µCT to determine if the effect of the various structures identified in Chapter 5 and Chapter 6 can be quantified and used to predict the degradation of a single particle that is subjected to impact loading. It was found that the effect of the microstructures present in a single coal particle can be quantified, but the results cannot be used to predict the particle size distribution of a single particle. The distribution of a population of particles, however, can be fitted using a Rosin-Rammler distribution.

Chapter 8: Conclusions

In Chapter 8 the information that were generated in Chapter 2 through to Chapter 7 are collated, and the pertinent conclusions of the various chapters summarised. Chapter 8 gives a number of suggestions that may improve the application of µCT to any future degradation research. One burning question that still remains after the information in Chapter 2 through to Chapter 7 were assimilated, is what determines whether a feature that is present in the coal will contribute to the final network of cracks?

Chapter 1 - References

1. Chaline, E. 2012. Fifty minerals that changed the course of history. Cape Town: Struik Nature.

2. Osborne, D., *ed*. 2013. The Coal Handbook: towards cleaner production. Vol. 1: coal production. Cambridge: Woodhead. (Woodhead Publishing Series in Energy).

3. Höök, M. & Aleklett, K. 2010. A review on coal-to-liquid fuels and its coal consumption. *International journal of energy research*, 34(10):848-864.

4. Jeffrey, L. 2005. Characterization of the coal resources of South Africa. *Journal of the South African Institute of Mining and Metallurgy*, 105(2):95-102.

5. Mohale, S., Masetlana, T.R., Bonga, M., Ikaneng, M., Dlambula, N., Malebo, L. & Mwape, P. Department of Mineral Resources. 2015. South Africa's mineral industry 2013-2014. Pretoria.

6. Ansolabehere, S., Beer, J., Deutch, J., Ellerman, A., Friedmann, S., Herzog, H., Jacoby, H., Joskow, P., Mcrae, G. & Lester, R., *eds*. 2007. The future of coal: options for a carbon-constrained world. Cambridge, MA: Massachusetts Intitute of Technology.

7. Hancox, P.J. & Götz, A.E. 2014. South Africa's coalfields: a 2014 perspective. *International journal of coal geology*, 132:170-254.

8. Scholtz, J., Du Plessis, K., Roche, R., Cresswell, M., Toerien, L., Voges, J., Reddy, D., De Korte, J., Craddock, M., Lok, G., McMillan, K., Buthelezi, V., Darley, P., Jacobs, J., Campbell, Q.P. & Jacobs, J., *eds*. 2015. Coal preparation in Southern Africa. 5th ed. Witbank: Southern African Coal Processing Society.

9. SABS. 2004. South African guide to the systematic evaluation of coal resources and coal reserves. Pretoria: Standards South Africa.(South African National Standard (SANS) 10320:2004).

10. Anon. Department of Energy. 2001. National inventory discard and duff coal. Pretoria.

11. Teo, C., Waters, A. & Nicol, S. 1990. Quantification of the breakage of lump materials during handling operations. *International journal of mineral processing*, 30(3):159-184.

12. Tao, D., Groppo, J.G. & Parekh, B.K. 2000. Enhanced ultrafine coal dewatering using flocculation filtration processes. *Minerals engineering*, 13(2):163-171.

13. Sahoo, R.K. & Roach, D. 2005. Effect of different types of impact surface on coal degradation. *Chemical engineering and processing*, 44(2):253-261.

14. Menacho, J.M. 1986. Some solutions for the kinetics of combined fracture and abrasion breakage. *Powder technology*, 49(1):87-95.

15. Sahoo, R. 2007. Degradation characteristics of steel making materials during handling. *Powder technology*, 176(2):77-87.

16. Tavares, L.M. & de Carvalho, R.M. 2011. Modeling ore degradation during handling using continuum damage mechanics. *International journal of mineral processing*, 101(1–4):21-27.

17. Esterle, J., Kolatschek, Y. & O'Brien, G. 2002. Relationship between in situ coal stratigraphy and particle size and composition after breakage in bituminous coals. *International journal of coal geology*, 49(2):195-214.

18. Sahoo, R. & Roach, D. 2005. Degradation behaviour of weathered coal during handling for the COREX process of iron making. *Powder technology*, 152(1–3):1-8.

19. Sahoo, R., Weedon, D. & Roach, D. 2004. Single-particle breakage tests of Gladstone Port Authority's coal by a twin pendulum apparatus. *Advanced powder technology*, 15(2):263-280.

20. Sahoo, R. & Roach, D. 2005. Quantification of the lump coal breakage during handling operation at the gladstone port. *Chemical engineering and processing*, 44(7):797-804.

21. Sahoo, R., Weedon, D. & Roach, D. 2004. Degradation model of Gladstone Port Authority's coal using a twin-pendulum apparatus. *Advanced powder technology*, 15(4):459-475.

22. Broadbent, S. & Calcott, T. 1957. Coal breakage processes: the analysis of a coal transport system. *Journal of the institute of fuel*, 1957(30):13-25.

23. Sahoo, R. 2006. An investigation of single particle breakage tests for coal handling system of the gladstone port: a review. *Powder technology*, 161(2):158-167.

24. Esterle, J., O'Brien, G. & Kojovic, T. 1994. Influence of coal texture and rank on breakage energy and resulting size distributions in Australian coals. (*In* 6th Australian Coal Science Conference, Newcastle, NSW: Australian Institute of Energy. p. 175-181).

25. Pan, J., Meng, Z., Hou, Q., Ju, Y. & Cao, Y. 2013. Coal strength and Young's modulus related to coal rank, compressional velocity and maceral composition. *Journal of structural geology*, 54:129-135.

26. Chandramohan, R., Holtham, P.N. & Powell, M. 2010. The influence of particle shape in rock fracture. (*In* XXV International Mineral Processing Congress 2010 organised by Australasian Institute of Mining and Metallurgy, Brisbane: The Australasian Institute of Mining and Metallurgy. p. 3163-3171).

27. Shi, F. & Kojovic, T. 2007. Validation of a model for impact breakage incorporating particle size effect. *International journal of mineral processing*, 82(3):156-163.

28. Genç, Ö. & Benzer, A. 2009. Single particle impact breakage characteristics of clinkers related to mineral composition and grindability. *Minerals engineering*, 22(13):1160-1165.

Chapter 2 - A review of coal degradation and the factors impacting degradation

Chapter 2 is a detailed literature review of coal degradation when subjected to impact breakage, compression breakage, and rapid temperature increases. A number of properties that influence coal degradation are identified and reviewed. The methods used to test coal degradation and the models used to model coal degradation were also identified and reviewed. From the review, gaps in the current knowledge base were identified.

Abstract

Coal fines negatively impact all parts of coal beneficiation and utilisation processes, and are poorly understood. This is a review of available literature on the physical properties that influence coal degradation, as well as the methods used to test and model coal degradation. Degradation due to impact, compression, and thermal stresses will be considered in an effort to establish potential gaps in the available literature, specifically any gaps that exist in terms of the influence of particle properties on the degradation of coal.

From literature, it is clear that a myriad of properties can have an influence on the degradation characteristics of various ores; these properties include the particle size, particle shape and composition, coal rank, breakage energy, impact surface, heating rate, and residence time in a reactor. Of the properties that influence the degradation characteristics of coal, the influence of particle shape, impact orientation, and coal microstructure was not well established. Any future fundamental research that clarifies the effect these properties have on coal degradation will greatly contribute to the existing body of coal degradation literature.

Degradation

The degradation of coal, or the unwanted production of fines, is a big problem facing coal producers and users the world over.[11, 15, 16, 18, 29] The presence of unwanted fines in a coal product can negatively impact many bulk coal properties including voidage, particle size distribution (PSD) and moisture content. The voidage and PSD of bulk coal is important for the utilisation of coal where it affects the hydrodynamic behaviour in the reactors, a PSD that is too fine can cause channelling and uneven reaction zones.[11, 13, 15, 20, 21, 29-35] This, in turn, will negatively affect the efficiency of these processes. The PSD of bulk coal affects the price of the coal, as large lump coal demands a higher price in some markets (feed to the COREX process, blast furnaces and sinter plants) than fine particles.[11, 15, 20] Some contracts also stipulate penalties be paid should the product specifications not be fulfilled; minimum product size and moisture content are two of quality parameters that are commonly specified.[11, 15, 20] The moisture content of coal is influenced by the percentage fines present:[36, 37] as the fines increase so does the moisture content due to the increased surface area, and decreased interparticulate voidage compared to lump coal. The higher moisture content of fine coal will increase the transport cost, and simultaneously decrease the nett-as-received (NAR) calorific value of the coal.[35-38] So, a decrease in the fines percentage will reduce the transport cost, and increase the NAR calorific value.[12, 36, 37]

Coal degradation can occur at various steps within the mining, coal beneficiation and coal utilisation process value chains.[11, 13, 15, 16, 18, 20, 21, 35, 38, 39] This includes degradation that occurs at the coal face due to high energy mining methods i.e. blasting in open pit mining and the use of continuous miners in underground mining. During transport, coal degrades due to the movement of conveyors over its idler rollers and at transfer points where coal is moved from one conveyor to another. Coal also undergoes degradation when it is dropped from the conveyors into silos and onto stockpiles; and again when the coal is reclaimed from the silos or stockpiles. Thermal degradation (fragmentation and exfoliation) occurs at the inlet to heated reactors due to high particle heating rates and increased internal particle pressure due to devolatilisation.[30, 32, 33, 40-45]

A better understanding of coal breakage fundamentals may help to minimise or alleviate coal degradation during mining, beneficiation, and utilization as well as improve degradation modelling.[24, 26, 31, 32, 46-50]

Degradation mechanisms

During mechanical processes coal degrades through either attrition or fracture, and during thermal processes coal degrades through either fragmentation or exfoliation.[11, 14, 15, 20, 32, 35, 40, 44, 45, 51] The various degradation mechanisms are defined by the progeny of the degraded coal. Fracture or volume breakage occurs when the breakage energy applied to the coal is in excess of the particle strength; the resultant progeny has a wide distribution of particle sizes, all smaller than the parent particle.[11, 15, 20, 51] Another definition for volume breakage, used by Tavares and de Carvalho (2011), is if a particle lost more than 10% of its initial mass.[16] Attrition or surface breakage occurs when coal degrades at energies below the particle strength; the resultant progeny has a very narrow size distribution with a single particle close to the initial size of the parent.[11, 15, 20, 51] Fracture is the main mechanism during large drops, whilst attrition is the main mechanism during rolling or sliding.[15] However, fracture rarely occurs in isolation:[14, 51] if the stress applied is sufficiently large, particles will experience fracture as well as attrition at the contact points.[51, 52] Figure 2.1 shows example discrete particle size distributions for particles experiencing fracture (volume breakage) and attrition (surface breakage).[51]

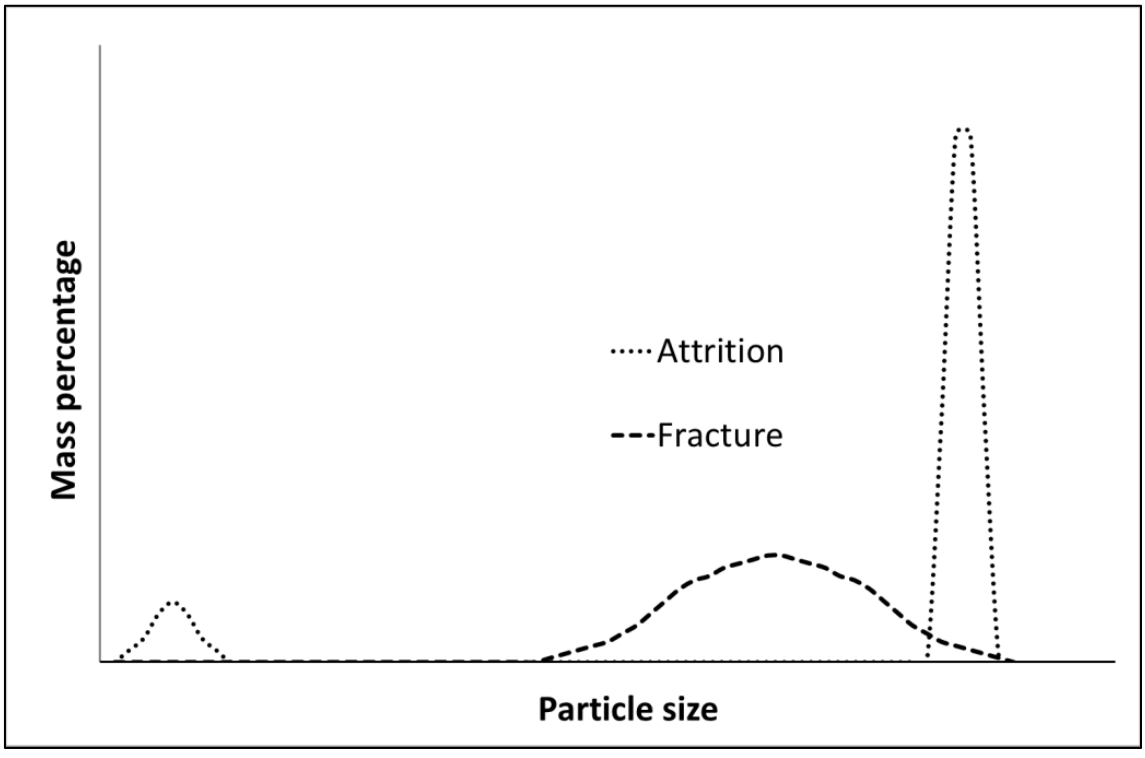

Figure 2.1: Example PSD (after Kelly and Spottiswood (1982))[51]

Particle degradation during thermal stress is a combination of exfoliation and fragmentation at the particle centre.[32, 40, 44, 45] Exfoliation is due to thermal stresses, and progeny are

produced from the outer shell of the particle; exfoliation results in a narrow particle size distribution.[31, 32, 40-45] Fragmentation at the particle centre occurs as a result of pressure build-up during devolatilisation, resulting in overpressure at the particle centre; fragmentation products show a wide particle size distribution.[31, 32, 40-45] The conditions that determine the degradation mechanism is the particle size, temperature, and heating rate: small particles, high temperatures, and high heating rates tend to favour exfoliation; whilst large particles, lower temperatures, and lower heating rates tend to favour fragmentation.[43, 44] There is, however, no clear distinction. A single particle of sufficient size may also undergo multiple breakage events i.e. exfoliation, fragmentation or both.[43, 44]

Crack propagation theories

Irrespective of the degradation mechanism, breakage occurs due to the fatal propagation of tiny flaws in the material.[32, 47, 51, 52] According to Wang and Shrive (1995) the similarities between the brittle fractures of various materials point to a common cause for fracture.[53] This implies that the fracture of coal can be superficially compared to the fracture of other brittle materials. It is commonly held that all fatal cracks that form during brittle fracture initiates at flaws within the particle.[51] These flaws refer to any pre-existing discontinuity within the particles: cracks, pores, cleats, mineral inclusions, grain boundaries, or other boundaries such as microlithotype boundaries in coal.[54]

In his treatise, Inglis (1913) stated that the cracks and other flaws within the particle act as concentrators allowing a force that is usually not sufficient to damage a brittle material, to fatally damage the material.[55, 56] He deduced, mathematically, how much the force that is applied to a test specimen will be amplified by holes of various shapes and sizes.

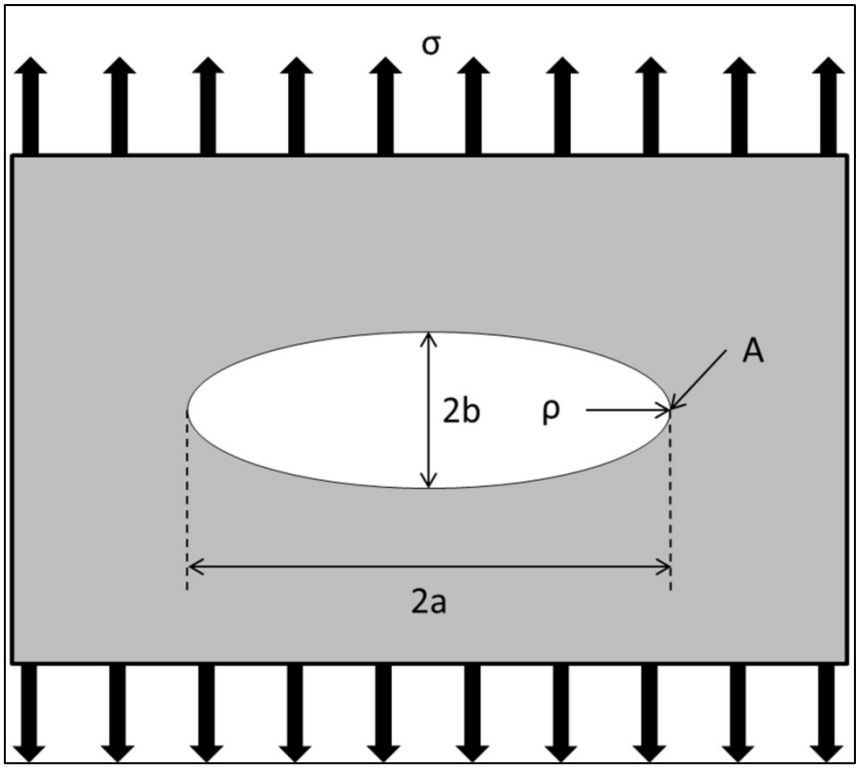

Figure 2.2: Inglis crack

Considering the plate and hole in Figure 2.2, Inglis (1913) derived the formula in Equation 2.1 to calculate the concentration of force that occurs at point *A* along the edge of an elliptic hole. An idealised crack can be seen as an ellipse that is significantly longer than it is wide.

$$\sigma_A = \left[1 + 2\sqrt{\frac{a}{\rho}}\right] \qquad \text{Equation 2.1}$$

Where *ρ* is the radius of the curve at the end of the ellipse (Equation 2.2)

$$\rho = \frac{b^2}{a} \qquad \text{Equation 2.2}$$

If enough tension is applied to the crack it will start lengthening; as the length of the crack increases the forces at the tip of the crack will be concentrated to a larger degree until the crack lengthens uncontrollably and the specimen fails.

Griffith (cited by Fischer-Cripps (2007)) extended the work of Inglis (1913) by considering the size of a flaw and the energy balance around the crack tip; he stated that all materials

contains a large population of randomly distributed flaws, and for a crack to propagate the molecular bonds at the crack tip must be broken, and the energy released at the tip of the crack must exceed the energy required to form the two new surfaces.[11, 15, 47, 52, 56-58]

Properties influencing degradation

The amount of degradation, and the type of degradation mechanism by which degradation occurs, is highly dependent on both the properties of the coal that is being handled as well as the properties of the machines used to handle or utilise the coal.[17, 50, 59]

The most obvious influence on the breakage of coal is the energy that is imparted to the coal during the breakage event. The degradation of coal will increase as the strain rate increases during compression tests, or the impact velocity increases during single or double impact tests.[11, 13, 15, 17-20, 23, 24, 39, 48, 50] Other than the breakage energy various properties have an influence on the degradation of coal:

Particle size

Particle size greatly influences the breakage of coal particles that are loaded or heated. The typical trend is for bigger particles that are compressed or impacted to produce more degradation products.[13, 15-17, 19, 20, 23, 24, 27, 60-63] This phenomenon is commonly held to be due to the distribution of flaws within the particles.[24, 29, 49, 64] As the size of a particle increases so does the amount of flaws within the particle that are able to act as force concentrators and initiate a crack. Another possible explanation for the decrease in strength as particle size increases, is that as the particle size increases the size of the possible flaws increase as well, thereby increasing the force concentration at the crack tip resulting in a weaker particle (see Equation 2.1).[65] Scholtès et al. (2011) showed, using discrete element modelling, that, if the distribution of flaws within a coal particle stayed constant as the particle size increased, the strength of the coal remained constant.[66]

Particle size also influences the fragmentation of thermally stressed particles. As the size of the particle increases so does the fragmentation. This is due to the increased devolatilisation pressure build-up in larger particles.[30, 40, 43, 45] Dacombe et al. (1999), however, suggested that the apparent correlation between particle size and fragmentation count is due to the decreased strength of the coal particle rather the size of the particle specifically.[40]

Particle shape & Impact orientation

The shape and orientation of coal particles influence the breakage of the particles.[13, 26, 67, 68] Chandramohan et al. (2010) found a difference in the breakage characteristics of granite between slab-like particles and cubic particles.[26] The amount of breakage experienced by a slab-like particle is dependent on whether the particle is loaded onto the larger or the smaller surface area. Slab-like particles that are loaded onto the smaller surface area show less degradation than the cubic particles and slab-like particles impacted unto the larger surface area show more degradation than the cubic particles.[26, 68]

The orientation of the bedding planes within a coal particle also influences the breakage characteristics.[24, 67] Esterle et al. (1994) found that coal impacted with its bedding plane parallel to the applied force (along the bedding plane) showed more degradation than particles impacted with its bedding plane perpendicular to the applied force.[24]

Coal microstructure

Work done by Lindqvist et al. (2007) show a dependence between the microstructure and strength of an ore.[54] The microstructures that influence the breakage characteristics of the ore were the mineralogy of the ore, grain size, boundary shape, mineral orientation and porosity as well as pre-existing cracks within the ore.[54] Greater disorder (wider grain size distribution, less orientated structures and more complex grain boundaries), and smaller structures (smaller grain sizes) increase the resistance to breakage, whilst, large ordered structures decrease the resistance to breakage. The properties of the individual minerals that constitute the ore limit its properties i.e. the ore strength is limited by the strength of the individual minerals.

Although coal has an inherently disordered structure due to its depositional nature, some analogies can be drawn between coal and other ores in the way that the microstructures react during breakage. The microstructure in coal that may influence the breakage characteristics are the lithotype boundaries, lithotype-mineral boundaries, as well as pre-existing cracks and cleats.[67, 68] These structures can act as force concentrators that aid in the initiation of cracks, in propagating cracks, or act as discontinuities halting crack propagation.[17, 31, 54, 65, 67, 69]

Nie et al. (2014) found that during the compression breakage of a coal block the new cracks form along the boundaries between the coal matrix and skeleton.[70] Hlatshwayo et al. (2007) found that, during pyrolysis, new cracks formed on the boundaries between two different

macerals, as well as on the boundaries between coal and minerals.[31] Esterle et al. (2002) found that the weaker macerals tend to be the first to break, and thicker lithotypes show less resistance to breakage when compared to thinner lithotypes consisting of the same maceral.[17]

Mineral matter

The boundaries between the mineral matter and the coal matrix can either aid the propagation of a crack, or act as a discontinuity and arrest a propagating crack.[52] According to Ward (2002) the mineral matter present in coal is either detrital or precipatory in nature.[71] The biogenic precipatory mineral matter is the transformed remains of phytoliths, diatoms, molluscs and other organisms. Other precipatory minerals were present as dissolved salts during peat formation, as the coalification took place these minerals precipitated into the coal matrix. Some minerals precipitate during the formation of the coal seam (syngenetic), others after the seam formed (epigenetic). The epigenetic mineral formation usually takes place in other epigenetic structures, like cleats and cracks, filing the open space with minerals; while[71] syngenetic mineral inclusions usually occur as discrete inclusions (see Figure 2.3 for a graphical representation).[71]

Man et al. (1998) found that, for very fine particle sizes (<150 µm), as the particle size decreased the mineral matter increased.[72] The increase in mineral matter was attributed to the separation of discrete mineral grains from the coal matrix.[72] Eswaraiah et al. (2008) showed that fines generation in an impact crusher increased with an increase in carbon content, and decreased with an increase in moisture content and mineral matter content.[29]

Maceral and lithotype composition

Coal macerals and lithotypes are the petrographic constituents that form during diagenesis, or coalification, of coal. Depending on the conditions prevalent during the diagenesis and the plant materials that are available, different macerals will form.[73, 74] Coal consists of an organic and inorganic component. The organic component is the macerals that are present in coal, classified as vitrinite, inertinite, and liptinite.[73, 74] Coal also includes a number of minerals that can be closely associated with the coal macerals. Different combinations of the macerals are called microlithotypes. Table 2.1 gives an overview, albeit non-exhaustive list, of microlithotypes and its compositions.[73] In order for any individual maceral or mineral to contribute to the naming of the microlithotype it must constitute more than 5% of the total area. If the minerals in the microlithotype constitute more than 20% (more than 5% for Pyrite) of the area it is considered a carbominerite.

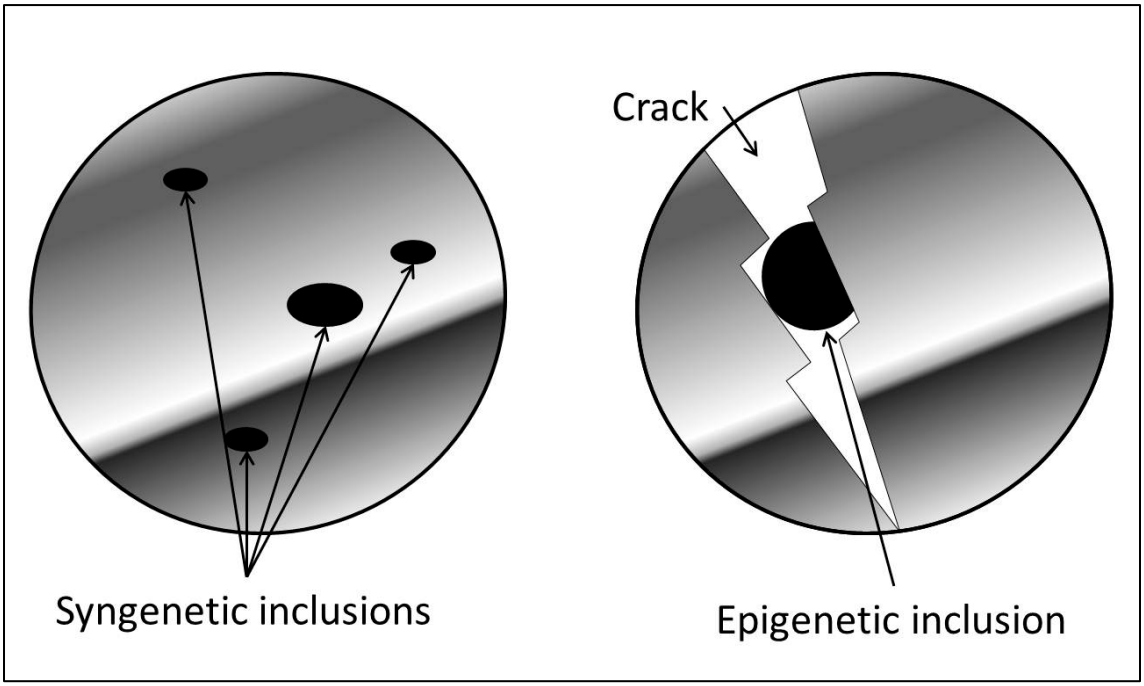

Figure 2.3: Graphic representation of syngenetic and epigenetic inclusions (after Falcon and Snyman (1986))[74]

As the macerals that constitute the microlithotypes have differing breakage properties, each microlithotype will have breakage properties that are dependent on the maceral composition.[24, 75] Vitrinite is very brittle due to cracks and cleats that form because of shrinkage that occur during diagenesis, whilst liptinite and inertinite raise the strength of the coal.[64, 74, 76, 77] Esterle et al. (2002) demonstrated that, when a drill core is repeatedly dropped the vitrinite rich lithotypes concentrated in the smaller fractions, thereby confirming this hypothesis.[17]

The thickness of the lithotype can also contribute to the strength, with the thicker lithotype layers showing a decrease in strength.[17] There is a correlation between the coal rank and its strength; according to Pan et al. (2013), the compressive strength of coal increases as it ages.[25] Pan et al. (2013) used the vitrinite reflectance to correlate the Young's modulus and uniaxial compressive strength, and suggested that the increase in coal strength is due to the increased ordering that accompanies an increase in the coal rank or an increase in the degree of maturity. On the other hand, Esterle et al. (1994) found that the energy required for single particle breakage decreased as coal rank increased.[24]

Table 2.1: Microlithotype Composition[73]

Microlithotype	Maceral Composition	Group
Vitrite	Vitrinite > 95%	Monomacerals
Liptite	Liptinite > 95%	
Inertite	Inertinite > 95%	
Clarite	Vitrinite + Liptinite > 95%	Bimacerals
Durite	Inertinite + Liptinite > 95%	
Vitrinertite	Vitrinite + Inertinite > 95%	
Duroclarite	Vitrinite > Liptinite, Inertinite (min 5%)	Trimacerals
Vitrinertoliptite	Liptinite > Vitrinite, Inertinite (min 5%)	
Clarodurite	Inertinite > Vitrinite, Liptinite (min 5%)	
Carbominerite	Coal + 20 – 60% (volume %) mineral matter (5-20% if Pyrite)	Carbominerite

Pre-existing cracks and cleats

Cleats are fractures that occur naturally in coal due to diagenesis and tectonic processes.[76] Cleats are classified as either face cleats or butt cleats: face cleats are the set of fractures that form first resulting in longer cracks, while the butt cleats often terminate in face cleats. The face- and butt cleats usually occur perpendicular to one another, and also perpendicular to the coal bedding plane.[76]

Cracks and cleats that are present in the coal before loading provide points where new cracks can initiate from, as well as routes along which cracks can propagate.[64, 67, 75, 78] The presence of pre-existing cracks can also halt propagating cracks, and increasing the resistance to breakage of a particle.[57, 67, 78]

Moisture & volatile matter

Many authors have tried to relate the moisture, volatile matter, and mineral matter content to the strength of coal.[25, 29, 40, 42, 43, 45] Senneca et al. (2009) showed that higher moisture

content in bituminous coal increased the fragment count when the coal particles were subjected to a sudden temperature increase, although no possible explanation was given for this phenomenon.[42] Eswaraiah et al. (2008) showed that fines generation in an impact crusher increased with an increase in carbon content and moisture, but decreased with an increase in mineral matter content.[29] Vuthaluru et al. (2003) found that as the moisture content of a Western Australian coal increased, so did its Hardgrove grindability index.[79]

Weathering

As coal is exposed to the elements its moisture content changes due to changes in humidity and wetting during rain. Coal particles can swell and shrink as a result of moisture content variations. As the inside and outside of a coal particle lose and gain moisture at different rates it also swells and shrinks at different rates, causing cracks to form at or near the surface of the particle.[18] These cracks on the surface of the coal will increase the friability of the coal and reduce its strength. Sahoo (2007), and Sahoo and Roach (2005) found that this weakening of coal occurs for up to nine months of storage; after nine months the generation of fines did not significantly increase for longer periods of weathering.[15, 18]

Stabilisation and fatigue

As a particle is repeatedly loaded the particle strength decreases, this strength reduction is due to damage accumulation; damage accumulation can be a lengthening of existing flaws present in the particle or a production of new flaws.[16, 47, 49, 50, 80] Damage accumulation in particles can occur due to repeated impacts, compression cycles, multi-point compression cycles and thermal shock.[47]

When large populations of particles are subjected to repeated loading cycles the mean strength of the population initially increases as the weaker particles are removed from the population. The strength of the individual particles still decreases as damage is accumulated.[15, 16, 18, 81] In some cases the accumulation of damage within a particle can increase the strength of a particle by providing discontinuities that arrest cracks propagation.[80]

Cushioning and impact surface

When a large sample of sized coal is dropped from a drop-tower, the initial fines content has been found to reduce the amount of new coal fines produced.[11, 13, 15, 16, 18] As the initial fines content of the sample increases, the production of new fines decreases.[11, 13, 15, 16, 18]

Sahoo and Roach (2005) found that the surface onto which a coal particle impacts will influence the degradation of the particle. The highest amount of fines is produced when a particle is impacted onto a steel surface, whereas the least amount of degradation products are formed when a coal particle is impacted onto a bed of coal particles.[13, 15, 16]

Temperature, heating rate and residence time

The temperature to which, and the rate at which, a particle is heated will influence the thermal degradation of a coal particle.[44, 45] When a particle is exposed to high temperatures and heating rates, a large number of small progeny is produced from the outer shell of the particle, but, when a particle is exposed to lower temperatures and heating rates a small number of large progeny is produced from the centre of the particle.[43, 44]

The time a particle spends in the elevated temperatures will also affect the number of progeny that are formed. The fragment count increases up to a specific residence time, after this the fragment count decreases as the smaller fragments are completely burnt away.[40, 45]

Degradation testing and modelling

From the above summary, it is clear that many factors affect the degradation of coal. Some of the properties mentioned above are intrinsic to the testing apparatus used to determine the degradation, so it is necessary to differentiate between the various methods used to test the degradation. For the mechanical degradation of coal, the testing apparatus can be divided into four basic categories: single impact tests, double impact tests, slow compression tests and tumbling tests.[11, 20, 23, 60, 82, 83]

Degradation testing

Single impact tests simulate the degradation that occurs during a drop, like the degradation that occurs at a conveyor transfer point.[23] These machines are of simple design and drop either a single particle or a large sample from a set distance. The impacted particle(s) are then collected and screened to determine degradation.[11, 20]

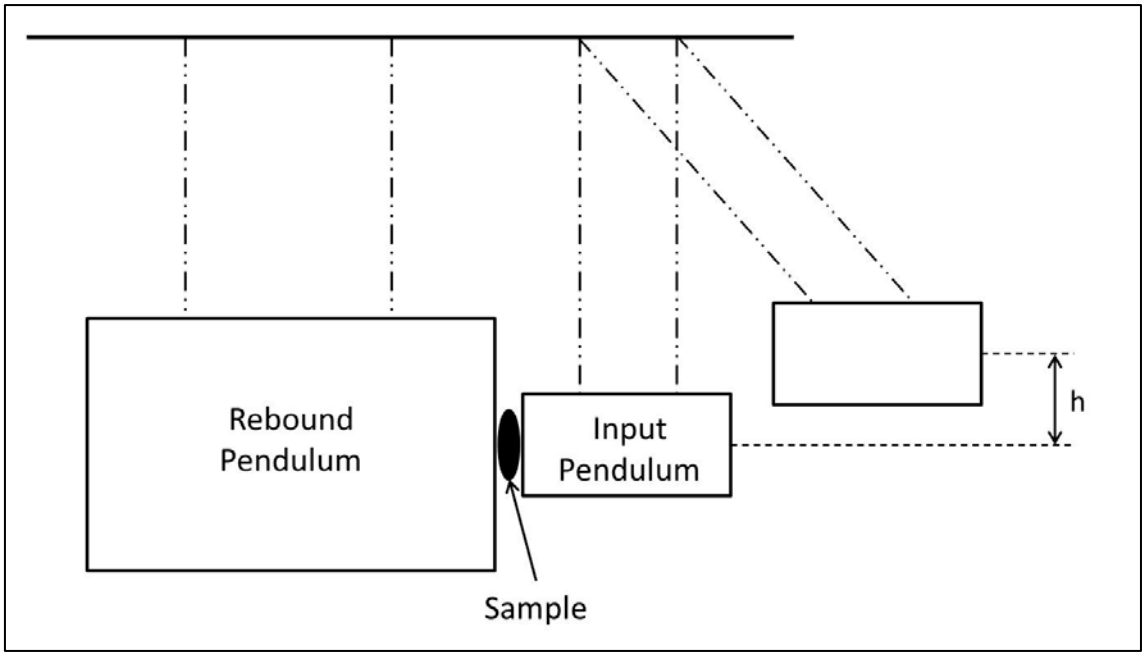

Figure 2.4: Double pendulum testing device (after Sahoo et al. (2004))[19]

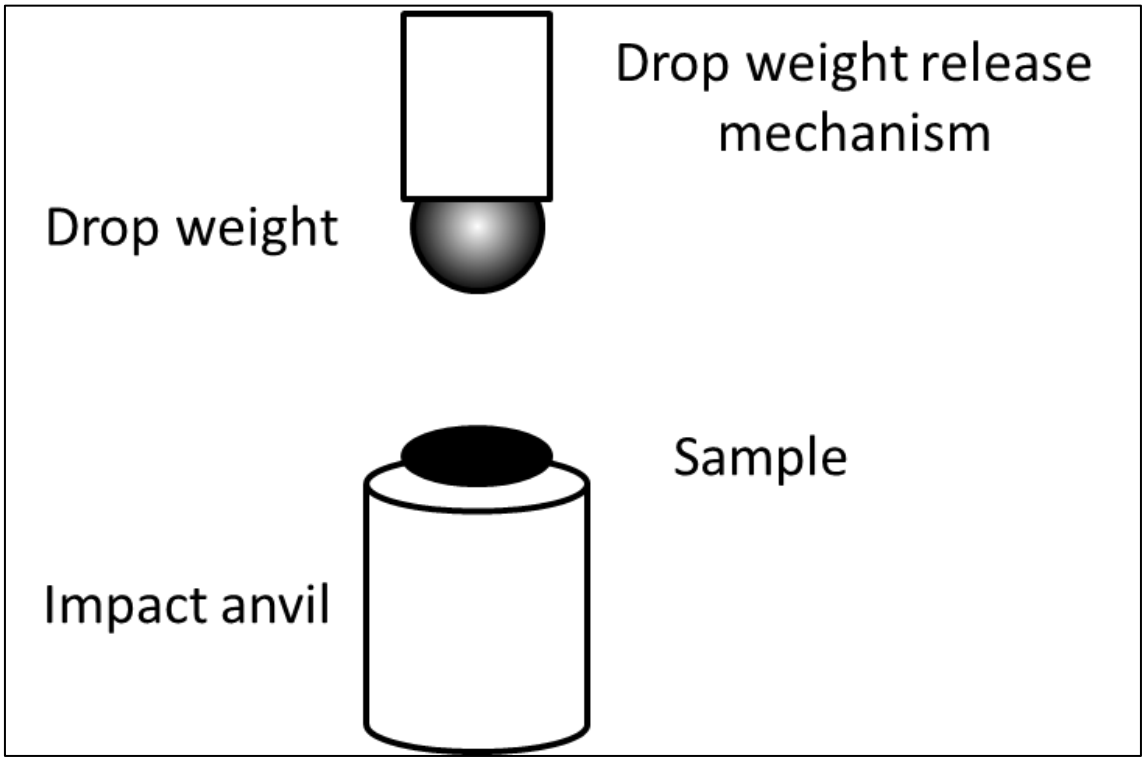

Figure 2.5: Drop weight test (after Bourgeois and Banini (2002))[84]

Double impact tests simulate a particle that is crushed quickly between two surfaces. Double impact tests are also exceptionally well suited to determine the specific breakage energy. The two common designs for a double impact test are pendulum or drop weight tests.[60]

Figure 2.4 shows the basic components of a pendulum test. The design consists of two pendulums that are restricted in motion to only a single plane. The particle is attached to the rebound pendulum. The impact pendulum is then raised to a specific height and let go, the impact pendulum then swings to strike the particle. Any energy that is not dissipated in the breakage of the particle or the generation of heat and sound (usually assumed to be negligible) causes the rebound and impact pendulum to swing back.[19, 23] By measuring the height that the two pendulums swing back to, the specific breakage energy can be determined.

Figure 2.5 shows a typical drop weight test.[84] Here the particle is placed on top of a stationary anvil, and a weight dropped onto the particle.[28, 83, 85] Again, by measuring the rebound height of the dropped weight the specific impact energy can be calculated. Often the anvil is equipped with stress sensors to determine the deformation of the anvil. From the rebound height of the dropped weight and the deformation of the anvil the specific breakage energy can be determined.[19, 47, 84]

In slow compression tests, the particle is placed between two platens that slowly move towards each other while the pressure applied and subsequent deformation is measured.[61, 70, 75, 86] This data is plotted on a load-extension curve (see Figure 2.6), which is used to determine the strength of the particle.

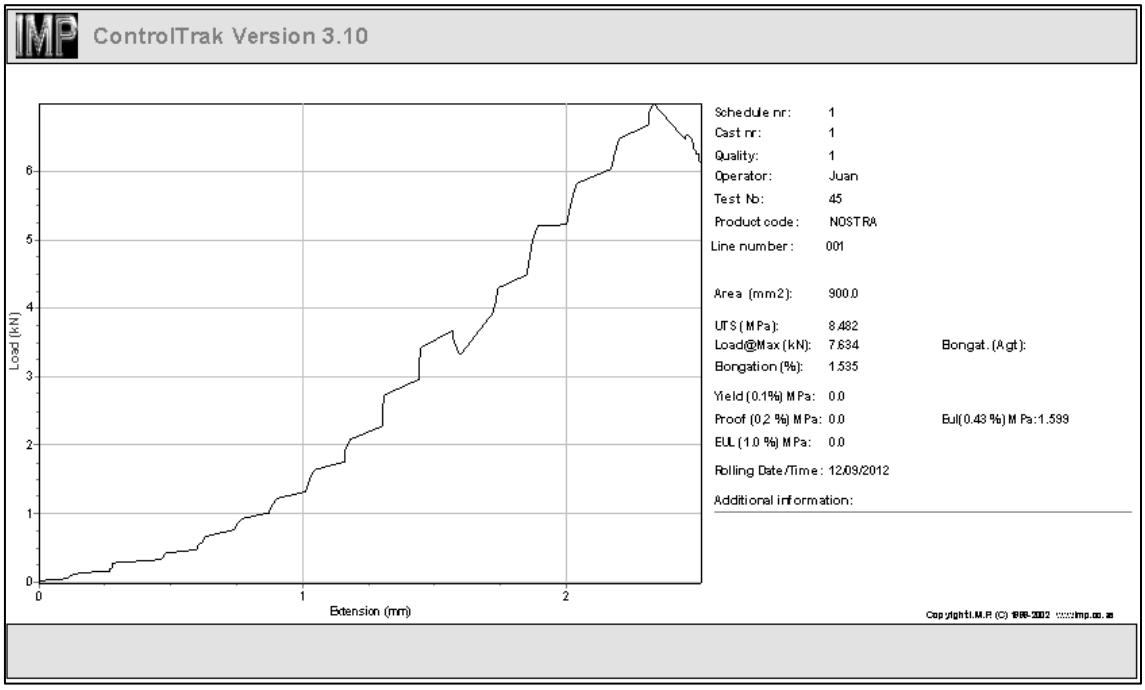

Figure 2.6: Example load-extension curve output of a Mansanto tensometer

Tumbling tests simulate the complex mechanisms that occur in tumbling mills, where a combination of impact, attrition and compression is responsible for comminution. A tumbling test, in its simplest form, is a drum filled with material and grinding media (known as the mill charge). This drum is then rotated for a set time or a set number of rotations; the charge is removed and screened to determine the breakage indices. This test has traditionally been used to determine parameters such as the Bond work index, Hardgrove Grindability Index and the breakage & selection functions. Sahoo and Roach (2005) used a tumbling test to determine the attrition degradation of coal.[11, 20] There is however some critique towards using tumbling test to determine the breakage characteristics, since the effect of volume breakage and attrition breakage cannot be separated.[11, 18]

To test the thermal fragmentation of coal, a number of tests were designed by various authors, but there is no single test that is widely used.[30, 33, 40-42, 44, 45, 87] Some of the experimental setups used are drop tube furnaces (DTF);[40] heated-strip reactors;[33, 41, 42, 44, 87] fluidised bed reactors;[45] muffle furnaces,[33] and industrial reactor turn-out.[30]

- The maximum temperature in the DTF used by Dacombe et al. (1999) was controlled in two zones: a high entrance temperature to simulate the temperature near burners and a lower exit zone to simulate the temperature near the exit of the combustion chamber. The residence time was determined by where in the DTF the fragmented particles were removed; the removal of the fragmented particles was achieved by a moveable, water cooled sampling probe.[40]

- Senneca et al. (2009) and Senneca et al. (2011) used a heated strip reactor to determine the primary fragmentation characteristics of coal.[42, 44] The coal was placed in the reactor, the reactor flushed with nitrogen and heated to the desired temperature. After a set time had passed, the reactor was turned off and the progeny removed.[42, 44] The strip reactor could achieve heating rates of up to 10^6 °C.min^{-1} and maximum temperatures of 2200 °C.[41, 42, 44] Senneca et al. (2011) also pressurised the reactor to enable tests to be conducted at a maximum pressure of 15 bar.[44]

- Zhang et al. (2002) used a small fluidised bed reactor loaded with a specific number of particles which ran for a pre-determined time to determine the breakage characteristics of coal in fluidised beds.[45]

- van Dyk (2001) used a muffle furnace heated to a maximum of 900 °C at a rate of 12 °C.min^{-1} to study coal fragmentation during pyrolysis.[33]

- Bunt and Waanders (2008) performed a turn-out of an industrial fixed bed gasifier and determined that primary fragmentation takes place in the drying and fast pyrolysis zones of the gasifiers.[30] The gasifier turn-out was done by de-pressurising and quenching the gasifier before slowly turning the grate at the bottom, and removing the material that fell through, layer by layer.[30]

All of the tests, except the reactor turn-out, that are used have at least two common features. Firstly, some method to increase the temperature of the sample rapidly to a temperature sufficient to cause fragmentation, and secondly, some method to control the time the sample was exposed to the elevated temperatures.

Modelling

To try to model coal degradation many models have been proposed over the years; from simple empirical models to highly advanced computer based models. One of the models that is currently finding application, is the JKMRC breakage model that allows for particle top size to be incorporated (t_{10} degradation model).[62] This model is based on the probability model originally proposed by Vogel and Peukert (2002) and modified by Shi and Kojovic (2007) to the form given in Equation 2.3.[27, 28, 48, 58, 62, 88, 89]

$$t_{10} = M\{1 - exp[-f_{mat}kx(E_{cs} - E_{min})]\} \qquad \text{Equation 2.3}$$

In Equation 2.3 t_{10} is the mass of material smaller than $^1/_{10}{}^{th}$ the original particle size, and is determined by interpolation of particle size distribution data;[19] M (%) is the maximum t_{10} value for the material tested; f_{mat} is the material breakage property; k is the amount of impacts the material was subjected to; x (m) is the size of the parent particle; E_{cs} (J.kg^{-1}) and E_{min} (J.kg^{-1}) is the mass specific breakage energy and the threshold breakage energy respectively. The threshold energy is the impact energy below which no breakage will occur.

The original probability model is derived from either a combination of Hertzian contact theory and Weibull statistics or Rumpf's similarity consideration.[27, 50, 59, 88, 89] Hertzian contact theory describes the size of the contact area of a spherical particle as it impacts onto another surface.[50, 89] Weibull statistics describes the probability of a chain breaking based on the weakest link in the chain.[27, 50, 89] Rumpf's similarity consideration states that if two particles

with different properties have the same distribution of cracks present, the breakage properties are going to be similar.[27, 50, 89] The derivation of the original probability model can be found in the works of Vogel and Peukert (2002) and Vogel and Peukert (2003),[50, 88] and the modification to the form given in Equation 2.3 can be found in Shi and Kojovic (2007).[27]

Other models that are used to model mechanical comminution are the semi-theoretical models developed by Rittinger and Kick, as well as the empirical model developed by Bond.[57] According to Rittinger, the energy required to break a particle is proportional to the new surface area that is produced, whilst Kick stated that the energy required to break a particle is proportional to the reduction in volume of a particle.[47, 52, 57, 65] Finally, Bond based his empirical model on the assumption that the energy required for breakage is proportional to the new length of a crack tip formed during breakage.[52, 65] The general form for all three models mentioned above is given by Equation 2.4.

$$\mathrm{d}E_0 = -K\mathrm{d}\frac{d}{d^n} \qquad \text{Equation 2.4}$$

For Rittinger's Law n=2 (Equation 2.5).

$$E_0 = K\left(\frac{1}{d_o} - \frac{1}{d_i}\right) \qquad \text{Equation 2.5}$$

For Kick's Law n=1 (Equation 2.6).

$$E_0 = Kln\left(\frac{d_i}{d_o}\right) \qquad \text{Equation 2.6}$$

For Bond's law n=1.5 (Equation 2.7).

$$E_0 = K\left(\frac{1}{\sqrt{d_{80,o}}} - \frac{1}{\sqrt{d_{80,i}}}\right) \qquad \text{Equation 2.7}$$

Where (in Equation 2.4 to Equation 2.7) K is a particle property constant, E_0 is the specific energy required to form the new surface and d is the particle size. The subscripts i and o represent the initial and final particle sizes; the subscript 80 indicates that 80% of the particles are smaller than the size specified.

The form of Bond's theory most commonly used to calculate the power requirement for comminution machines is of the form given in Equation 2.8.

$$W = 10W_i\left(\frac{1}{\sqrt{d_{80,o}}} - \frac{1}{\sqrt{d_{80,i}}}\right) \qquad \text{Equation 2.8}$$

Where W (kWh.t^{-1}) is the mass specific power requirement and W_i is the Bond work index. The Bond work indices are determined experimentally and gives the energy required to reduce the size of a material from $d_{80,i}$ to $d_{80,o}$.[52] Higher work indices indicate that the material is harder to grind. The work indices of various materials have been determined and are available in literature. The Bond work index for coal varies greatly between different coals, depending on the associated characteristics.[51, 52, 90]

Each of the three laws mentioned above are, when used in comminution, applicable to a certain size range. Kick's law is accurate in the order of 1 cm and above, Rittinger's law is applicable in the fine grinding range (10-1000 µm), whilst Bond's theory works well in the traditional rod- and ball mill range (0.1-10 mm).[52]

Another model commonly used to model comminution processes is the population balance model (selection for breakage model). This model describes the breakage that occurs as two functions: the first function describes the probability of a particle to undergo breakage (selection function); the next function describes the particle size distribution of the particle that underwent breakage (breakage function).[51, 52] The generalised form of the selection-for-breakage function is given in Equation 2.9.

$$p = B.S.f + (1 - S).f \qquad \text{Equation 2.9}$$

Here p is the product produced by comminution; B is the breakage function; S is the selection function and f is the feed.[52] The product in a specific size is equal to the mass of particles produced from all sizes larger, as well as the mass of unbroken particles in that interval.

For the slow compression breakage of a brittle particle, various models are in use: energy based models; stress models; sliding crack models; lattice models and continuum damage mechanics.

- Energy based models rest on the principle that if the energy dissipated in the growth of the crack is greater than the energy required to create the two new surfaces, the crack will initiate or propagate.[53]

- Stress based models assume that any particle contains a population of finitely small, randomly orientated elliptical flaws. Breakage occurs when a crack starts to propagate from the flaw that is orientated in such a way that it would be the first to sufficiently concentrate the stress in the particle. The crack propagation commences as soon as the stress at any point along the flaw is sufficient to overcome the interatomic cohesion forces of the material.[53]

- The sliding crack model states that if a pre-existing flaw is subjected to shear stress and the two surfaces of the flaw start to slide the local stresses at the tips of the crack will form two wing cracks.[53]

- Lattice models breaks down a particle into a number of brittle bar or beam elements. The heterogeneity of the sample is approximated by allotting each separate element different properties. As the simulated crack grows the elements are removed to form the crack. Although the lattice models can approximate very complicated cracking, it is still only a shadow of the real cracking phenomena.[53]

- The final type of model that is used to describe the compression breakage is continuum damage mechanics (CDM) models. In order to model breakage using CDM models three things must be defined: what is damage; the way in which stress and strain relates to damage, and finally damage evolution. Although CDM models describe the observed phenomena very accurately, CDM cannot be used to gain insight into the breakage mechanisms that occur during compression.[53]

The metrics most commonly used to determine and model the primary fragmentation of coal, is the fragmentation index defined by Zhang et al. (2002), and the Sauter mean diameter.[45] Both these metrics are used to track the changes that occur during the primary fragmentation event. The fragmentation index is characterised by three indices: the particle

multiplication factor, the variation factor of feed particles, and the fragmentation index.[42, 43, 45] The particle multiplication factor is the ratio of the number of particles after fragmentation to the number of particles before fragmentation (Equation 2.10). The variation of feed particles characterises the change in PSD of the feed particles (Equation 2.11). The fragmentation index characterises the increase in particle count and decrease in particle size due to fragmentation, as well as the increase in particle size due to swelling if present (Equation 2.12). A higher fragmentation index indicates a more intense fragmentation.[45]

The fragmentation ratio is given by Equation 2.10[32, 45] where N_{out} is the number of particles after fragmentation and N_{in} is the number of particles before fragmentation.

$$N_f = \frac{N_{out}}{N_{in}} \qquad \text{Equation 2.10}$$

The variation of feed particles is given by Equation 2.11[32, 45] where X_i is the mass of the particles in the interval i, d_i is the average diameter of the fragmented particles in interval i and d_a the average diameter of the feed particles.

$$F_d = \sum_{i=1}^{n} X_i \frac{d_i}{d_a} \qquad \text{Equation 2.11}$$

Finally the fragmentation index is given by Equation 2.12.[32, 45]

$$S_f = \frac{N_f}{F_d} \qquad \text{Equation 2.12}$$

A higher fragmentation index indicates a more intense fragmentation.[45]

The Sauter mean diameter (d_{32}), also called the Ergun index, is defined as the diameter of a sphere that has the same volume to surface area ratio as the entire PSD.[30, 33, 91] The Sauter mean diameter is given by Equation 2.13, where i is the interval number; x_i is the mass fraction on top of the screen i and $d_{p,i}$ is the aperture size of the screen.[30]

$$d_{32} = \frac{1}{\sum_i \left(\frac{x_i}{d_{p,i}}\right)} \qquad \text{Equation 2.13}$$

van Dyk (2001) used the Ergun index prior to and after fragmentation to define the extent of thermal fragmentation as presented in Equation 2.14 where the subscripts *i* and *f* indicate the initial and final Sauter mean diameters.[33]

$$Extent\ of\ thermal\ fragmentation = \frac{d_{32,i} - d_{32,f}}{d_{32,i}} \times 100 \qquad \text{Equation 2.14}$$

Dacombe et al. (1999) modelled the thermal stresses that develop within a particle due to thermal gradients, where particle failure occurs when the stresses exceed particle strength.[40] Using the fragmentation index Senneca et al. (2009), Senneca et al. (2011), and Paprika et al. (2013), numerically modelled the thermal fragmentation of coal.[32, 42, 44] Senneca et al. (2013) modelled the thermal stresses and overpressure due to devolatilisation to predict the breakage probability and fragmentation ratio.[43] Paprika et al. (2013) modelled particle failure due to the initialisation, growth and merger of cracks within the coal particle.[32] Senneca et al. (2009), Senneca et al. (2011), and Zhang et al. (2002), also used the fragmentation index to determine the effect of various process conditions on the fragmentation characteristics of coal,[42, 44, 45] whilst van Dyk (2001) used the Ergun index to determine the same.[33] Bunt and Waanders (2008) used the Ergun index to determine where in a commercial scale fixed bed gasifier fragmentation takes place.[30]

Conclusion

The manuscript is a comprehensive review of the available literature on coal degradation: the mechanisms used to describe coal degradation, the properties that influence the degradation of coal, the common experimental setups used to test coal degradation during various loading scenarios, and the common methods used to model coal degradation during various loading scenarios.

Coal degradation negatively affects coal beneficiation as well as coal utilisation, and despite a large body of literature, is poorly understood. Degradation occurs due to impact, compression and thermal stresses, with various models available that can describe the large scale degradation very well.

From this review it is clear that, although a number of studies have tried to model coal degradation, especially during transport, it is still impossible to predict how a single particle will degrade in any of the three loading scenarios (impact loading, compression loading and rapid temperature increases). From literature it is clear that, the degradation of a population of coal particles, or the degradation of a single particle, is dependent on a large number of particle properties (particle size, particle shape, coal composition, rank, weathering, stabilisation and fatigue) and apparatus or reactor properties (energy, impact surface, temperature, heating rate and residence time). Of the properties that influence coal degradation, the effect of particle size and the energy imparted to the particle is the best researched, but the effect of some of the other properties are not well researched. Properties that will benefit from studies dedicated to determining the influence of the properties on the degradation of coal are: the effect of particle shape, impact orientation, and microstructure.

The t_{10} model described in the manuscript is used to model the degradation of various materials, including coal, but has not been shown to be applicable for the South African coals.

Chapter 2 - References

11. Teo, C., Waters, A. & Nicol, S. 1990. Quantification of the breakage of lump materials during handling operations. *International journal of mineral processing*, 30(3):159-184.

12. Tao, D., Groppo, J.G. & Parekh, B.K. 2000. Enhanced ultrafine coal dewatering using flocculation filtration processes. *Minerals engineering*, 13(2):163-171.

13. Sahoo, R.K. & Roach, D. 2005. Effect of different types of impact surface on coal degradation. *Chemical engineering and processing*, 44(2):253-261.

14. Menacho, J.M. 1986. Some solutions for the kinetics of combined fracture and abrasion breakage. *Powder technology*, 49(1):87-95.

15. Sahoo, R. 2007. Degradation characteristics of steel making materials during handling. *Powder technology*, 176(2):77-87.

16. Tavares, L.M. & de Carvalho, R.M. 2011. Modeling ore degradation during handling using continuum damage mechanics. *International journal of mineral processing*, 101(1–4):21-27.

17. Esterle, J., Kolatschek, Y. & O'Brien, G. 2002. Relationship between in situ coal stratigraphy and particle size and composition after breakage in bituminous coals. *International journal of coal geology*, 49(2):195-214.

18. Sahoo, R. & Roach, D. 2005. Degradation behaviour of weathered coal during handling for the COREX process of iron making. *Powder technology*, 152(1–3):1-8.

19. Sahoo, R., Weedon, D. & Roach, D. 2004. Single-particle breakage tests of Gladstone Port Authority's coal by a twin pendulum apparatus. *Advanced powder technology*, 15(2):263-280.

20. Sahoo, R. & Roach, D. 2005. Quantification of the lump coal breakage during handling operation at the gladstone port. *Chemical engineering and processing*, 44(7):797-804.

21. Sahoo, R., Weedon, D. & Roach, D. 2004. Degradation model of Gladstone Port Authority's coal using a twin-pendulum apparatus. *Advanced powder technology*, 15(4):459-475.

23. Sahoo, R. 2006. An investigation of single particle breakage tests for coal handling system of the gladstone port: a review. *Powder technology*, 161(2):158-167.

24. Esterle, J., O'Brien, G. & Kojovic, T. 1994. Influence of coal texture and rank on breakage energy and resulting size distributions in Australian coals. (*In* 6th Australian Coal Science Conference, Newcastle, NSW: Australian Institute of Energy. p. 175-181).

25. Pan, J., Meng, Z., Hou, Q., Ju, Y. & Cao, Y. 2013. Coal strength and Young's modulus related to coal rank, compressional velocity and maceral composition. *Journal of structural geology*, 54:129-135.

26. Chandramohan, R., Holtham, P.N. & Powell, M. 2010. The influence of particle shape in rock fracture. (*In* XXV International Mineral Processing Congress 2010 organised by Australasian Institute of Mining and Metallurgy, Brisbane: The Australasian Institute of Mining and Metallurgy. p. 3163-3171).

27. Shi, F. & Kojovic, T. 2007. Validation of a model for impact breakage incorporating particle size effect. *International journal of mineral processing*, 82(3):156-163.

28. Genç, Ö. & Benzer, A. 2009. Single particle impact breakage characteristics of clinkers related to mineral composition and grindability. *Minerals engineering*, 22(13):1160-1165.

29. Eswaraiah, C., Gupta, A., Nagarajan, R., Rajavel, M. & Nandakumar, K. 2008. Minimization of fines generation in size reduction of coals by impact crusher. *Fuel processing technology*, 89(7):704-714.

30. Bunt, J.R. & Waanders, F.B. 2008. An understanding of lump coal physical property behaviour (density and particle size effects) impacting on a commercial-scale Sasol-Lurgi FBDB gasifier. *Fuel*, 87(13–14):2856-2865.

31. Hlatshwayo, H.L., Pinetown, K.L. & Campbell, Q.P. 2007. Fundamental understanding of the influence of physical properties on the thermal fragmentation of coal. (*In* International Conference on Coal Science and Technology organised by The University of Nottingham, Nottingham).

32. Paprika, M.J., Komatina, M.S., Dakić, D.V. & Nemoda, S.Đ. 2013. Prediction of coal primary fragmentation and char particle size distribution in fluidized bed. *Energy & fuels*, 27(9):5488-5494.

33. van Dyk, J.C. 2001. Development of an alternative laboratory method to determine thermal fragmentation of coal sources during pyrolysis in the gasification process. *Fuel*, 80(2):245-249.

34. Keyser, M.J., Conradie, M., Coertzen, M. & Van Dyk, J.C. 2006. Effect of coal particle size distribution on packed bed pressure drop and gas flow distribution. *Fuel*, 85(10–11):1439-1445.

35. Oberholzer, V. & van der Walt, J. 2009. Investigation of factors influencing the attrition breakage of coal. *Journal of the South African Institute of Mining and Metallurgy*, 109(4):211-216.

36. Le Roux, M. & Campbell, Q. 2003. An investigation into an improved method of fine coal dewatering. *Minerals engineering*, 16(10):999-1003.

37. Le Roux, M., Campbell, Q., Watermeyer, M. & de Oliveira, S. 2005. The optimization of an improved method of fine coal dewatering. *Minerals engineering*, 18(9):931-934.

38. Le Roux, M. 2008. The effect of thermal drying on the mechanical strength of South African coals. *Journal of the South African Institute of Mining and Metallurgy*, 108(12):783-787.

39. Esterle, J., O'Brien, G., Sexty, G., Thornton, D., Kojovic, T., Djordjevic, N., Kolatschek, Y., Firth, B. & Clarkson, C. 1998. Assessing coal fines and their impact on plant performance. (*In* XIII International Coal Preparation Conference, Brisbane. p. 173-182).

40. Dacombe, P., Pourkashanian, M., Williams, A. & Yap, L. 1999. Combustion-induced fragmentation behavior of isolated coal particles. *Fuel*, 78(15):1847-1857.

41. Senneca, O., Allouis, C., Chirone, R. & Russo, S. 2010. Set up of an experimental apparatus for the study of fragmentation of solid fuels upon severe heating. *Experimental thermal and fluid science*, 34(3):366-372.

42. Senneca, O., Russo, S. & Chirone, R. 2009. Primary fragmentation of coal particles at high heating rate. *Chemical engineering transactions*, 18:569-574.

43. Senneca, O., Urciuolo, M. & Chirone, R. 2013. A semidetailed model of primary fragmentation of coal. *Fuel*, 104:253-261.

44. Senneca, O., Urciuolo, M., Chirone, R. & Cumbo, D. 2011. An experimental study of fragmentation of coals during fast pyrolysis at high temperature and pressure. *Fuel*, 90(9):2931-2938.

45. Zhang, H., Cen, K., Yan, J. & Ni, M. 2002. The fragmentation of coal particles during the coal combustion in a fluidized bed. *Fuel*, 81(14):1835-1840.

46. Powell, M.S. & Morrison, R.D. 2007. The future of comminution modelling. *International journal of mineral processing*, 84(1–4):228-239.

47. Tavares, L. & King, R. 1998. Single-particle fracture under impact loading. *International journal of mineral processing*, 54(1):1-28.

48. Özer, C.E. & Whiten, W.J. 2012. A multi-component appearance function for the breakage of coal. *International journal of mineral processing*, 104-105:37-44.

49. Han, T., Kalman, H. & Levy, A. 2003. Theoretical and experimental study of multi-compression particle breakage. *Advanced powder technology*, 14(5):605-620.

50. Vogel, L. & Peukert, W. 2003. Breakage behaviour of different materials—construction of a mastercurve for the breakage probability. *Powder technology*, 129(1):101-110.

51. Kelly, E.G. & Spottiswood, D.J. 1982. Introduction to mineral processing. New York: John Wiley.

52. Wills, B.A. & Napier-Munn, T. 2006. Wills' mineral processing technology: an introduction to the practical aspects of ore treatment and mineral recovery. 7th ed. Oxford: Elsevier.

53. Wang, E.Z. & Shrive, N.G. 1995. Brittle fracture in compression: mechanisms, models and criteria. *Engineering fracture mechanics*, 52(6):1107-1126.

54. Lindqvist, J.E., Åkesson, U. & Malaga, K. 2007. Microstructure and functional properties of rock materials. *Materials characterization*, 58(11–12):1183-1188.

55. Inglis, C. 1913. Stresses in a cracked plate due to the presence of cracks and sharp corners. *Transaction of Naval Architects*, 60:213.

56. Fischer-Cripps, A.C. 2007. Introduction to contact mechanics. 2nd ed. New York, NY: Springer. (Mechanical Engineering Series).

57. Gilvarry, J. 1961. Fracture of brittle solids: distribution function for fragment size in single fracture (theoretical). *Journal of applied physics*, 32(3):391-399.

58. Bruchmüller, J., van Wachem, B.G.M., Gu, S. & Luo, K.H. 2011. Modelling discrete fragmentation of brittle particles. *Powder technology*, 208(3):731-739.

59. Meier, M., John, E., Wieckhusen, D., Wirth, W. & Peukert, W. 2009. Generally applicable breakage functions derived from single particle comminution data. *Powder technology*, 194(1–2):33-41.

60. Austin, L.G. 2002. A treatment of impact breakage of particles. *Powder technology*, 126(1):85-90.

61. Zhong, S., Baitalow, F., Nikrityuk, P., Gutte, H. & Meyer, B. 2014. The effect of particle size on the strength parameters of German brown coal and its chars. *Fuel*, 125:200-205.

62. Shi, F. 2014. Coal breakage characterisation: part 2: multi-component breakage modelling. *Fuel*, 117:1156-1162.

63. Shi, F. & Zuo, W. 2014. Coal breakage characterisation: part 1: breakage testing with the JKFBC. *Fuel*, 117:1148-1155.

64. Poulsen, B.A. & Adhikary, D.P. 2013. A numerical study of the scale effect in coal strength. *International journal of rock mechanics and mining sciences*, 63:62-71.

65. Oka, Y. & Majima, H. 1970. A theory of size reduction involving fracture mechanics. *Canadian metallurgical quarterly*, 9(2):429-439.

66. Scholtès, L., Donzé, F.-V. & Khanal, M. 2011. Scale effects on strength of geomaterials, case study: coal. *Journal of the mechanics and physics of solids*, 59(5):1131-1146.

67. Viljoen, J., Campbell, Q.P., le Roux, M. & De Beer, F. 2015. An analysis of the slow compression breakage of coal using microfocus X-ray computed tomography. *International journal of coal preparation and utilization*, 35(1):1-13.

68. Campbell, Q.P. & Viljoen, J. 2011. Single particle impact breakage of coal. (*In* Morsi, B., *ed*. 28th Annual International Pittsburgh Coal Conference organised by University of Pittsburgh, S.S.o.E., Pittsburgh, PA: International Pittsburgh Coal Conference. p. 1-16).

69. Garcia, D., Lin, C. & Miller, J. 2009. Quantitative analysis of grain boundary fracture in the breakage of single multiphase particles using X-ray microtomography procedures. *Minerals engineering*, 22(3):236-243.

70. Nie, B., He, X., Li, X., Chen, W. & Hu, S. 2014. Meso-structures evolution rules of coal fracture with the computerized tomography scanning method. *Engineering failure analysis*, 41:81-88.

71. Ward, C.R. 2002. Analysis and significance of mineral matter in coal seams. *International journal of coal geology*, 50(1–4):135-168.

72. Man, C.K., Jacobs, J. & Gibbins, J.R. 1998. Selective maceral enrichment during grinding and effect of particle size on coal devolatilisation yields. *Fuel processing technology*, 56(3):215-227.

73. Falcon, R. 2013. Coal petrography. *(In* Osborne, D., *ed.* The coal handbook: towards cleaner production. Woodhead. p. 53-79).

74. Falcon, R.M. & Snyman, C. 1986. An introduction to coal petrography: atlas of petrographic constituents in the bituminous coals of South Africa. Johannesburg: Geological Society of South Africa.

75. Wang, G.X., Wang, Z.T., Rudolph, V., Massarotto, P. & Finley, R.J. 2007. An analytical model of the mechanical properties of bulk coal under confined stress. *Fuel*, 86(12–13):1873-1884.

76. Laubach, S.E., Marrett, R.A., Olson, J.E. & Scott, A.R. 1998. Characteristics and origins of coal cleat: a review. *International journal of coal geology*, 35(1–4):175-207.

77. Klawitter, M., Esterle, J. & Collins, S. 2015. A study of hardness and fracture propagation in coal. *International journal of rock mechanics and mining sciences*, 76:237-242.

78. Tavares, L.M. & das Neves, P.B. 2008. Microstructure of quarry rocks and relationships to particle breakage and crushing. *International journal of mineral processing*, 87(1–2):28-41.

79. Vuthaluru, H.B., Brooke, R.J., Zhang, D.K. & Yan, H.M. 2003. Effects of moisture and coal blending on Hardgrove Grindability Index of Western Australian coal. *Fuel processing technology*, 81(1):67-76.

80. Salman, Russell, A., Aman, S. & Tomas, J. 2015. Breakage probability of granules during repeated loading. *Powder technology*, 269:541-547.

81. Han, T., Petukhov, Y., Levy, A. & Kalman, H. 2006. Theoretical and experimental study of multi-impact breakage of particles. *Advanced powder technology*, 17(2):135-157.

82. Rozenblat, Y., Portnikov, D., Levy, A., Kalman, H., Aman, S. & Tomas, J. 2011. Strength distribution of particles under compression. *Powder technology*, 208(1):215-224.

83. Genc, O., Ergun, L. & Benzer, H. 2004. Single particle impact breakage characterization of materials by drop weight testing. *Fizykochemiczne problemy mineralurgii*, 38:241-255.

84. Bourgeois, F. & Banini, G. 2002. A portable load cell for in-situ ore impact breakage testing. *International journal of mineral processing*, 65(1):31-54.

85. Barrios, G., de Carvalho, R. & Tavares, L. 2011. Extending breakage characterisation to fine sizes by impact on particle beds. *Mineral processing and extractive metallurgy*, 120(1):37-44.

86. Jin, P., Wang, E., Liu, X., Huang, N. & Wang, S. 2013. Damage evolution law of coal-rock under uniaxial compression based on the electromagnetic radiation characteristics. *International journal of mining science and technology*, 23(2):213-219.

87. Salatino, P., Senneca, O. & Masi, S. 1999. Assessment of thermodeactivation during gasification of a bituminous coal char. *Energy & fuels*, 13(6):1154-1159.

88. Vogel, L. & Peukert, W. 2002. Characterisation of grinding-relevant particle properties by inverting a population balance model. *Particle & particle systems characterization*, 19(3):149-157.

89. Vogel, L. & Peukert, W. 2004. Determination of material properties relevant to grinding by practicable labscale milling tests. *International journal of mineral processing*, 74:S329-S338.

90. Aslan, N. & Cebeci, Y. 2007. Application of Box–Behnken design and response surface methodology for modeling of some Turkish coals. *Fuel*, 86(1–2):90-97.

91. Filippa, L., Trento, A. & Álvarez, A.M. 2012. Sauter mean diameter determination for the fine fraction of suspended sediments using a LISST-25X diffractometer. *Measurement*, 45(3):364-368.

Chapter 3 - Single particle impact breakage of coal

In Chapter 2 it was identified that the current coal degradation knowledge base lacks information on the effect of particle shape and particle impact orientation on coal degradation. There is also very little work that confirms whether the t_{10} degradation model (the JKMRC breakage model that allows for particle top size to be incorporated) can be applied to a South African Highveld coal. In Chapter 3 the effect that coal particle shape and the orientation with which a coal particle impacts a steel surface has on the degradation of coal during impact breakage was investigated. The applicability of the t_{10} degradation model for South African Highveld coal was also investigated.

The content of Chapter 3 was presented at the 28th International Pittsburgh Coal Conference held in Pittsburgh, PA, USA from 12-15 September 2011 and a version of Chapter 3 was published in the digital conference proceedings.[*] The individual contribution of the co-author is given on page ix.

[*] Campbell, Q.P. & Viljoen, J. 2011. Single particle impact breakage of coal. (*In* Morsi, B., ed. 28th Annual International Pittsburgh Coal Conference organised by University of Pittsburgh, S.S.o.E., Pittsburgh, PA: International Pittsburgh Coal Conference).

Abstract

The size degradation of coal has long been a thorn in the side of coal producers and coal users alike. In an effort to better understand the degradation, with the hopes of minimising degradation, the various factors that influence this phenomenon were investigated.

A sample of South African Highveld coal was used for this investigation. The coal sample was divided into four size fractions, and from each size fraction particles of various shapes were hand-picked. Enough particles were selected to drop 20 particles of each shape and size from three heights. The impact of these particles onto a 20 mm thick steel plate was recorded using a high-speed video camera, and the footage used to determine the impact velocity as well as the orientation of the particle during impact. The progeny of each particle was collected after impact to calculate degradation from particle size distribution data, and to determine the proximate analysis.

The orientation of a particle moments before impact were shown to greatly influence the breakage characteristics of a particle, with particles impacting horizontally producing the most progeny. The coal degradation data could not be fitted to the t_{10} degradation model, but an empirical model was proposed for South African Highveld coal.

Keywords: Highveld coal; Impact velocity; High-speed videography; Coal degradation; t_{10} degradation model.

Introduction

The degradation of coal as defined by Sahoo and Roach (2005) is “the reduction of a given size fraction to a smaller size fraction through a range of final products expressed as a percentage of the whole” or, more colloquially, as “the percentage of an unwanted size fraction that results from handling and transport”.[20, 23] As most end users of coal demand that a shipment of coal is of a specific quality, the degradation of coal can be a serious problem.

The degradation of coal is divided into two categories depending on the degradation product: attrition or fracture. Surface breakage, or attrition, is where the parent particle is rounded due to chipping and abrasion by contact with any surface;[14] the parent particle stays mostly intact but is rounded, while the progeny produced are significantly smaller than the parent particle. Volume breakage, or fracture, is where the parent particle breaks apart due to excess energy applied;[14] the parent particle is no longer recognisable, and all of the progeny particles are smaller than the parent.

Teo et al. (1990) as well as Sahoo and Roach (2005) stated that the probability of a particle undergoing volume breakage increases as the height from which a particle impacts increase.[11, 20] With any drop over two metres more likely to result in volume breakage than surface breakage. This however does not mean that drops from low drop heights will not result in volume breakage. Tavares and de Carvalho (2011) believe that as a particle is repeatedly dropped from a low impact height the particle accumulates damage, and as the damage increases the particle may fracture from an impact that would normally only cause minor surface damage.[16]

Apart from the height from which a particle is dropped other factors also influence the breakage and degradation of particles: the cushioning effect of fines in a sample, the surface on which a sample impacts, the size of a particle, particle conditioning, and the effect of weathering, to name but a few.[13, 15, 20, 21]

In order to quantify the influence of each of these factors on degradation, it is necessary to model the data. The t_{10} degradation model (modified JKMRC breakage model that allows size to be incorporated) modified by Shi and Kojovic (2007), and represented in Equation 3.1, is to be used as starting block for the modelling in this study.[27] The t_{10} degradation model has previously been successfully applied at the North-West University[92, 93] to study the degradation of South African coal,[92, 93] and at other institutions to study the degradation of coal and other minerals.[21, 83]

$$t_{10} = M\{1 - \exp[-f_{mat}.x.k(E_{cs} - E_{min})]\}$$ Equation 3.1

Where t_{10} (%) is the mass percentage of progeny smaller than a tenth of the original parent particle's size, M (%) is the maximum t_{10} value, f_{mat} (kg.J^{-1}.m^{-1}) is a material property term, x (m) is the initial particle size, k is the number of impacts a sample undergoes, E_{cs} (J.kg^{-1}) is the specific comminution energy, and E_{min} (J.kg^{-1}) is the threshold energy below which no degradation will occur. It has been found that for the impact energies likely to be found in a coal handling scenario, coal only breaks in the relatively linear bottom section of the graph as illustrated by Figure 3.1 (reproduced from Foord (2008)).[92] As coal only breaks in this linear section and the energies required to determine the M-term cannot be achieved under free-fall, the model was rewritten in the form presented in Equation 3.2 with all symbols retaining the definitions as in Equation 3.1.

$$t_{10} = -f_{mat}.x.(E_{cs} - E_{min})$$ Equation 3.2

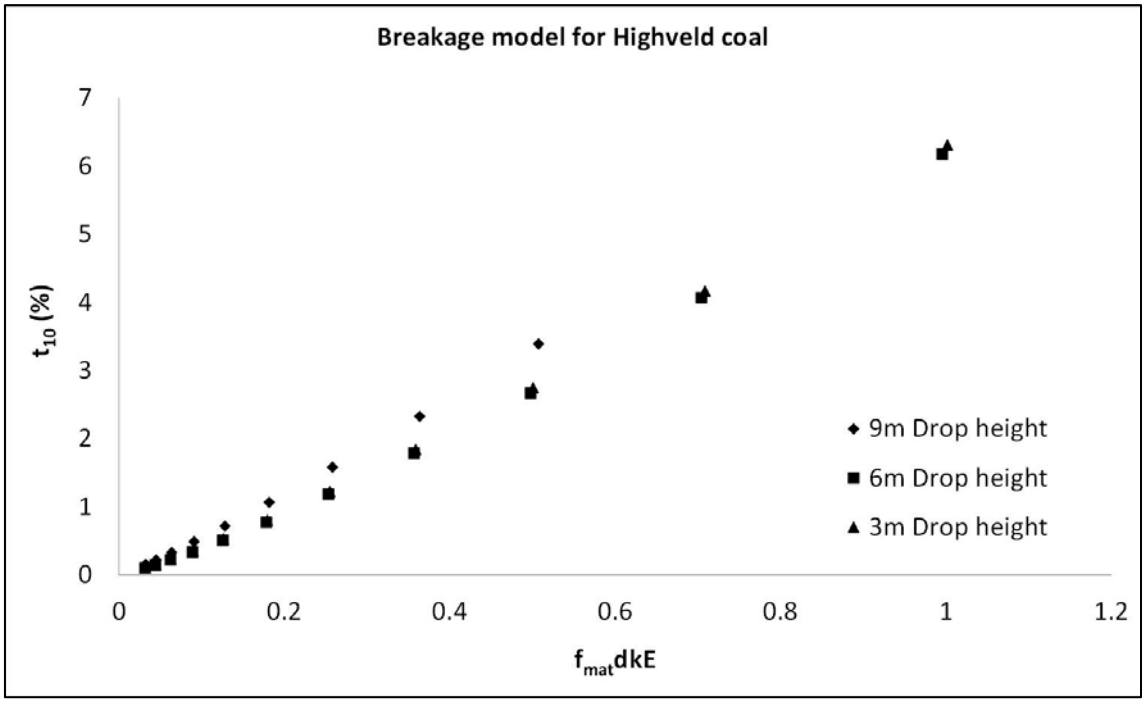

Figure 3.1: t_{10} model results obtained by Foord (2008) at the NWU[92]

Experimental

The four common methods for breakage testing are dual impact tests, single impact tests, slow compression tests, and tumbling tests.[23] Dual impact tests, such as the pendulum- and drop weight test, and slow compression tests were considered but, due to the fact that in these tests the force is applied from two directions, rejected. The experimental setup, a single particle drop shatter test, and the experimental procedure are described below.

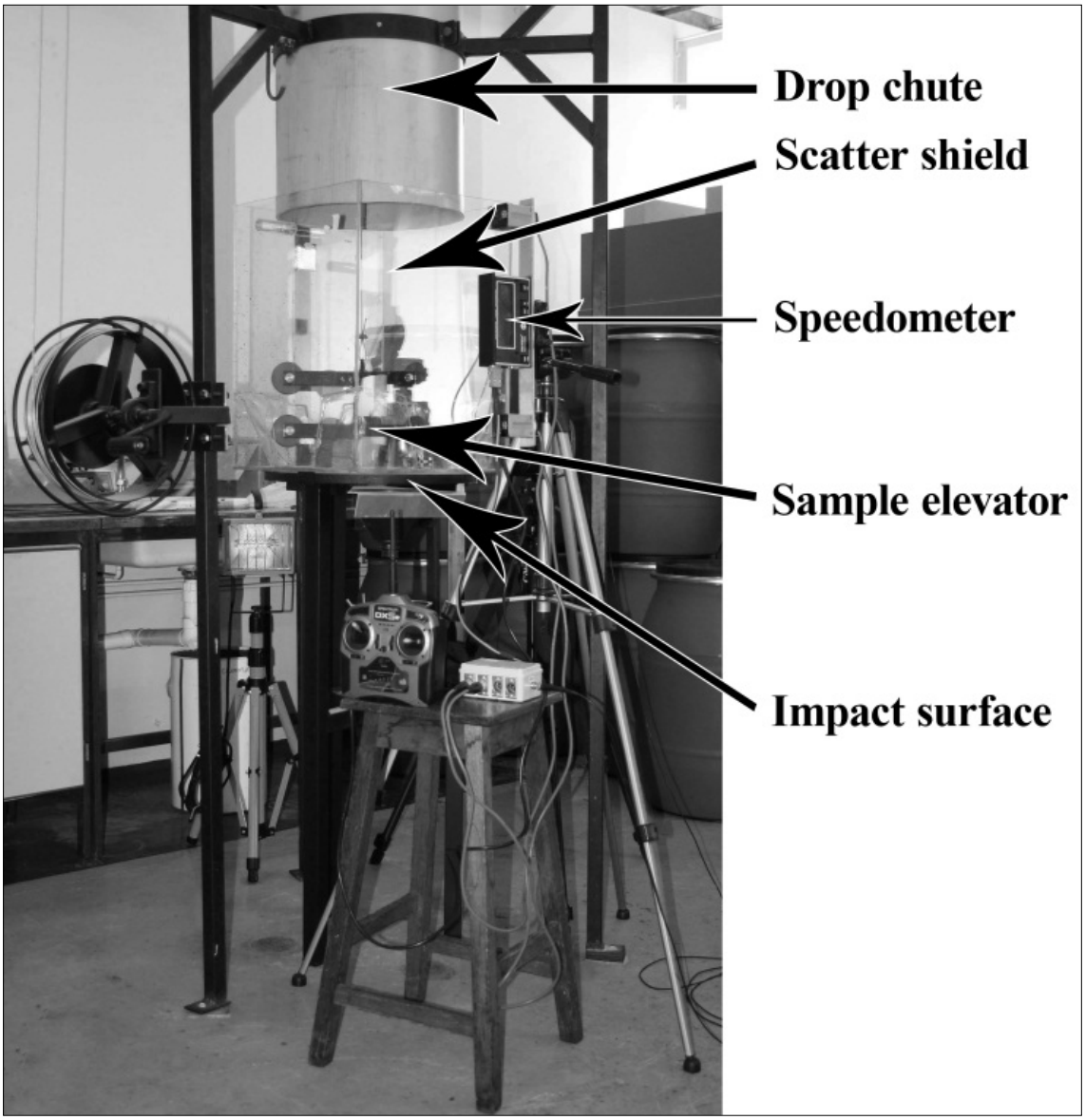

Figure 3.2: Experimental setup

Experimental setup

The experimental setup (pictured in Figure 3.2) consisted of a 380 mm PVC drop chute, a sample elevator with a remote controlled clamp to transport the sample to the desired drop height, a two centimetre thick impact plate, a scatter shield to prevent sample loss during impact, and a speedometer/high speed camera.

The impact events were recorded using an Olympus iSpeed 3 high-speed camera. Initially a speedometer, developed by Truvello SA, was used but later discarded due to difficulties in ensuring that the particle will fall through an extremely narrow measuring zone. The scatter shield was manufactured from clear plastic, and the corners rounded to facilitate the removal of the progeny particles produced.

Experimental Procedure

Sample selection

In an effort to ensure that the most statistically representative set of data was created, a sample of South African Highveld coal was screened into four size fractions (-9.5+6.7 mm, -19+13.2 mm, -37.5+26.5 mm, and -75+53 mm), the particles in all of the intervals were divided into three shape classes (flattened, elongated, and spherical / cubic). From each of the shape classes, 20 particles were hand selected and impacted from three different heights (six particles from 2 m, seven particles from 5 m, and seven particles from 7 m). Table 3.1 summarises the size fractions, particle shapes, and drop heights used during the study.

A total of 240 particles were selected and named according to the following convention: A/B/C/D; where A represents the sample number, B represents the passing size fraction, C represents the sample shape, and D represents the height from which the sample was dropped.

The Highveld coal used during this study was a bituminous, high-ash coal. Table 3.2 gives the results of the proximate analyses performed at the North-West University laboratories.

Table 3.1: Breakdown of the experimental conditions (screen intervals, particle shapes, and drop heights) used.

Screen interval	Particle shape	Drop height
-9.5+6.7 mm	Flattened: a particle where one of the orthogonal dimensions is significantly smaller than the other two	7 m
-19+13.2 mm	Elongated: a particle where one of the orthogonal dimensions is significantly larger than the other two	5 m
-37.5+26.5 mm	Spherical / Cubic: a particle where all three of the orthogonal dimensions are similar	2 m
-75+53 mm		

The exceptionally large standard deviations noted in Table 3.2 were due to a proximate analysis being done for every single particle dropped and suggests that there was a large amount of variability between the individual particles.

Table 3.2: Proximate Analysis of coal sample

Proximate Analysis	
Inherent Moisture	4.3 ± 0.7 %
Volatiles (Moisture Free)	18.1 ± 4.5 %
Ash (Moisture Free)	40.3 ± 16.3 %
Fixed Carbon (Moisture Free)	41.6 ± 14.8 %

Impact procedure

In order to drop a particle from a specific height, the sample was held by the sample elevator in remote controlled clamps while the sample elevator rose to 2 m, 5 m, or 7 m. After the sample elevator reached the correct height, the particle was dropped. The particle then impacted onto a 20 mm thick steel plate, and the impact event recorded using an Olympus iSpeed 3 high-speed camera. The iSpeed 3 is capable of a maximum frame rate of

150000 fps, but the maximum resolution of 1280 x 1024 px is achieved at a frame rate of 2000 fps. When using maximum resolution, an event lasting a maximum of 4.9 sec could be recorded and replayed. After impact, the progeny particles were collected, labelled, and stored in resealable plastic bags until they could be analysed. The impact energy was assumed to be equal to the kinetic energy of each particle prior to breakage and was calculated using Equation 3.3

$$E = 0.5mv^2 \qquad \text{Equation 3.3}$$

where m (g) is the mass of the particle, and v ($^{m}/_{s}$) is the velocity before impact.

Sample analysis

Particle size distribution

To extract the t_{10} data, every sample that was dropped was put through a √2 sieve series consisting of the following sieves: 600 µm; 850 µm; 1180 µm; 1700 µm; 2360 µm; 3350 µm; 4.75 mm; 6.7 mm; 9.5 mm; 13.2 mm; 19 mm; 26.5 mm; 37.5 mm and 53 mm. Any additional damage to the impacted samples were minimised by gently shaking the samples by hand for as short a time as possible. The shaking time was considered sufficient when the amount of particles in the pan no longer increased observably.

Video analysis

The footage of each impact event was analysed to determine the orientation at impact, and to identify any common, or unique, breakage patterns (see Qualitative results). All video analyses were completed using proprietary software supplied by Olympus for the iSpeed 3 high-speed video camera.

Results

Qualitative results

During the analysis of the numerous impact events' high-speed video, the behaviour of individual particles during impact was studied. It was found that the majority of the particles behaved in one of a few distinct ways:

- The particle impacts on a flat surface and breaks apart.

- The particle impacts on a point or protrusion and the point disintegrates with very little damage to the rest of the particle.
- The particle impacts on the one edge and see-saws over to the other edge.
- The particles impacts on the edge and spins along the edge of the particle in a coin-like fashion.

In this section the behaviour of five different particles are discussed.

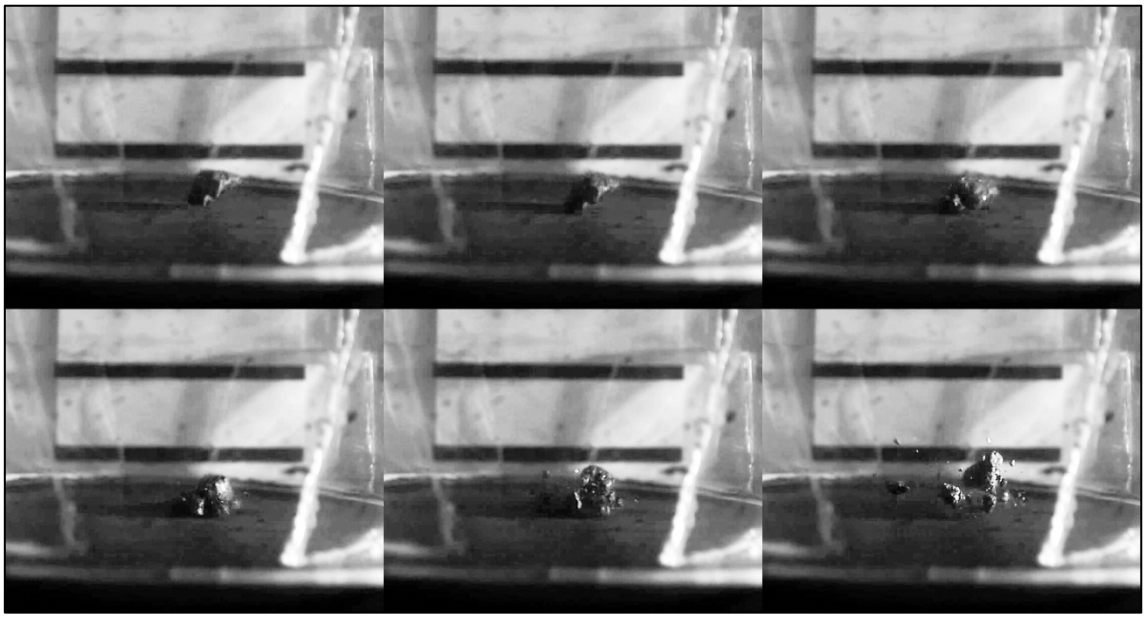

Figure 3.3: A sequence of six individual frames taken from 12 µs worth of high speed video of sample 2/37/2/7 impacting onto a steel plate.

Figure 3.3 shows a -37 mm particle that was dropped from seven metres. The particle impacted with a kinetic energy of 4.79 J and an orientation factor of 3 (see Figure 3.9 for a description of the impact orientation factors). After the initial impact the particle spun along its edge in a movement analogous to that of a coin spinning, and as the particle spun along its edge, progeny continually broke away from the parent particle.

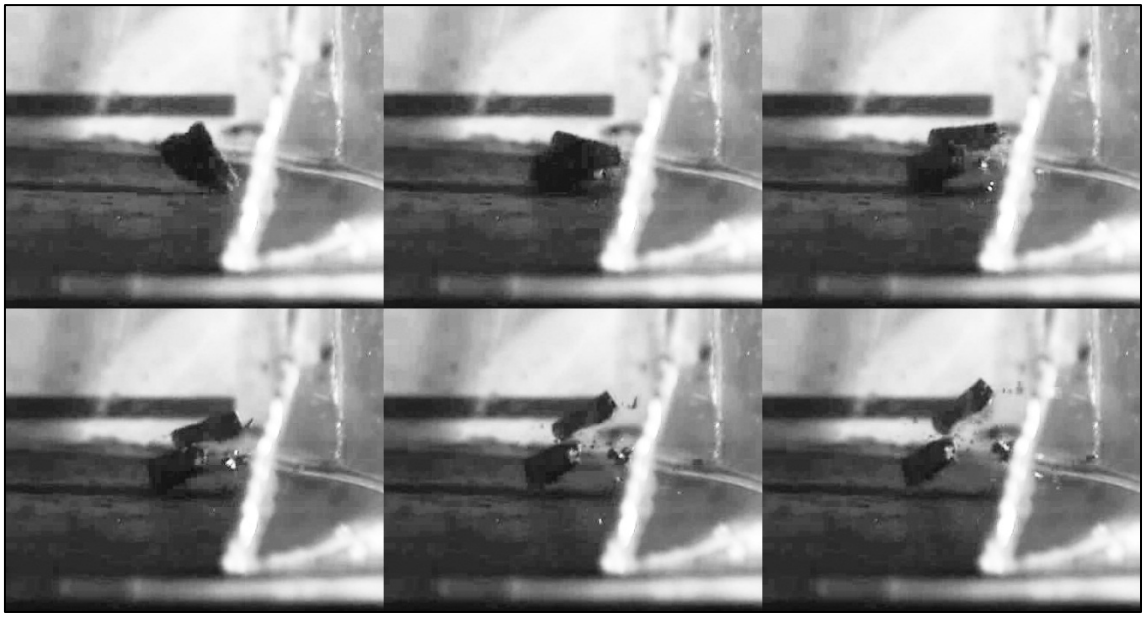

Figure 3.4: A sequence of six frames taken from 8 µs worth of high speed video of sample 2/37/3/7 impacting onto a steel plate.

Figure 3.4 also shows a -37.5 mm particle that was dropped from seven metres. The difference between the two particles in Figure 3.3 and Figure 3.4 was the shape of the particles. The particle shown in Figure 3.3 had a slightly elongated shape, whilst the particle in Figure 3.4 has a cubic/spherical shape. The particle in Figure 3.4 impacted with kinetic energy of 3.81 J and an orientation factor of 3. The difference in impact energy for similarly sized particles are due to mass variations between the particles. The particle impacts first on the one side of the particle, and then rolls over to the other edge of the particle along the rounded bottom surface of the particle. As the particle rolls over to the other side, a section of the particle breaks away from the top and moves upward while the other daughter particle continues the rolling movement.

Figure 3.5 shows the impact of a -75 mm particle; the particle impacted with 19.56 J of kinetic energy and an orientation factor of 3. During this impact, the elongated particle first impacts on one edge of the particle, after the initial impact the particle tilts over to the other edge in a movement analogous to that of a see-saw. During the secondary impact the particle then breaks apart. In the majority of the particles that impacted in a see-saw-like fashion the breakage takes place mostly during the second part of the event. The breakage that does occur during the first part of the event is disintegration of the impact point.

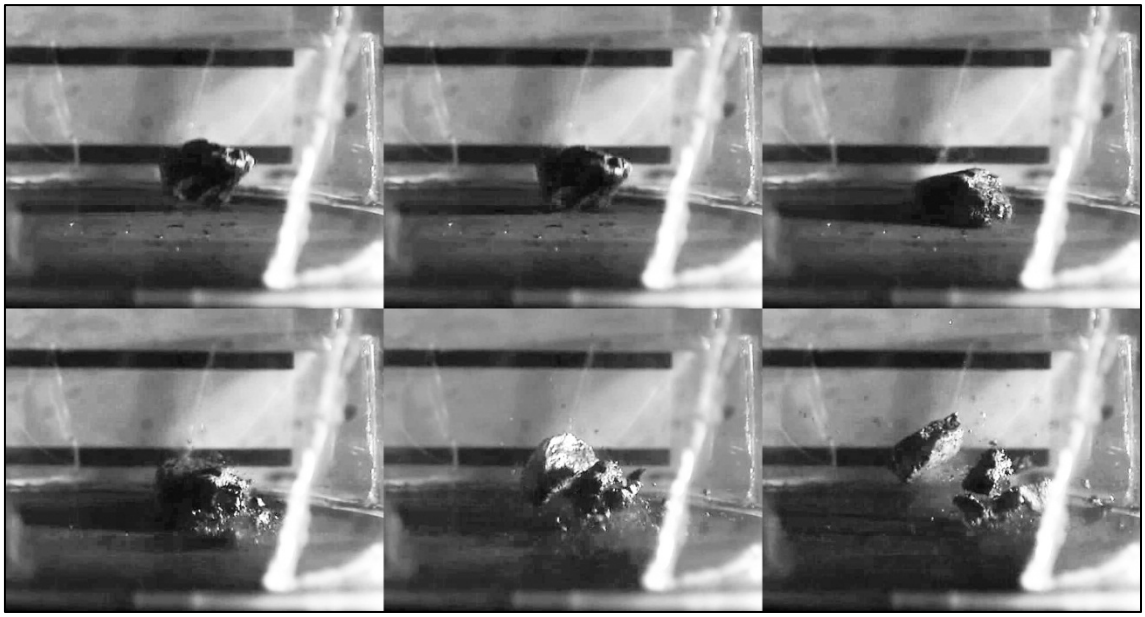

Figure 3.5: A sequence of six frames taken from 26 µs worth of high speed video of sample 3/75/2/7 impacting onto a steel plate.

The impact represented in Figure 3.6 is of a -37.5 mm particle impacting with 4.05 J of energy and an orientation factor of 3. This is again a see-saw like impact with very little degradation taking place during the primary impact and the particle breaking apart after the particle tilts over to the other side.

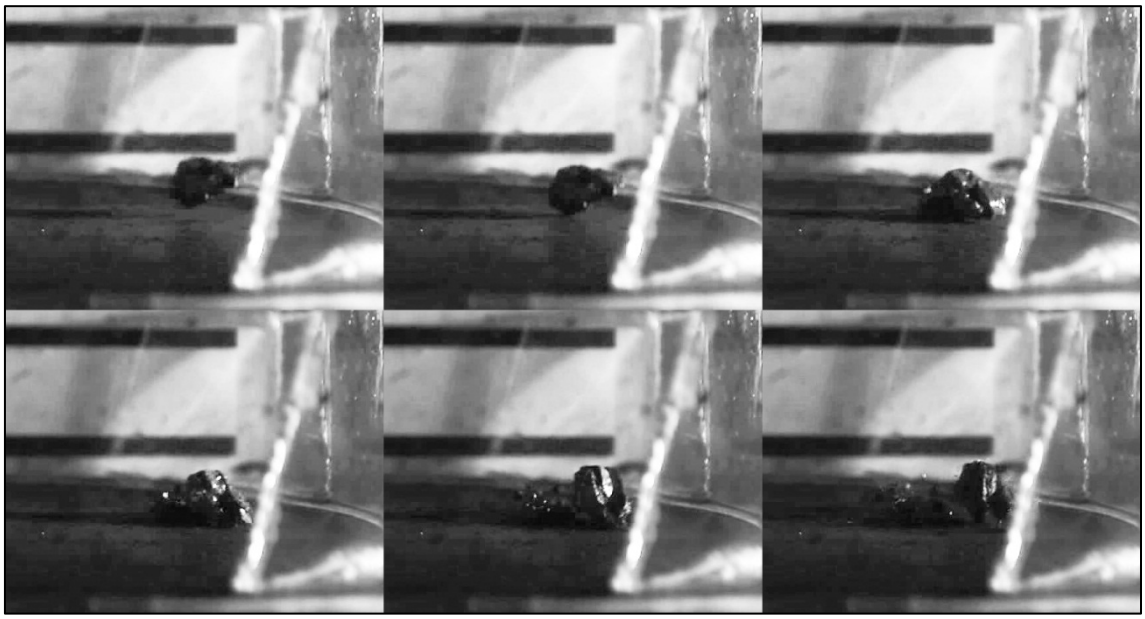

Figure 3.6: A sequence of six frames taken from 7 µs worth of high speed video of sample 6/37/3/7 impacting onto a steel plate.

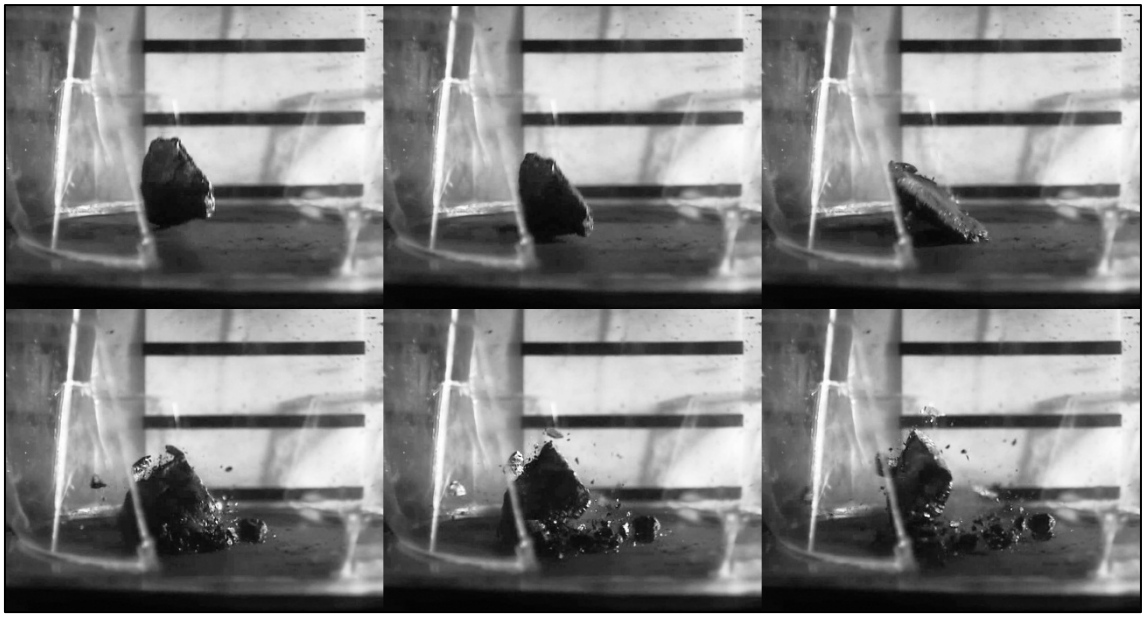

Figure 3.7: A sequence of six frames taken from 15 µs worth of high speed video of sample 7/75/1/7 impacting onto a steel plate.

Finally Figure 3.7 shows a -75 mm particle that impact with 32.92 J of energy and an orientation factor of 2. After the particle impacts on the edge it begins to spin in a coin-like fashion, and as the particle rolls along the edge, progeny particles continually break away from the parent particle leaving the centre of the parent particle mostly intact.

Quantitative results

The following section presents quantitative results obtained from the sieve size analyses and the high-speed footage analyses. The parameters that were determined were the t_{10} values from the PSD data, and the impact orientation values obtained from the high-speed footage.

PSD results

To obtain the particle size distribution for each of the samples a sieve size analysis was performed using a √2 sieve series. The following sieves were included in the series: 600 µm, 850 µm, 1180 µm, 2360 µm, 3350 µm, 4.75 mm, 6.7 mm, 9.5 mm, 13.2 mm, 19 mm, 26.5 mm, 37.5 mm, and 53 mm. Figure 3.8 shows the average size distribution graphs for three groupings of -37.5 mm particles (Figure 3.8a-c). These groupings correspond to the top size of the progeny particles after impact. The shaded area on the graph shows the area where all of the size distributions for each of the groupings occurred.

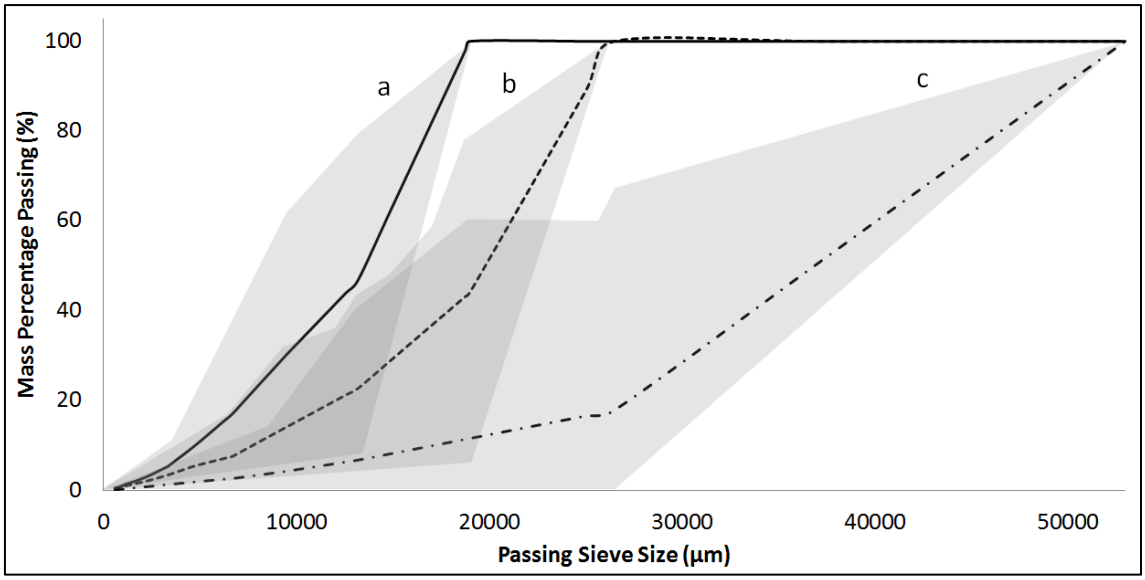

Figure 3.8: Average PSD of all -37.5 mm parent particles dropped from 2 m, 5 m, and 7 m. The groupings correspond to the top size of the progeny particles after impact.

From Figure 3.8 it can be seen that all of the particles break in one of three ways, and are classified based on the top size of the progeny particles. The averages of each classification are marked a, b, and c:

a) The parent particle stays intact and any progeny particles produced are significantly smaller than the parent particle (implies surface breakage).
b) The size of the parent particle is reduced to less than 70 % of its initial size and is still recognisable. None of the progeny falls into the same size fraction as the parent (implies a combination of volume and surface breakage).
c) The parent particle breaks apart completely and is no longer recognisable; all progeny particles produced are smaller than half the size of the parent (implies volume breakage).

Impact orientation factor

Figure 3.10 shows the influence of the impact orientation factor (OF) on the t_{10} values for all of the particles impacted. Figure 3.9 shows a schematic of the different orientation factors; the impact orientation factors for all particles were subjectively determined from the high-speed video of the impacts.

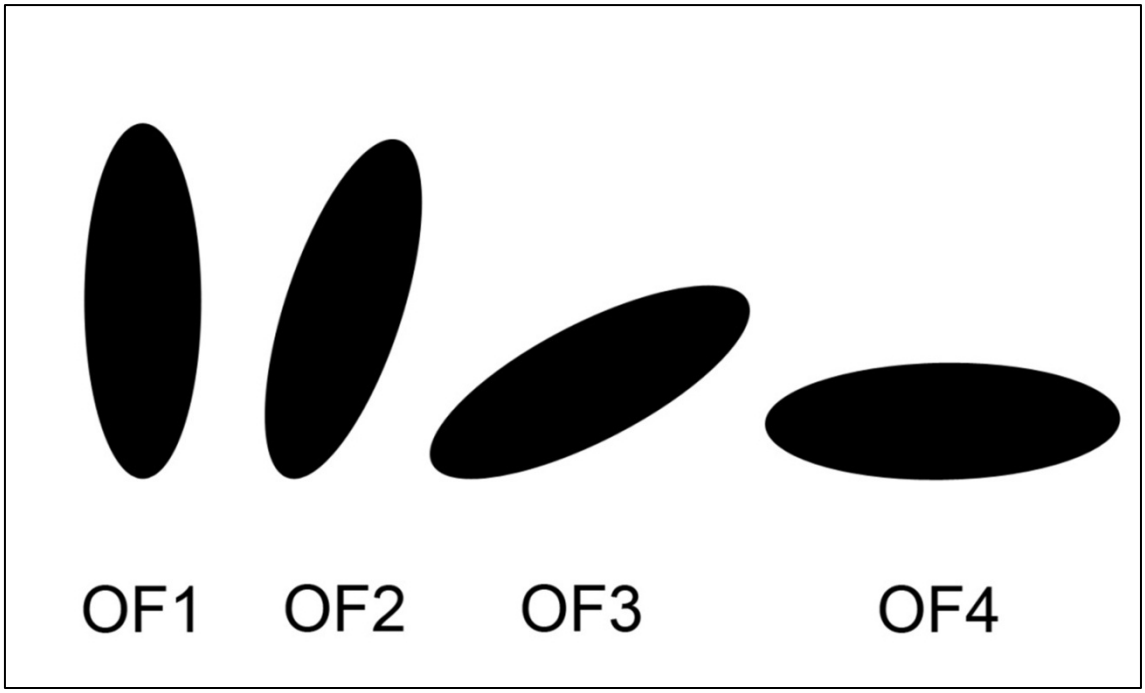

Figure 3.9: Representation of the orientation factors

OF1: Particles Impact vertically or on a definite protrusion.

OF2: Particles impact between 85°-45°.

OF3: Particles impact between 45°-5°.

OF4: Particles impact horizontally or on a flat surface.

Figure 3.10 shows that the orientation with which the particle impacts, influences the degradation of the particle. The graph clearly shows that particles impacting vertically or on a protrusion (OF1) shows the highest apparent strength and produce the least degradation products, whilst particles that impact horizontally or on a flat surface (OF4) shows the lowest apparent strength and produce the most degradation products. Where the impact orientation of a particle lies between these two extremes (OF2 & OF3), the amount of degradation product produced is also between the extremes. This agrees with work done by Chandramohan et al. (2010) on granite,[26] who found that if a flake is horizontally loaded into a drop weight tester it is much weaker (produces more progeny) than if it loaded vertically, and the strength of non-flake particles are somewhere in between.

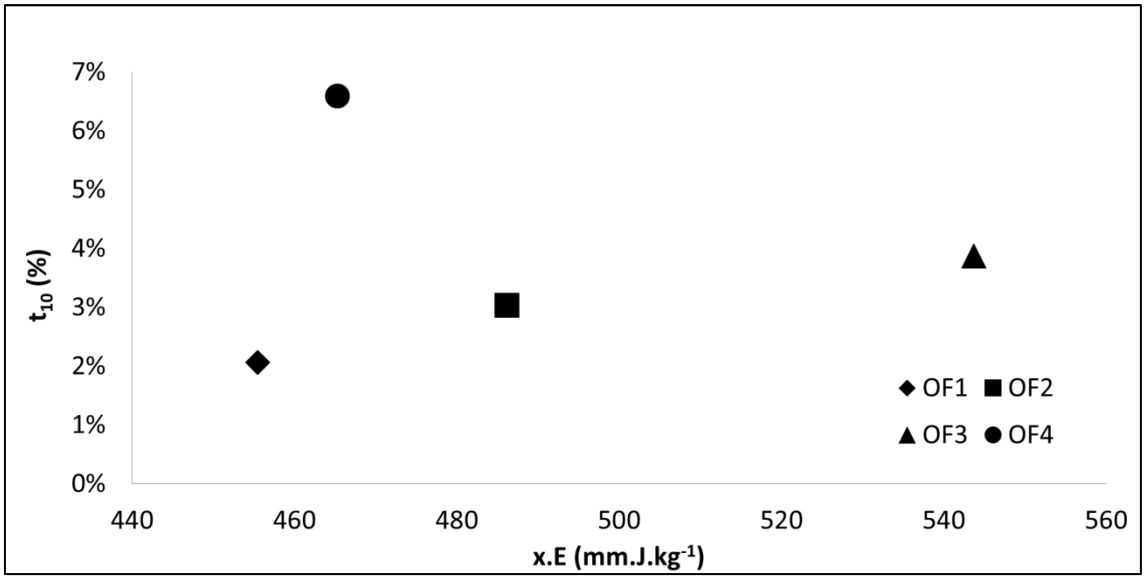

Figure 3.10: Influence of the impact orientation factor on the t_{10} parameter.

t_{10} vs. x.E Graphs

One of the goals of this study was to confirm and refine the t_{10} model, proposed by Shi and Kojovic (2007), for South African Highveld coal.[27] The data generated during this study exhibited a high degree of scatter, and initially, no trends in the data were obvious. In an effort to make sense of the data, all particles that were similarly sized and impacted from a similar height were grouped together. Figure 3.11 shows a plot of the t_{10} values (see Equation 3.1) against the size dependant impact energy ($x.E$; mm.J.Kg^{-1}) of each grouping. By grouping the particles, the assumption is made that all of the particles within that group passed the same sieve and were dropped from the same height, in a single drop, with every particle experiencing only a single breakage event with no interaction between the different particles.

The data shows a highly linear relationship between the impact energy and the amount of degradation product produced. This shows that coal, dropped from a height of seven metres or lower, does not have the characteristic exponential shape produced by harder ores.

Model

The original model that was used as basis during this study was the model modified by Shi and Kojovic (2007).[27] This model, although it was sufficient in previous studies conducted at the North-West University,[92-94] did not accurately fit the data generated during this study.

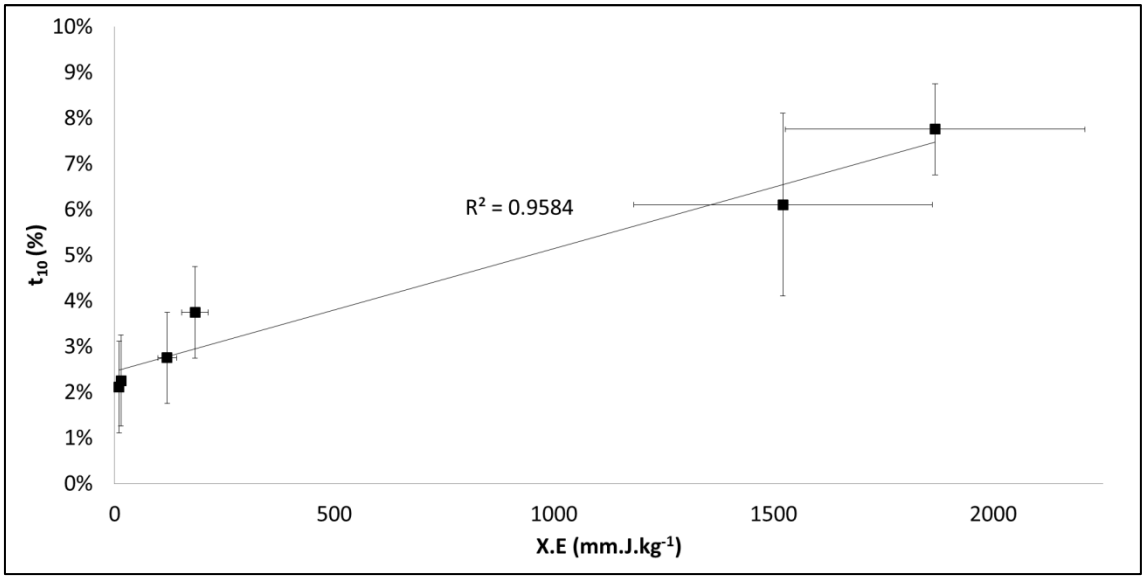

Figure 3.11: t_{10} vs. *x.E* when samples are grouped by passing size and drop height. Error bars indicate the 95% confidence interval.

If the data did fit the t_{10} model, the x-intercept of the linear trend in Figure 3.11 would have passed through either the origin or to the positive side of the x-axis. In Figure 3.11 each of the data points is a grouping of all particles that passed the same top size, and were dropped from the same height. The error bars included in Figure 3.11 show the 95% confidence interval. The following empirical relation (Equation 3.4) is proposed to describe the influence of particle size on the degradation of South African Highveld coal.

$$t_{10} = X.E.f_{mat} + A \qquad \text{Equation 3.4}$$

The model is an empirical, direct relation that holds true to the assumption that coal degrades only in the linear section of the t_{10}-curve. The constant (*A* in Equation 3.4) can, as yet, not be explained; however, it is hypothesized that it may be due to factors that influence a specific particle such as the pre-existing cracks, mineral content, and coal texture or factors that influence the impact event such as the impact orientation or particle rotation prior to impact.

Further study will determine the validity and accuracy of the proposed model. Further studies are also planned to pinpoint the factors that influence the f_{mat} and *A* terms in the Equation 3.4.

Conclusions

A direct relation, to predict the degradation of South African Highveld coal, was proposed for a population of particles; however, due to the heterogeneity of coal it is very hard, if not impossible, to predict the breakage products for a single coal particle. The results shown are for particles grouped together as if the entire group were dropped as a single sample. By grouping particles that are the same size and dropped from the same height, the assumption can be made that there is no interaction between particles during the drop, and all of the particles experience only a single breakage event.

The data generated during this study show that all the degradation products fall into one of three categories: all progeny are smaller than half the parent particle, the parent particle stayed mostly intact, and the parent particle experience very little degradation.

The impact orientation factor does influence the degradation of the particles. Particles that impact with an orientation factor of 4 (where particles impact horizontally or on a flat surface) are the weakest and produce the most degradation products; and particles that impact with a factor of 1 (where particles Impact vertically or on a definite protrusion) are the strongest and produce the least degradation products.

Chapter 3 - References

11. Teo, C., Waters, A. & Nicol, S. 1990. Quantification of the breakage of lump materials during handling operations. *International journal of mineral processing*, 30(3):159-184.

13. Sahoo, R.K. & Roach, D. 2005. Effect of different types of impact surface on coal degradation. *Chemical engineering and processing*, 44(2):253-261.

14. Menacho, J.M. 1986. Some solutions for the kinetics of combined fracture and abrasion breakage. *Powder technology*, 49(1):87-95.

15. Sahoo, R. 2007. Degradation characteristics of steel making materials during handling. *Powder technology*, 176(2):77-87.

16. Tavares, L.M. & de Carvalho, R.M. 2011. Modeling ore degradation during handling using continuum damage mechanics. *International journal of mineral processing*, 101(1–4):21-27.

20. Sahoo, R. & Roach, D. 2005. Quantification of the lump coal breakage during handling operation at the gladstone port. *Chemical engineering and processing*, 44(7):797-804.

21. Sahoo, R., Weedon, D. & Roach, D. 2004. Degradation model of Gladstone Port Authority's coal using a twin-pendulum apparatus. *Advanced powder technology*, 15(4):459-475.

23. Sahoo, R. 2006. An investigation of single particle breakage tests for coal handling system of the gladstone port: a review. *Powder technology*, 161(2):158-167.

26. Chandramohan, R., Holtham, P.N. & Powell, M. 2010. The influence of particle shape in rock fracture. (*In* XXV International Mineral Processing Congress 2010 organised by Australasian Institute of Mining and Metallurgy, Brisbane: The Australasian Institute of Mining and Metallurgy. p. 3163-3171).

27. Shi, F. & Kojovic, T. 2007. Validation of a model for impact breakage incorporating particle size effect. *International journal of mineral processing*, 82(3):156-163.

83. Genc, O., Ergun, L. & Benzer, H. 2004. Single particle impact breakage characterization of materials by drop weight testing. *Fizykochemiczne problemy mineralurgii*, 38:241-255.

92. Foord, D. 2008. The determination of single particle breaking characteristics of different coal samples. Potchefstroom: North-West University. (Mini-dissertation - B.Eng, Unpublished).

93. van der Merwe, W. 2008. Single particle impact-breakage tests on different South African coal sources. Potchefstroom: North-West University. (Mini-dissertation - B.Eng, Unpublished).

94. Button, R. 2007. The determination of single particle breaking characteristics of different coal sample. Potchefstroom: North-West University. (Mini-dissertation - B.Eng, Unpublished).

Chapter 3 - Additional notes

After determining that there is a gap in literature concerning the effect of particle shape, and the effect of a particle's impact orientation on the degradation of a single coal particle in Chapter 2, a series of experiments to determine the effect of a particle's shape and impact orientation on the degradation characteristics of single coal particles were designed and concluded. The data generated was fitted to the t_{10} model to confirm the applicability of this model for South African Highveld coal.

The publication could neither definitively prove nor disprove the applicability of the t_{10} degradation model to South African Highveld coal. The size dependent impact energy ($x.E$) vs. the extent of breakage (t_{10}) data generated during the course of the study (Figure 3.11) showed a fairly straight line with a negative x-intercept. Even though previous research on coal at the North-West University showed that coal in general, does not give the characteristic exponential shape,[92-94] it was expected that the y-intercept would be zero. An apparent positive y-intercept, as in Figure 3.11, implies that close to zero breakage energy is required to produce some progeny. A possible reason for this is the sieve size analyses of the progeny may have contributed enough energy to have this effect, but all efforts were made to conduct the sieve size analyses without damaging the progeny particles any further. Rather, this very low energy breakage is due to the pre-existing structural features like cracks and cleats that originate from the previous handling and preparation of the particles required virtually no energy to break, or the very weak and brittle nature of coal. Where any amount of energy applied to the coal would result in some damage, and cause the shift in the linear section of the t_{10} graph. Powell et al. (2014) confirmed that the t_{10} model is not applicable to soft, bimodal natural resources like coal.[95] A bimodal resource consists of two distinct phases with differing breakage properties. Additional notes Figure 3.1 shows the t_{10} values plotted against the ash yield of all particles impacted from 7 metres and 5 metres. This figure illustrates the variability in the generated data and shows that the coal studied is a bimodal ore, with the particles with high ash yields showing lower t_{10} values compared to the particles with lower ash yields.

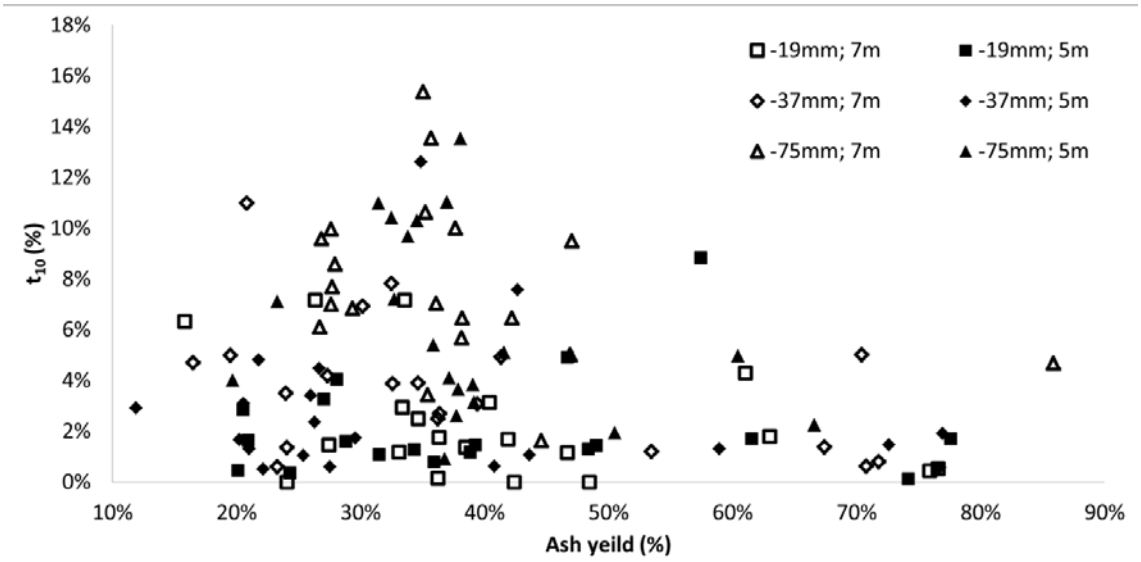

Additional notes Figure 3.1: Plot of each particle's t_{10} value against its ash yield showing the heterogeneity of the coal used during this study

Additional notes Figure 3.2 shows a graph of the size specific impact energy vs. t_{10} values for all particles to further underscore the variation in the data. Note that the X-axis in Additional notes Figure 3.2 is logarithmic.

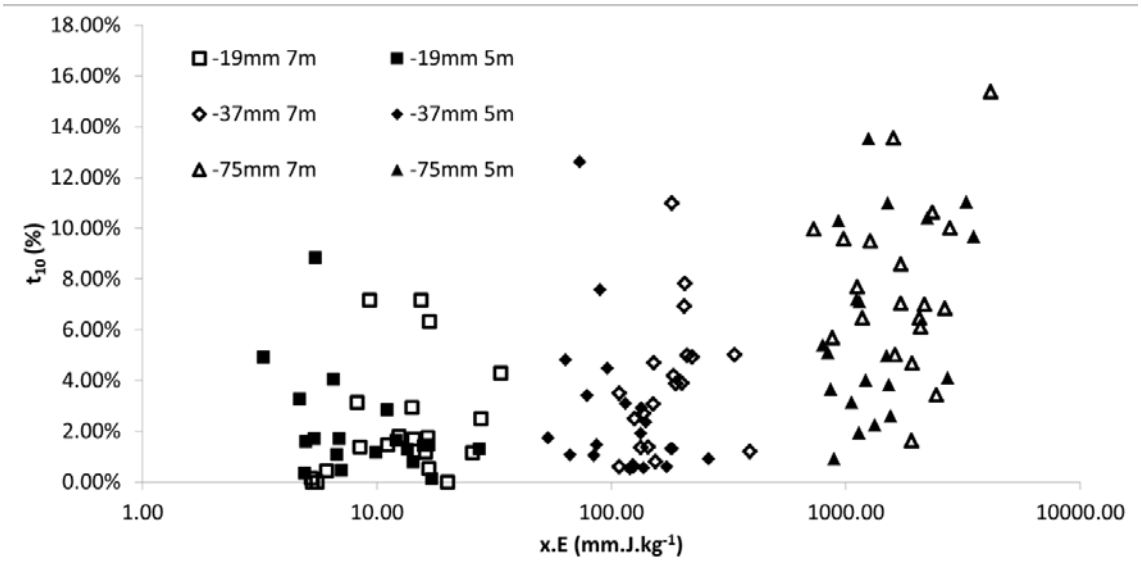

Additional notes Figure 3.2: Plot of each particle's t_{10} value against its size specific impact energy.

Despite the fact that the South African Highveld coal used during this study cannot be modelled using the t_{10} breakage model, the use and definition of the t_{10} index will be retained during the thesis as it is a convenient way to present the amount of degradation a coal

particle undergoes as a single value. The t_{10}-index is defined as the mass percentage of the progeny produced that is smaller than $^{1}/_{10}^{th}$ the size of the parent particle.

The particle shapes used in this publication were slab-like particles (particles where one of the three orthogonal dimensions is significantly smaller than the other two dimensions), elongated particles (particles where one of the three orthogonal dimensions is significantly larger than the other two dimensions), and cubic particles (particles where all three orthogonal dimensions are similar). The publication clearly shows the influence of the particle shape on the breakage characteristics: the slab-like particles show increased fines production (a higher t_{10}-index value) when compared to the t_{10}-index value generated by the cubic particles, especially if the slab-like particles impact with a large contact area.

The publication also clearly shows the influence of the particle impact orientation: particles (either slab-like or cubic) that impact on an edge or a protrusion show less degradation than particles that impact onto a large flat surface (see Figure 3.10 and Figure 3.9). Another observation that was made during the events where particles impact on a protrusion is that the point where the particle contacted during impact disintegrated into very fine progeny, whilst the bulk of the particle remained unaffected. The majority of the energy imparted to the particle is dissipated by the disintegrating protrusion so that there is little energy available to degrade the bulk of the particle; this resulted in a progeny size distribution similar to that expected for surface breakage.

Chandramohan et al. (2010) found that, for well-defined granite particles, the breakage increased as the contact area between the particles and the impact surface increased.[26] It is concluded that the same is true for coal particles, and the increased breakage for particles that did not impact on an edge or protrusion is due to the larger contact area. For particles that impacted onto a small protrusion, the force concentration close to the contact area is very high and the protrusion disintegrated into very fine progeny, dissipating the energy and preventing excessive damage to the rest of the particle.

During the analysis of the high-speed footage generated for the study it was observed that some of the particles broke apart along a very distinct plane through the particle (see Figure 3.5). It was assumed that this breakage occurred along a bedding plane within the particle, but there was no way of proving this assumption true during this study. Another breakage pattern that occurred were slab-like particles that impacted at an angle and spinning along the edge in a coin-like fashion. As the particle spun around the edge, progeny particles continuously broke away from the edge of the parent particle. The questions that resulted

from these observations were: what caused the distinct breakage patterns, and are there any microscopic features present in the particle that contributed to the coal degradation?

In order to answer these questions it is necessary to accurately control the orientation of the bedding planes in relation to the impact surface; and to study the internal features of a single coal particle, non-destructively, before breakage and after breakage. Comparing the internal structure of a coal particle both before and after breakage will allow any changes in the coal microstructure to be observed and quantified. Chapter 4 will demonstrate that micro-focus X-ray computed tomography (µCT) is a technology uniquely suited to observe the internal structure of opaque objects, such as coal, and is finding application in a myriad of industries. The use of µCT to study the internal structure of coal is confirmed for compression breakage in Chapter 5, and for both impact breakage and thermal breakage in Chapter 6. In an effort to confirm the contribution of the bedding planes, and the orientation of the bedding planes relative to the applied force, to the breakage of single particles during impact, the experimental setup was redesigned. The new experimental setup, in conjunction with µCT, was used in subsequent publications (Chapter 6 and Chapter 7) specifically to study the contribution of the bedding plane orientation to single particle breakage of coal.

Chapter 3 - Additional notes references

26. Chandramohan, R., Holtham, P.N. & Powell, M. 2010. The influence of particle shape in rock fracture. (*In* XXV International Mineral Processing Congress 2010 organised by Australasian Institute of Mining and Metallurgy, Brisbane: The Australasian Institute of Mining and Metallurgy. p. 3163-3171).

92. Foord, D. 2008. The determination of single particle breaking characteristics of different coal samples. Potchefstroom: North-West University. (Mini-dissertation - B.Eng, Unpublished).

93. van der Merwe, W. 2008. Single particle impact-breakage tests on different South African coal sources. Potchefstroom: North-West University. (Mini-dissertation - B.Eng, Unpublished).

94. Button, R. 2007. The determination of single particle breaking characteristics of different coal sample. Potchefstroom: North-West University. (Mini-dissertation - B.Eng, Unpublished).

95. Powell, M., Hilden, M., Ballantyne, G., Liu, L. & Tavares, L.M. 2014. The appropriate and inappropriate application of the JKMRC t_{10} relationship. (*In* Yianatos, J., *ed*. XXVII International Mineral Processing Congress organised by Universidad de Chile, Santiago: Gecamin Digital Publications. p. 133-144).

Chapter 4 - A review of micro-focus computed tomography and its application in coal breakage and degradation studies

In Chapter 3 it was shown that although the particle shape and impact orientation affects the degradation of coal, it is not clear why these properties influence the degradation. It was suggested that the influence may be due to the internal microstructure of the coal.

Chapter 4 is a comprehensive review of micro-focus X-ray computed tomography (µCT), the tomography process, relevant material interactions between the X-rays and materials and the application of µCT in geological sciences focussing on coal breakage and degradation. In Chapter 4 it is shown that µCT is a technology uniquely suited to study the internal microstructure of coal.

Abstract

Micro-focus X-ray computed tomography is a non-destructive analytical technique that can be used to visualise the internal structure of an opaque object by the physical differences of its constituent elements. This review aims to give a short background on the development and applications of the technique, with specific focus on material analyses, and specifically, the application in coal breakage and degradation studies.

Introduction

History

Since the accidental discovery of X-radiation by Wilhelm Röntgen in 1895, X-rays have been widely used to observe the internal features of objects without destroying them. The most common use of X-ray technology is in diagnostic radiology, where X-rays are used to image the inside of the human body. Figure 4.1 shows the first medical radiograph taken by Wilhelm Röntgen in 1895.

Figure 4.1: Print of the first medical X-ray radiograph (Public domain image)

The biggest issue with radiographs is that the information of a three-dimensional (3D) object is superimposed onto and integrated into a two-dimensional (2D) image, obscuring much of

the information. The advancement in two separate fields, X-ray radiography and computer science, enabled this problem to be overcome when, in 1971, the first clinical computerised tomography (CT) scan was performed using a CT scanner (known as a tomograph) developed by a team headed by Sir Godfrey Houndsfield. The first ever clinical CT scan (tomogram) consisted of a slice with an 80 x 80 voxel matrix, each voxel representing a 3 x 3 x 13 mm section; the scan took 4.5 minutes to complete and 90 seconds to reconstruct using an algebraic reconstruction technique.[96-98]

Since the development of the first CT scanner there has been a lot of development with the modern industrial tomograph able to produce tomograms with a spatial resolution of 10µm and modern medical tomographs able to complete scans of the entire body in less than 2 minutes.[97] CT is currently applied in three main fields: diagnostic radiology, materials analysis and in dimensional metrology.[99] The fundamental concepts in all three applications are the same, but the devices and the procedures used differ from one another.[99] The focus of this review is on materials analysis, specifically coal breakage and degradation.

Computed tomography process

Computed tomography is achieved by generating a number of views, which look similar to radiographs for cone beam geometries, of an object that is rotated relative to an X-ray source-detector combination. The views are captured from various step angles between 0° and 360°. After the views are captured and stored, the views are combined, using a reconstruction algorithm, into a tomogram. A tomogram is a three dimensional representation of the internal attenuation coefficient differences (in the case when X-rays are used, the density differences), of the total object. This simplified description, as illustrated in Figure 4.2, is true for all forms of X-ray transmission tomography. In medical CT however, the source-detector combination is rotated around the patient not, like in material analysis, the object within the X-ray beam. Medical tomographs are further classified by the way in which the source-detector combination rotates around the patient: translation-rotation of a pencil beam; translation-rotation of a narrow fan beam; rotation of a fan beam; rotation of a fan beam with a fixed detector ring; helical rotation of a fan beam and helical rotation of a cone beam.[100] In the tomographs used for industrial and non-destructive testing (NDT) purposes the source detector combination is usually fixed and the object to be investigated is rotated within the generated X-ray cone beam. Any reference to a tomograph hereafter refers to such an industrial CT scanner.

For the successful implementation of the tomography principle, the configuration of source, then sample, and then detector is vital. The sample also needs to be rotated within the X-ray

cone beam as the different views from various step-angles are recorded. Finally the tomogram is reconstructed, displayed, and analysed on a computer.[101]

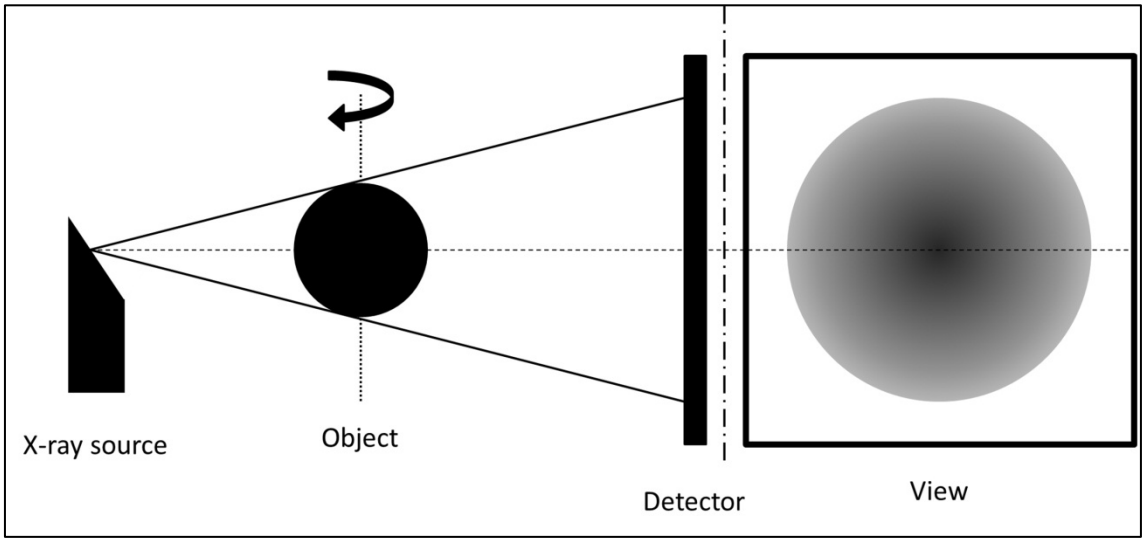

Figure 4.2: Simplified principle of CT acquisition (After Hoffman and De Beer (2012) and SABS (2005))[101, 102]

The object property that is recorded in an X-ray tomograph is the density distribution, through the difference in the attenuation coefficient of the materials. The attenuation coefficient of an object is a measure of how much of the X-ray beam is absorbed or scattered from the direct X-ray beam path. The linear attenuation coefficient of a homogeneous material is given by Equation 4.1 below.

$$\mu = \rho\left(a + b\frac{Z^{3.8}}{E^{3.2}}\right) \qquad \text{Equation 4.1}$$

In Equation 4.1, μ is the linear attenuation coefficient; ρ is the physical density of the material; Z is the atomic number of the material; E is the energy of the monochromatic X-rays, and a and b are constants that correspond to the Compton scattering and photoelectric absorption.[103]

X-ray generation:

X-rays are generated in an X-ray tube that consists of an electron gun (cathode) and a solid metal target (anode).[100] The electron gun projects a stream of focused fast electrons at the solid metal target, the electrons decelerate in the target surface layer due to interaction with its atoms and a spectrum of X-rays are produced.[99, 100, 104] These X-rays then propagate away from the target and are shaped by the X-ray tube diaphragm or collimators.[99, 100] Figure

4.3 shows a schematic representation of an X-ray tube. In the electron gun, the fast electrons are produced when a thoriated tungsten filament is heated to 2400 K to cause thermionic emission.[100] The electrons emitted from the filament are then accelerated and focused using Wehnelt optics (focussing cup).[100] The electrons enter the metal target where interactions with the atoms in the target decelerate the electrons. Every interaction of an electron with an atom generates, and radiates, electromagnetic waves with a single electron potentially undergoing several scattering interactions before coming to a complete standstill. This type of radiation is known as *bremsstrahlung* (deceleration radiation). The maximum energy of the *bremsstrahlung* spectrum is produced when an electron collides with the atom nucleus and produces a single photon, this is however a very rare process. Other interactions produce a spectrum of X-ray energies interspersed with a number of characteristic X-ray peaks. The peaks are due to direct interaction by the fast electron with the inner shell electron of the target's atoms. As the fast electron interacts with the inner shell electron, the inner shell electron is ejected and the atom is ionised. An electron from one of the higher shells fills the vacant position in the inner shell generating a large number of photons with a specific energy, creating characteristic peaks in the *bremsstrahlung* spectrum.[100] The peaks produced by a specific target material is unique to that material.[100] The total energy of the X-ray beam is only about 1% of the incident electron's energy, the rest is converted to heat.[99] Acceleration voltage determines the maximum energy of the X-ray beam and the current through the anode determines the X-ray flux, or the amount of X-ray photons produced.

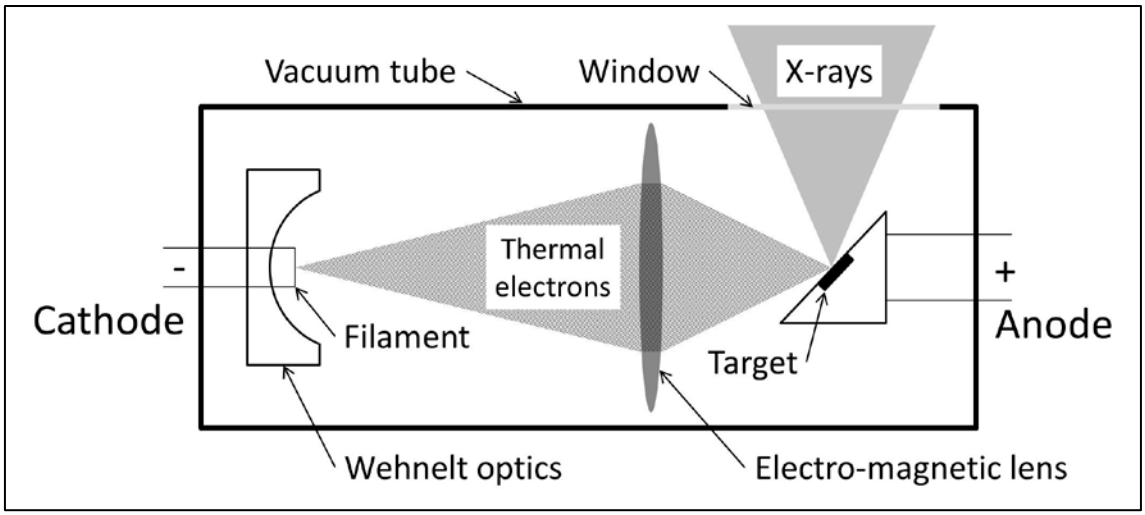

Figure 4.3: Schematic representation of an X-ray tube (redrawn after Buzug (2008), Bushberg et al. (2002), Simons et al. (1997), and Wikiradiography.net (2012))[96, 100, 105, 106]

X-ray interaction principles with materials:

Below an X-ray potential of 100 keV the photoelectric effect is the dominant X-ray material interaction, and above 100 keV Compton scattering is the dominant material interaction.[96] The other material interactions that can occur are Rayleigh scattering and pair production. Rayleigh scattering occurs at very low X-ray energies (15-30 keV), whilst pair production only occurs at very high X-ray energies (>1.02 MeV).[96, 100] Neither Rayleigh scattering nor pair production will have a significant influence in the X-ray energy ranges required to scan coal effectively, and therefore will not be discussed in this review.

Both Compton scattering and the photoelectric effect occurs when an incoming photon interacts with the valence electrons of an atom. Compton scattering is dependent on only the physical density of the material and occurs when the incident photon is deflected from the direct beam path after interaction with the material.[104] When a photon transfers all of its kinetic energy to an electron, in the process ejecting the electron from the atom, the interaction is called the photoelectric effect.[96] The photoelectric effect is dependent on the electron density of the material as well as the energy of the incident X-ray.[104] In the energy range that is used to characterise coal (~100 kV potential and thus for a W-target ~ 33 keV photon energies), the attenuation coefficient of a coal is independent of its chemical composition.[104, 107]

Tomography equipment infrastructure & principles:

The attenuated X-rays that pass through the object are recorded by the detector, the object is then rotated and the acquisition repeated for a pre-determined number of step angles. The step angle by which the object is rotated depends on the number of projections required. If, for instance, 500 projections are required the angle by which the object will be rotated between projections are: 360° / 1000 = 0.36° per step angle. The number of projections is a compromise between the quality of the tomogram and he time taken to acquire the tomogram. The sample is rotated and manipulated by the kinematic system. In medical CT systems, the source-detector combination rotates around the patient, but in industrial systems the object is manipulated within the X-ray beam. The kinematic system should be able to manipulate the object with high accuracy as inconsistencies influence the quality of the tomograms.[99] The kinematic system manipulates the object in all three dimensions: horizontally between the source and detector to achieve the desired magnification; horizontally and vertically parallel to the detector in order to ensure the object is within the field of view.[99] Finally, the kinematic system must be able to rotate the object at identical stepwise intervals.[99]

One of the advantages of μCT is the Image magnification achievable by moving the object closer to the X-ray source. Figure 4.4 shows this phenomenon visually. As the geometric magnification increases, however, the sharpness of the tomogram decreases due to increasing penumbral blurring.[104, 108] A larger X-ray spot size will also result in images with more penumbral blurring. The magnification (*M*) of the object can be described by the ratio of the distance between the source and the detector (*SD*), and the distance between the source and the object (*SO*), $M = \frac{SD}{SO}$.[99]

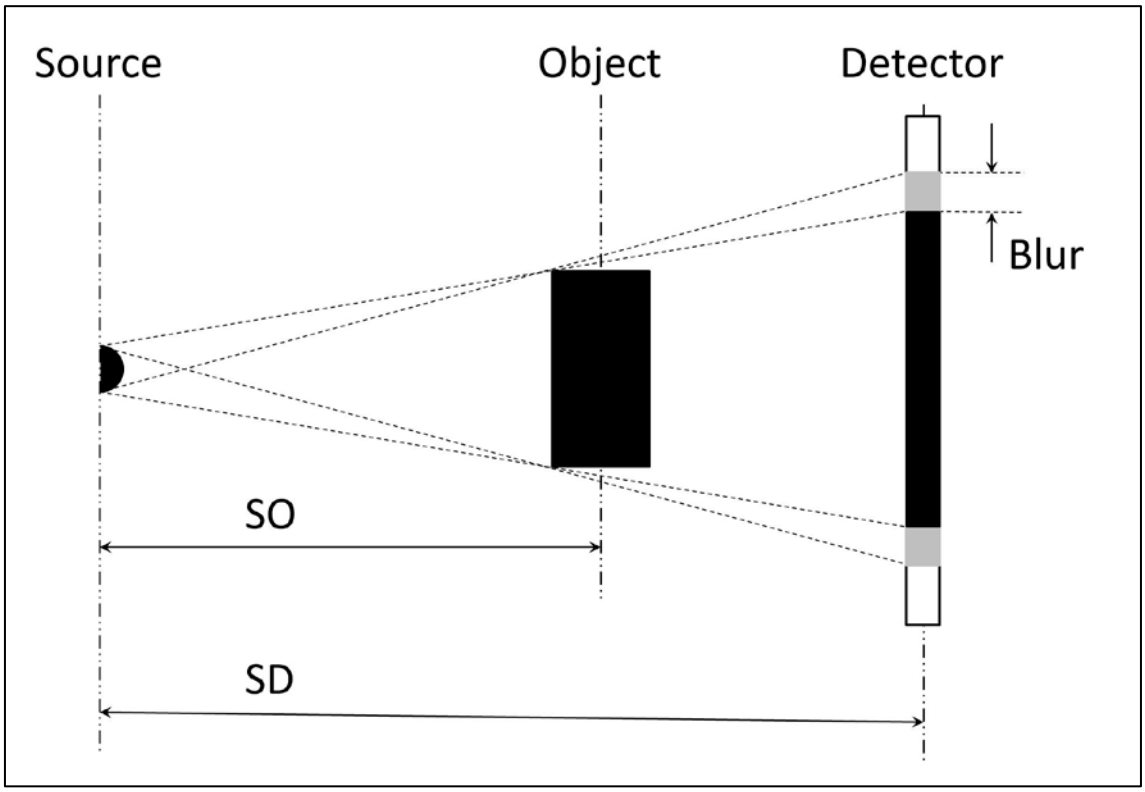

Figure 4.4: Image magnification in a cone beam projection (after Simons et al. (1997))[104]

The intensity of the attenuated X-ray beam is recorded by either a gas or solid-state detector. Solid-state detectors are the most common detectors used in current technology.[100] Solid-state detectors use a scintillator to convert the incident ionising radiation to visible light. The visible light is then converted into an electrical signal, proportional to the intensity of the light, by a photodiode. A flat panel detector is a matrix of photodiodes on a single glass substrate with the scintillator coating evaporated onto the matrix. Some of the common scintillator materials used for flat panel detectors are caesium iodide (CsI), bismuth germanate (BGO) and cadmium tungstate ($CdWO_4$).[100]

The intensity of the attenuated X-rays can be determined using Beer's law (Equation 4.2).

$$I = I_0 \exp(-\mu h) \qquad \text{Equation 4.2}$$

In Equation 4.2, I_0 is the incident X-ray intensity, I is the attenuated X-ray intensity, h is the thickness of the material that the X-rays have to traverse, and μ is the attenuation coefficient of the material (see Equation 4.1).

Equation 4.2 is a severe simplification of the actual situation as it assumes homogeneous material and monochromatic X-rays. In reality very few materials are homogenous, and very few X-ray sources deliver monochromatic X-rays. In Equation 4.3 below the heterogeneity of the material is taken into account, but monochromatic X-rays are still assumed with the entire X-ray spectrum represented by a single effective energy.[109]

$$\ln\left(\frac{I}{I_0}\right) = \int_0^L \mu\big(h(x,y)\big)\mathrm{d}h \qquad \text{Equation 4.3}$$

In Equation 4.3, $h(x,y)$ is the two dimensional coordinates of the linear attenuation coefficient and dh denotes the distance along the ray-path L. Figure 4.5 shows the summation of the different attenuation coefficients through an object visually. The black arrow represents the beam path and the blocks of varying shades of grey materials of differing attenuation coefficients. The attenuated intensity of the X-ray is dependent on the attenuation of every material it passes through, as well as the distance the ray travels through the material. In Figure 4.5, $\mu_{1\text{-}4}$ represents the attenuation coefficients of the various constituents the beam is travelling through and $h_{1\text{-}4}$ represent the length of the beam path through the respective material.

Another essential part of a tomograph is the computer that is used to control the scan operation and to manipulate the generated data. The two functions are not necessarily handled by the same computer. Several computers are used to control the motion of the object within the X-ray beam, control the operation of the X-ray source, control the data acquisition from the detector, perform the reconstruction of the sample into a 3D-tomogram, the visualisation and analysis of the acquired dataset in 3D, as well as the control of data storage and retrieval.

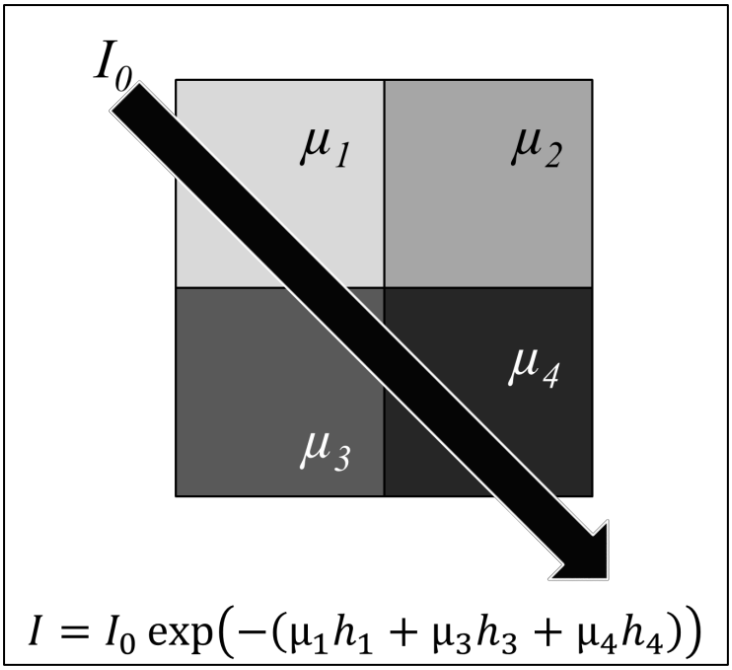

Figure 4.5: Visual representation of the linear attenuation coefficient (redrawn after Van Geet et al. (2001))[108]

Reconstruction

The reconstruction of a tomogram is done on the basis of the Radon transform. The Radon transform of an object describes the density of the object along all possible line integrals through the object.[110] The Radon transform of a single slice can be visually represented by a sinogram (Figure 4.6), and is a plot of all the linear attenuation coefficients for all views around a slice, and all applicable distances from the axis of rotation. The sinogram in Figure 4.6 shows 1000 projections around a coal particle. Numerical values of the attenuated X-ray beams are presented on a grey scale with the higher attenuated X-ray beams as black or dark grey and the lower attenuated constituents as light grey.

The sinogram is the basis when using back-projection and filtered back-projection (FBP) as reconstruction methods. Back-projection is the process whereby data in the sinogram is projected back along the X-ray beam path. The back-projections from all the views are averaged and an approximation of the scanned object is then produced. FBP improves the approximation that is generated by filtering the back-projected data, improving the resolution of fine detail.[101, 110] Other reconstruction methods include algebraic reconstruction techniques,[107] statistical reconstruction techniques, iterative least squares techniques and the two-dimensional Fourier transform.[107] FBP is the most common method used due to the relative ease of computation.[111] The reconstructed tomogram is usually shown as a negative to ensure consistency with how the images are displayed in traditional radiography.[107] For

cone beam geometries however the FDK algorithm (developed by Feldkamp et al. (1984)) must be used for reconstruction.[99, 112] The reconstruction is done by computer software packages, running on high performance computers, often supplied by the tomograph manufacturers.

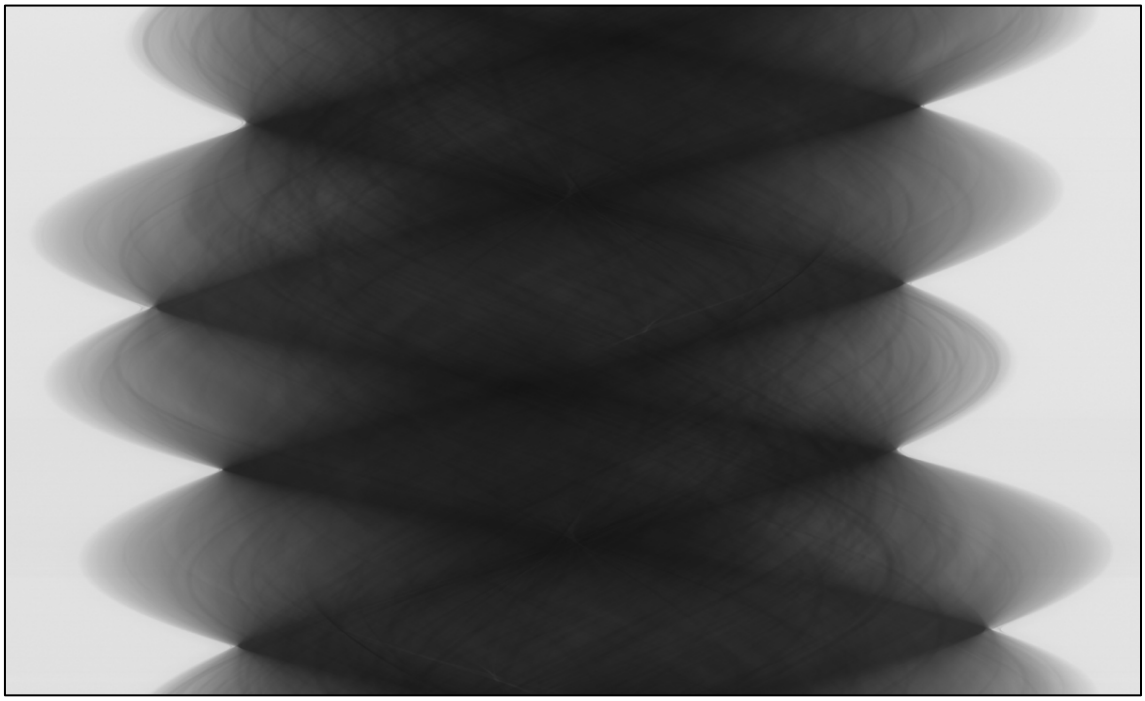

Figure 4.6: Sinogram of the centre slice of a coal particle scanned at 160 keV and 70mA on a NIKON XTH 225 ST tomograph from 1000 rotational views

The final step in the acquisition process is the visualisation and segmentation of the tomogram. During this process the reconstructed tomogram is displayed on a computer screen as a 3D rendering of the object. The rendered object can be manipulated to aid in the perception of the object or sliced in any of the three orthogonal directions or obliquely. Segmentation is the process where the tomogram is separated into the various constituents based on the grey values produced during the reconstruction process. When X-rays are used to generate the tomogram, the grey values are effectively a representation of the density distribution in the object, especially if the constituents have a similar composition. Finally the surface of the object can be extracted and used for various measurements during metrology. A large number of software packages are available for the visualisation and segmentation of the tomograms. See Cunningham et al. (2014) for a list of software packages used in palaeontology.[113]

µCT quality and artefacts

Quality

The quality parameters of a tomogram are affected by the properties of the tomograph hardware and the acquisition settings selected by the operator. These include the X-ray beam characteristics, the geometry and composition of the scanned object, operator input and detector characteristics.[99, 114]

The characteristics of the X-ray beam is determined by the type of target that is used to generate the X-rays, the size of the spot where the incident electrons impact the target, the current used during the generation of the fast electrons, and the voltage used to accelerate the fast electrons. The intensity (the amount of photons emitted) of the X-ray beam is influenced by the proton number of the target and the current used to generate the fast electrons: as the current through the filament is increased the number of electrons generated increases. As a result the number of electrons that hit the target increases, increasing the number of X-ray photons produced. The target material additionally influences the penetrating power of the X-rays. The acceleration voltage used to accelerate the electrons from the cathode to the anode in the source influences the maximum X-ray energy, penetrating power of the X-rays and the X-ray intensity. The size of the spot where the fast electrons hit the target, and the X-rays are produced, is a particularly important factor influencing the quality of the tomogram,[115] and determines the amount of blurring that occurs during acquisition (see Figure 4.4), this in turn, influences the maximum possible resolution of the tomogram. Other properties that influence the resolution of the tomogram are: physical interactions that occur as the X-rays pass through the object (scattering and absorption), the geometric enlargement of the object (see Figure 4.4), and the physical size of the detector pixels.[116]

Another quality issue arises with the reproducibility of tomograms generated on different tomographs, especially when the data from one institution is compared to that of another institution (or between two tomograms with different scanning parameters). This is due, in part, to the many factors that influence the quality of the various scans.[106] Carmignato (2012) conducted a study where the metrological data generated by a number of institutions were compared, and found that participants could determine measurements with sub-voxel accuracy. However, due to the lack of any international standards for uncertainty evaluation or standards to evaluate the performance of tomographs used for metrology, participants could not accurately determine the measurement uncertainty.[106]

Artefacts

Artefacts are another factor that influences the quality of the tomograms. Although artefacts are not easily mistaken for any part of the physical structure of the tomograms, the artefacts may obscure important features.[117] Artefacts are dependent on a number of scan parameters including the X-ray source, tomograph geometry, sample- and detector properties.[114] The important artefacts and errors that can occur in micro-focus computed tomography (µCT) tomograms are: metal artefact, beam hardening, ring artefacts and noise. Figure 4.7 shows some examples of a metal artefact and ring artefacts.

Beam hardening occurs due to the erroneous assumption that the entire spectrum of X-rays produced can be characterised by a single characteristic energy. As the X-ray beam travels along the beam-paths the lower energy photons (soft X-rays) are attenuated before the more energetic photons (hard X-rays). This causes the mean energy of the X-ray beam to rise, which in turn causes the centre of the object to appear less attenuating, and the shorter beam paths to appear more attenuating than longer beam paths. Beam hardening manifests as cupping, starbursts around highly attenuating inclusions,[117] dark streaks between two highly attenuating inclusions and the rounding of flat edges.[118] As beam hardening is considered by some to be the most detrimental and most common artefact, numerous studies has been done on the prevention and correction of beam hardening.[103, 119]

Figure 4.7: Examples of a metal- and ring artefact

The methods used to minimise beam hardening include software corrections, as well as hardware filters, and wedge calibration to pre-harden the beam. Dual energy scanning techniques can also be applied to reduce beam hardening. For the minimisation of beam hardening during coal tomography hardware filters are able to eliminate the beam hardening to a large degree.[103, 120] Hardware filters are usually a thin metal foil that is inserted between

the X-ray source and the object. The metallic foil pre-attenuates or pre-hardens the X-ray beam removing many of the soft X-ray photons reducing the beam hardening but lowering contrast and introducing noise.[103, 118, 120, 121] An analogous method to hardware filters is wedge calibration that involves calibrating the tomograph using a material with a similar density to that of the sample. The object to be characterised is then surrounded by this material and scanned. Using this method the beam hardening can be virtually eliminated.[122] Software corrections usually involves transforming the data generated for the polychromatic X-rays to data equivalent to that generated by monochromatic X-rays, this process is known as linearisation.[118, 122] The linearisation can be improved by segmenting the object that is scanned into a number of homogenous materials and correcting the linearisation curve for each of these materials.[122] Linearisation is however not suited to heterogeneous materials such as coal, as an *a priori* knowledge of the structure is required, and cannot be accurately determined for coal.[118] In a dual energy scan the object that is characterised is scanned at two different X-ray energies. One dataset is generated where the dominant material interaction is photoelectric absorption, and one where the dominant material interaction is Compton scatter. The two scans are then combined into a single tomogram.[121, 122] Dual-energy tomograms show decreased beam hardening but do suffer from increased noise. According to Remeysen and Swennen (2006) the noise produced by the dual energy technique is lower than the noise produced by hardware filtering.[118]

Ring artefacts present as a number of concentric circles around the axis of rotation (see Figure 4.7). Ring artefacts are not sample dependent but are due to the response of the detector and are produced when the measured attenuation at a specific detector element differs from the real value.[123] This can occur due to dust or scratches on the detector, due to a faulty detector element or incorrect calibration.[117] A number of methods to minimise ring artefacts have been proposed, either correcting the sinogram before reconstruction or modifying the acquisition procedure.[119, 123]

Noise can be caused in the detector itself while the number of photons is counted, or can occur as a by-product of signal amplification.[96] Scatter occurs due to the physical interaction of the X-ray beam with the source projection window, the scanned object, or the detector. As the X-rays are projected through the projection window of the source and the object, some of the X-ray photons are deflected from the beam path, and are recorded by the detector at another position. Scattering can also occur at the detector where the visible light that is produced by the scintillator is erroneously recorded by adjacent elements.[100]

Applications of µCT

Other than the application of computed tomography (CT) in diagnostic radiology, for which it is most widely known, CT and micro-focus X-ray computed tomography (µCT) have found application in diverse other fields including applications in the geological sciences. Since the first use of CT in palaeontology, CT has been applied to study the 3D structure of various materials, as well as monitoring transient processes like fluid flow in porous samples.[107] The structures investigated included porosity, fractures and particles shape. The influence of these structures on the swelling, shrinkage and sorption capacity was investigated as well. Due to the high scanning speed that can be attained using medical tomographs, these tomographs are often used to study transient processes such as the flow of water, oil and gas through porous media in 3D.

A number of reviews give the applications of µCT to the geosciences amongst them Duliu (1999), Cnudde and Boone (2013), and Kyle and Ketcham .[107, 119, 124] Below are some of the studies conducted using µCT in the geosciences, coal sciences, coal degradation, and coal breakage to showcase the versatility of µCT. The reviews by Kruth et al. (2011) and De Chiffre et al. (2014) give some of the applications of µCT in dimensional metrology.[99, 115]

Geoscience

The review by Duliu (1999) lists some of the applications of CT and µCT in soil science, sedimentology, coal geology, and rock mechanics;[107] and concluded that CT provides useful data about the structure of the materials studied. Cnudde et al. (2006) called µCT a promising technique and lists palaeontology, sedimentology, petrology, soil science, and fluid flow research as applications.[116] Cnudde and Boone (2013) lists some of the applications as 3D pore characterisation, 3D grain analysis, fracture analysis, ore analysis, monitoring structural dynamic processes, fluid flow analysis, and morphological characterisation of fossils.[124] The authors also mention multi-scale imaging, where a section from the original tomogram is again imaged using higher resolution techniques, and registering these high resolution images to the original tomogram in order to gain a better understanding of the features imaged.

Figure 4.8, reproduced from Fisher et al. (2014), shows an example of how CT is applied in palaeontology.[125] The CT scans of the two calves studied in the article by Fisher et al. (2014) gave detailed information on the development of the calves and some insight into cause of death.[125]

Cnudde and Boone (2013) concluded that although the technology is reaching maturity there are still a number of limitations that must be taken into account to use the technology optimally. Kyle and Ketcham list some of the applications as differentiation of ore minerals, textural analysis, petrological investigations of ore types and structural studies. Kyle and Ketcham concluded that the use of µCT not only contributes to the scientific knowledge of an ore's origin but can be applied, practically, to ore processing.[119] Ketcham and Carlson (2001) also give a number of examples where µCT is used in the geosciences.[126] Mees et al. (2003) lists a number of studies that use µCT ranging from studies in palaeontology, petrology, petroleum geology, flow characterisation and fracture characterisation to studies comparing the porosity values from µCT and traditional techniques.[121]

Other than the studies and applications mentioned above, µCT has been applied to determine the compressive stress of coke, to liberation studies to determine the number and locations of sphalerite grain in dolomite particles, as well as to determine the aperture of fractures present in sandstone borehole drill core. [127-129] The size of the features that can be detected using µCT is $\frac{1}{10}^{th}$ the spatial resolution depending on the tomogram quality.[126, 130] Lin and Miller (2005) used µCT to characterise the shape of various irregularly shaped particles.[131] Garcia et al. (2009) applied µCT to determine the interfacial area of the inclusions in a sulphide copper ore.[69] Miller (2010) reviewed the use of µCT in the study of particulate systems to study comminution and liberation of a packed bed of particles as well as the flow through a packed bed.[132] Liberation of multiphase mineral particle was also studied by Lin and Miller (1996), whom concluded that the use of µCT can overcome the limitations of liberation studies using polished sections.[127]

Coal Science

X-ray CT has been applied to coal science where it is used to determine the porosity of a coal particle, it is used in 3D petrography, to study the cleat structure of coal, to characterise the strength of coal, and the changes that occur during pyrolysis and combustion.

Yao et al. (2009) compared the coal porosity determined by µCT, helium pycnometry and water saturation; finding a strong correlation between the results obtained for µCT and helium pycnometry, and a moderate correlation between the results obtained from µCT and water saturation. The authors attributed this discrepancy to the fact that µCT also considered closed pores in the calculation and the finite nature of the µCT resolution.[133] Li et al. (2012) used µCT to determine the porosity of four Chinese coals in different stages of deformation.[134]

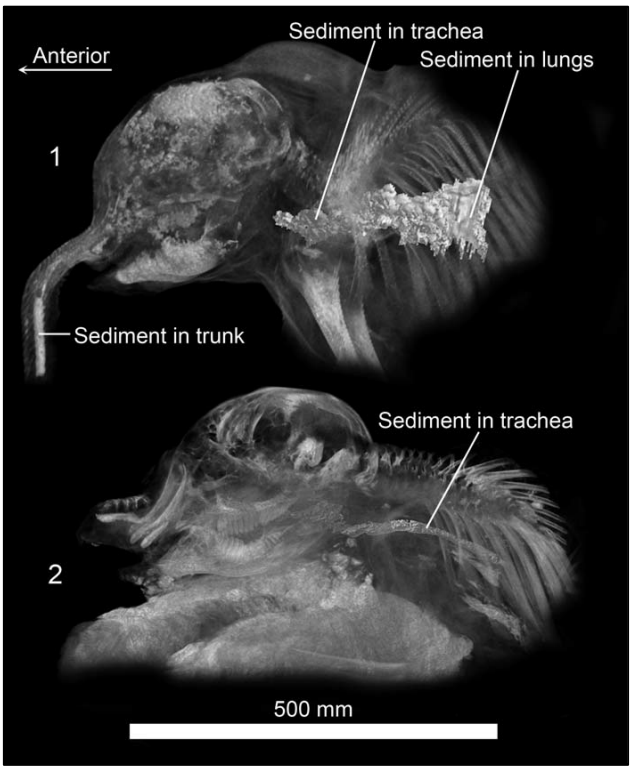

Figure 4.8: CT scan of two Mammoth calves showing cause of death as aspirated mud (reproduced from Fisher et al. (2014))[125]

Various authors used µCT to determine the density of various coal macerals identified using optical imaging (colour image analysis (CIA)).[103, 104, 108, 135, 136] Table 4.1 compares the values determined by Verhelst et al. (1996), Van Geet et al. (2001), and Van Geet et al. (2000) to values found in literature. A number of issues exist when using µCT to determine the density of coal macerals:

- CIA uses the surface percentages to determine the maceral composition, whilst µCT cannot be used on the surface of the particles due to imaging artefacts, and the analysis must be done slightly away from the surface introducing inaccuracies.[136] Although both the surface and the slice taken just below the surface describe essentially the same properties if the layering of the coal stays more or less constant throughout the sample.[104]

- Due to the differences in the spatial resolution of CIA and µCT some of the features that influence the data generated by µCT cannot be identified in µCT, but can be identified using CIA.[136]

- The close association of minerals and macerals influences the density of the macerals determined by µCT.[136]

- Some of the minerals can be misidentified as coal macerals during CIA and raise the density determined from µCT.[103, 136] Pyrite can be mistaken for inertinite, and clays can be mistaken for liptinite.[135]

- Without an *a priori* knowledge of the sample composition, the energy spectrum of the X-rays required to minimise the influence of photoelectric scattering cannot be determined.[104]

The use of dual energy techniques was suggested as a possible method to increase the accuracy of density determinations, as not only can the tomo-density be determined but the physical density can also be accurately determined.[103, 108, 135]

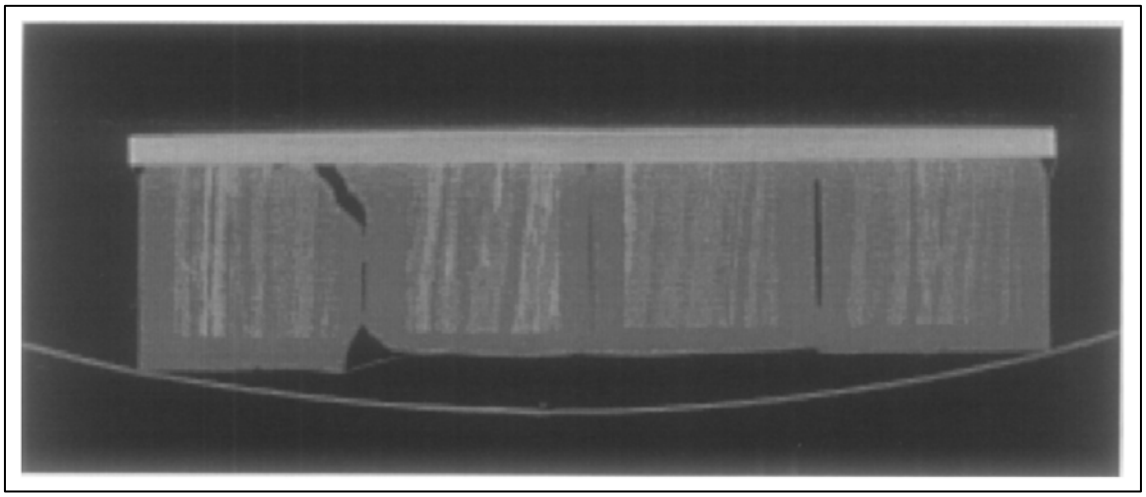

Figure 4.9: Tomographic cross-section of a sample used to determine the density of coal macerals using CT and CIA (reproduced from Verhelst et al. (1996))[136]

Figure 4.9 shows the tomographic cross-section of one of the samples that Verhelst et al. (1996) used to determine densities for the various coal maceral components.[136] The thick, light-grey line at the top of Figure 4.9 is a glass plate that was used to cover the polished surface where CIA was done. Note the density variations along the length of the sample cross-section.

Van Geet and Swennen (2001), Ketcham et al. (2010), Van Geet et al. (2000), and Mazumder et al. (2006) used µCT to determine the aperture of cracks and cleats present in coal.[120, 130, 135, 137] Ketcham and Carlson (2001), and Ketcham et al. (2010) determined that even though many of the cracks are smaller than the resolution of the tomograms, the

aperture can be measured thanks to the partial volume effect; features as small as $^{1}/_{10}^{th}$ the spatial resolution can be measured.[126, 130] Van Geet et al. (2000) and Van Geet and Swennen (2001) found that there is a linear relation between the CT number and the aperture of the features.[120, 135] Mazumder et al. (2006) used µCT to determine the cleat length, orientation and the spacing.[137]

Table 4.1: Comparison of densities calculated by various authors using µCT and those found in literature

Component	Density calculated by Verhelst et al. (1996) (kg/m^3)[136]	Density calculated by Van Geet et al. (2000) (kg/m^3)[103, 135]	Density from literature (Stach and Murchison (1982) (kg/m^3))[108, 138]	Density from literature (Falcon and Snyman (1986) (kg/m^3))[74]
Vitrinite	1375	1310	1300-1360	1250-1400
Liptinite	2450	1740	<1300	<1300
Inertinite	1590	5640	1600	1350-1750

Naudé et al. (2013), Hoffman (2012), and Hoffman and De Beer (2012) applied µCT to coal pyrolysis.[102, 139, 140] Hoffman (2012) showed how the structure of the particles changes during the various stages of pyrolysis.[140] Naudé et al. (2013) quantified the changes that occur in coal during pyrolysis and found that µCT was able to generate information on the porosity, inorganic and organic constituents. Naudé et al. (2013) found that the porosity of coal increased during pyrolysis, but that the increase was not constant for all of the samples tested; organic content decreased during pyrolysis while the inorganic material formed agglomerates. Naudé et al. (2013) could, however, not differentiate between the various iron-bearing minerals nor could the various maceral phases be identified definitively using µCT.[139]

Pone et al. (2009) and Pone et al. (2010) used µCT and feature tracking to determine the changes that occur within the coal structure during CO_2 sorption and desorption.[141, 142] During feature tracking a number of distinct and unique points within a coal particle were identified; using groups of four points a tetrahedron was formed, and the movement of the

tetrahedron centroid tracked before and after the sorption and desorption experiments. Although the identification of the fiducial points in the various tomograms were time consuming Pone et al. (2009) and Pone et al. (2010) determined that the technique can be successfully applied, and provides information on the relationship between coal microstructure and deformation during CO_2 sorption and desorption.[141, 142] Karacan and Mitchell (2003) also used µCT to study the porosity and sorption rates for coal microlithotypes under confining pressure and found that vitrinite swells during CO_2 sorption.[143]

Golab et al. (2013) used µCT to study the spatial distribution and modes of occurrence of the mineral matter present in coal; the authors concluded that µCT is an invaluable tool in understanding the distribution, origin and modes of occurrence of the various mineral phases that exist in coal.[144]

Coal breakage

CT has been applied to the breakage and fracture characterisation of various materials, although very little of the applications were in coal impact breakage and no studies on degradation. Most of the studies focused on the permeability of coal and other materials. Nie et al. (2014) confirmed that the determination of the mechanical properties of coal are very difficult due to its structural complexity.[70] Although Van Geet and Swennen (2001), Van Geet et al. (2000), Ketcham et al. (2010), and Mazumder et al. (2006) used µCT to determine the aperture of cracks and cleats present in coal, the studies were not applied to the evolution of the fractures during breakage.[120, 130, 135, 137]

Hlatshwayo et al. (2007) found that, during thermal fracture, the cracks tended to form at the microlithotype boundaries and at mineral boundaries.[31] Figure 4.10 is a tomogram slice (reproduced from Hlatshwayo et al. (2007)) from a particle that underwent thermal fracture and shows two pyrite inclusions with a number of cracks that appear to have initiated at the mineral inclusions.

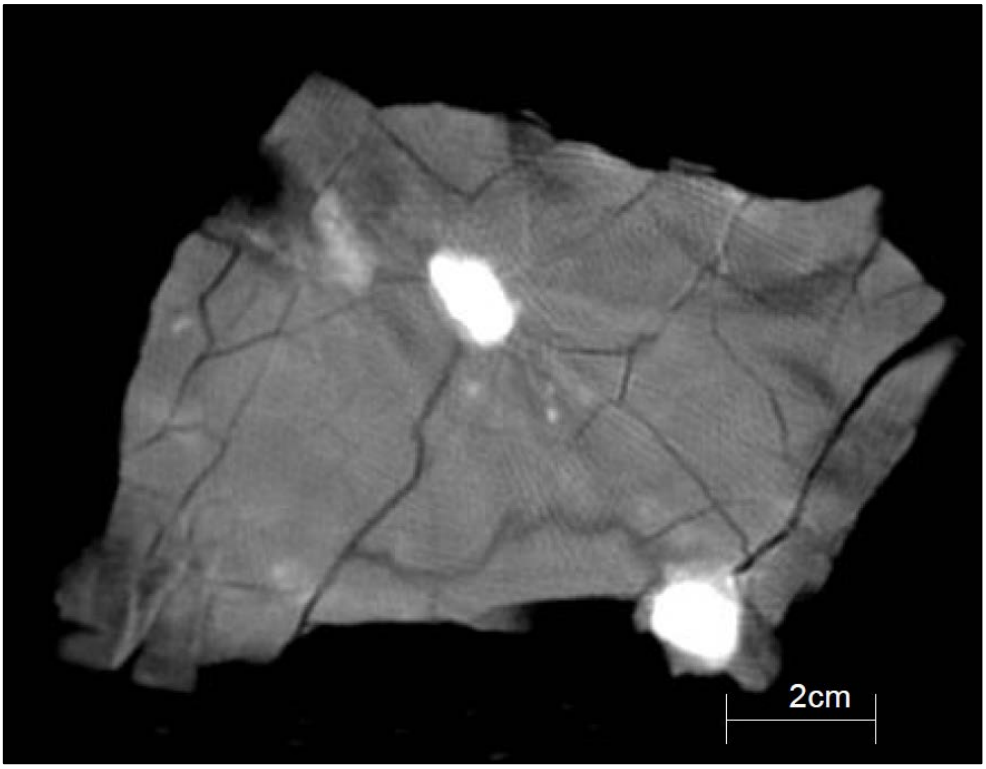

Figure 4.10: Tomogram slice that shows how cracks radiate from mineral inclusions during thermal fragmentation (reproduced from Hlatshwayo et al. (2007))[31]

Nie et al. (2014) used μCT to determine the crack evolution during the uniaxial compression of coal particles, and determined that the cracks that form during compression form at weaknesses within the coal matrix.[70]

Conclusions

The preceding review introduced micro-focus X-ray computed tomography (µCT) and gives a summary of the tomography process, the relevant interactions between materials and X-rays, and the applications of µCT in geosciences. Although the technology has been widely applied in geosciences, including studies in coal, there is very little literature that describes the application of µCT to coal degradation. Micro-focus X-ray computed tomography has successfully been applied to identify and measure the cleat structure of coal, as well as tracking the changes that occurs during CO_2 sorption. It is assumed that µCT will be uniquely suited to study the internal features of coal and the influence that these features have coal degradation. Further studies are required to confirm the technology's applicability in coal degradation research.

Chapter 5 applies µCT to the compression breakage of coal in order to confirm its applicability to identify and track the changes that occurs within coal during slow compression breakage.

Chapter 4 - References

31. Hlatshwayo, H.L., Pinetown, K.L. & Campbell, Q.P. 2007. Fundamental understanding of the influence of physical properties on the thermal fragmentation of coal. (*In* International Conference on Coal Science and Technology organised by The University of Nottingham, Nottingham).

69. Garcia, D., Lin, C. & Miller, J. 2009. Quantitative analysis of grain boundary fracture in the breakage of single multiphase particles using X-ray microtomography procedures. *Minerals engineering*, 22(3):236-243.

70. Nie, B., He, X., Li, X., Chen, W. & Hu, S. 2014. Meso-structures evolution rules of coal fracture with the computerized tomography scanning method. *Engineering failure analysis*, 41:81-88.

74. Falcon, R.M. & Snyman, C. 1986. An introduction to coal petrography: atlas of petrographic constituents in the bituminous coals of South Africa. Johannesburg: Geological Society of South Africa.

96. Bushberg, J.T., Seibert, J.A., Leidholdt, E.M., Jr. & Boone, J.M. 2002. The essential physics of medical imaging. 2nd ed. Philadelphia, PA: Lippincott, Williams & Wilkins.

97. Cierniak, R. 2011. X-ray computed tomography in biomedical engineering. London: Springer.

98. Beckmann, E.C. 2006. CT scanning the early days. *The British journal of radiology*, 79(937):5-8.

99. Kruth, J.P., Bartscher, M., Carmignato, S., Schmitt, R., De Chiffre, L. & Weckenmann, A. 2011. Computed tomography for dimensional metrology. *CIRP annals - manufacturing technology*, 60(2):821-842.

100. Buzug, T.M. 2008. Computed tomography: from photon statistics to modern cone-beam CT. Berlin: Springer.

101. SABS. 2005. Non-destructive testing - radiation methods - computed tomography. Pretoria: South African Bereau of Standards (SABS).(South African National Standard (SANS) 15708-1:2005).

102. Hoffman, J.W. & De Beer, F. 2012. Characteristics of the Micro-Focus X-ray Tomography Facility (MIXRAD) at Necsa in South Africa. (*In* 18th World Conference on Nondestructive Testing, Durban: South African Institute for Non-Destructive Testing. p. 1-12).

103. Van Geet, M., Swennen, R. & David, P. 2001. Quantitative coal characterisation by means of microfocus X-ray computer tomography, colour image analysis and back-scattered scanning electron microscopy. *International journal of coal geology*, 46(1):11-25.

104. Simons, F.J., Verhelst, F. & Swennen, R. 1997. Quantitative characterization of coal by means of microfocal X-ray computed microtomography (CMT) and color image analysis (CIA). *International journal of coal geology*, 34(1–2):69-88.

105. Wikiradiography.net. 2012. Physics of the X-ray tube. http://www.wikiradiography.net/page/Physics+of+the+X-Ray+Tube Date of access: 13 April 2016.

106. Carmignato, S. 2012. Accuracy of industrial computed tomography measurements: experimental results from an international comparison. *CIRP annals - manufacturing technology*, 61(1):491-494.

107. Duliu, O.G. 1999. Computer axial tomography in geosciences: an overview. *Earth-science reviews*, 48(4):265-281.

108. Van Geet, M., Swennen, R. & Wevers, M. 2001. Towards 3-D petrography: application of microfocus computer tomography in geological science. *Computers & geosciences*, 27(9):1091-1099.

109. Akin, S. & Kovscek, A.R. 2003. Computed tomography in petroleum engineering research. *(In* Mees, F., Swennen, R., van Geet, M. & Jacobs, J., *eds.* Applications of X-ray computed tomography in the geosciences. London: Geological Society. p. 23-38).

110. Markoe, A. 2006. Analytic tomography. New York: Cambridge University Press. (Encyclopedia of mathematics and its applications).

111. Banhart, J., *ed*. 2008. Advanced tomographic methods in materials research and engineering. Oxford: Oxford University Press. (Monographs on the Physics and Chemistry of Materials).

112. Feldkamp, L.A., Davis, L.C. & Kress, J.W. 1984. Practical cone-beam algorithm. *Journal of the Optical Society of America*, 1(6):612-619.

113. Cunningham, J.A., Rahman, I.A., Lautenschlager, S., Rayfield, E.J. & Donoghue, P.C.J. 2014. A virtual world of paleontology. *Trends in ecology & evolution*, 29(6):347-357.

114. Krimmel, S., Stephan, J. & Baumann, J. 2005. 3D computed tomography using a microfocus X-ray source: analysis of artifact formation in the reconstructed images using simulated as well as experimental projection data. *Nuclear instruments and methods in physics research*, 542(1–3):399-407.

115. De Chiffre, L., Carmignato, S., Kruth, J.P., Schmitt, R. & Weckenmann, A. 2014. Industrial applications of computed tomography. *CIRP annals - manufacturing technology*, 63(2):655-677.

116. Cnudde, V., Masschaele, B., Dierick, M., Vlassenbroeck, J., Hoorebeke, L.V. & Jacobs, P. 2006. Recent progress in X-ray CT as a geosciences tool. *Applied geochemistry*, 21(5):826-832.

117. Barrett, J.F. & Keat, N. 2004. Artifacts in CT: recognition and avoidance. *RadioGraphics*, 24(6):1679-1691.

118. Remeysen, K. & Swennen, R. 2006. Beam hardening artifact reduction in microfocus computed tomography for improved quantitative coal characterization. *International journal of coal geology*, 67(1–2):101-111.

119. Kyle, J.R. & Ketcham, R.A. 2015. Application of high resolution X-ray computed tomography to mineral deposit origin, evaluation, and processing. *Ore geology reviews*, 65(4):821-839.

120. Van Geet, M. & Swennen, R. 2001. Quantitative 3D-fracture analysis by means of microfocus X-Ray computer tomography (μCT): an example from coal. *Geophysical research letters*, 28(17):3333-3336.

121. Mees, F., Swennen, R., Van Geet, M. & Jacobs, P. 2003. Applications of X-ray computed tomography in the geosciences. *(In* Mees, F., Swennen, R., van Geet, M. & Jacobs, J., *eds.* Applications of X-ray computed tomography in the geosciences. London: Geological Society. p. 1-6).

122. Ketcham, R.A. & Hanna, R.D. 2014. Beam hardening correction for X-ray computed tomography of heterogeneous natural materials. *Computers & geosciences*, 67:49-61.

123. Titarenko, S., Withers, P.J. & Yagola, A. 2010. An analytical formula for ring artefact suppression in X-ray tomography. *Applied mathematics letters*, 23(12):1489-1495.

124. Cnudde, V. & Boone, M.N. 2013. High-resolution X-ray computed tomography in geosciences: a review of the current technology and applications. *Earth-science reviews*, 123:1-17.

125. Fisher, D.C., Shirley, E.A., Whalen, C.D., Calamari, Z.T., Rountrey, A.N., Tikhonov, A.N., Buigues, B., Lacombat, F., Grigoriev, S. & Lazarev, P.A. 2014. X-ray computed tomography of two mammoth calf mummies. *Journal of paleontology*, 88(4):664-675.

126. Ketcham, R.A. & Carlson, W.D. 2001. Acquisition, optimization and interpretation of X-ray computed tomographic imagery: applications to the geosciences. *Computers & geosciences*, 27(4):381-400.

127. Lin, C. & Miller, J. 1996. Cone beam X-ray microtomography for three-dimensional liberation analysis in the 21st century. *International journal of mineral processing*, 47(1):61-73.

128. Gagarin, S. 2012. Study of coke structure by computerized X-ray tomography: a review. *Coke and chemistry*, 55(2):56-61.

129. Keller, A. 1998. High resolution, non-destructive measurement and characterization of fracture apertures. *International journal of rock mechanics and mining Sciences*, 35(8):1037-1050.

130. Ketcham, R.A., Slottke, D.T. & Sharp, J.M. 2010. Three-dimensional measurement of fractures in heterogeneous materials using high-resolution X-ray computed tomography. *Geosphere*, 6(5):499-514.

131. Lin, C. & Miller, J. 2005. 3D characterization and analysis of particle shape using X-ray microtomography (XMT). *Powder technology*, 154(1):61-69.

132. Miller, J. 2010. Characterisation, analysis and simulation of multiphase particulate systems using high resolution X-ray micro computed tomography (HRXMT). (*In* XXV Internation Mineral Processing Congress (IMPC), Brisbane, QLD, Australia).

133. Yao, Y., Liu, D., Che, Y., Tang, D., Tang, S. & Huang, W. 2009. Non-destructive characterization of coal samples from China using microfocus X-ray computed tomography. *International journal of coal geology*, 80(2):113-123.

134. Li, S., Tang, D., Xu, H. & Yang, Z. 2012. Advanced characterization of physical properties of coals with different coal structures by nuclear magnetic resonance and X-ray computed tomography. *Computers & geosciences*, 48:220-227.

135. Van Geet, M., David, P. & Swennen, R. 2000. Three dimensional coal characterisation (maceral, mineral and cleats) by means of X-ray microfocus computer tomography (µCT). (*In* Podemski, M. & Jureczka, J., *eds*. European Coal Conference IV, Warsaw, Poland: Polish Geological Institute. p. 263-270).

136. Verhelst, F., David, P., Fermont, W., Jegers, L. & Vervoort, A. 1996. Correlation of 3D-computerized tomographic scans and 2D-colour image analysis of Westphalian coal by means of multivariate statistics. *International journal of coal geology*, 29(1–3):1-21.

137. Mazumder, S., Wolf, K.-H., Elewaut, K. & Ephraim, R. 2006. Application of X-ray computed tomography for analyzing cleat spacing and cleat aperture in coal samples. *International journal of coal geology*, 68(3):205-222.

138. Stach, E. & Murchison, D.G. 1982. Stach's textbook of coal petrology. 3rd ed. Berlin: Gebrüder Borntraeger.

139. Naudé, G., Hoffman, J., Theron, S.J. & Coetzer, G. 2013. The use of X-ray computed tomography in the characterisation of coal and associated char reductants. *Minerals engineering*, 52:143-154.

140. Hoffman, J.W. 2012. Ionizing radiation as imaging tool for coal characterization and gasification research. Potchefstroom: North-West University. (Dissertation - M.Eng).

141. Pone, J.D.N., Hile, M., Halleck, P.M. & Mathews, J.P. 2009. Three-dimensional carbon dioxide-induced strain distribution within a confined bituminous coal. *International journal of coal geology*, 77(1):103-108.

142. Pone, J.D.N., Halleck, P.M. & Mathews, J.P. 2010. 3D characterization of coal strains induced by compression, carbon dioxide sorption, and desorption at in-situ stress conditions. *International journal of coal geology*, 82(3):262-268.

143. Karacan, C.Ö. & Mitchell, G.D. 2003. Behavior and effect of different coal microlithotypes during gas transport for carbon dioxide sequestration into coal seams. *International journal of coal geology*, 53(4):201-217.

144. Golab, A., Ward, C.R., Permana, A., Lennox, P. & Botha, P. 2013. High-resolution three-dimensional imaging of coal using microfocus X-ray computed tomography, with special reference to modes of mineral occurrence. *International journal of coal geology*, 113:97-108.

Chapter 5 - An analysis of the slow compression breakage of coal using micro-focus X-ray computed tomography

In Chapter 3 it was shown that the particle shape and the impact orientation of a particle affects the degradation of coal, although it was not clear why these properties affect degradation. It was suggested that the internal structures of the coal particles may contribute to the coal breakage. Chapter 4 showed that micro-focus X-ray computed tomography (µCT) is uniquely suited to examine the internal structure of coal. Micro-focus X-ray computed tomography was applied, with great success, to determine the changes that occur within a coal particle during carbon dioxide (CO_2) sorption.

The content of Chapter 5 is a paper presented at the XVII International Coal Preparation Congress held in Istanbul, Turkey from 1 – 6 October 2013; after the congress the paper was peer-reviewed and a version published in the International Journal of Coal Preparation and Utilization.[*] The article confirms the applicability of µCT to identify and track the changes that occur within a coal particle during slow compression breakage.

In Chapter 3 it was shown that the contact area during impact breakage affects the degradation. In order to minimise the impact of the contact area during this study, the coal particles were machined to produce uniform particles. The particles were machined to ensure that the contact surface between the coal particle and the compression platens were as uniform as possible. The definition of the extent of breakage was borrowed from the definition of t_{10}. The extent of breakage is the mass percentage of daughter particles smaller than $^{1}/_{10}^{th}$ the size of the parent particles.

Chapter 5 was written in collaboration with Prof. Quentin P Campbell, Prof. Marco le Roux and Mr. Frikkie de Beer. The individual contributions of co-authors to the publication are given on page ix, page xi, and page xv.

[*] Viljoen, J., Campbell, Q.P., le Roux, M. & De Beer, F. 2015. An analysis of the slow compression breakage of coal using microfocus X-ray computed tomography. *International journal of coal preparation and utilization*, 35(1):1-13.

Abstract

The degradation of coal and the production of coal fines during handling and transport is a serious problem in processes that depend on closely sized large particles. To minimise the production of fines a fundamental understanding of coal breakage is required, so to clarify the complex nature of coal breakage a series of experiments were conducted to determine the influence of the internal physical coal structures on compression breakage characteristics. The structures investigated are the cleat and layered structure of coal and the mineral inclusions. Samples of uniform size and shape were prepared from a large block of South African Waterberg coal. The samples were analysed non-destructively using micro-focus X-ray tomography, then wrapped in cling-film and mechanically compressed while the pressure applied was measured. The virtual three-dimensional volume tomograms of the initial sample and the progeny were compared and the changes qualitatively analysed. Conclusions were drawn as to where the fatal cracks initialised and how the cracks propagated. Particle-size distributions were measured to quantify the extent of breakage versus the breakage strength of the sample. It was found that, of all the internal structures, the inherent crack distribution has the biggest influence on the resultant particle size distribution during breakage and breakage patterns of coal.

Keywords: micro-focus computed tomography; compression breakage; micro-structure; coal degradation

Introduction

The generation of fines during various handling stages is considered one of the great challenges in coal beneficiation. The presence of fines in the beneficiated product can cause a loss of efficiency in processes that require closely sized coal.[29, 30] It can also have financial implications as many contracts demand penalties be paid should the product not be within specifications.[11] The cost of fine coal beneficiation is also high (cleaning and dewatering) and it is difficult to transport.[17]

Degradation, defined as the unwanted generation of fines, is caused at various places in the beneficiation process: during mining, comminution, screening, conveying, stockpiling, reclaiming, and loading as well as at transfer points.[11, 15] The dominant mechanism for degradation is a combination of impact and compression breakage.

In order to improve the design of equipment that may minimise the production of fines, a better understanding of the governing fundamentals in coal breakage is required.[46] Various studies have attempted to elucidate the effects that coal- and equipment properties have on coal degradation. It has been found that the greatest influence is breakage energy and particle size.[16, 59] Other contributing factors include particle shape[26] and composition[17] of the sample as well as the hardness of the impact surface.[13] A finer progeny will result from an increase in either breakage energy, particle size or the hardness of the impact surface. As the shape of the particle changes from round to flaky the progeny size will decrease, and as the vitrinite content of the particle increases so does the fineness of the progeny. These studies all focussed on the macro features of coal (particle size and shape), none of the studies analysed the influence of microstructures (existing cracks, coal texture, and mineral inclusions) on coal breakage characteristics.[78]

This study aims to determine the suitability of micro-focus X-ray computed tomography (µCT) as a non-destructive probe for the analysis of coal breakage. This study also aims to determine if the internal physical structures of coal has any influence on its breakage characteristics. An effort will also be made to qualitatively describe the breakage process by referring to possible crack initiation sites and crack propagation routes. Because of the exploratory nature of the study, a limited sample will be used with the focus being not on statistically representative results, but on testing µCT as an analytical probe and describing breakage phenomena.

The internal structures that were considered are the texture of the coal particles, existing cracks or cleats in the coal particles, as well as the mineral inclusions in the particles. The

minerals present in the coal usually present as either discrete inorganic particles or cleat filling inclusions. The origin of the minerals in coal can be detrital, biogenic, due to syngenetic or epigenetic precipitation, and non-mineral inorganics;[71] while the presence of cleats in coal is due to the contraction of the coal bed.[74]

It was expected that the 3D reconstructed X-ray tomograms of the samples would show the structures that would, in some way, influence the breakage characteristics of the coal. It was found that the greatest influence is that of the inherent cracks, followed by the mineral inclusion boundaries as well as maceral boundaries.

Micro-focus X-ray computed tomography

Computed tomography (CT) is a non-destructive technique developed in the medical sciences where the most commonly known application is in diagnostic radiology.[145] An X-ray beam is projected at, and through, the object to be investigated. The intensity loss of the X-ray beam due to absorption and scattering of the X-rays out of the direct radiation beam is recorded after it travels through the object. This collection of transmission data is processed and a two-dimensional (2D) projection displayed - called a radiograph. A tomogram is a collection of radiographs made from many step angles of the sample and is a three-dimensional (3D) representation of the total sample and the internal structure of the scanned object.[146] For the purpose of this study, no detailed mathematical understanding or description will be presented about the computer driven reconstruction process or algorithms used in the µCT process to establish a representative 3D digital virtual image (tomogram) of the sample.

As with any analytical technique there are certain physical limitations that degrade the data, and must be taken into account. Two that must be taken note of are ring artifacts as well as beam hardening.

Ring artifacts are introduced during the reconstruction process and are due to faulty detector elements or scintillator elements.[146] Ring artifacts also occur when the detector response to high and low energy x-rays are nonlinear or if any of the detector elements respond in a dissimilar fashion.[111] During the reconstruction of the object into a three dimensional representation these elements form a series of concentric circles that is visible in the final tomogram and degrades its quality.[146]

Beam hardening is a severe artifact that occurs due to the preferential absorption of low energy X-rays by the sample from the X-ray beam. According to Van Geet et al. (2001), the

use of hardware filters (e.g. Cu, Mo, Al of less than 1mm thick) to remove the low energy X-rays is extremely efficient when the technique is applied in coal studies.[103]

The main advantage in using micro-focus X-ray tomography (µCT), rather than medical CT, is the increase in resolution. Resolutions obtained with a medical CT are generally in the range of 60 x 60 x 500 µm, whereas resolutions as low as 10 x 10 x 10 µm can be obtained using µCT when investigating small samples.[108] This increase in resolution is accomplished by focusing the generated electrons in the X-ray tube on a 1-3 μm^2 area (focal spot) on the Tungsten-target to produce X-rays. Another advantage that emerges, because of the small size of the focal spot, is that lack of geometrical sharpness in the 2D radiographs is reduced and small samples can be geometrically enlarged. The lack of geometrical sharpness is directly related to the size of the focal spot of the X-ray source.[104] Geometrical enlargement occurs when the object is placed away from the detector. Simons et al. (1997) gives a graphical representation of this effect (see Figure 4.4).[104]

The instrument used for the scanning of the samples in this study was a NIKON XTH 225 ST system that is residing at the Micro-focus X-ray Radiography and Tomography (MIXRAD) facility at the South African Nuclear Energy Corporation (Necsa) near Pretoria. The system has a Tungsten-target X-ray point source with a spot size between 1 and 3 µm, is operational at potentials between 30 and 225 kV, and with X-ray currents between 0 and 1 mA. The detector is a 40 x 40 cm PERKIN-ELMAR flat panel Americium/Silicon-detector with a pixel size of 200 x 200 µm. Hoffman and De Beer (2012) gives a detailed description of the MIXRAD system. [102]

The reconstruction of the three dimensional tomogram was done on CT-PRO reconstruction software. The reconstructed volume is then imported for 3D visualisation, segmentation and analysis into VGStudio MAX 2.1 visualisation software. A more detailed description of the analysis procedure follows in “Experimental procedure”.

Experimental procedure

The samples used for the study was cut from a single block (0.85 m x 1 m x 0.5 m) of run of mine (ROM) coal sourced from the Waterberg coal field in South Africa. The samples were either cut from a homogenous, dull lithotype or from a more heterogeneous, bright-dull banded lithotype, i.e. in the heterogeneous samples, the bedding planes are clearly visible, while in the homogenous samples the bedding plane is not as clearly visible. The

composition of the homogenous band is carbonaceous shale or mudstone while the composition of the heterogeneous samples is bands of coal interspersed with carbonaceous shale (see Chapter 5 - Additional notes).

The Waterberg formation, a medium rank C bituminous coal,[147] is known to have a much-layered texture with numerous thin coal beds separated by carbonaceous mudstone and mudstone. The dispositional environment of the formation was one of low energy into a continental fresh water basin. The effect of this was the formation of vitrinite as the dominant maceral. Other macerals, like liptinite, inertinite, and reactive semifusinite occur in minor quantities.[148] Figure 5.1 shows the block of coal that all samples were prepared from, with the homogenous (dull) lithotypes as well as the heterogeneous (bright-dull) lithotypes indicated.

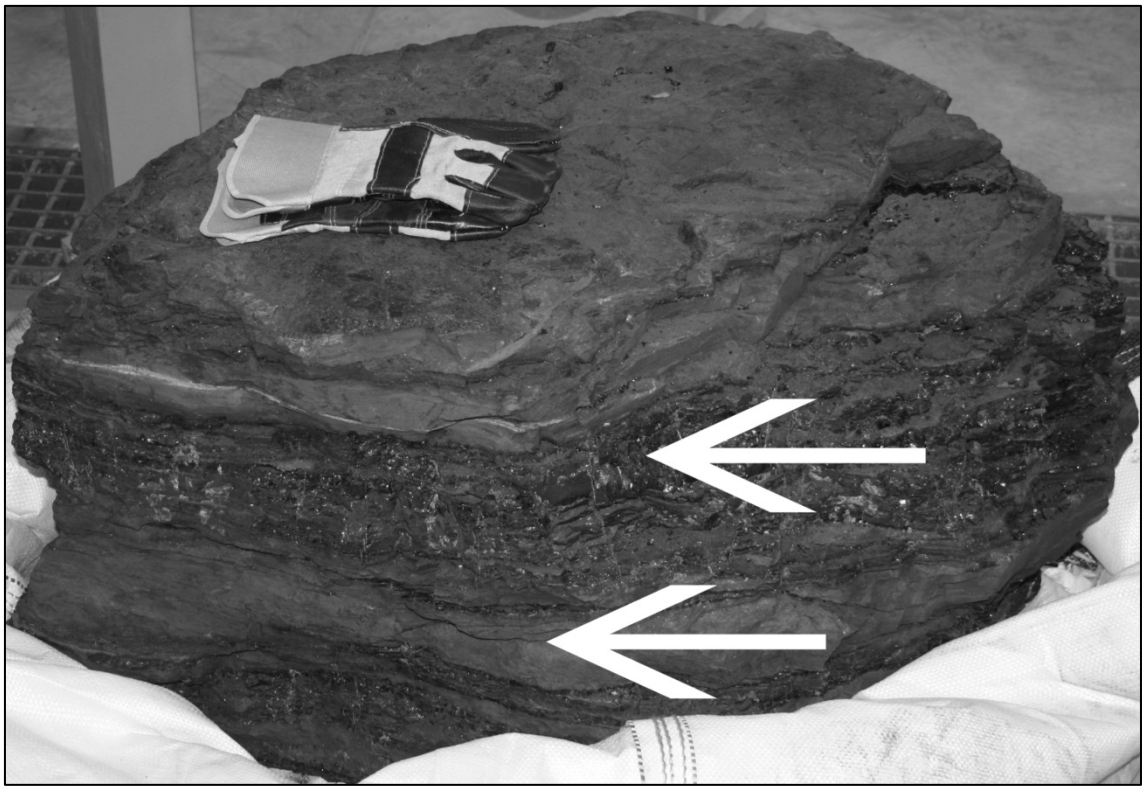

Figure 5.1: ROM coal from which all samples were prepared. The arrows indicate the dull lithotypes and bright-dull lithotypes

The samples were cut from the block of coal to 30 mm cubic particles, using a metal saw. Two opposite surfaces of the cubes were then flattened using a belt sander. Although the mechanical preparation of the samples may have introduced cracks or weaknesses, it was assumed that the damage done to the samples by the mechanical preparation is no more

than would be accumulated during crushing, therefore only enhancing the already existing fault lines.

After sample preparation, the samples were sent to the MIXRAD facility at Necsa for µCT data acquisition. Twenty-two samples were prepared for the experiment of which six samples were scanned. An X-ray radiation beam with a potential of 100 kV and current of 100 mA was used. One thousand 2D-projections were made in equal angular increments in 360° with a magnification (geometric enlargement) of 2.5. The average spatial resolution obtained was 24±3 µm.

After these six samples were scanned using the MIXRAD tomogram, all twenty-two samples were subjected to compression in a Monsanto tensometer. The tensometer was incapable of recording the strain rate achieved accurately, but during this study, the displacement necessary to cause fracture (2.5 mm to 3 mm) was achieved in 20 seconds to 30 seconds, giving a strain rate of around 0.125 mm/s for all particles. The relation between the applied load (kN) and the sample compression (mm) was obtained and the load at first fracture was measured. The load at first fracture was measured where the applied load decreased significantly for the first time. Each sample was loaded with a specific bedding plane orientation, either parallel or perpendicular to the applied load (either along the bedding plane or across the bedding plane), in order to determine if the breakage pattern is a function of the applied compression force in a specific bedding plane orientation.

To aid in the reconstruction of the broken samples, each was tightly wrapped with low-density polyethylene cling film prior to compression. The cling film is highly permeable to X-rays and does not affect the quality of the tomograms. Wrapping the particles in cling film also keep any progeny particles close to the position from where they originated.

Following the crushing of the samples, the six samples that underwent µCT scanning prior to crushing were scanned again. A comparison of the two scans aided in identifying the contribution of different microstructures in the coal towards crack formation and propagation. The tomograms of the sample, both before crushing and thereafter, were first converted to image stacks using VGStudio MAX visualisation software. The image stacks of both the pre- and post-crushing tomograms were loaded simultaneously into VGStudio MAX and registered so that one slice from the pre-crushing tomograms closely resembled the slice from the post-crushing tomogram. This allowed the two tomograms to be compared in a slice-by-slice manner.

A particle-size distribution analysis was performed using a standard √2 sieve series, to determine the breakage extent of each individual sample.

Breakage results

Figure 5.2 shows a plot of the compression load at first fracture vs. the extent of breakage (mass percentage of progeny smaller than $^{1}/_{10}{}^{th}$ of the parent particle size) of all samples under investigation. The samples prepared from the dull lithotypes are named homogeneous, whilst heterogeneous samples are those prepared from the bright-dull banded lithotypes.

The extent of breakage is defined as the mass percentage of the progeny that is smaller than $^{1}/_{10}{}^{th}$ $^{1}/_{10}$ tha tenth of the size of the parent sample.[27] This metric is commonly used during breakage modelling in the minerals industry and is useful to describe the generation of fine material. The average values in Figure 5.2, indicated using filled markers, are the average for each of the classifications: The Homogeneous – Perpendicular samples were prepared from the dull lithotypes and compressed with the compression force applied across the bedding plane; the Homogeneous – Parallel samples were prepared from the dull lithotypes and compressed with the compression force applied along the bedding plane; the Heterogeneous – Perpendicular samples were prepared from the bright-dull banded lithotypes and compressed with the applied compression force across the bedding plane; and the Heterogeneous – Parallel samples were prepared from the bright-dull banded lithotypes and compressed with the compression force applied along the bedding plane.

Although the data presented in Figure 5.2 is by no means statistically representative, due to a lack of representative testing, one clear trend is still apparent. The homogeneous particles compressed perpendicular to the bedding plane showed the least fines generation (lowest extent of breakage). The homogeneous samples compressed perpendicular to the bedding plane also had the highest values for the load at first fracture, i.e. these particles displayed the highest resistance to breakage. Thus, it can be postulated that when the force is applied parallel to the bedding plane, more of the inherent flaws act as either crack initiation sites or crack propagation sites e.g. the structural weaknesses between layer boundaries cause slip, resulting in more damage. When the applied force is perpendicular to the bedding plane, however, the same inclusions still help to propagate the crack, but a higher energy needs to be applied for crack propagation through the maceral boundaries, because the boundaries can halt the propagation of cracks at low energy.[78]

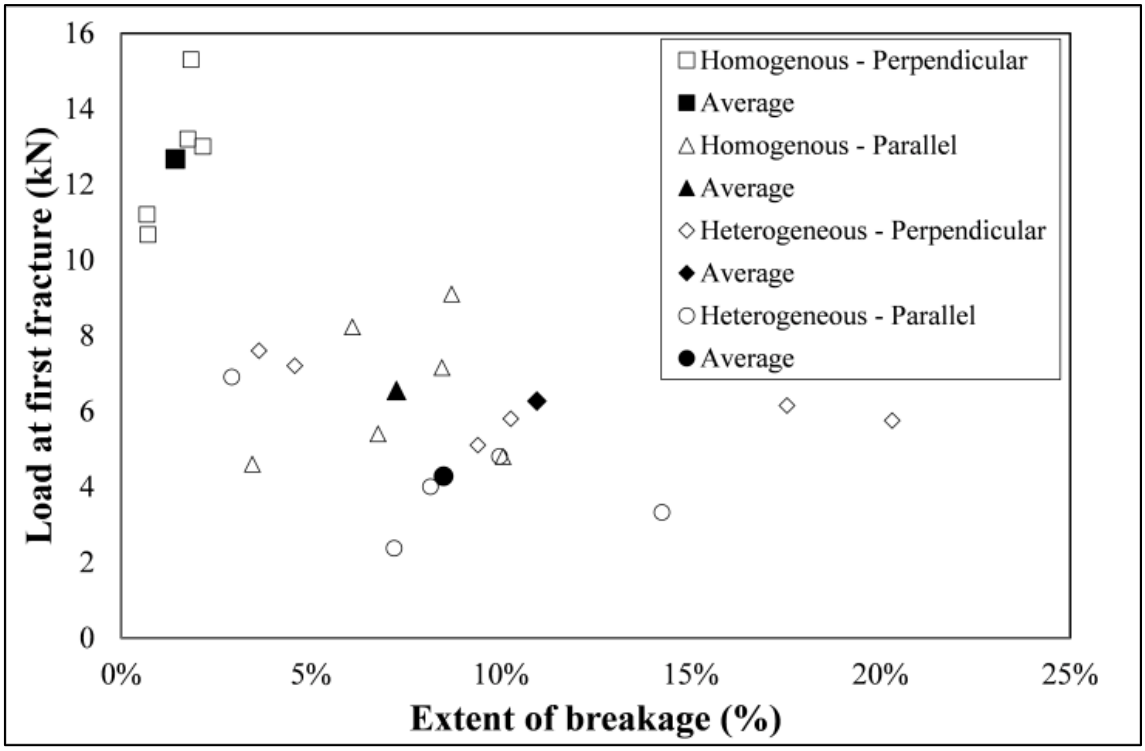

Figure 5.2: Extent of breakage vs. Load at first fracture for all particles tested

The large spread in the data of the heterogeneous particles indicates that the higher intra-particulate variability, and the higher incidence of low-density macerals, greatly contribute to the breakage characteristics of this Waterberg coal.

Figure 5.2 also shows that homogeneous samples show an increase in resistance to fracture as opposed to heterogeneous samples. This is again attributed to an increase in structural weakness between the different macerals and mineral inclusions, and higher flaw concentrations in the heterogeneous samples.

Tomography results

Figure 5.3 shows the centre 2D-slice for a heterogeneous sample where the load was applied perpendicular to the bedding planes. The slice within the virtual 3D volume of the sample (LEFT) (i) represents the coal morphology before, and the slice (RIGHT) (ii) the morphology at the same location in the sample after the compression force was applied.

The arrows point to features in the parent sample that had an influence on the breakage of the sample.

Note that most of the cracks that formed during the compression of the sample is orientated parallel to the applied force i.e. across the bedding plane in Figure 5.3. When comparing the pre-scan (i) with the post-scan (ii) in Figure 5.3, it can be deduced that crack formation followed the path of least resistance by propagating along existing faults. This is true for all cracks that occurred between A_1 and A_3, and between B_1 and B_3. However, the largest crack occurred between points D_1 and D_2. There are also signs of the sample surface crumbling at these points. These points indicated the area where maximum load application occurred due to localised contact between the sample and the tensometer. The localised contact is due to an irregularly shaped surface, despite precautions being taken during preparation to ensure flat surfaces.

The main crack in the sample propagated along the shortest distance between D_1 and D_2, because of the damage caused by the irregular load application and irrespective of the existence of fault lines elsewhere in the sample. The direction of the load application is shown on each figure. Plotting the path of crack propagation is much more difficult, and can at best be estimated after the analysis above. If it is assumed that the main crack occurred first between points D_1 and D_2 (a valid assumption considering that it is the shortest distance between the applied force contact and the opposite surface) it can be concluded that the remaining energy dispersed from this point along existing faults at $A_{1\text{-}3}$ and $B_{1\text{-}3}$, and around mineral inclusions at point C. The crack at A most probably started at point A_1 and continued downwards through point A_2 until it reached A_3.

The area pointed by C is an area where there is a high-density difference between the mineral inclusions and the material surrounding it. The boundaries between the minerals and the macerals (grain boundaries) can arrest cracks that initiated at low energies.[78] Of the multi-branched cracks that initiated at $D_{1,}$ some terminated at the grain boundaries at C, whilst the cracks that propagated away from this area did so along the grain boundary, terminating in another crack.

No crack formation and/or propagation was observed along the bedding planes despite the heterogeneity of the sample. The direction of the applied force across the bedding plane countered the formation of slip between the different planes.

Figure 5.4 shows the central slice from each of the tomograms before (i) and after (ii) a compression force was applied to a heterogeneous sample. The compressive forces were applied along the bedding plane.

There is a large degree of similarity between the crack formation and propagation seen in Figure 5.3 and Figure 5.4. The initial cracks originated close to the sample-tensometer interface, migrating to the opposite surface in the direction of the applied force. For the sample in Figure 5.4, two distinct low-density areas are visible at B and A_4. These low density bands can be associated with the more brittle vitrinite maceral. As a result, two cracks formed in these regions, instead of a single crack as in Figure 5.3. Vitrinite is known to be a brittle maceral due to a high concentration of shrinkage cracks or cleats.[74]

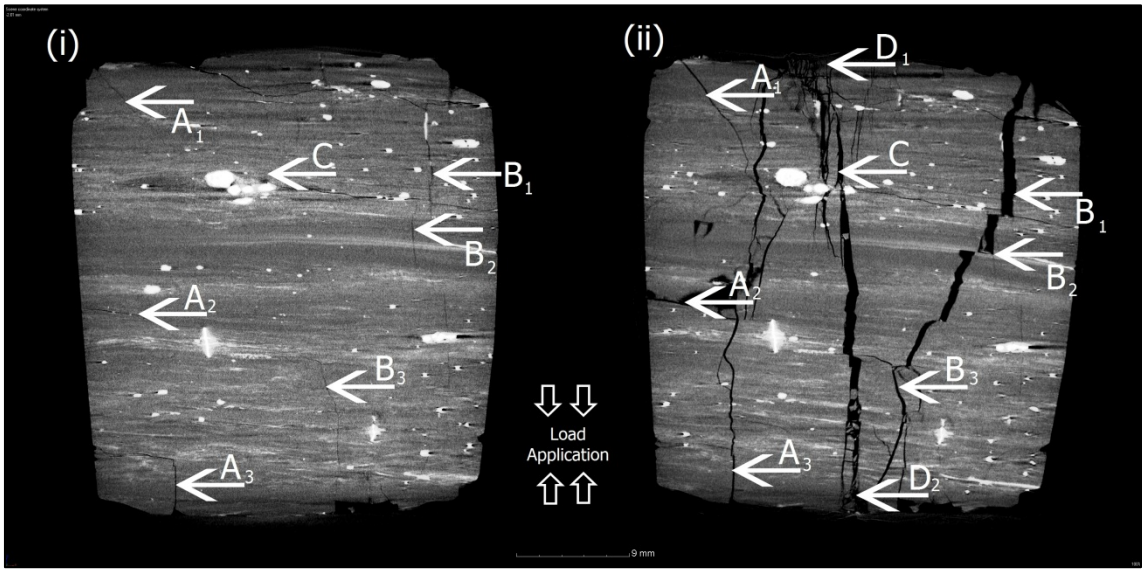

Figure 5.3: Centre slice of a heterogeneous particle with the load applied perpendicular to the bedding planes with (i) before and (ii) after application of the compressive force

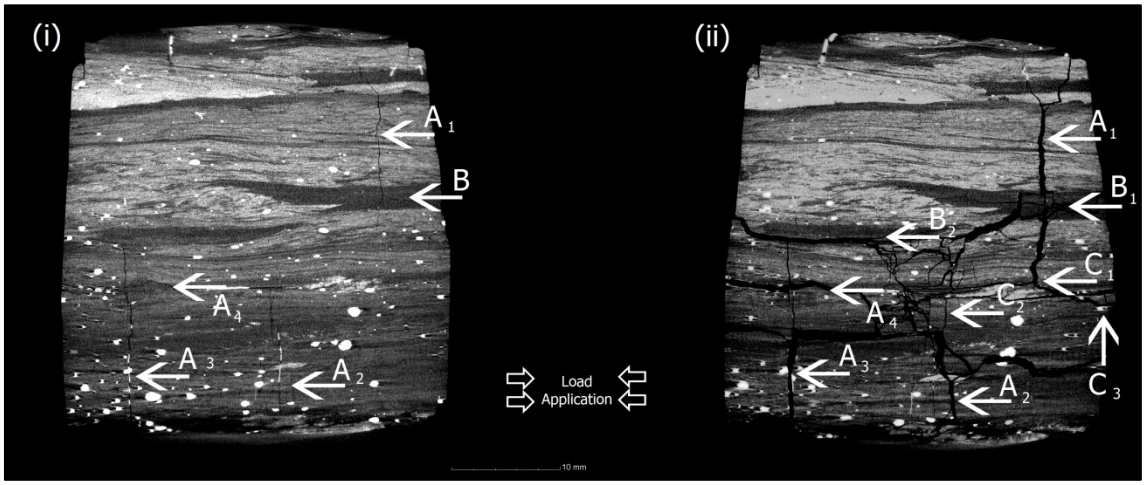

Figure 5.4: Centre slice of a heterogeneous particle with the load applied parallel to the bedding planes with (i) before and (ii) after application of the compressive force

These initial cracks propagated, and intercepted pre-existing inherent cracks. These faults in the sample opened up, forcing the energy, and hence the cracks, in a direction perpendicular to the applied force.

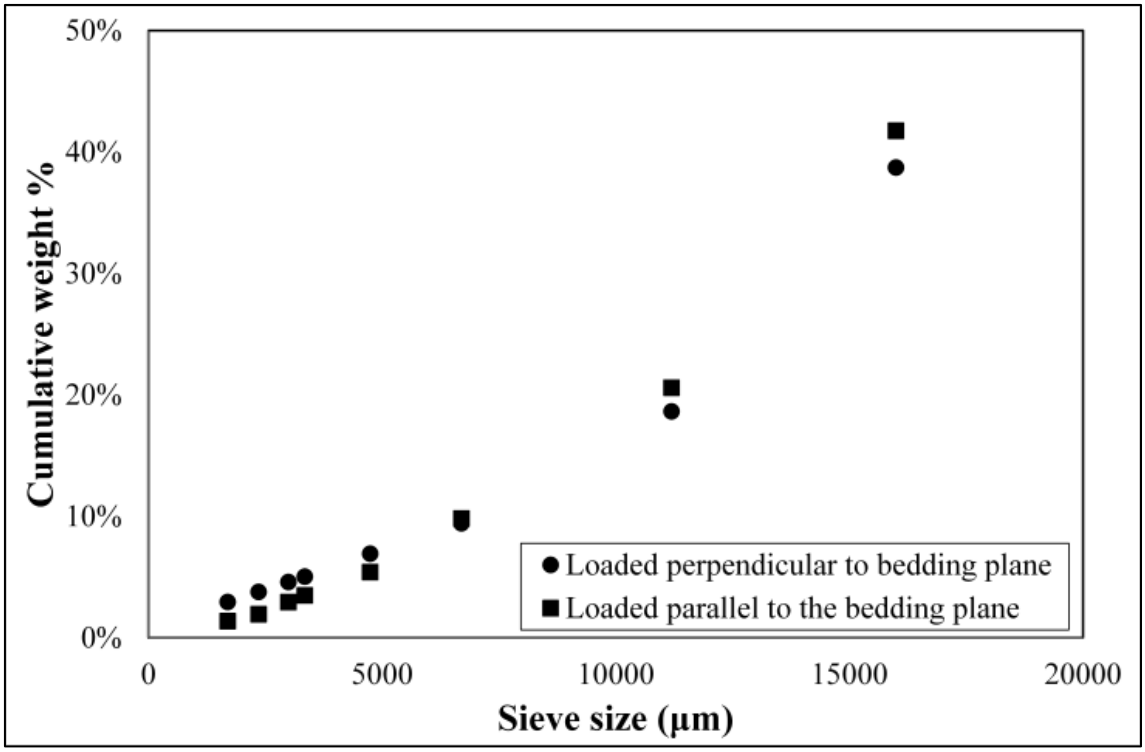

Figure 5.5: Comparative particle size distribution of the heterogeneous samples compressed parallel and perpendicular to the bedding planes

The result is an even distribution between parallel and perpendicular cracks in the sample. At C_1 there is an area where there are many boundaries between high and low density material. It should be noted how the cracks moved around this area, rather than through it. In the area around C_2 there is another area of low density material where much damage occurred. Label C_3 shows a possible crack initiation area at the boundary of a mineral inclusion.

The extent of breakage (i.e. the amount of material less than one tenth of the size of parent particle) for the sample in Figure 5.3 is 4.5% at a load at first fracture of 7.2 kN, and for the sample in Figure 5.4 it is 2.9% at 6.9 kN. A comparison of the PSDs of the samples shown in Figure 5.3 and Figure 5.4 is given in Figure 5.5.

Figure 5.6 shows the centre slice of a homogenous sample where the compressive force was applied across the bedding plane. Here, there is very little of note except that the orientation of the major cracks is again mainly in the direction of the applied force. The fact

that there is little damage is not surprising, considering that Figure 5.2 showed homogenous particles to have the highest apparent strength when the compressive force is applied perpendicular to the bedding plane. The arrow in Figure 5.6 indicates a possible crack initiation site at a mineral boundary.

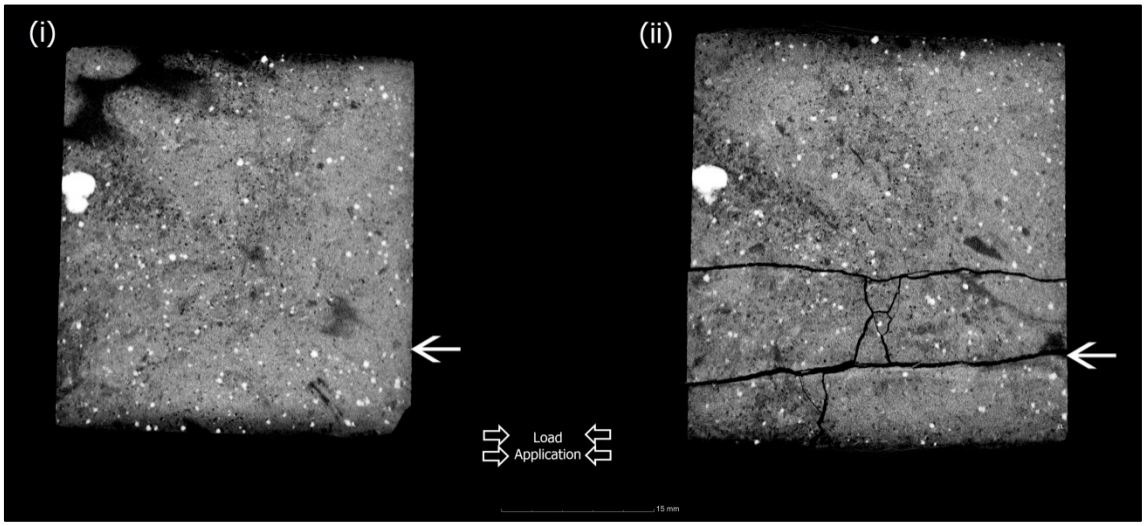

Figure 5.6: Centre slice of a homogeneous particle with the load applied perpendicular to the bedding planes with (i) before and (ii) after application of the compressive force

Figure 5.7 shows the central slice from each of the tomograms before (i) and after (ii) a compressive force was applied to a homogenous sample. The compressive force was applied along the bedding plane.

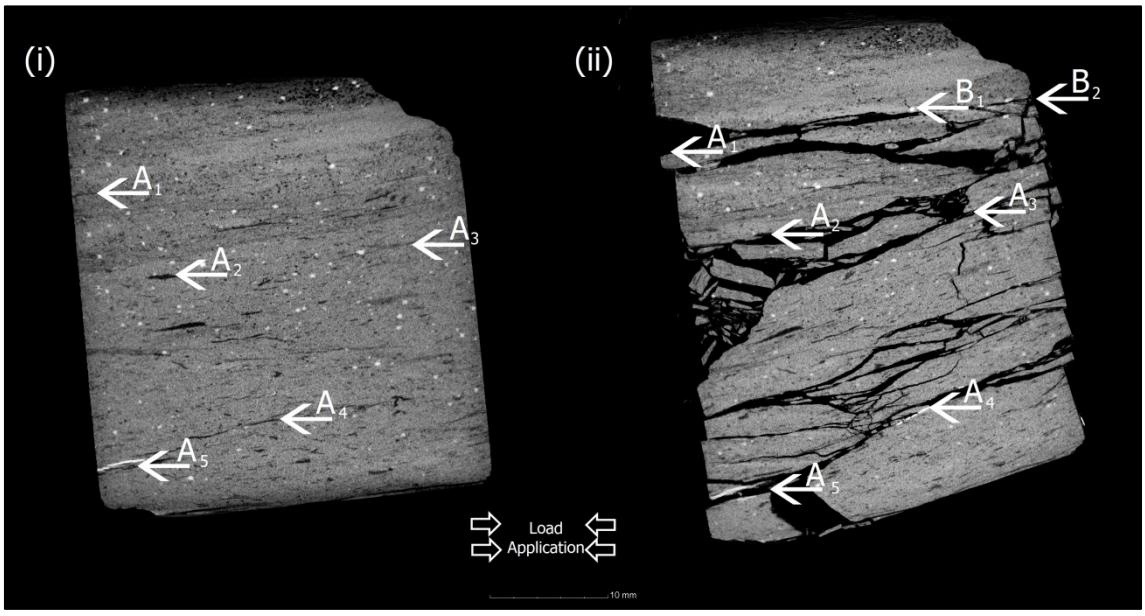

Figure 5.7: Centre slice of a homogeneous particle with the load applied parallel to the bedding planes with (i) before and (ii) after application of the compressive force

This sample showed a very high amount of damage with the majority of the cracks aligned with the direction of force application. One possible cause of the high damage may be the equal application of the load to a larger area of the sample, as opposed to the localised application seen in Figure 5.3. A comparison can also be made between the sample described by Figure 5.7 and the sample in Figure 5.4. Both are compressed along, or parallel to, the bedding plane, causing damage along the maceral boundaries and inherent flaws. Where cracks parallel to the bedding plane change direction it is due to the presence of inherent cracks.

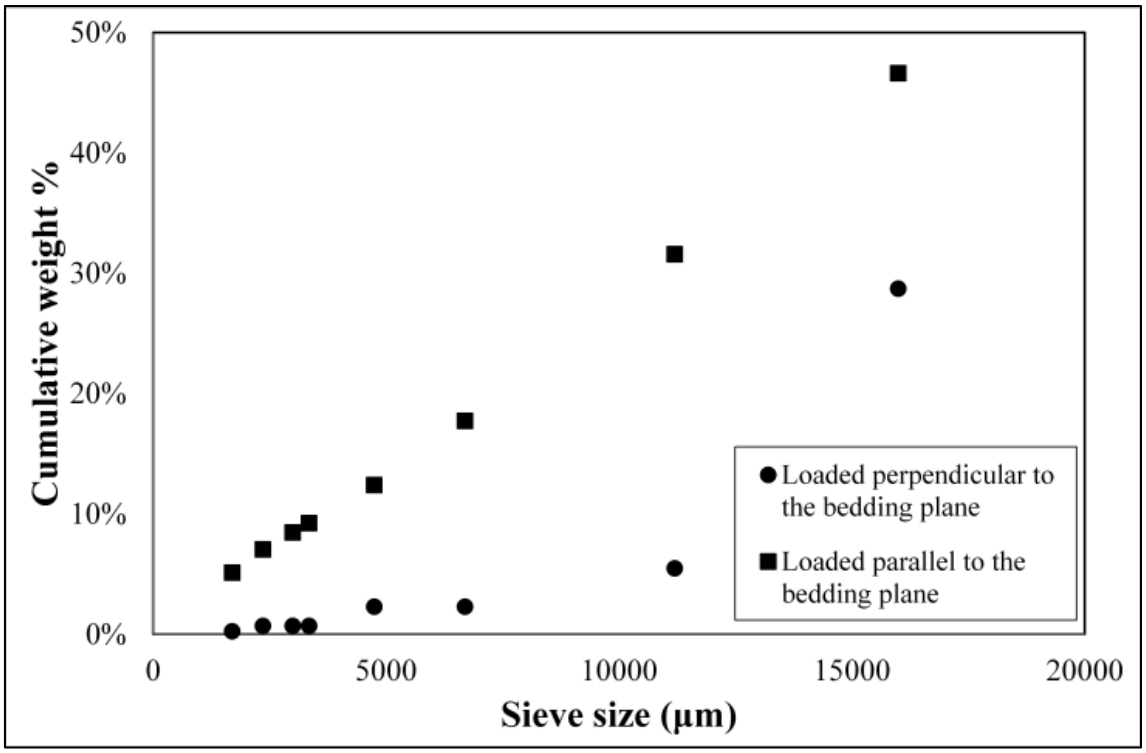

Figure 5.8: Comparative particle size distribution of the homogeneous samples compressed parallel and perpendicular to the bedding planes

The labels A_1 to A_5 show some of the pre-existing cracks that enlarged extensively due to the compression force. The crack that passed through A_4 and A_5 shows some cleat filling minerals. The crack that passed through B_1 and B_2 again shows how a crack propagates along a grain boundary if one is present.

The extent of breakage for the sample in Figure 5.6 is 0.7% at a load at first fracture of 11.2 kN, and for the sample in Figure 5.7 it is 8.5% at 7.2 kN. This agrees with the conclusion from Figure 5.2, that the application of compressive force perpendicular to the bedding plane of a homogeneous particle increases the apparent strength of the particle. A further reason for the increased breakage in Figure 5.7 is the higher concentration of initial

flaws. A comparative PSD is given in Figure 5.8. The significant difference can be ascribed to both the influence of the bedding plane orientation and the lack of flaws in Figure 5.6.

Conclusions

This study investigated the utilisation of µCT to determine the effect of the internal physical structures of coal on the compressive breakage characteristics of coal. The magnitude of the load where crack initiation started shows that, for heterogeneous particles the strength of a particle depended on the flaw concentration in the particle, with a higher flaw concentration resulting in greater breakage. For a homogeneous particle, the orientation of the bedding plane played a major role in the apparent strength of a particle, with the perpendicular load application showing less breakage.

Comparative analysis of the tomographic scans before and after crushing of single samples shows that physical structures do affect the breakage of coal. The following conclusions were made from this study:

- The direction of the applied force (either parallel or perpendicular to the bedding planes) has a great influence on where cracks initiate and the direction in which cracks propagate. For all samples in this study, the majority of the cracks originated and propagated in the same direction as the applied load.

- The inherent cracks in a sample increased the amount of breakage through weakening the sample. The inherent cracks also changed the direction of propagating cracks that pass close by.

- The boundaries between macerals of different densities aid to either change the direction of a propagating crack or to terminate the crack.

- When a crack passes through a maceral-mineral boundary, the crack either changes direction and continues propagation along the boundary, or the crack terminates in the maceral-mineral interface.

- Fines generation due to branching cracks was more likely to occur in areas of low density than in adjacent higher density areas.

- Homogeneous samples, in general, have fewer sites (maceral boundaries or inherent cracks) for crack initiation and generate fewer fines.

From the conclusions made above, it is evident that µCT, applied as non-destructive analytical technique, was successful in determining that the physical internal structures of

coal play a major role in its breakage and determine breakage patterns when compressive forces are applied. However, it is extremely difficult to determine which cracks were formed first from only evaluating two tomograms (prior to and after breakage). It is recommended that further studies in this regard follow a controlled stepwise increase of compressive force and a CT analysis after each step in an attempt to reduce the assumptions made.

Acknowledgements

We, the authors, would like to thank the personnel at the MIXRAD facility, Necsa, for their enthusiasm, patience, advice, and assistance with the scanning, sample evaluation, and paper review processes. Lastly, a special acknowledgement to Wynand Breytenbach and Juan Nelson for conducting the experimental work. This work was presented at the 27th International Coal Preparation Congress (ICPC) in Istanbul, Turkey. We thank the international organising committee of the 27th ICPC for the opportunity and for a wonderful congress.

Funding

We would like to thank the Southern African Coal Processing Society (SACPS) for funding the project and the DST-NRF for funding the Nikon system at Necsa and for their support.

Chapter 5 - References

11. Teo, C., Waters, A. & Nicol, S. 1990. Quantification of the breakage of lump materials during handling operations. *International journal of mineral processing*, 30(3):159-184.

13. Sahoo, R.K. & Roach, D. 2005. Effect of different types of impact surface on coal degradation. *Chemical engineering and processing*, 44(2):253-261.

15. Sahoo, R. 2007. Degradation characteristics of steel making materials during handling. *Powder technology*, 176(2):77-87.

16. Tavares, L.M. & de Carvalho, R.M. 2011. Modeling ore degradation during handling using continuum damage mechanics. *International journal of mineral processing*, 101(1–4):21-27.

17. Esterle, J., Kolatschek, Y. & O'Brien, G. 2002. Relationship between in situ coal stratigraphy and particle size and composition after breakage in bituminous coals. *International journal of coal geology*, 49(2):195-214.

26. Chandramohan, R., Holtham, P.N. & Powell, M. 2010. The influence of particle shape in rock fracture. (*In* XXV International Mineral Processing Congress 2010 organised by Australasian Institute of Mining and Metallurgy, Brisbane: The Australasian Institute of Mining and Metallurgy. p. 3163-3171).

27. Shi, F. & Kojovic, T. 2007. Validation of a model for impact breakage incorporating particle size effect. *International journal of mineral processing*, 82(3):156-163.

29. Eswaraiah, C., Gupta, A., Nagarajan, R., Rajavel, M. & Nandakumar, K. 2008. Minimization of fines generation in size reduction of coals by impact crusher. *Fuel processing technology*, 89(7):704-714.

30. Bunt, J.R. & Waanders, F.B. 2008. An understanding of lump coal physical property behaviour (density and particle size effects) impacting on a commercial-scale Sasol-Lurgi FBDB gasifier. *Fuel*, 87(13–14):2856-2865.

46. Powell, M.S. & Morrison, R.D. 2007. The future of comminution modelling. *International journal of mineral processing*, 84(1–4):228-239.

59. Meier, M., John, E., Wieckhusen, D., Wirth, W. & Peukert, W. 2009. Generally applicable breakage functions derived from single particle comminution data. *Powder technology*, 194(1–2):33-41.

71. Ward, C.R. 2002. Analysis and significance of mineral matter in coal seams. *International journal of coal geology*, 50(1–4):135-168.

74. Falcon, R.M. & Snyman, C. 1986. An introduction to coal petrography: atlas of petrographic constituents in the bituminous coals of South Africa. Johannesburg: Geological Society of South Africa.

78. Tavares, L.M. & das Neves, P.B. 2008. Microstructure of quarry rocks and relationships to particle breakage and crushing. *International journal of mineral processing*, 87(1–2):28-41.

102. Hoffman, J.W. & De Beer, F. 2012. Characteristics of the Micro-Focus X-ray Tomography Facility (MIXRAD) at Necsa in South Africa. (*In* 18th World Conference on Nondestructive Testing, Durban: South African Institute for Non-Destructive Testing. p. 1-12).

103. Van Geet, M., Swennen, R. & David, P. 2001. Quantitative coal characterisation by means of microfocus X-ray computer tomography, colour image analysis and back-scattered scanning electron microscopy. *International journal of coal geology*, 46(1):11-25.

104. Simons, F.J., Verhelst, F. & Swennen, R. 1997. Quantitative characterization of coal by means of microfocal X-ray computed microtomography (CMT) and color image analysis (CIA). *International journal of coal geology*, 34(1–2):69-88.

108. Van Geet, M., Swennen, R. & Wevers, M. 2001. Towards 3-D petrography: application of microfocus computer tomography in geological science. *Computers & geosciences*, 27(9):1091-1099.

111. Banhart, J., *ed*. 2008. Advanced tomographic methods in materials research and engineering. Oxford: Oxford University Press. (Monographs on the Physics and Chemistry of Materials).

145. Natterer, F. 1982. The mathematics of computerized tomography. Philadelphia: Society for Industrial and Applied Mathematics. (Classics in applied mathematics).

146. Stock, S.R. 2008. Microcomputed tomography: methodology and applications. Boca Raton: Taylor & Francis.

147. Wagner, N.J. & Tlotleng, M.T. 2012. Distribution of selected trace elements in density fractionated Waterberg coals from South Africa. *International journal of coal geology*, 94:225-237.

148. Faure, K., Willis, J.P. & Claris Dreyer, J. 1996. The grootegeluk formation in the Waterberg coalfield, South Africa: facies, palaeoenvironment and thermal history — evidence from organic and clastic matter. *International journal of coal geology*, 29(1–3):147-186.

Chapter 5 - Additional notes

The preceding paper successfully applied micro-focus X-ray computed tomography (µCT) to identify microstructures present in coal that contribute to coal degradation, and to determine if the changes that occur during degradation can be tracked. The three structures present in coal tracked during this study were pre-existing cracks and cleats, boundaries between coal microlithotypes and mineral inclusions, as well as boundaries between coal microlithotypes of differing density. Chapter 5 only confirmed the technology when applied to compression breakage of single particles. Chapter 6 will explore the applicability of µCT to the impact breakage of single coal particles and to degradation due to rapid temperature increases.

The study found that the pre-existing cracks as well as the boundaries between the coal microlithotypes and mineral inclusions could contribute to the degradation of the coal particles, with the biggest influence attributed to the pre-existing cracks. The orientation of the bedding plane in relation to the applied compressive force and the homogeneity of the coal particle further influenced the degradation and strength of the particles. Particles compressed along the bedding plane, i.e. the compressive force applied parallel to the bedding plane, showed decreased strength and increased fines production compared to particles compressed perpendicular to the bedding planes. It is assumed that the boundaries between the various microlithotypes act to aid the propagation of cracks when the particles are compressed parallel to the bedding planes, conversely, the boundaries between the various microlithotypes act to halt crack propagation when the particle are compressed perpendicular to the bedding planes. Particles that showed higher variation (less homogeneity) also showed decreased strength and increased fines production due to the higher number of likely force concentrators within the particles. The particles that showed the most degradation were particles with a high amount of variability within the particle and compressed parallel to the bedding plane. The lower density microlithotypes showed a propensity towards higher crack formation compared to the higher density microlithotypes and the direction of the applied load determined the direction in which the majority of the new cracks propagated.

Figure 5.3 shows that breakage occurs due to a combination of mechanisms: a large amount of fines are produced close to the contact points between the coal particle and the compression platens, a characteristic of attrition breakage, while further away from the contact point the breakage is characteristic of volume breakage.

In Chapter 4, it was shown that the dominant material interaction at X-ray energies in the range of 100 keV is Compton scattering. Compton scattering is dependent only on the

physical density of the material and not the atomic number; therefore, the assumption that the grey value of a microlithotype is an indication of its physical density could be made with confidence. However, in order to verify this assumption, a single coal particle was set in resin and two sets of images created: a series of images generated using a reflected light microscope and a tomogram slice taken parallel to, and just below, the surface. The reflected light microscope images were taken along a line perpendicular to the bedding plane, combined into a single large photomicrograph collage that spanned the length of the particle, and superimposed over the tomogram slice with the correct position determined visually (horizontal line cross the bottom of Additional notes Figure 5.1) The combined photomicrographs were printed as a single image (the printed image measured 6 m x 1 m) using a high quality printer and ink onto high quality gloss paper. This photomicrograph collage was used to identify a section that contained vitrinite, inertinite and carbominerite in a small area and Additional notes Figure 5.1 produced.

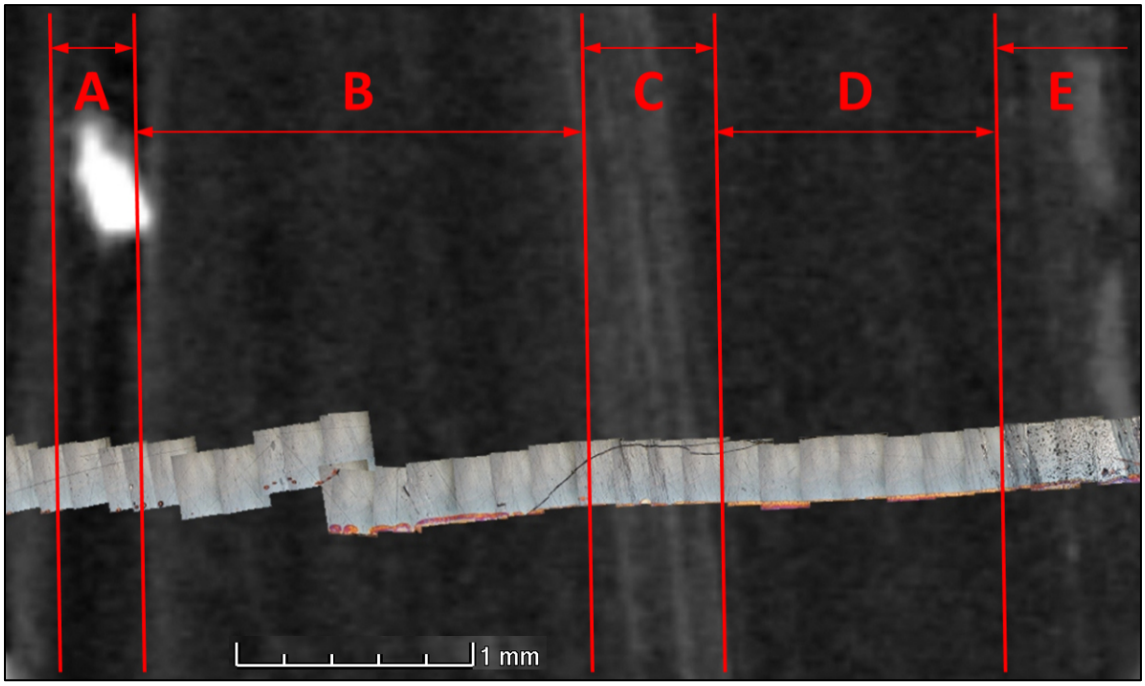

Additional notes Figure 5.1: Comparison of images generated using µCT and reflected light microscopy

Additional notes Figure 5.1 was divided into five Sections according to the apparent grey values: Section A has very low grey values (darker tones), Sections C and E has high grey values (lighter tones) and Sections B and D has grey values that fall between the values of Section A and Section C. According to a petrographical analysis done on the combined photomicrographs Sections A, B, and D is telovitrinite; Section B is a carbominerite dominated by silicates; and Section E is semifusinite. The density of the telovitrinite is lower than the density of the semifusinite and the carbominerite (Table 2.1 on page 23

summarises the density of various macerals as given in literature and Additional notes Table 5.1 gives the densities of particles from the bright-dull banded lithotypes and the dull lithotypes). Thus, the higher density microlithotypes are represented by higher grey values. Although it is not possible to determine the exact maceral composition of the microlithotypes from the tomograms, it is possible to distinguish between microlithotypes based on the microlithotype's density. Because the coal used in this study is a Waterberg coal that contains very little liptinite (see the maceral composition of Waterberg coal in Table 7.1 on page 158, and Additional notes Table 5.1 below), it can be assumed that the lower density microlithotypes contains a high percentage of vitrinite and the higher density microlithotypes contains a high percentage inertinite or minerals.

To verify the comparison between tomography and petrography the densities of particles from the bright and dull lithotypes were determined using mercury submersion and a sample from both the bright and dull lithotypes were sent for petrographic analysis at Bureau Veritas. Additional notes Table 5.1 shows the comparative petrographic analysis, and the densities.

Additional notes Table 5.1: Petrographic analysis and densities of the bright-dull banded and dull lithotypes determined using mercury submersion

		Bright-dull banded lithotypes	Dull lithotypes
Maceral Composition (%)	Vitrinite	73.5	39.6
	Liptinite	1.6	3.7
	Inertinite	16.5	34.7
	Mineral Matter	8.4	22.0
	Density	1331.2 ± 7.2	1721.5 ± 161.5

It is important to note that even though Section A in Additional notes Figure 5.1 is telovitrinite the grey value in this section is very low compared to the other telovitrinite sections. This is due to the mineral inclusion (large white spot just below the A) at the top of Section A. Because of the high density of the mineral inclusion, beam hardening occurred and severely altered the grey values of the surrounding area. This shows how the presence of beam-hardening artefacts can influence the data gathered from a tomogram slice.

One of the suggestions made in Chapter 5 to improve the quality of the data generated for the compressive breakage of coal is to increase the number of tomograms generated during the application of the load: in a sense taking snapshots during the transient compression breakage process. To achieve this, a tomogram is generated and a small compressive load applied to the particle. After the load is applied, a tomogram is again generated and the load applied slightly increased. This cycle of increasing the applied load and generating a tomogram after the increase is repeated until the particle fails. Studying this series of tomograms might provide insight into the timing of cracks initiating and extending, as well as provide insight into what causes a specific feature to activate and contribute to breakage. In Chapter 4, it was mentioned that the acquisition times achievable using medical CT systems are far greater than those of µCT systems. This could lead to a simplification of the process above, negating the necessity of stopping the load increase while the tomogram is generated. The problem with applying medical CT, however, is that the resolutions achievable is considerably lower than the resolutions achievable using µCT; causing many of the smaller features, that can be identified using µCT, to be unidentifiable when using medical CT. Many of the features identified during this study would not be identified using medical CT, thus the use of medical CT was not considered any further.

In Chapter 5 the particles that were studied were wrapped in X-ray translucent cling-film to ensure that the progeny generated stayed as close as possible to the position within the parent particle where the progeny originated. Wrapping the coal particles in cling-film proved very effective in ensuring the least possible movement after breakage. As a result, the particles tested during impact in Chapter 6 and Chapter 7 were again wrapped in cling-film to keep the progeny produced as close to its original positions as possible.

Chapter 6 - The qualification of coal degradation with the aid of micro-focus X-ray computed tomography

Chapter 5 confirmed that micro-focus computed tomography (µCT) can be applied to identify and track the changes that occur in a particle during the slow compression breakage of a single particle. Chapter 6 aims to demonstrate the application of µCT to identify and track the changes that occur during both impact degradation and thermal degradation of single coal particles. Additionally, Chapter 6 aims to determine if any new information can be gained from the stepwise increase of the applied compressive load suggested in Chapter 5.

Chapter 6 is a paper presented at the 1st Imaging with Radiation conference and workshop (ImgRad-1) held in Pretoria, South Africa from the 23rd – 27th September 2013. After completion of the conference and workshop, the paper was submitted for peer-review and a version published in the South African Journal of Scienc.*

Chapter 6 was published in collaboration with Prof. Quentin P. Campbell, Prof. Marco le Roux and Mr Jakobus W. Hoffman. The individual contributions co-authors are given on page ix, page xi, and page xiii.

*Viljoen, J., Campbell, Q.P., Le Roux, M. & Hoffman, J. 2015. The qualification of coal degradation with the aid of micro-focus computed tomography: identifying invisible factors influencing coal breakage. *South African journal of science*, 111(9/10):1-10.

Abstract

The production of unwanted fines during the handling and utilisation of coal is a serious problem in processes that rely on large or closely sized particles. Coal degradation occurs at many different steps within the beneficiation or utilisation processes and through many different mechanisms, none of which are understood thoroughly. In an effort to describe the degradation mechanisms, the changes within a number of coal particles was tracked using micro-focus X-ray computed tomography (µCT). The observed changes were caused by impact loading, compressive loading and thermal shock. The resolution of the µCT tomograms enabled the identification and tracking of changes in the coal microstructure. A comparison of the tomograms taken before, during and after breakage and fracture showed that the microstructure of coal had an influence on the breakage characteristics. For impact- and compressive loading, as well as during thermal treatment, the biggest structural contributor was shown to be the network of pre-existing cracks and cleats within a particle. Lower density macerals contributed more to breakage than the higher density macerals, and any structure (pre-existing cracks, lithotypes boundaries and mineral boundaries) present within the particles had the potential to either act as a crack initiation site, change the direction of a propagating crack or arrest crack propagation. The direction of the applied loads during compressive and impact loading are the biggest contributor to the directionality of newly formed cracks. For thermal treatment the vitrinite rich microlithotypes showed more new crack formation compared to the other microlithotypes present; the particles also show no evidence of devolatilisation but did show evidence of thermal drying.

Keywords: Coal microstructure; Compressive breakage; Impact breakage; Thermal breakage; X-ray; Micro-focus X-ray computed tomography (µCT)

Introduction

Degradation

One of the biggest challenges in coal beneficiation as well as coal utilisation is the unwanted production of coal fines, known as degradation.[11, 13] The presence of coal fines in processes that rely on a closely sized feed can reduce the process efficiency;[29, 30] the presence of fines in a beneficiated product can also have financial implications for the suppliers as many contracts specify penalties for product that does not meet specifications.[11, 13, 15, 16, 149] Fine coal is also hard to clean, relying on wet processes like flotation, spirals, and dense medium cyclones to wash the coal.[36, 38, 149] The wet, fine coal is then significantly harder to dewater[35-37] and due to the increased moisture content the transport cost of fine coal is greatly increased.[36, 38] The high moisture content can also incur financial penalties for out-of-spec product.[35, 38]

Fines generation can occur at any step during the beneficiation process where the coal is mechanically stressed:[13, 15, 16, 20, 22, 38] during comminution, screening, conveying, loading, stockpiling, and reclaiming.[13, 16, 35] Fines are also generated when coal particles enter a reactor (be it a pyrolysis or combustion process) due to thermal shock and devolatilisation.[30, 32, 33, 43, 45] The presence of fines in a large particle reactor can reduce bed permeability,[20, 30, 32, 33] process efficiency,[42, 43, 45, 150] and throughput.[20, 150]

In both the case of physical degradation and thermal fracture, the breakage and fracture mechanisms are not well understood.[46, 49] Clarification of these mechanisms can help design improved comminution technologies and improved coal handling and transport processes, which may lead to a reduction in fines production.[26, 46, 47] Over the years, various studies have tried to shed some light on the effect that physical properties have on the breakage characteristics of coal.[11, 16, 17, 23, 26, 29, 30, 38, 47] The effect of comminution technology properties on the breakage characteristics of coal has also been studied.[13, 15-17, 20, 23, 26]

For the impact breakage of coal it has been found that the drop height (impact energy) increases coal degradation.[15-17, 20, 23, 26] The impact surface also influences the degradation: the harder the surface the higher the degradation.[13, 15, 16] The shape and orientation of the impacted particle has an influence on the breakage of coal:[26, 38] rounded particles show less degradation than slab-like particles (particles where one of the three orthogonal dimensions are significantly smaller than the other two).[26, 67] The composition of the coal also plays a role: with an increased amount of vitrinite an increase in degradation will occur.[17] For single particles, bigger particles have lower specific breakage strengths and produce more

degradation products.[11, 16, 17, 26, 27, 47] This is due to bigger particles having more inherent weaknesses, and is referred to as the particle size effect.[17, 27, 29, 47, 64] For samples containing multiple particles and subjected to multiple drops: the removal of fines after each drop increased the total fines generation when compared to the same amount of drops without removal of the fines, the latter being referred to as cushioning.[13, 15, 20]

The size effect is also documented for the compressive loading of coal.[64] During uniaxial strength tests coal samples undergo a reduction in strength as the sample size increase, until a characteristic value is reached in samples with diameter larger than 1.5 m.[64] This is again due to an increased amount of defects present in the larger samples.[49, 64] These defects include micro-cracks, cleats, and inclusions. Fatigue is another mechanism that has an effect on the compressive breakage strength of coal.[16, 47, 49] Fatigue is the repeated application of a force, which although not strong enough to damage a particle, eventually destroys the particle due to damage accumulation within the particle.

For thermal fracture, it was found that an increase in furnace temperature cause the degradation to increase;[40, 45] an increase in particle size will increase both the size of the progeny as well as the particle count of the progeny.[40, 42, 45] It was also found that the longer the particle stays in the furnace, the lower the particle count becomes due to the progeny being burnt away.[40, 45] It was also found that an increase in the volatile content of the particles would increase the degradation,[42, 43] although some authors found no connection between volatile content and fragmentation.[40] Taking this into account, Dacombe et al. (1999) postulated that there are two mechanisms responsible for thermal degradation: exfoliation and fragmentation.[40] Exfoliation is the formation of many small progeny from the outside of the particle,[40, 43] and occurs due to thermal stresses that occur at higher heating rates.[40, 43, 45] Fragmentation is when the particle centre remaining after exfoliation breaks into larger (when compared to exfoliation) progeny, and happens due the build-up of internal pressure as the volatile matter in the coal particle is released.[40, 43, 45]

A common theme in all of the degradation scenarios is the presence of micro-defects within the particles. These micro-defects can act as sites where crack propagation can either start or arrest.[78] Micro defects that can occur within coal are mineral inclusions,[17, 47] pre-existing cracks and cleats,[17, 47, 64, 120, 137] as well as microlithotype boundaries.[17, 47] The macerals that occur in coal can be grouped into three main classes: vitrinite, inertinite, and liptinite.[74, 108] For coal degradation, vitrinite is the most important one, as it is known to be a very brittle, weak maceral.[17, 64] It also has the most flaws present,[17, 64] as it experiences the highest degree of shrinkage during coalification.[74] Cleats are cracks that are inherent to coal and are formed during the coalification process by the shrinkage and expansion of the coal

matrix.[64, 74, 76, 137] The mineral inclusions present in coal are usually in the form of either discrete mineral inclusions[71] or as cleat filling minerals.[71, 74] The minerals can become part of the coal matrix through detrital deposition[71] and through biogenic, syngenetic or epigenetic precipitation.[71, 74] Various studies have applied micro-focus X-ray computed tomography (µCT) to identify these microstructures in coal.[102, 107, 121, 124, 126, 129, 130]

X-ray computed tomography is a technique that was originally developed in the medical sciences where it is commonly used during diagnostic radiology.[116, 120, 121, 126] Since the 1980s the technique has also been widely used in the geosciences for non-destructive characterisation.[116, 120, 121, 124, 126] During the application of the technique an X-ray cone beam is projected at and through the sample to be analysed. As the beam travels through the sample the intensity of the beam diminishes due to absorption and scatter from the direct beam path. A detector records the intensity of the beam after it passes through the sample as a radiograph.[104, 108, 114, 116, 137] A number of radiographs, made by rotating the sample along its axis, is combined to form a tomogram, or a three-dimensional (3D) representation of the scanned sample, using filtered back-projection.[102, 108, 114, 116, 126, 130] A detailed mathematical treatment of the technique and reconstruction is beyond the scope of this study, there is however a large body of literature available on the subject.[103, 107, 108, 116, 124, 126]

The attenuation coefficient or tomo-density determines the absorption and scattering of the X-ray energy from the direct beam path, and is a combination of the physical density, mean atomic number of the sample elements and the energy of the X-ray beam.[104, 107, 124]

Micro-focus X-ray computed tomography is an improvement over traditional medical CT. These improvements are mostly because there is no limit in the radiation dose that can be applied to samples typically scanned using µCT.[126] Higher energies, longer exposure times and higher resolutions are possible.[126] The resolution of a medical CT is in the range of 250 x 250 x 250 µm[124] to 0.6 x 0.6 x 1 mm,[120, 121] while the resolution of a µCT tomogram can be as low as 10 x 10 x 10 µm,[103, 108, 120, 121] depending on the size of the sample that is to be analysed.[103, 104] This reduction in resolution is due to the minimisation of the X-ray spot size by focusing the electron beam prior to the electron beam hitting the target as well as lowering the X-ray current. [104, 116, 124] The focussing of the electron beam also has another advantage, namely improving the geometrical sharpness of the tomogram.[104]

The aim of this study is to explore the applicability of µCT as an analytical tool in the study of coal breakage and degradation, and forms part of a larger study on coal degradation. To this end, a small number of samples were loaded, both mechanically and thermally, and µCT was used to track the breakage that take place during loading. Changes to the experimental setups that may improve the experimental accuracy were also recommended.

Experimental

All of the tomograms for the experiments below were generated on the NIKON XTH 225 ST system that is housed at the Nuclear Energy Corporation of South Africa (Necsa) in the Micro-focus X-ray Radiography and Tomography (MIXRAD) department. The system is operational between 30 and 225 kV, and between 0 and 1 mA with a point source of between 1 and 3 µm. The detector is a 40 x 40 cm flat Perkin Elmar panel detector with 200 x 200 µm pixels. All tomograms were generated with 1000 projections in 360° and an exposure time of one second per projection. The resolutions obtained during these studies vary from 17 µm to 50 µm depending on the specimen size of the coal samples. Hoffman and De Beer (2012) gives a detailed description of the MIXRAD facility.[102] All of the reconstructions were done using Metris CT-Pro and the analyses were done using the VGStudio visualisation software package.

All of the mechanically loaded particles were wrapped in cling film to minimise the loss of material during breakage and to simplify the comparison of the before and after tomograms. It is assumed that the radio translucent cling film did not deteriorate the quality of the tomograms, as the cling film has a low physical density (0.92 g.cm^{-3}), and the sample is wrapped in a very thin layer of cling film.[151]

The experimental procedures for all three types of degradation experiments (compression loading, impact loading and thermal treatment) are given below.

Compressive loading

To determine the effect that the internal structures have on the compression breakage characteristics two experiments were conducted. During the first experiment, the samples were prepared from a single large (approx. 1 x 0.5 x 0.4 m) block of run of mine (ROM) coal sourced from the Waterberg coalfield in South Africa. The samples, prepared from the heterogeneous, bright-dull banded lithotypes, were cut to 30 x 30 x 30 mm cubic particles.

Two surfaces, on opposite sides of the particle, were machined flat and the uniaxial compression applied to these surfaces. A number of the samples were sent for data acquisition at the MIXRAD facility. After data acquisition the particles were wrapped in cling film, loaded into a Monsanto tensometer and compressed while the displacement was measured. Figure 6.1 shows the Monsanto tensometer (left) that was used during the first round of compression tests and the experimental setup used during the impact breakage tests (right). The labels on the left of Figure 6.1 indicate the load cell (A) that was used to measure the applied load during the compression tests and two surfaces between which the particles were compressed (B). The load was applied either perpendicular or parallel to the bedding plane until the first crack that split the parent particle into two or more progeny was detected, and the force required to generate the first fatal crack (load at first fracture) was recorded. The load at first fracture was measured as the applied force where the displacement showed a sudden increase. After loading, the particles were again scanned, and the tomograms generated before and after fracture compared. From the comparison new crack formation, probable crack initiation sites and propagation routes were identified. The tomograms were generated at 100 kV and 100 µA; an average spatial resolution of 24 µm was achieved.

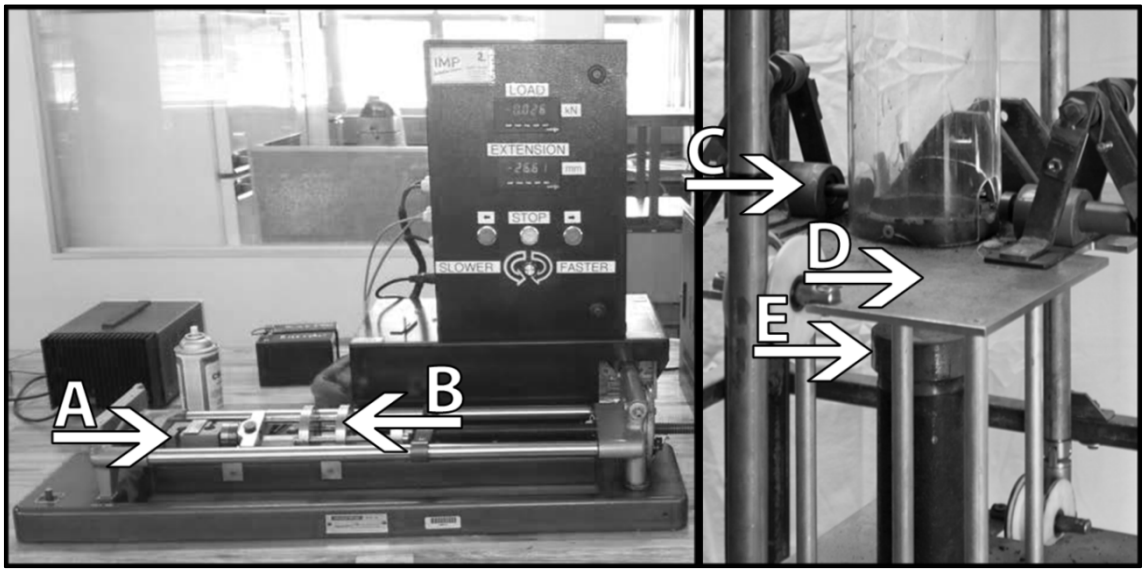

Figure 6.1: Experimental setups for the compressive breakage tests (left) and the impact breakage tests (right). A is the load cell and B the compression surfaces of the tensometer; C, D and E are the sample clamps, impact carriage and impact anvil respectively

During the first set of experiments it was found that it is very hard to come to a solid conclusion as to the probable propagation routes of the cracks if the only information available is at the start and at the end of the loading cycle. A second set of experiments

were therefore performed where particles were subjected to compressive loading that was incrementally increased. The particles were placed into a specifically designed, radio translucent test cartridge. The test cartridge was built from poly(methyl methacrylate), and in such a fashion that the uniaxial compressive force applied to the particle could be increased incrementally. The particle placed in the cartridge was scanned, the applied load increased and the particle again scanned. This process of tomogram generation and load increase was repeated until the particle failed. All of the tomograms generated were compared to determine new crack formation, crack initiation sites, and crack propagation routes. Tomograms were generated at 130 kV and 100 µA with a spatial resolution of 29 µm.

Impact loading

A number of coal particles were prepared from a single block of ROM coal sourced from the Waterberg coalfield. The samples were cut to 50 x 50 x 50 mm square particles and three sides machined flat. One side where the impact was to take place and two sides, opposite one another, where the sample clamps gripped the particles. In order to ensure that there were as many maceral boundaries and pre-existing cracks as possible to study, the samples were prepared from the bright-dull banded lithotypes of the block, and impacted parallel and perpendicular to the bedding planes. The crack network for each particle was characterised using µCT, wrapped in cling film and dropped onto a steel anvil at 4.5 $m.s^{-1}$. The impact velocity is equivalent to a drop from one meter. The rig was developed in such a way that the bedding plane orientations of the particles could be accurately controlled (see Chapter 7: Experimental for a more detailed description). Half the particles were dropped with the bedding planes parallel to the impact surface and the other half with the bedding planes perpendicular to the impact surface. After the particles were dropped, they were again scanned using µCT. Figure 6.1 shows the Monsanto tensometer (left) that was used during the first round of compression tests and the experimental setup used during the impact breakage tests (right). The labels on the right side of Figure 6.1 indicate the sample clamps (C), impact carriage (D) and impact anvil (E).The tomograms generated both before impact and after were generated at 160 kV and 70 µA and an average spatial resolution of 48 µm was achieved. A comparison of the before and after tomograms were made and new crack formation, crack initiation sites and probable propagation routes were identified.

Fracture due to thermal treatment

In order to determine the effect that the maceral boundaries and crack network has on the thermal breakage properties of coal, a number of cylindrical samples, with a height of 30 mm

and a diameter of 19 mm, were prepared from large particles of a Witbank coal. The thermal fracture samples were prepared from a Witbank coal to prevent any damage to the graphite crucibles as the Witbank coal is non-swelling while the Waterberg coal is a medium-swelling (Free Swelling Index of 6.5) coal.[152] The prepared samples were placed in graphite crucibles that could be rapidly heated in a radio frequency (RF) induction furnace. The mechanical sample preparation was done to ensure that the samples fit tightly into the radio translucent graphite crucibles; this ensured that a clear tomogram was generated. If the samples did not fit tightly in the crucibles there would have been a possibility of the samples moving while being scanned, introducing errors and reducing the sharpness of the tomogram. The crucibles containing the samples were scanned before and after being heated, and comparisons of the tomograms made to determine new crack formation, crack initiation sites and probable crack propagation routes. The heating rate within the graphite crucible was controlled by changing the potential difference through the RF furnace coil, and the maximum temperature controlled by the residence time within the furnace. The heating rates ranged from 30 °C.s^{-1} to 75 °C.s^{-1} with final temperatures reaching between 700 °C and 800 °C. The residence times varied between 10 seconds and 30 seconds. The heating rates, maximum temperatures and residence times were varied with all samples. All experimental runs were conducted in an air atmosphere. The temperatures stated are the outside crucible temperatures, and were measured using a pyrometer that determines the crucible's temperature by the infrared radiation it emits. Due to the exploratory nature of the study, and the difficulty in measuring the internal temperature without introducing errors, the internal temperatures were not measured or estimated. The particle temperature was, however, high enough to cause thermal drying but not so high to cause any detectable devolatilisation. The tomograms were generated at 130 kV and 100 µA with voxel sizes of 17 µm. A comparison, to determine new crack formation, crack initiation sites and probable propagation routes, were made.

Results and discussion

Figures 6.2 to 6.9 show comparisons of slices from the tomograms generated. The slices on the left in all figures are from the tomograms generated before loading (or thermal treatment) and the slices on the right are from the tomograms generated after loading (or thermal treatment). Where there are three slices in a figure, the centre slice is from a tomogram generated during loading.

In all of the tomogram slices that are presented in this study, the varying shades of grey represent the variation in the linear attenuation of the particles. Black areas are areas where no sample material is present, dark grey areas are areas of lower attenuation, light grey areas are areas of higher attenuation, and white areas represent mineral matter. The light grey macerals are assumed to be either inertinite or carbominerite rich microlithotypes, while the darker grey areas are assumed vitrinite rich microlithotypes. This is due to the higher density of the inertinite and carbominerite rich macerals compared to the vitrinite rich macerals.[135, 139]

Compressive loading

Figure 6.2 shows a comparison of the before and after tomogram of a particle that was compressed perpendicular to the bedding plane in the Monsanto tensometer, whilst Figure 6.3 shows a particle loaded parallel to the bedding plane. The load application perpendicular to the bedding plane indicates that the particle was compressed from the top and bottom of the slice given in Figure 6.2, while the parallel load application indicates that the particle in Figure 6.3 was compressed from the left and right of the slice.

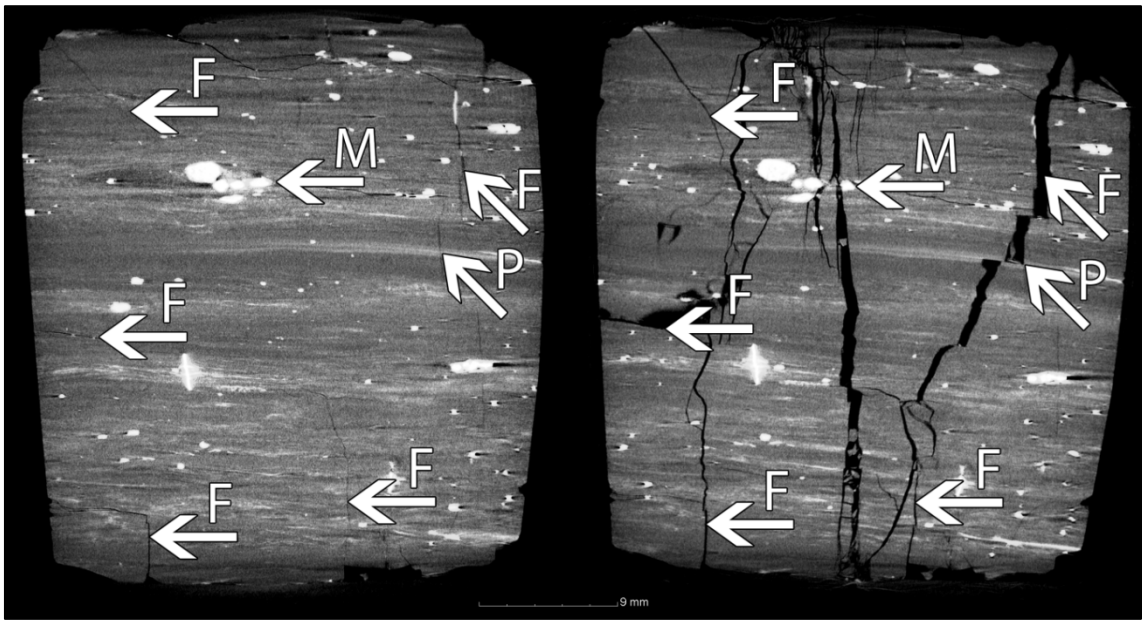

Figure 6.2: Comparison of a particle compressed perpendicular to the bedding plane

Both particles shown were prepared from the bright-dull banded lithotype of a single block of ROM coal from the Waterberg coalfield. All the arrows marked (F) in both Figure 6.2 and Figure 6.3 show cleats or cracks that existed in the pre-loaded particles that enlarged during compression. The arrows marked (M) show mineral inclusions that may have had an

influence on either crack initiation or crack propagation. Lastly, arrows marked (P) show either maceral-maceral boundaries or maceral-mineral boundaries that may have had an influence on crack initiation or propagation.

Figure 6.2 shows a number of cracks present in the original crack network that enlarged during compression. The largest new crack formed during compression however, is the crack that runs down the middle of Figure 6.2 (through M), in the post compression slice (right hand slice). This newly formed fracture did not form from any crack present, and although it did propagate through the mineral inclusions at M, show no influence of any microstructure in the particle. It is speculated that the newly formed crack is due to load concentration where the tensometer contacted the particle, thus forming a crack in the direction of the applied load. Due to the manual sample preparation, the sides of the particle could not be made perfectly smooth and parallel. This created some features where stress concentration could take place.

In Figure 6.3 it can again be seen that the major, newly formed cracks (through P_1; M_1 and M_2) formed parallel to the applied load, i.e. from the left and right. The left hand slice shows a significant number of cracks (marked F) that contributed to the new crack network; the majority of the cracks that are perpendicular to the load direction are due to the enlargement of these pre-existing cracks. P_1 shows where more new cracks formed in the vitrinite rich microlithotypes compared to the inertinite rich microlithotypes. Label P_2 shows where a boundary between two macerals caused the propagating crack to change direction. The mineral inclusion at M_1 shows a probable crack initiation site at a mineral inclusion, whilst M_2 shows a mineral inclusion that was in the path of a propagating crack, this inclusion may have helped with the crack propagation.

From the comparisons above it seems that the direction of the applied load shows a great influence, with the majority of the newly formed cracks propagating in the direction of load application. The cracks that did not form in the same direction as the load application are due to pre-existing cracks. In addition, of the microstructures observed, the existing crack- or cleat network has the greatest influence on crack initiation and propagation; with very few of the pre-existing cracks showing no change. It is also clear that the lower density macerals shows more new crack formation than the higher density macerals, and in some cases the boundaries between two macerals influenced the crack propagation.

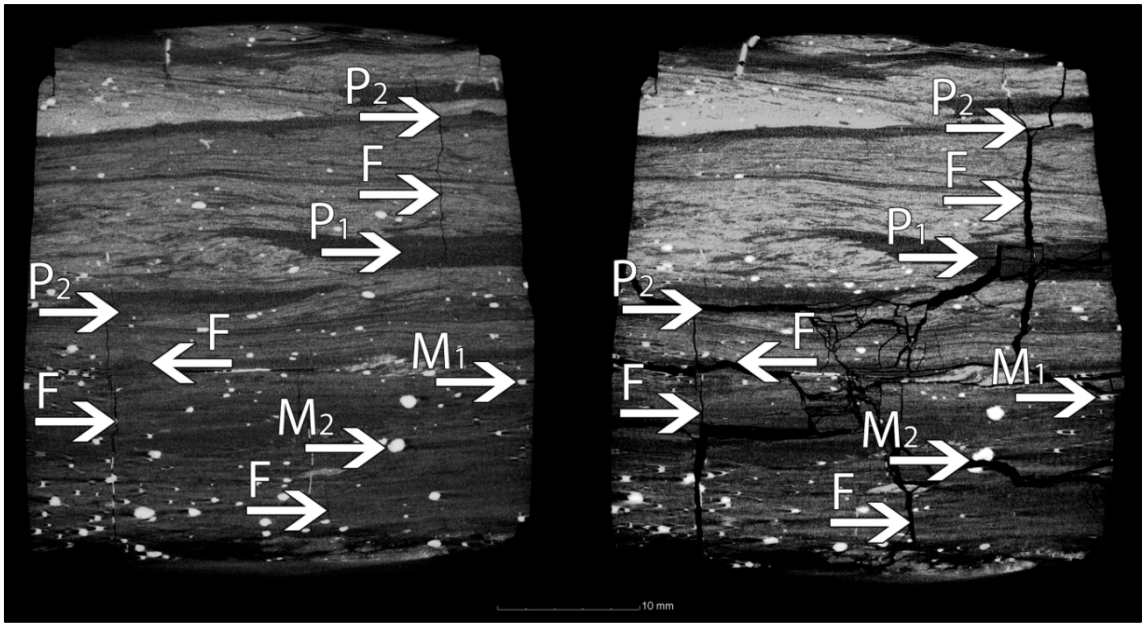

Figure 6.3: Comparison of a particle compressed parallel to the bedding plane

Although it is possible to speculate which of the microstructures influenced the propagation, and the chronology of the newly formed cracks, it is impossible to say so with certainty. To clarify this, another set of experiments were performed where the load application to the samples was increased incrementally until the particle failed; with the internal structure of the sample investigated after every increase. This was done to try to determine, with a higher degree of certainty, which of the microstructures will have a higher probability of influencing the crack propagation. To this end, Figure 6.4 and Figure 6.5 show three steps in the compression process of two particles that were compressed perpendicular (Figure 6.4, loaded top to bottom) and parallel (Figure 6.5, loaded top to bottom) to the bedding planes. Although there were many tomograms generated during the incremental load increase, Figure 6.4 and Figure 6.5 show only the tomograms generated before loading, after loading and a single tomogram generated during compression. The samples were again prepared from the bright-dull banded lithotypes of the large block of Waterberg ROM coal. The arrows marked F, M and P has the same meaning as in Figure 6.2 and Figure 6.3.

The labels marked F_1 in Figure 6.4 show a number of cracks that are thought to contribute to the formation in the large crack in far right slice of Figure 6.4. Label P shows a maceral-maceral boundary that influenced the crack propagation, whilst M shows a mineral inclusion that did the same. Label F_2 shows a number of cracks that were present in the particle but due to the pressure applied, closed in the middle slice. Another crack that closed while being compressed is shown at F_3. Even though the closed crack is no longer apparent in the middle slice, this does not mean that the closed crack no longer contributes to crack

propagation; in the final slice it is clear that the closed crack influenced the propagation of the crack through F_1 and F_3.

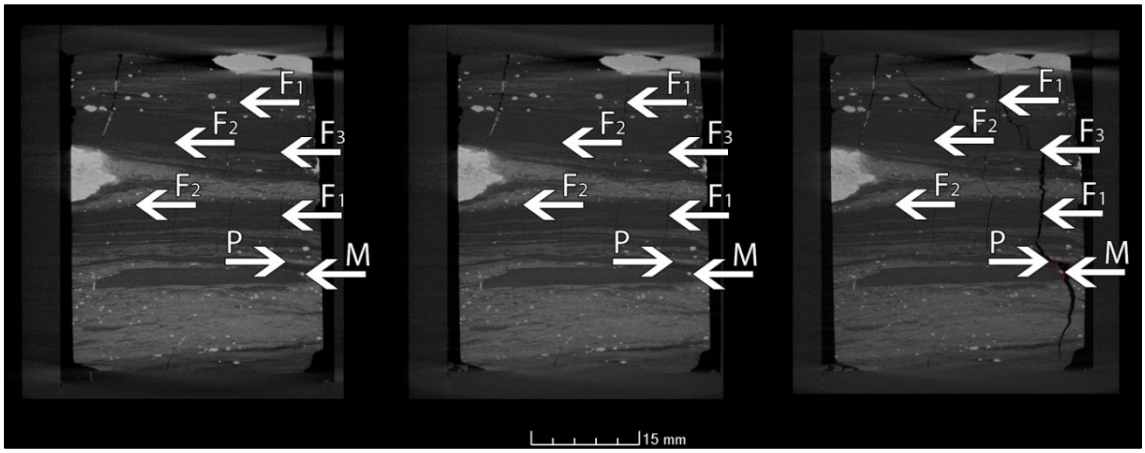

Figure 6.4: Comparison of a particle compressed incrementally perpendicular to the bedding plane

Figure 6.5 again shows some pre-existing cracks (F) that contributed to the final crack network, as well as a lower density maceral (P_1) where a higher amount of newly formed cracks can be observed. Label P_2 shows a maceral-maceral boundary that also contributed to the propagation of a crack. Figure 6.5 shows no cracks that closed due to the applied load, in fact, the opposite is observed: there are some cracks that, despite the load applied perpendicular to the cracks, enlarged.

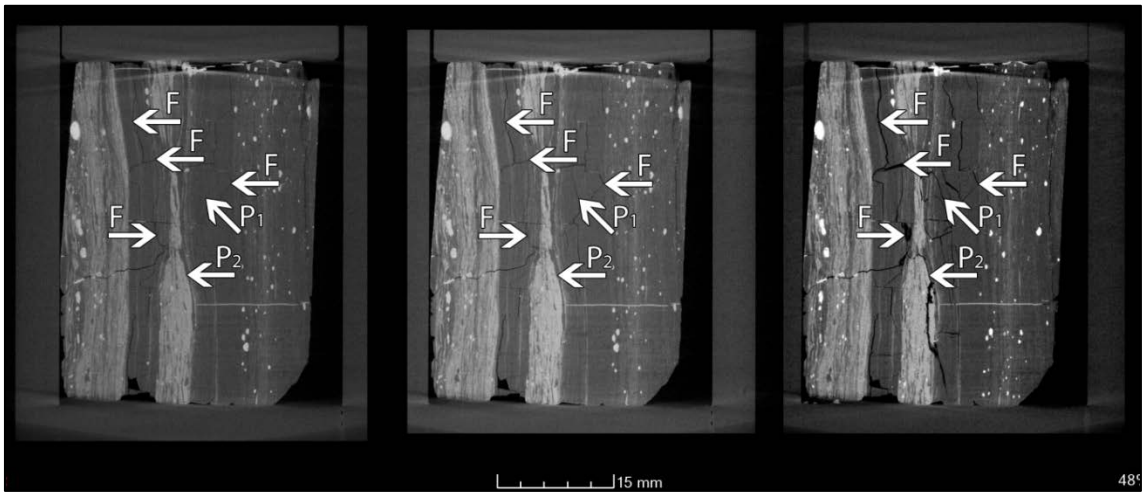

Figure 6.5: Comparison of a particle compressed incrementally parallel to the bedding plane

From incremental loading, the same conclusions can be reached as to the effect of the directionality of the applied load, as well as to the influence of the original microstructure on the crack evolution. It was also observed that, in the particle where the compression was

perpendicular to the bedding plane, some of the cracks that were perpendicular to the applied load closed due to the applied load. This, however, was only observed in the particle that was compressed perpendicular to the bedding plane

From the comparison it is also clear that the incremental load increase was still too large to deduce with any higher degree of certainty the propagation routes and hierarchy. Due to the time required to generate a tomogram, the crack propagation cannot be observed, only the after effects i.e. the newly formed cracks. If the load increase with each increment is reduced, and more tomograms generated during compression (6-8 tomograms generated instead of 3-4), it may be possible to observe the order in which new cracks form and the propagation routes deduced.

Impact loading

Figure 6.6 and Figure 6.7 show comparisons of the tomograms generated before and after impact of two samples prepared from a large block of ROM coal sourced from the Waterberg coalfield. The samples in both Figure 6.6 and Figure 6.7 were impacted onto a steel anvil, at a velocity of 4.5 $m.s^{-1}$. The impact velocity is equivalent to a drop from 1 m; a low impact velocity was specifically selected to study the degradation at low impact energy. Figure 6.6 shows a particle that was impacted with the bedding plane parallel to the anvil, while Figure 6.7 shows a particle that was impacted with the bedding plane perpendicular to the anvil. In both Figure 6.6 and Figure 6.7 the surface of the particle that was in contact with the impact anvil (impacted surface) is the bottom edge of the slice or the edge closest to the scale bar.

In Figure 6.6 the majority of the cracks that formed, formed from pre-existing cracks (F) within the particle. There is however some new cracks that formed in the lower density, vitrinite rich, macerals (P).

Figure 6.7 also shows a number of existing cracks that enlarged during impact. Some of the other trends observed in the compression loaded particles can also be seen in Figure 6.7. Label P_1 shows where a newly formed crack propagated along a maceral boundary and P_2 indicate cracks formed in a vitrinite rich microlithotype. Several cracks end at the mineral inclusion indicated by M in Figure 6.7.

From the comparisons made in both Figure 6.6 and Figure 6.7, it is clear that the main contribution to crack initiation and propagation is the existing crack network of the coal. The final crack network did not show a high dependence on the direction of the applied impact load when compared to the compressive loading in Figure 6.2 to Figure 6.5. It is

hypothesised that this is due to the low impact velocity, equivalent to a drop of approximately 1 m onto a steel plate. This is supported by various studies where it was found that that a higher drop height increased the breakage and degradation.[15-17, 20, 23, 26]

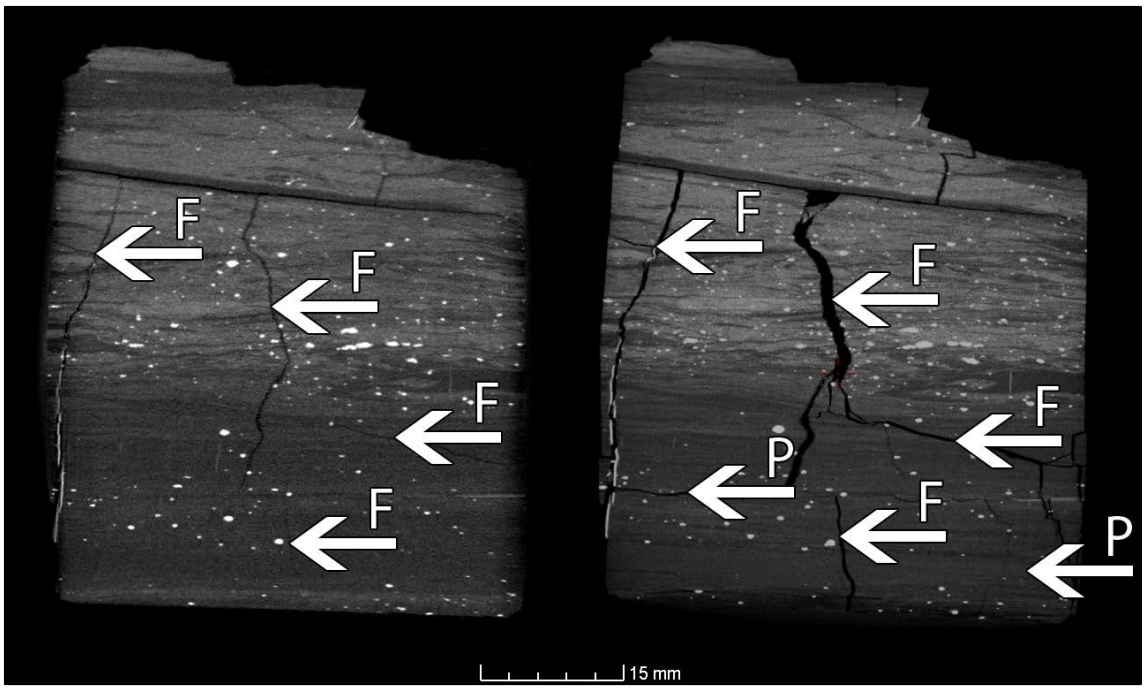

Figure 6.6: Comparison of a particle impacted with the bedding plane parallel to the anvil

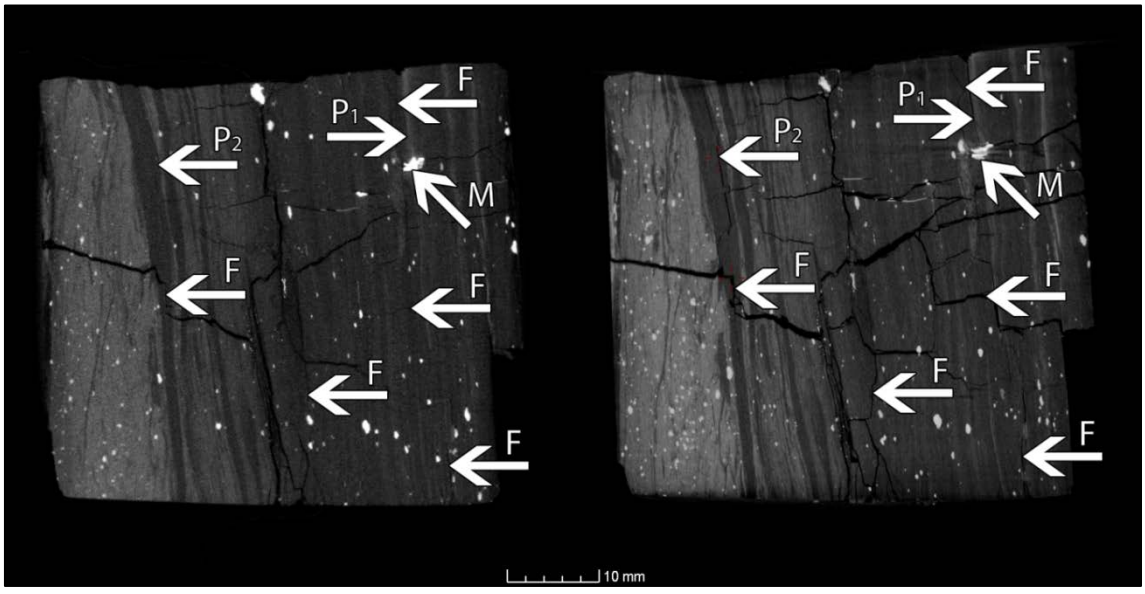

Figure 6.7: Comparison of a particle impacted with the bedding plane perpendicular to the anvil

Fracture due to temperature increase

Figure 6.8 and Figure 6.9 show comparisons of the tomograms generated before and after thermal treatment. A Witbank coal was used rather than a Waterberg coal to prevent damage to the graphite crucibles. Figure 6.8 shows the comparison of a particle heated to 800°C at a rate of 30°C/s. Figure 6.9 shows the comparison of a particle heated to 700°C at a rate of 50°C/s.

Figure 6.8 shows two fractures (F) present in the coal before heating, both of which contributed to crack propagation. The crack that propagated along the line indicated by the arrows marked M, shows the crack did not propagate through the mineral inclusions but along the outside of the tiny mineral inclusions. It is assumed that the two cracks that formed from the initial cracks marked F were the first to form. Note, that many of the cracks that radiate from these initially formed cracks do so almost perpendicular to the main cracks. According to Mathews et al. (2011) this occurs during thermal drying due to particle shrinkage.[153] Figure 6.8 also shows no structural changes indicative of devolatilisation, indicating a discrepancy between the outside crucible temperature and the particle temperature.

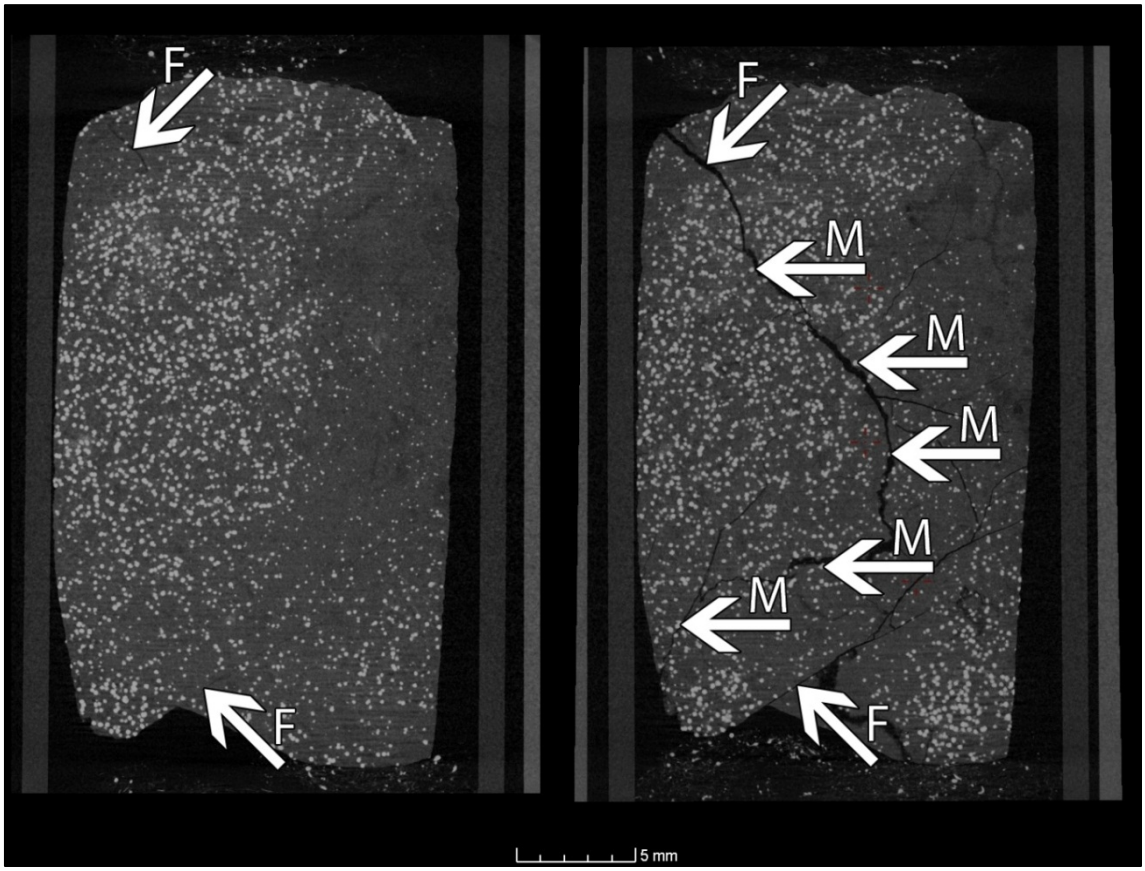

Figure 6.8: Comparison of a particle heated to 800ºC at a rate of 31ºC.s^{-1}

Figure 6.9 shows that during the thermal treatment of coal, pre-existing cracks (F_1) present in coal enlarges. Again it can be seen in Figure 6.9 that new cracks form perpendicular to pre-existing cracks (F_2) indicating that thermal drying took place. The enlarged sections in Figure 6.9 show that the vitrinite rich layers, indicated by P, show an increase in new crack formation when compared to the rest of the particle. The enlargements in Figure 6.9 also show how the vertical, mineral filled cleats act as discontinuities, with cracks terminating at the mineral filled cleats.

In both Figure 6.8 and Figure 6.9, it was observed that pre-existing cracks expand during the thermal treatment of coal particles. It is also assumed that any new cracks that form will do so either from an initial crack or in the lower density macerals, and crack propagation will occur along lines of weakness such as maceral-mineral boundaries.

Even though the heating rates (30; 50 and 75 °C.s^{-1}), final temperatures (700 and 800 °C) and residence times (10; 15; 25 and 30 seconds respectively) were varied, no influence of these changes could be detected. It was assumed that this is due to the residence times being far too short for the particle temperature to reach the maximum crucible temperature. Although there is no evidence of devolatilisation taking place the particle did show evidence of thermal drying.

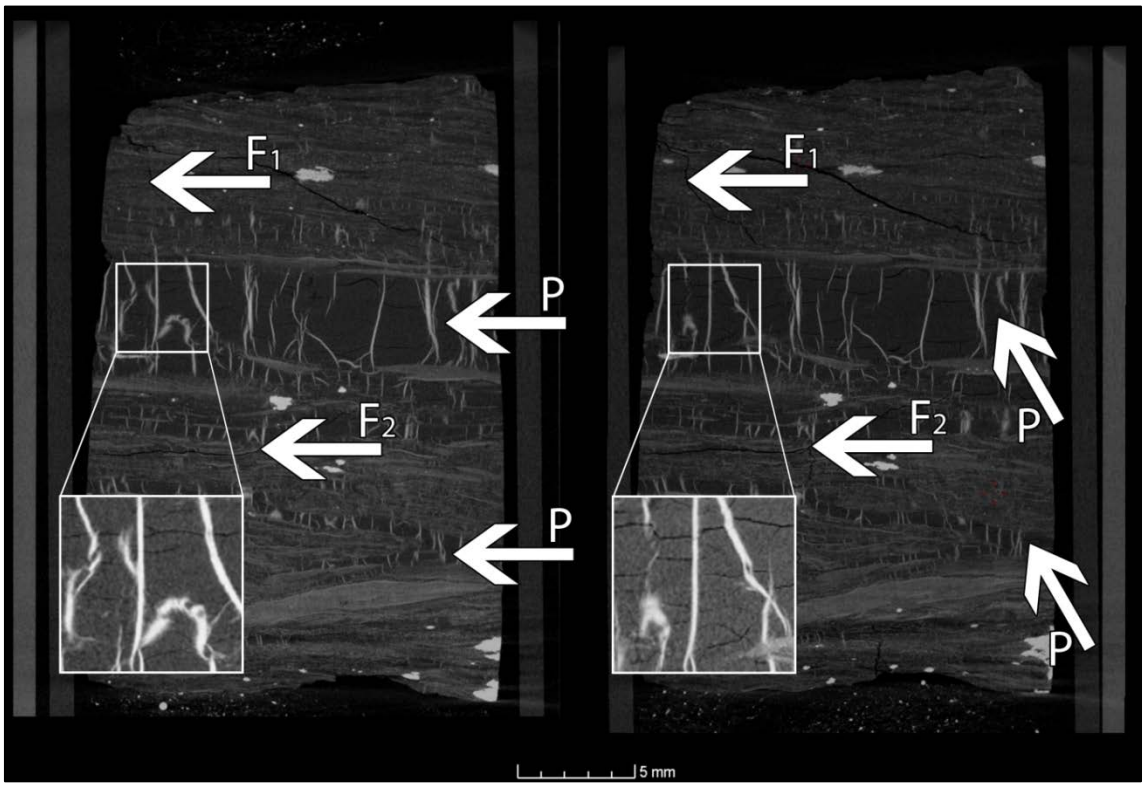

Figure 6.9: Comparison of a particle heated to 700ºC at a rate of 51ºC.s^{-1}

Conclusions

The microstructure of coal was investigated using µCT to determine if the influence of the microstructure on the coal breakage characteristics can be ascertained. To this end, a number of degradation processes were simulated using single particles: slow compression breakage, impact breakage and primary (thermal) fracture. During the mechanical loading, a number of particles were prepared from a ROM sample of Waterberg coal and loaded in such a way that the influence of the microstructures could be identified. The following conclusions were drawn from the comparisons:

- During the compressive loading of coal one of the biggest influences on the enlargement of existing cracks, and the propagation of newly formed cracks is the direction of the applied load.

- It was found that if a particle is compressed, with the bedding plane perpendicular to the load direction, some of the cracks that are parallel to the bedding plane will close. However, the cracks that did close still influence the development of the crack network around it, as other cracks can still terminate and initiate within them. This was not observed with the particles loaded parallel to the bedding plane.

- In both the compressive and impact loading scenarios the pre-existing cracks within a particle have the biggest influence of the microstructures present.

- The macerals and maceral boundaries also influence the formation of new cracks and the crack propagation; the lower density, vitrinite rich, macerals show a tendency towards increased crack formation and some of the maceral boundaries can affect the propagation of a crack.

For the thermal loading of coal, samples were hand selected and prepared from a large sample of washed and sized Witbank coal; and exposed to various temperatures and heating rates. The conclusions drawn are as follows:

- The pre-existing crack network influences the final network by increasing in both length and aperture; the network also acts as an initiation site for new cracks.

- The lower density macerals show a propensity to form more new cracks than the denser macerals.

- Cracks propagate along the maceral-mineral boundaries present.

Thus, it is clear that the microstructure of coal can be identified using µCT as an analytical technique. The change in the microstructure can also be tracked using µCT, but some modifications to the experimental procedures and set-ups are required to tell with greater certainty how the cracks formed and propagated. For the compressive loading of coal, the incremental load increase should be reduced to try to isolate the decisive moments in the very fast crack initiation and propagation process. For the impact loading of coal, the impact energy range should be expanded (i.e. higher impact energies and lower impact energies) to enable the study of the effect of impact energy on crack development. This will allow for a better understanding of the mechanisms by which coal breaks during impact. Finally, according to literature the temperature, heating rate and residence time affects the thermal degradation of coal but none of these effects were observed in this study. Should the ranges for the temperature, heating rate and residence times be increased, and the internal temperature gradients determined, a better understanding of crack development during heating may be gained.

Acknowledgements

Thank you to Juan Nelson, Wynand Breytenbach, Charlotte Badenhorst and Carla Hatting for their help with the experimental work; the personnel at the MIXRAD facility, Necsa for their assistance, patience and enthusiasm and two anonymous reviewers for their invaluable input. This project was funded by the Southern African Coal Processing Society. The work presented in this paper is based on the research supported by the South African Research Chairs Initiative of the Department of Science and Technology and National Research Foundation of South Africa (Coal Research Chair Grant No. 86880). Any opinion, finding or conclusion or recommendation expressed in this material is that of the author(s) and the NRF does not accept any liability in this regard.

Chapter 6 - References

11. Teo, C., Waters, A. & Nicol, S. 1990. Quantification of the breakage of lump materials during handling operations. *International journal of mineral processing*, 30(3):159-184.

13. Sahoo, R.K. & Roach, D. 2005. Effect of different types of impact surface on coal degradation. *Chemical engineering and processing*, 44(2):253-261.

15. Sahoo, R. 2007. Degradation characteristics of steel making materials during handling. *Powder technology*, 176(2):77-87.

16. Tavares, L.M. & de Carvalho, R.M. 2011. Modeling ore degradation during handling using continuum damage mechanics. *International journal of mineral processing*, 101(1–4):21-27.

17. Esterle, J., Kolatschek, Y. & O'Brien, G. 2002. Relationship between in situ coal stratigraphy and particle size and composition after breakage in bituminous coals. *International journal of coal geology*, 49(2):195-214.

20. Sahoo, R. & Roach, D. 2005. Quantification of the lump coal breakage during handling operation at the gladstone port. *Chemical engineering and processing*, 44(7):797-804.

22. Broadbent, S. & Calcott, T. 1957. Coal breakage processes: the analysis of a coal transport system. *Journal of the institute of fuel*, 1957(30):13-25.

23. Sahoo, R. 2006. An investigation of single particle breakage tests for coal handling system of the gladstone port: a review. *Powder technology*, 161(2):158-167.

26. Chandramohan, R., Holtham, P.N. & Powell, M. 2010. The influence of particle shape in rock fracture. (*In* XXV International Mineral Processing Congress 2010 organised by Australasian Institute of Mining and Metallurgy, Brisbane: The Australasian Institute of Mining and Metallurgy. p. 3163-3171).

27. Shi, F. & Kojovic, T. 2007. Validation of a model for impact breakage incorporating particle size effect. *International journal of mineral processing*, 82(3):156-163.

29. Eswaraiah, C., Gupta, A., Nagarajan, R., Rajavel, M. & Nandakumar, K. 2008. Minimization of fines generation in size reduction of coals by impact crusher. *Fuel processing technology*, 89(7):704-714.

30. Bunt, J.R. & Waanders, F.B. 2008. An understanding of lump coal physical property behaviour (density and particle size effects) impacting on a commercial-scale Sasol-Lurgi FBDB gasifier. *Fuel*, 87(13–14):2856-2865.

32. Paprika, M.J., Komatina, M.S., Dakić, D.V. & Nemoda, S.Đ. 2013. Prediction of coal primary fragmentation and char particle size distribution in fluidized bed. *Energy & fuels*, 27(9):5488-5494.

33. van Dyk, J.C. 2001. Development of an alternative laboratory method to determine thermal fragmentation of coal sources during pyrolysis in the gasification process. *Fuel*, 80(2):245-249.

35. Oberholzer, V. & van der Walt, J. 2009. Investigation of factors influencing the attrition breakage of coal. *Journal of the South African Institute of Mining and Metallurgy*, 109(4):211-216.

36. Le Roux, M. & Campbell, Q. 2003. An investigation into an improved method of fine coal dewatering. *Minerals engineering*, 16(10):999-1003.

37. Le Roux, M., Campbell, Q., Watermeyer, M. & de Oliveira, S. 2005. The optimization of an improved method of fine coal dewatering. *Minerals engineering*, 18(9):931-934.

38. Le Roux, M. 2008. The effect of thermal drying on the mechanical strength of South African coals. *Journal of the South African Institute of Mining and Metallurgy*, 108(12):783-787.

40. Dacombe, P., Pourkashanian, M., Williams, A. & Yap, L. 1999. Combustion-induced fragmentation behavior of isolated coal particles. *Fuel*, 78(15):1847-1857.

42. Senneca, O., Russo, S. & Chirone, R. 2009. Primary fragmentation of coal particles at high heating rate. *Chemical engineering transactions*, 18:569-574.

43. Senneca, O., Urciuolo, M. & Chirone, R. 2013. A semidetailed model of primary fragmentation of coal. *Fuel*, 104:253-261.

45. Zhang, H., Cen, K., Yan, J. & Ni, M. 2002. The fragmentation of coal particles during the coal combustion in a fluidized bed. *Fuel*, 81(14):1835-1840.

46. Powell, M.S. & Morrison, R.D. 2007. The future of comminution modelling. *International journal of mineral processing*, 84(1–4):228-239.

47. Tavares, L. & King, R. 1998. Single-particle fracture under impact loading. *International journal of mineral processing*, 54(1):1-28.

49. Han, T., Kalman, H. & Levy, A. 2003. Theoretical and experimental study of multi-compression particle breakage. *Advanced powder technology*, 14(5):605-620.

64. Poulsen, B.A. & Adhikary, D.P. 2013. A numerical study of the scale effect in coal strength. *International journal of rock mechanics and mining sciences*, 63:62-71.

67. Viljoen, J., Campbell, Q.P., le Roux, M. & De Beer, F. 2015. An analysis of the slow compression breakage of coal using microfocus X-ray computed tomography. *International journal of coal preparation and utilization*, 35(1):1-13.

71. Ward, C.R. 2002. Analysis and significance of mineral matter in coal seams. *International journal of coal geology*, 50(1–4):135-168.

74. Falcon, R.M. & Snyman, C. 1986. An introduction to coal petrography: atlas of petrographic constituents in the bituminous coals of South Africa. Johannesburg: Geological Society of South Africa.

76. Laubach, S.E., Marrett, R.A., Olson, J.E. & Scott, A.R. 1998. Characteristics and origins of coal cleat: a review. *International journal of coal geology*, 35(1–4):175-207.

78. Tavares, L.M. & das Neves, P.B. 2008. Microstructure of quarry rocks and relationships to particle breakage and crushing. *International journal of mineral processing*, 87(1–2):28-41.

102. Hoffman, J.W. & De Beer, F. 2012. Characteristics of the Micro-Focus X-ray Tomography Facility (MIXRAD) at Necsa in South Africa. (*In* 18th World Conference on Nondestructive Testing, Durban: South African Institute for Non-Destructive Testing. p. 1-12).

103. Van Geet, M., Swennen, R. & David, P. 2001. Quantitative coal characterisation by means of microfocus X-ray computer tomography, colour image analysis and back-scattered scanning electron microscopy. *International journal of coal geology*, 46(1):11-25.

104. Simons, F.J., Verhelst, F. & Swennen, R. 1997. Quantitative characterization of coal by means of microfocal X-ray computed microtomography (CMT) and color image analysis (CIA). *International journal of coal geology*, 34(1–2):69-88.

107. Duliu, O.G. 1999. Computer axial tomography in geosciences: an overview. *Earth-science reviews*, 48(4):265-281.

108. Van Geet, M., Swennen, R. & Wevers, M. 2001. Towards 3-D petrography: application of microfocus computer tomography in geological science. *Computers & geosciences*, 27(9):1091-1099.

114. Krimmel, S., Stephan, J. & Baumann, J. 2005. 3D computed tomography using a microfocus X-ray source: analysis of artifact formation in the reconstructed images using simulated as well as experimental projection data. *Nuclear instruments and methods in physics research*, 542(1–3):399-407.

116. Cnudde, V., Masschaele, B., Dierick, M., Vlassenbroeck, J., Hoorebeke, L.V. & Jacobs, P. 2006. Recent progress in X-ray CT as a geosciences tool. *Applied geochemistry*, 21(5):826-832.

120. Van Geet, M. & Swennen, R. 2001. Quantitative 3D-fracture analysis by means of microfocus X-Ray computer tomography (μCT): an example from coal. *Geophysical research letters*, 28(17):3333-3336.

121. Mees, F., Swennen, R., Van Geet, M. & Jacobs, P. 2003. Applications of X-ray computed tomography in the geosciences. *(In* Mees, F., Swennen, R., van Geet, M. & Jacobs, J., *eds.* Applications of X-ray computed tomography in the geosciences. London: Geological Society. p. 1-6).

124. Cnudde, V. & Boone, M.N. 2013. High-resolution X-ray computed tomography in geosciences: a review of the current technology and applications. *Earth-science reviews*, 123:1-17.

126. Ketcham, R.A. & Carlson, W.D. 2001. Acquisition, optimization and interpretation of X-ray computed tomographic imagery: applications to the geosciences. *Computers & geosciences*, 27(4):381-400.

129. Keller, A. 1998. High resolution, non-destructive measurement and characterization of fracture apertures. *International journal of rock mechanics and mining Sciences*, 35(8):1037-1050.

130. Ketcham, R.A., Slottke, D.T. & Sharp, J.M. 2010. Three-dimensional measurement of fractures in heterogeneous materials using high-resolution X-ray computed tomography. *Geosphere*, 6(5):499-514.

135. Van Geet, M., David, P. & Swennen, R. 2000. Three dimensional coal characterisation (maceral, mineral and cleats) by means of X-ray microfocus computer tomography (µCT). (*In* Podemski, M. & Jureczka, J., *eds*. European Coal Conference IV, Warsaw, Poland: Polish Geological Institute. p. 263-270).

137. Mazumder, S., Wolf, K.-H., Elewaut, K. & Ephraim, R. 2006. Application of X-ray computed tomography for analyzing cleat spacing and cleat aperture in coal samples. *International journal of coal geology*, 68(3):205-222.

139. Naudé, G., Hoffman, J., Theron, S.J. & Coetzer, G. 2013. The use of X-ray computed tomography in the characterisation of coal and associated char reductants. *Minerals engineering*, 52:143-154.

149. England, T., Hand, P.E., Michael, D.C., Falcon, L.M. & Yell, A.D., *eds*. 2002. Coal preparation in South Africa. 4th ed. Pietermaritzberg: The South African Coal Processing Society.

150. Bunt, J.R., Wagner, N.J. & Waanders, F.B. 2009. Carbon particle type characterization of the carbon behaviour impacting on a commercial-scale Sasol-Lurgi FBDB gasifier. *Fuel*, 88(5):771-779.

151. Dhillon, R.K., Singh, P., Gupta, S.K., Singh, S. & Kumar, R. 2013. Study of high energy (MeV) N^{6+} ion and gamma radiation induced modifications in low density polyethylene (LDPE) polymer. *Nuclear instruments and methods in physics research*, 301:12-16.

152. Coetzee, S., Neomagus, H.W.J.P., Bunt, J.R., Strydom, C.A. & Schobert, H.H. 2014. The transient swelling behaviour of large (−20 + 16 mm) South African coal particles during low-temperature devolatilisation. *Fuel*, 136:79-88.

153. Mathews, J.P., Pone, J.D.N., Mitchell, G.D. & Halleck, P. 2011. High-resolution X-ray computed tomography observations of the thermal drying of lump-sized subbituminous coal. *Fuel processing technology*, 92(1):58-64.

Chapter 6 - Additional Notes

After micro-focus computed tomography (µCT) was successfully applied to identify and track the changes in coal microstructure that occurs during slow compression breakage in Chapter 5, Chapter 6 successfully applied µCT to track the changes in microstructure due to impact and thermal shock. Chapter 6 also incorporated the improvements to the compression breakage experiments suggested in Chapter 5. During the compressive breakage experiments conducted for Chapter 6, the compressive force applied to the particles was increased incrementally and a tomogram generated after each increase. After the particle failed, all of the tomograms generated during compression were compared.

In this article, published in the South African Journal of Science, a detailed description of the impact breakage rig was not included in order to increase the readability of the article. A detailed description of the rig was published in a later article (Chapter 7) and is repeated here for clarity:[*] An innovative impact breakage device was designed in such a way that the bedding plane orientation of the particle relative to the impact surface, as well as the impact energy, could be accurately controlled. Lower impact energies could be obtained due to the design of the apparatus. The device (pictured in Figure 7.2) consisted of a sliding carriage, into which the particle was clamped, falling freely in a rigid frame. The clamp was set to release the particle a short distance (usually a few centimetres) above a height adjustable steel impact anvil, and this ensured that the particle was free falling with a given orientation moments before impact. The height from which the carriage was released controlled the impact energy of a particle, since the impact energy of a particle is related to the kinetic energy of the particle just before impact. A twin laser beam speedometer measured the velocity of the carriage and particle just before impact. The velocity was used to calculate the kinetic energy. A digital still camera, triggered by a proximity switch on the falling carriage, recorded the moment of impact to confirm impact orientation. The impact anvil is topped with a 50 mm thick steel plate and secured to the concrete floor.

In addition to substantiating the conclusions drawn in Chapter 5, the incremental increase of the applied load during compression showed that, when a particle is compressed with bedding planes perpendicular to the applied force, some of the cracks that are perpendicular to the applied force were initially forced closed. The fact that the cracks were no longer apparent on the tomograms did not diminish the contribution of the closed cracks to the final

[*] Viljoen, J., Campbell, Q., le Roux, M. & Hoffman, J. 2016? The influence of bedding plane orientation on the degradation characteristics of a South African Waterberg coal. *International Journal of Coal Preparation and Utilization*.

crack network. Cracks that propagated through the particle were still influenced by the closed cracks, either terminating or initiating in the closed cracks. When the particles were compressed with the bedding planes parallel to the applied compressive load, however, no cracks that were forced closed were observed. It is assumed that some of the stronger microlithotypes acted as pillars and prevent the cracks from closing. The fact that cracks close during low pressure compression also suggests that coal undergoes some elastic deformation during compression, not only brittle or inelastic deformation.

For coal degradation during impact, it was found that the biggest influence on the final crack network is the pre-existing cracks and cleats present within the coal particles. Additionally, it was found that newly formed cracks can either initiate, terminate or propagate along the microlithotype-microlithotype boundaries as well as the microlithotype-mineral boundaries and that lower density microlithotypes (vitrinite rich) produce more new cracks than the higher density microlithotypes (inertinite/mineral rich). The influence of the direction of applied impact load could not be observed, this is assumed to be due to the low energies of the impact events. The impacts were equivalent to a drop from 1 m with an impact velocity of 4.5 $m.s^{-1}$. Although the influence of the bedding planes could not be seen in this publication, Chapter 7 shows that it did influence the breakage.

For coal degradation due to rapid temperature increases is was found that the all of the features studied had the potential to influence degradation. For these experiments the type of coal used were changed from a Waterberg coal to a Witbank coal to prevent any damage to the experimental setup due to possible swelling. Witbank coals are non-swelling (low vitrinite content, ±30 %)[154], while some Waterberg coals do swell.[152] Cracks propagate along the boundaries between mineral matter and coal matrix, as well as either initiating or terminating at the boundaries between mineral matter and coal matrix. Due to the shrinking that occurs during thermal drying, new cracks form at right angles to pre-existing cracks present in the coal samples.[153] For thermal degradation it was also apparent that the lower density macerals produced more new cracks compared to the higher density macerals.

During the thermal degradation experiments performed, no evidence of devolatilisation was noted, although the temperatures of the graphite crucibles were high enough to cause devolatilisation. This is assumed to be due to the short residence times of the coal particles in the radio frequency (RF) induction furnace, and that the internal temperature of the coal particles did not reach the same temperatures as the graphite crucible. It is suggested that any future research should discard the use of RF induction furnaces and rather use a traditional furnace; if a traditional furnace is used a fine balance between the furnace

temperatures and residence time will ensure that the particles undergo devolatilisation but still remain intact enough for tomographic analysis.

From the conclusions above it is clear that any of the physical features, investigated during the course of this study, present in coal has the potential to contribute to the final cracks network: new cracks can initiate, terminate, or propagate along pre-existing cracks, microlithotype boundaries, or microlithotype-mineral boundaries. It is however unclear what causes a specific feature to activate and contribute to the degradation.

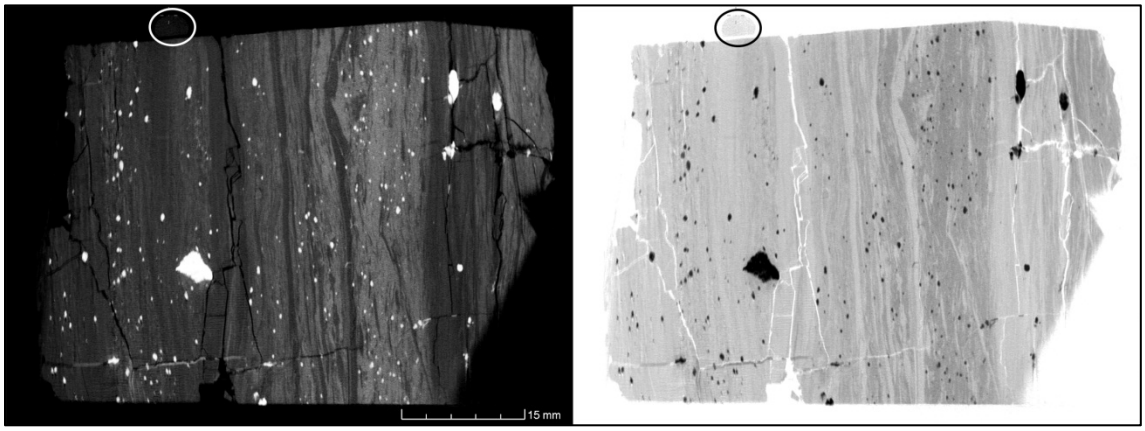

Additional notes Figure 6.1: Comparison of an original tomogram slice and its inverted tomogram slice

During the review process of the manuscript in Chapter 6 one of the reviewers made the comment that not all of the features referred to in the manuscript could be easily distinguished on the tomograms. This was especially true when the manuscript was printed and not viewed digitally. In an effort to ensure the features are more distinguishable in future publications the tomograms were inverted, i.e. black in the original tomograms were inverted to white, while white in the original tomograms were inverted to black. Additional notes Figure 6.1 show the comparison of a slice from the original tomogram compared to the same slice that has been inverted. The inversion was done using an image processing application.

From the comparison, it is clear that more of the features can be distinguished in the inverted tomogram compared to the original tomogram. As an example: in the top left corner of each slice is a drop of hot glue that is easier to distinguish in the inverted tomogram slice than in the original tomogram slice. Due to this fact, the eAppendix included on the CD accompanying the thesis contains inverted copies of all the tomograms.

Chapter 7 will focus on the application of µCT to determine the effect of the internal features, specifically the orientation of the bedding planes in relation to the impact surface, on coal

degradation during impact; Chapter 7 will also try to determine if the particle size distribution of a single particle can be predicted.

Chapter 6 - Additional notes references

152. Coetzee, S., Neomagus, H.W.J.P., Bunt, J.R., Strydom, C.A. & Schobert, H.H. 2014. The transient swelling behaviour of large (−20 + 16 mm) South African coal particles during low-temperature devolatilisation. *Fuel*, 136:79-88.

153. Mathews, J.P., Pone, J.D.N., Mitchell, G.D. & Halleck, P. 2011. High-resolution X-ray computed tomography observations of the thermal drying of lump-sized subbituminous coal. *Fuel processing technology*, 92(1):58-64.

154. Coetzee, G. 2011. The influence of particle size on the steam gasification kinetics of coal. Potchefstroom: North-West University. (Dissertation).

Chapter 7 - The influence of bedding plane orientation on the degradation characteristics of a Waterberg coal

Chapter 4 identified micro-focus X-ray computed tomography (µCT) as a technology that is uniquely suited to track the internal structures present in coal. Chapter 5 and Chapter 6 confirmed that µCT can be used to identify and track the changes that occur in a coal particle when subjected to compression breakage, impact breakage, and during thermal degradation. The features, identified in Chapter 5 and Chapter 6 that contribute to degradation of coal, are pre-existing cracks, boundaries between coal microlithotypes of differing densities, as well as the boundaries between microlithotypes and mineral inclusions. Chapter 7 aims to describe the use of µCT to determine the effect that bedding plane orientation has on the impact breakage of coal and will also try to predict the particle size distribution of a single particle based on the internal structure of that particle.

Chapter 7 is a manuscript submitted to the International Journal of Coal Preparation and Utilization (Submitted for peer-review: 09 November 2015, Manuscript ID.: GCOP-2015-0106; Published online: 01 February 2016)[*] and is currently in the review process.

The manuscript was written in collaboration with Prof. Quentin P. Campbell, Prof. Marco le Roux and Mr Jakobus Hoffman. The individual contributions of the co-authors are given on page ix, page xi, and page xiii.

[*] Viljoen, J., Campbell, Q., le Roux, M. & Hoffman, J. 2016? The influence of bedding plane orientation on the degradation characteristics of a South African Waterberg coal. *International Journal of Coal Preparation and Utilization*.

Abstract

A tomographic study of coal microstructure (coal bedding planes, pre-existing cracks, microlithotype boundaries and mineral boundaries) was undertaken to explain its influence on coal degradation due to impact. A number of samples were cut from a large block of Waterberg run-of-mine coal. It was characterised using micro-focus X-ray computed tomography before and after undergoing impact breakage in a single particle drop shatter test. The tomograms generated before and after impact were compared and the breakage characteristics determined. It was found that the internal structure of the coal samples influenced the breakage of coal, with new cracks initiating, terminating or propagating along pre-existing cracks, microlithotype-, and mineral grain boundaries. The contribution of the physical structures to the breakage characteristics could not be predicted for individual particles, but the overall effect on a population of particles was fitted using a Rosin-Rammler distribution. The orientation of the bedding planes in relation to the impact surface also influenced the propagation of cracks through the samples. Newly formed cracks propagated deeper into a particle if the impact force was applied along the bedding planes.

Keywords: Coal, Single particle impact, Degradation, Micro-focus X-ray tomography

Introduction

Coal degradation (the unwanted production of fines)[11, 20] is a serious problem for coal producers and users. Coal fines in a sized feed increases the transportation cost and the moisture levels, while, in the case of fixed bed operations like gasification, it decreases reactor efficiency due to hydrodynamic effects.[11, 15, 16, 20, 37] Degradation occurs at a number of unit operations during coal mining and beneficiation: at the mining face degradation occurs due to high energy input during cutting or blasting; during the beneficiation process, on conveyor belts, at conveyor transfer points, as well as during stockpiling and reclamation.[11, 13, 15, 16, 20] Very little is known about the fundamentals of coal degradation but it is thought to occur by two mechanisms: surface and volume breakage.[11, 15, 20, 46] Surface breakage or attrition occurs when the parent particle becomes rounded by the constant chipping and abrasion of the particle surface due to mild contact with other coal particles and solid surfaces; and volume breakage or fracture occurs when the parent particle is broken into a number of small fragments due to compression or impact. Some authors have suggested that the degradation of coal is not due to a single mechanism, but due to a combination of mechanisms.[13, 14, 16, 20, 23]

Although the breakage of mineral ores have been studied extensively, published literature on coal degradation is limited.[23] Properties like particle size, shape, orientation, the type of impact surface, and the composition of the coal (specifically the maceral composition) all influence coal breakage.[13, 17, 83] Increasing the breakage energy or using a larger initial particle results in more degradation products forming.[15, 21, 47, 60] Chandramohan et al. (2010) found that if slab-like rock particles (where one of the three orthogonal dimensions is significantly smaller than the other two) are compressed with larger contact areas, they showed reduced strength when compared to similar particles compressed with smaller contact areas.[26] A similar conclusion was drawn by Campbell and Viljoen (2011) who found that slab-like coal particles impacted on their narrow edges appeared stronger than particles impacted onto larger contact areas.[68] Regarding the coal composition, Esterle et al. (2002) found that when drill cores were subjected to impact breakage tests, the highest proportion of vitrinite were found in the fine fraction while the coarse fraction contained the highest proportion of mineral matter.[17] These findings supported Falcon and Snyman (1986) who reported that vitrinite is the most brittle of the coal macerals.[74] The type of impact surface also influences the breakage, with more breakage occurring due to an impact onto a steel plate compared to a conveyor belt's surface.[13, 15]

To quantify the changes that occur in the coal microstructure a non-destructive technique that is able to characterise the internal features of the coal samples was required. Viljoen et al. (2015) found that micro-focus X-ray computed tomography (µCT) is uniquely suited to this task when it was applied to track the changes that occurred within coal particles during degradation.[67]

Micro-focus X-ray computed tomography is a non-destructive analytical technique that is used to inspect the internal structure of opaque objects using X-rays.[104, 107, 126] The object under scrutiny is placed on a translation table and an X-ray cone-beam is projected through it as it rotates around a central axis, through a full revolution, at consistent step angle intervals. The attenuated X-rays are recorded by a digital flat panel detector as projection images of the object at each step interval. For this project, 1000 projections at a step-angle of 360° / 1000 = 0.36° were recorded and used to generate a tomogram: a virtual three-dimensional representation of the object.[101] The X-ray attenuation coefficient of the object depends on the atomic number, and consequently on the physical density of the constituents within the object.[103, 104, 126] A discussion of the theory and mathematics of the µCT reconstruction is beyond the scope of this publication, but it is described in detail by various authors.[100, 112, 126] The µCT process produces a number of visual artefacts that can influence the outcome and interpretation of the recorded data. Fortunately those artefacts can be minimized during data acquisition, reconstruction and analysis.[126]

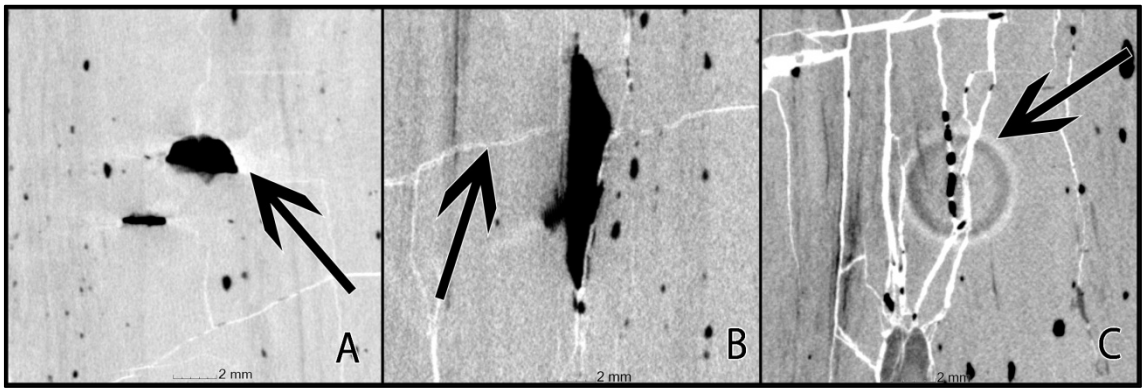

Figure 7.1: Tomographic artefacts: Beam hardening (A), motion artefacts (B), and ring artefacts (C)

A common artefact is beam hardening (Figure 7.1(A)) that occurs due to the preferential attenuation of lower energy X-rays as it passes through the object. One of the possible manifestations of beam hardening is where a tomogram erroneously shows no material next to highly attenuating material – an indication that the low X-ray energies in the X-ray radiation beam spectrum are absorbed by high density materials.[126] Another artefact due to motion (Figure 7.1(B)) occurs when the object is not properly anchored to the translation

table and shows up in the final tomogram as ghosting, or a duplication of unique features (also called a double-edge). Ring artefacts (Figure 7.1(C)) are caused by faulty detector elements, faulty scintillator elements, and dead pixels.[126]

In order to quantify the breakage that occurs during impact, the particle size distribution (PSD) of each sample after impact was fitted to a Rosin-Rammler distribution, given by Equation 7.1.[51]

$$y^{-} = 1 - \exp\left[-\left(d/d^{*}\right)^{n}\right] \qquad \text{Equation 7.1}$$

Where y^{-} is the cumulative mass fraction passing a specific size, d; the size modulus (d^{*}) is the screen aperture size that 62.3% of the sample mass passes and n is the distribution parameter related to the spread of the particle sizes.[51]

A convenient method to characterise the degradation of ore in general after impact is to define the t_{10} value - where t_{10} is defined as the mass percentage of progeny particles smaller than $1/10^{th}$ the size of the parent particle, and is determined from the PSD. The dependence of t_{10} on material properties as well as the properties of the test instrument is given in Equation 7.2.[27, 48, 50, 89]

$$t_{10} = M\left\{1 - e^{[-f_{mat}xk(E_{cs}-E_{min})]}\right\} \qquad \text{Equation 7.2}$$

Where M (%) is the maximum value of t_{10} for the material being studied; f_{mat} (kg.J^{-1}.m^{-1}) is some material dependent breakage property, x (m) is the initial particle size; k is the amount of successive impact events, E_{cs} (J.kg^{-1}) and E_{min} (J.kg^{-1}) is the specific comminution energy and threshold energy respectively. The threshold energy is the amount of energy that must be applied to the particle before any breakage will occur.

Campbell and Viljoen (2011) found that there is a discrepancy between the expected- and actual breakage behaviour of coal particles at low impact energies; where an exponential relationship between the degradation of the coal and the impact energy was expected (Equation 7.2), a linear trend with a positive y-intercept was evident (see Equation 7.3, where A is some constant).[68]

$$t_{10} = x.E.f_{mat} + A$$ Equation 7.3

This intercept is obviously not realistic (see Equation 7.2) and implies that very little energy input is required for the particle to undergo degradation. One possible explanation for this discrepancy is that the effect of the coal microstructure on breakage differs for low impact energies and high impact energies.

This study is a continuation of the above mentioned study by Campbell and Viljoen (2011), and Viljoen et al. (2015), aiming to develop a better understanding of the mechanisms by which breakage occurs at low energies and to characterise the influence of the coal microstructure (bedding plane orientation, pre-existing cracks, lithotype boundaries and mineral boundaries) on low impact energy degradation using µCT.[67, 68]

Experimental

An innovative impact breakage device was designed in such a way that the bedding plane orientation of the particle relative to the impact surface, as well as the impact energy, could be accurately controlled. Lower impact energies could be obtained due to the design of the apparatus. The device (pictured in Figure 7.2) consisted of a sliding carriage, into which the particle was clamped, falling freely in a rigid frame. The clamp was set to release the particle a short distance (usually a few centimetres) above a height adjustable steel impact anvil, and this ensured that the particle was free falling with a given orientation moments before impact. The height from which the carriage was released controlled the impact energy of a particle, since the impact energy of a particle is related to the kinetic energy of the particle just before impact. A twin laser beam speedometer measured the velocity of the carriage and particle just before impact. The velocity was used to calculate the kinetic energy. A digital still camera, triggered by a proximity switch on the falling carriage, recorded the moment of impact to confirm impact orientation. The impact anvil is topped with a 50 mm thick steel plate and secured to the concrete floor. Although some rebound did occur after impact, it is assumed that insignificant breakage occurs due to rebound.

The coal samples used during this study was cut from a single, large (0.85 m x 1 m x 0.5 m) block of run-of-mine (ROM) bituminous coal from a colliery in the Waterberg coalfield located in the Limpopo province of South Africa. This coal was chosen for its layered structure of alternating coal and mineral bands, enabling the selection of a wide variety of particle structure types. The microlithotype banding can be clearly seen in Figure 7.3 as alternating light- and dark grey areas. Table 7.1 gives a summary of the most important coal properties.

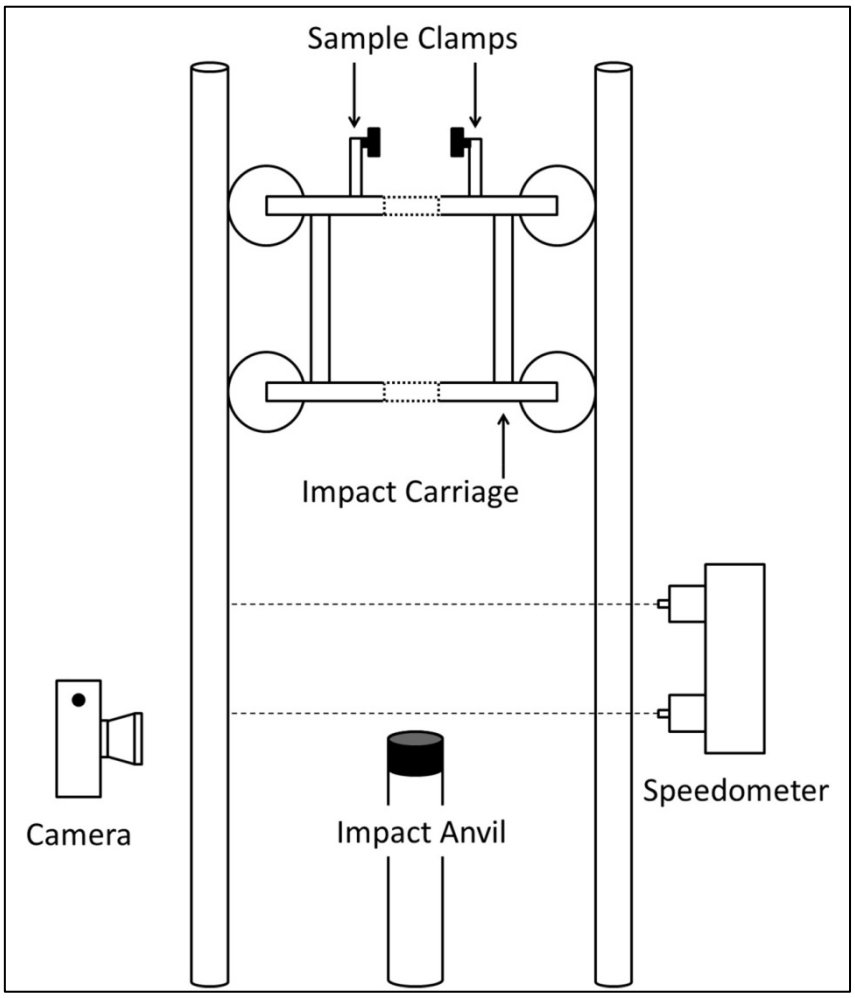

Figure 7.2: Experimental set-up

The prepared coal samples were characterised before and after breakage using a NIKON XTH 225 ST µCT system (MIXRAD) located at the South African Nuclear Energy Corporation's (Necsa) Pelindaba research facility. The tomograms were reconstructed using Nikon CT-PRO, and visualised and analysed using VGStudio MAX 2.1 software packages respectively. The MIXRAD system can be operated at a maximum power rating of 30 W with beam currents up to a maximum of 1 mA. A detailed description of the system and its capabilities can be found in Hoffman and De Beer (2012).

Figure 7.3 indicate some of the features tracked during this study that can be identified in the tomograms: cracks (A), vitrinite rich lithotypes (B), inertinite rich lithotypes (C), mineral inclusions (D) and microlithotype boundaries (E). Due to its analogues to conventional radiography, 2D tomogram slices are usually presented as negatives,[107] with high attenuation zones displayed as light grey values and low attenuation zones displayed as

dark grey values (Figure 7.3, left). The grey scales of all tomogram slices that are presented in this paper were inverted to better differentiate between the various attenuation regions (Figure 7.3, right), especially areas with lower X-ray attenuation. In the inverted presentation a dot of glue (circled), used to mark the orientation of the impacted particle, can be easily seen; while this feature is hard to differentiate in the traditional presentation.

Table 7.1: Properties of Waterberg coal

Volatiles, Ash content, and Vitrinite random reflectance		**Maceral composition[155] (volume percentage; mineral matter free)**	
Volatiles (mass percentage (m%), dry basis (DB))	27.35 ± 0.67	**Vitrinite**	63
Ash content (m%, DB)	11.93 ± 0.76	**Liptinite**	5
Vitrinite random reflectance[155]	0.73	**Inertinite**	33

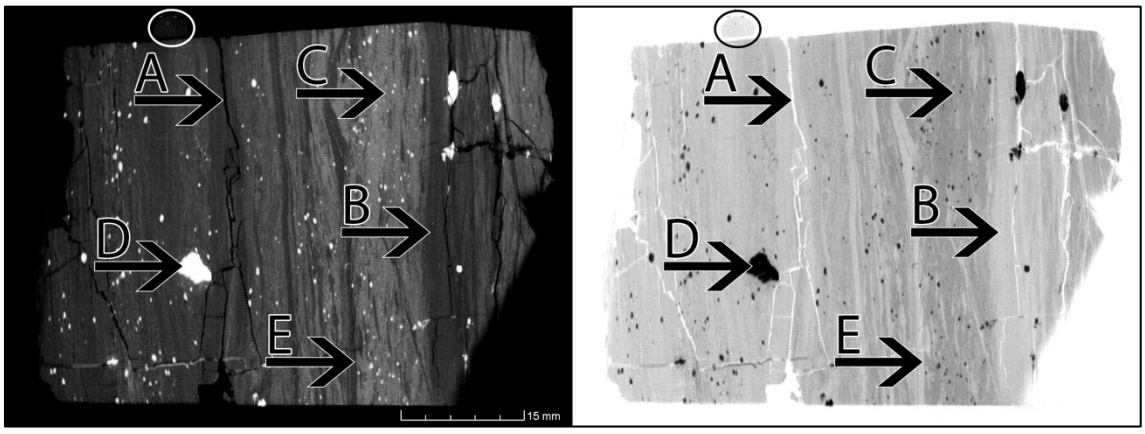

Figure 7.3: Comparison of the traditional- and inverted presentation as well as the internal coal structure investigated during this study: (A) Cracks and cleats; (B) lower density lithotypes; (C) higher density lithotypes; (D) mineral inclusions and (E) the boundaries between the high and low density lithotypes.

Twenty samples (cubes, roughly 55 mm to a side) were cut from the ROM coal block using an angle grinder, and three adjacent sides of the cube, at right angles to one another, were machined flat: two opposite sides of the cube would be clamped by the carriage, while

impact was to take place on the third surface. This impact surface was cut parallel to the natural bedding plane for half of the samples, while the rest was cut perpendicular to the bedding plane. This was done for the applied force to be directed either along the bedding plane (particles impacted perpendicular to the bedding plane) or across the bedding plane (particles impacted parallel to the bedding plane). The prepared samples were stored in vacuum sealed bags to minimize oxidation, since this could change the breakage characteristics of the coal.[15, 18] After the initial tomographic scans, the samples were wrapped in high density polyethylene (HDPE) cling-film to preserve the relative positions of the progeny after breakage and to facilitate tomographic analysis after impact. The number of samples for this study was restricted to twenty due to experimental constraints, such as the time taken for the analysis of the tomograms. Campbell and Viljoen (2011) also found that even if the sample size is greatly increased there would be no guarantee that the sample is going to be statistically significant due to the heterogeneous nature of the coal used, and the arbitrary nature of breakage.[68]

After the samples were impacted from a height equivalent to 1 m, the tomograms generated before and after impact were studied, compared, and conclusions drawn about the development of the crack networks. Sieve size analyses were done to determine the particle size distributions and the extent of breakage (t_{10}) of each sample.

Results

Tomographic results

Figure 7.4 to Figure 7.8 show some of the comparative tomograms generated during this study. These show the influences of the various internal structures on the breakage characteristics of the coal particles. The top row of images in Figure 7.4 to Figure 7.8 shows the tomograms generated before impact, while the bottom row of images shows the tomograms of the same feature generated after impact. Cracks are represented by the white or very light shades of grey in the figures, while the high-density constituents, like mineral inclusions, are represented by the darker shades. In each of the comparisons (Figure 7.4 to Figure 7.8) the impacted surface is towards the bottom of the figure.

The features that were the focus of this study were the bedding plane orientation, pre-existing cracks and cleats (A in Figure 7.3), the boundaries between mineral inclusions and the coal matrix (D in Figure 7.3), and the boundaries between the high and low density

lithotypes present (E in Figure 7.3). Any of these features were shown to influence the development of the crack network in one of four ways:

- No influence: the feature remains unchanged and does not contribute to the development of the final crack network.
- Initiation point: a newly formed crack starts, or initiates, at the feature.
- Propagation along the feature: a newly formed crack propagates along the boundary between higher- and lower density lithotypes or along the boundary between the coal matrix and a mineral inclusion.
- Termination point: A newly formed crack ends, or terminates, at the feature.

Due to the fact that the tomograms cannot give any information about the order in which new cracks formed, nor about the directionality of a propagating crack, no distinction will be made between crack initiation and termination points, but both will be referred to as termini, or end points.

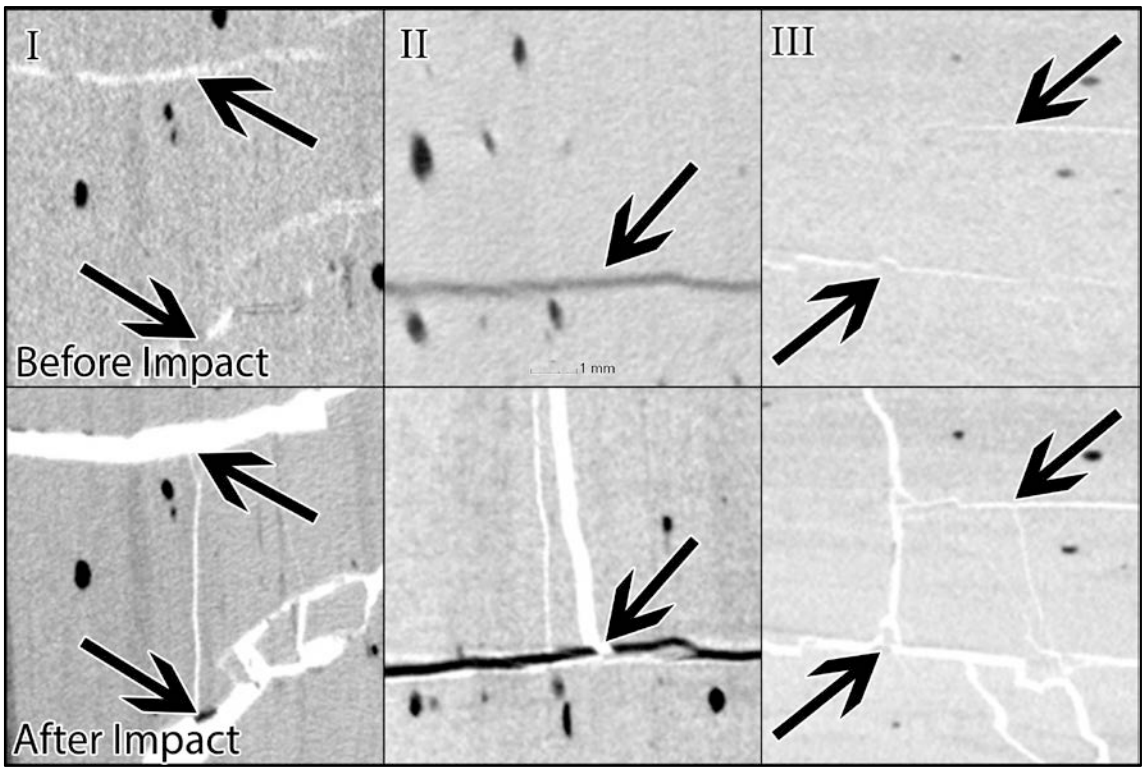

Figure 7.4: Examples of cracks terminating in pre-existing cracks from two particles (I, II) where the impact force application was along the bedding plane and one particle (III) impacted with the force applied across the bedding plane

Figure 7.4, Figure 7.5 and Figure 7.6 show slices from tomograms generated before and after impact, where a newly formed crack either initiated or terminated in a pre-existing feature of the particles. Figure 7.4 shows the influence of pre-existing cracks, Figure 7.5 shows the influence of the boundaries between the higher- and lower density microlithotypes, and Figure 7.6 shows the influence of boundaries between a mineral inclusion and the coal matrix. In Figure 7.4, Figure 7.5, and Figure 7.6 the arrows indicate the terminus of a new crack at the specific feature.

Figure 7.4(I) and Figure 7.4(II) show two particles that were impacted with their bedding planes perpendicular to the impact surface (force applied along the bedding plane). Figure 7.4(III) shows a particle impacted with its bedding plane parallel to the impact surface (force applied across the bedding plane). Figure 7.4(I) and Figure 7.4(III) shows newly formed cracks that terminated against empty cracks and Figure 7.4(II) shows a crack that terminated in a mineral filled cleat.

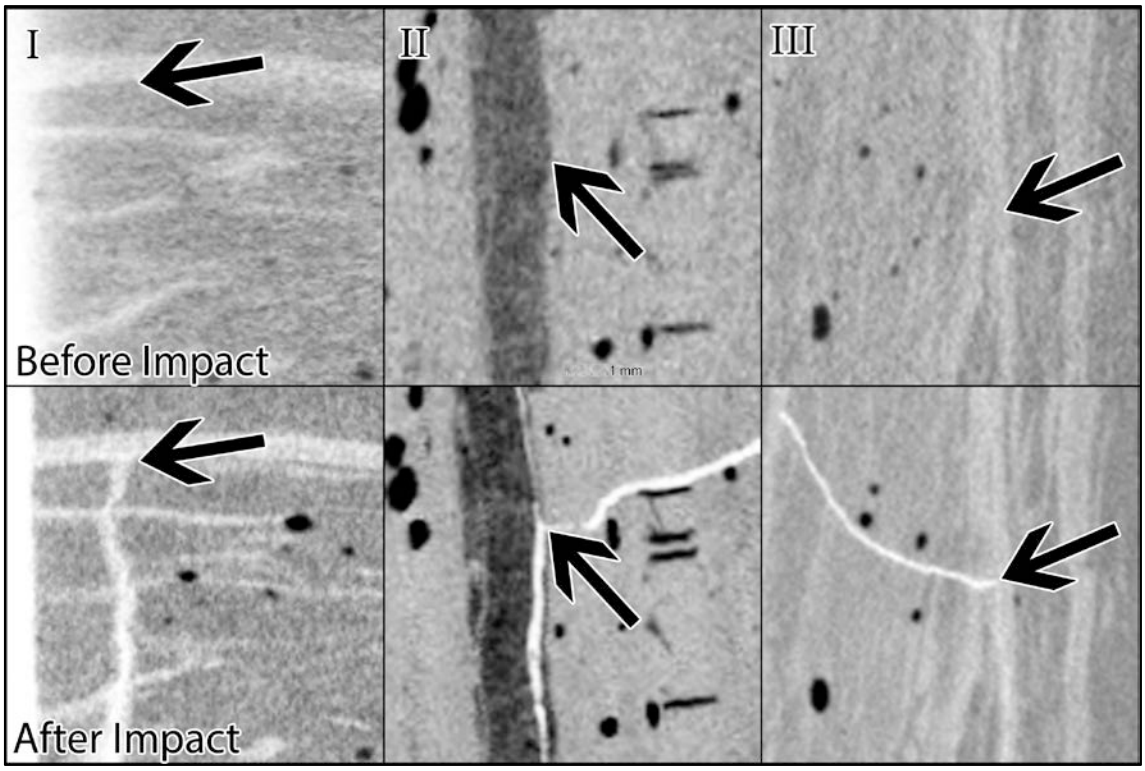

Figure 7.5: Examples of cracks terminating at a lithotype boundary from two particles (II, III) where the impact force application was along the bedding plane and one particle (I) impacted with the force applied across the bedding plane.

Figure 7.5 shows where newly formed cracks terminated at the boundary between two microlithotypes. The particle in Figure 7.5(I) was impacted with its bedding plane parallel to the impact surface, while the particles in Figure 7.5(II) and Figure 7.5(III) were impacted with

their bedding plane perpendicular to the impact surface. Figure 7.5(II) shows both a crack that terminated at the boundary between the two microlithotypes and a crack that propagated along the boundary.

The particles in Figure 7.6(I) and Figure 7.6(III) were impacted with their bedding planes perpendicular to the impact surface, while Figure 7.6(II) shows a particle impacted with its bedding plane parallel to the impact surface. Figure 7.6(I) shows a tomogram slice where two cracks terminated on two opposite sides of a large mineral inclusion, Figure 7.6(II) shows where a crack propagated between a cleat and a mineral inclusion, and Figure 7.6(III) shows where a crack terminated at a mineral inclusion. The tomogram generated after impact, in Figure 7.6(III) shows what seems to be a very wide crack above the inclusion (large white area); this is not a crack but a manifestation of beam hardening and shows how beam hardening can obscure features close to high density inclusions.

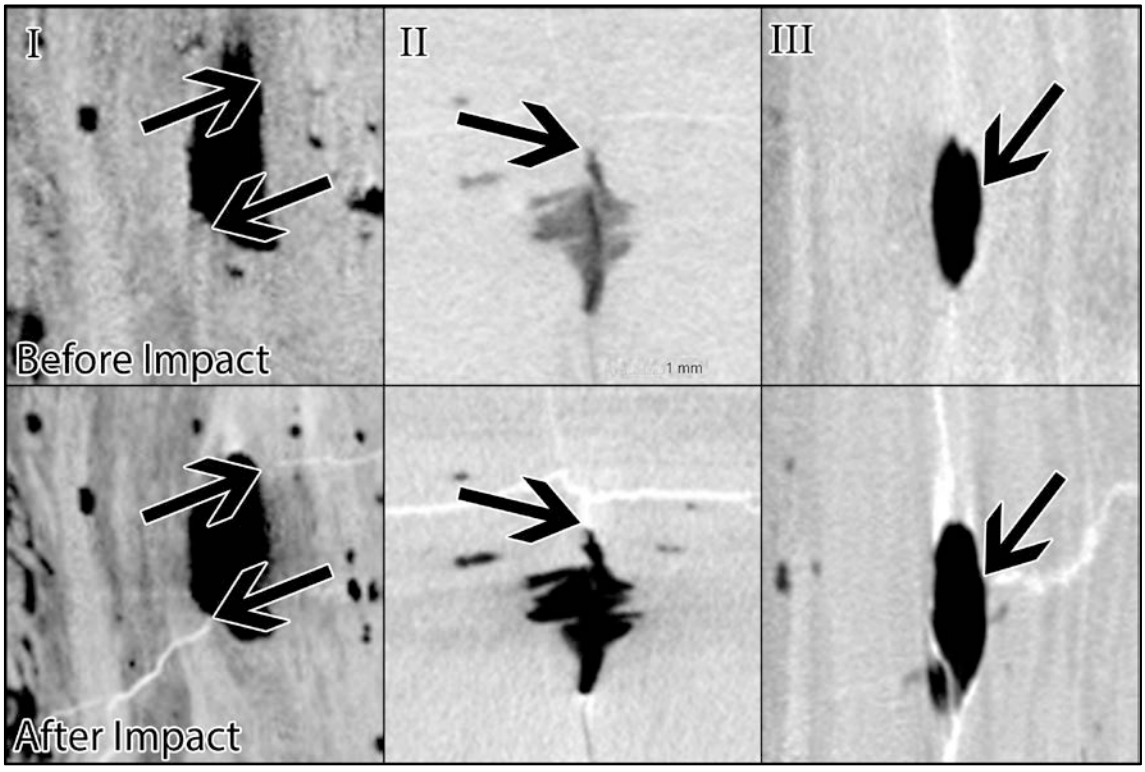

Figure 7.6: Examples of cracks terminating at a mineral boundary from two particles (I, III) where the impact force application was along the bedding plane and one particle (II) impacted with the force applied across the bedding plane.

Figure 7.7 and Figure 7.8 show slices from tomograms generated before and after impact, showing newly formed cracks that propagated along a feature present in the sample. Figure 7.7 shows cracks that propagated along the boundaries between microlithotypes of differing densities, whilst Figure 7.8 shows cracks that propagated along mineral boundaries. The

arrows in Figure 7.7 and Figure 7.8 indicate where new cracks propagated along boundaries within the coal.

Figure 7.7(I) and Figure 7.7(II) show two particles impacted with their bedding planes perpendicular to the impact surface, while the particle in Figure 7.7(III) was impacted with its bedding plane parallel to the impact surface. In Figure 7.7(I) and Figure 7.7(II) the new cracks propagated along a straight boundary, whilst in Figure 7.7(III) the cracks propagated along a boundary with a significant curve.

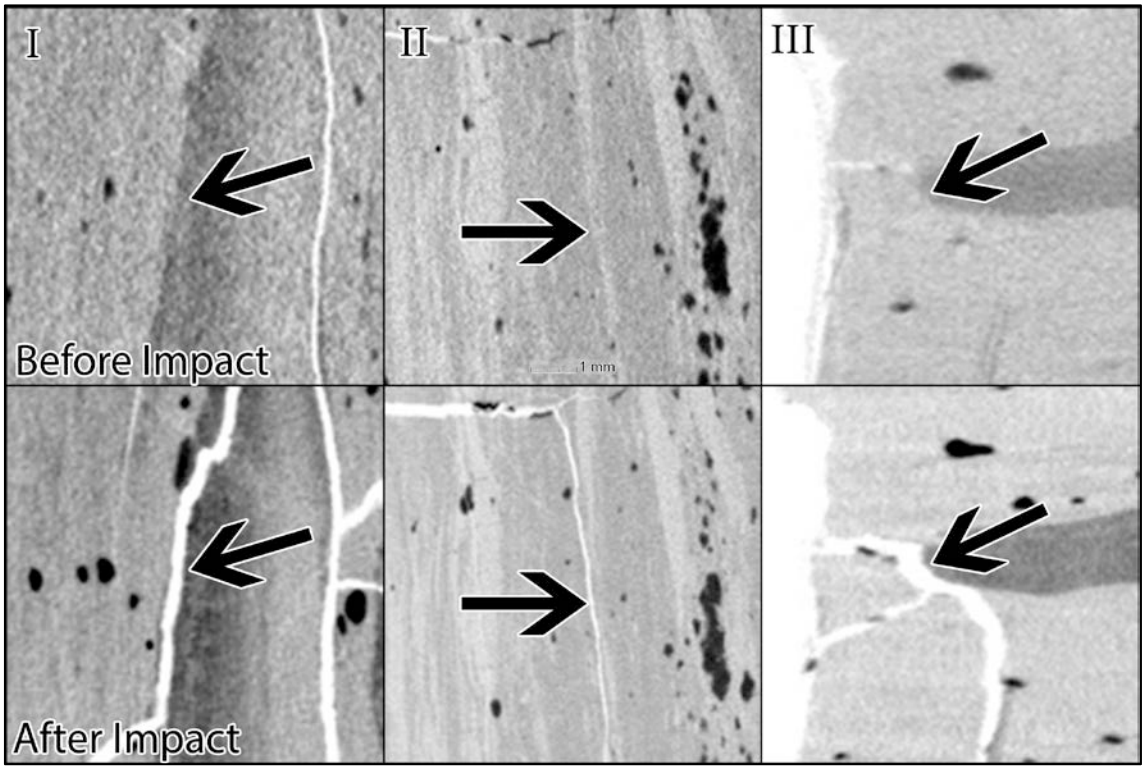

Figure 7.7: Examples of cracks propagating along lithotype boundaries from two particles (I, II) where the impact force application was along the bedding plane and one particle (III) impacted with the force applied across the bedding plane.

The particle in Figure 7.8(I) was impacted with its bedding plane perpendicular to the impact surface, whilst Figure 7.8(II) and Figure 7.8(III) show particles that were impacted with their bedding planes parallel to the impact surface. In Figure 7.8(I) the crack propagated along a mineral filled cleat and in Figure 7.8(II), as well as Figure 7.8(III), the new cracks propagated along a curved mineral matter inclusion.

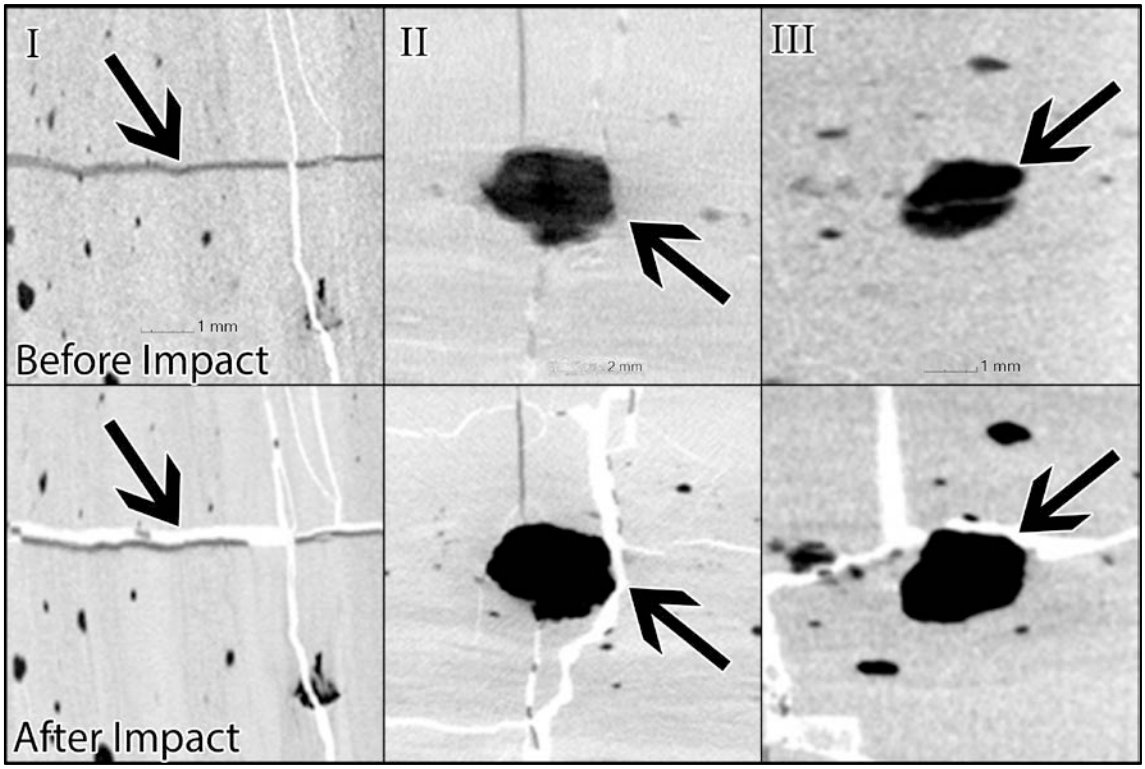

Figure 7.8: Examples of cracks propagating along mineral boundaries from one particle (I) where the impact force application was along the bedding plane and two particles (II, III) impacted with the force applied across the bedding plane.

The figures above show only a few of the examples where a specific feature contributed to the final crack network and are characteristic of what happens close to the features studied. The vast majority of the features that were present in the particles however, did not contribute to the degradation of the particles. The analysis of the tomograms gave no indication of what might cause a specific feature to contribute to the degradation of a particle. This needs to be studied in more detail.

Quantitative results

Figure 7.9 shows the number of new cracks formed in each sample after impact versus the size specific impact energy (x.E) of each sample. All of the particles were dropped from a constant height, so the variation in the impact energy is only due to variations in particle mass. The new cracks (as well as any pre-existing cracks that were clearly longer or wider than before impact) formed during impact were determined by counting the cracks in slices from two orthogonal directions perpendicular to the impact surface. The number of cracks present in the pre-impact tomogram was subtracted from the number of cracks present in the post-impact tomogram to determine the number of new cracks formed.

Figure 7.9 shows that, for the same size specific impact energy (x.E) range (100-125 mm.J.kg^{-1}) and similar size, indicated by the vertical dashed lines in Figure 7.9, the particles impacted with the force applied along the bedding plane formed more new cracks than the particles impacted with the applied across the bedding plane. The linear trends for the perpendicularly- and parallelly-impacted particles are included in Figure 7.9, and shows a slight increase in the number of new cracks formed with increasing energy for the perpendicularly impacted particles; whilst the particles impacted with their bedding planes parallel to the impact surface showed no significant change over the range of impact energies tested.

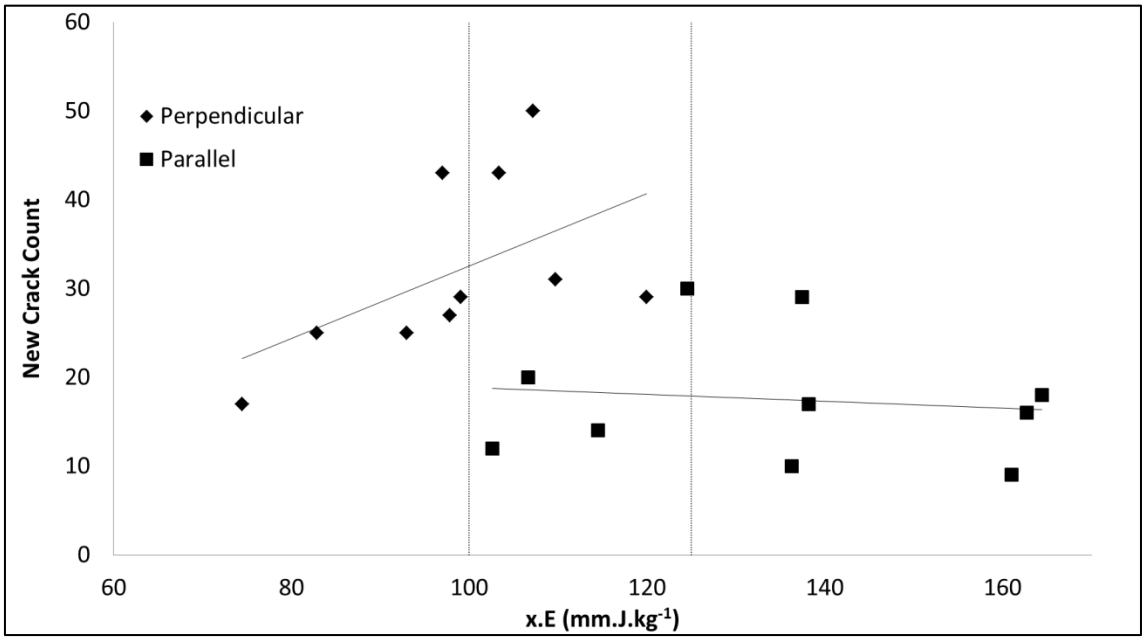

Figure 7.9: New crack count vs. impact energy (x.E)

The surface area per unit volume (given in Equation 7.4) was determined using the VGStudio 2.1 visualization package. In VGStudio a surface determination was done on each tomogram both before and after impact. From the surface determination the closed surface area and volume of the particles could be determined.

$$SSA = \frac{SA}{V} \qquad \text{Equation 7.4}$$

where *SSA* (M^{-1}) is the surface area per unit volume; *SA* (M^2) is the total exposed surface area of all particles in the sample and *V* is the total volume (M^3) of all particles in the sample. The surface area ratio is the ratio of the surface area per unit volume after impact and before impact. A surface area ratio of, for example, 1.5 would indicate that the surface area per unit

volume of the particle increased by 50% during impact. Figure 7.10 shows the relationship between the surface area ratio and the impact energy.

From Figure 7.10 it can be seen that, except for the outlier[†] at [102.6; 2.3], for the same impact energy range (100-125 mm.J.kg^{-1}) between the vertical, dotted lines), the perpendicularly impacted samples generated more specific surface area during impact than the samples that were impacted with their bedding plane parallel to the impact surface. The linear trends for the perpendicularly- and parallelly-impacted particles are included in Figure 7.10 and indicate that an increase in the impact energy will increase the specific surface area for both the perpendicularly- and parallelly-impacted particles.

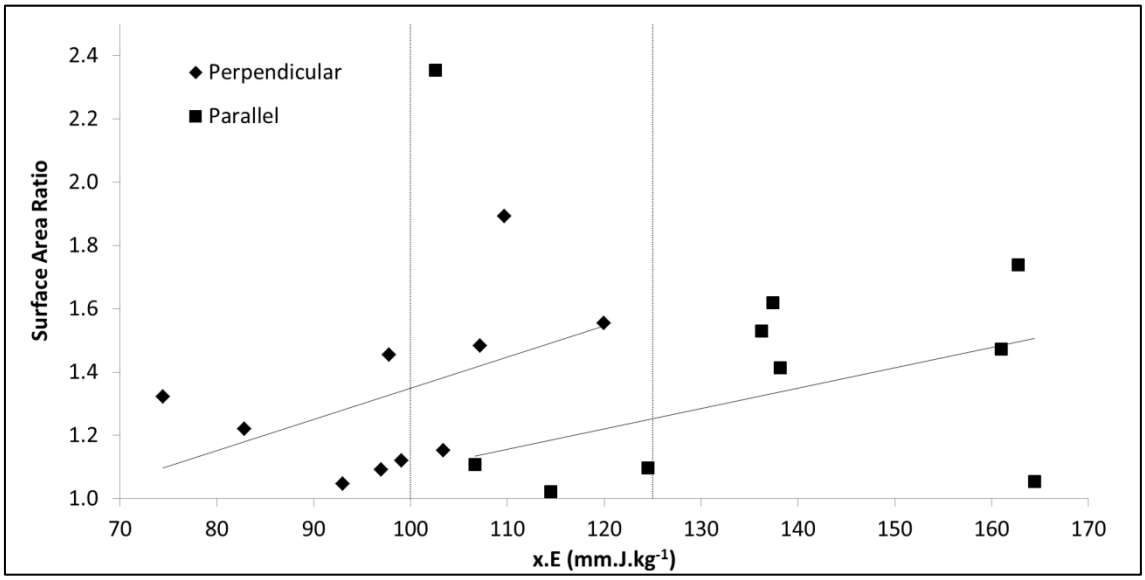

Figure 7.10: Impact energy (x.E) vs. specific surface area ratio

Figure 7.11 shows the average number of new cracks formed in the top, centre, and bottom layers for all particles during impact, where the top layer was the furthest away from the impact surface during impact and the bottom layer was the impacted surface. The averages for all of the particles impacted with their bedding plane parallel to the impact surface are shown on the upper half of Figure 7.11, whilst the averages for all of the particles impacted with their bedding planes perpendicular to the impact surface are shown on the lower half of Figure 7.11.

[†]The outlier is due to a large mineral inclusion present in the particle. This inclusion greatly affected the quality of the tomogram, reducing the dynamic range of the tomogram and introducing serious beam hardening- and edge artefacts. The errors caused by the inclusion justify the exclusion of the particle from the observation above.

From Figure 7.11 it can be seen that for the particles impacted with their bedding plane perpendicular to the impact surface there was a gradual decrease in the number of new cracks formed from bottom to top, whilst the samples impacted with their bedding planes parallel to the impact surface shows a large number of crack formed in the bottom slice when compared to the top and centre slices.

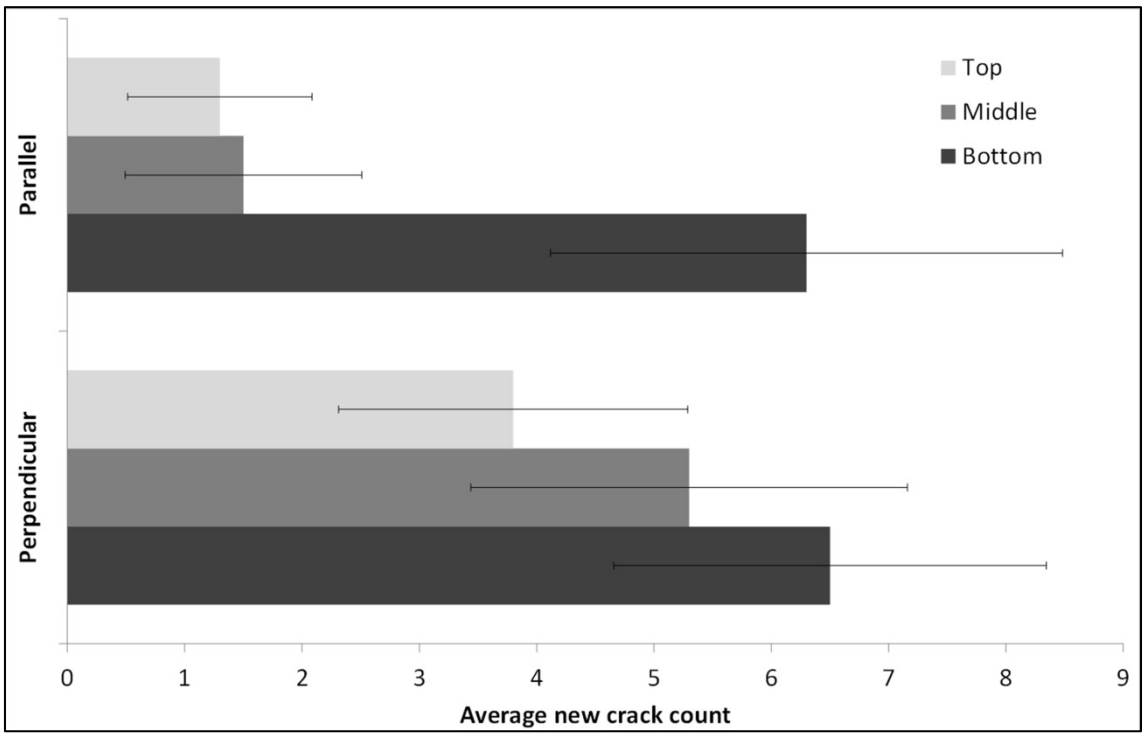

Figure 7.11: Average crack distribution in the top, centre and bottom of the samples impacted perpendicular and parallel to the bedding plane

It is postulated that the bedding plane either aid, or hinder, the propagation of cracks through the particle, depending on the orientation of the bedding plane in relation to the impact surface. Where the bedding plane is parallel to the impact surface, the boundaries between the different layers hinder crack propagation; where the bedding plane is perpendicular to the impact surface crack propagation is aided. In other words: those features that act as discontinuities in the parallelly impacted particles, aid the propagation of the cracks in the perpendicularly impacted particles. This may be a possible explanation why the number of new cracks formed in Figure 7.9 increases with an increase in energy for the perpendicularly impacted particles, while remaining unchanged for the parallelly impacted particles. Figure 7.12 shows a comparison between two samples, one impacted parallel (left) to the bedding plane and the other perpendicular (right) to the bedding plane. For the perpendicularly impacted samples the cracks propagated much more than for the samples impacted parallel

to the bedding plane, where the majority of the propagating cracks terminated in lithotype boundaries or in pre-existing cracks.

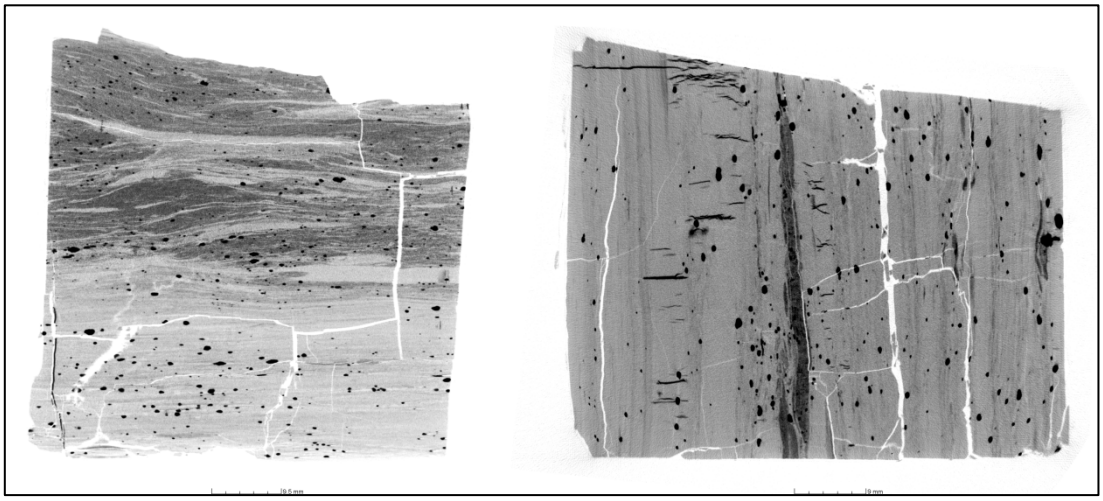

Figure 7.12: Comparison of crack propagation through the height of a particle impacted perpendicularly (right) and parallelly (left) to the impact surface

After the twenty particles were impacted and the post-impact tomograms generated the HDPE cling-film was removed and a sieve size analysis done to determine the resulting PSD of each impacted particle. Figure 7.13 shows the spread of the particle size distributions (PSD) for all of the particles that were impacted with their bedding plane parallel (Figure 7.13a), and perpendicular (Figure 7.13b), to their bedding planes. The shaded areas in Figure 7.13 show how widely the data generated for the PSD is distributed. The individual PSDs of all of the particles impacted in a specific orientation were combined on a mass basis to yield the PSD of the populations impacted parallel and perpendicular to the bedding plane. These distributions are shown as solid lines on the figure (Parallel RR in Figure 7.13a; Perpendicular RR in Figure 7.13b).

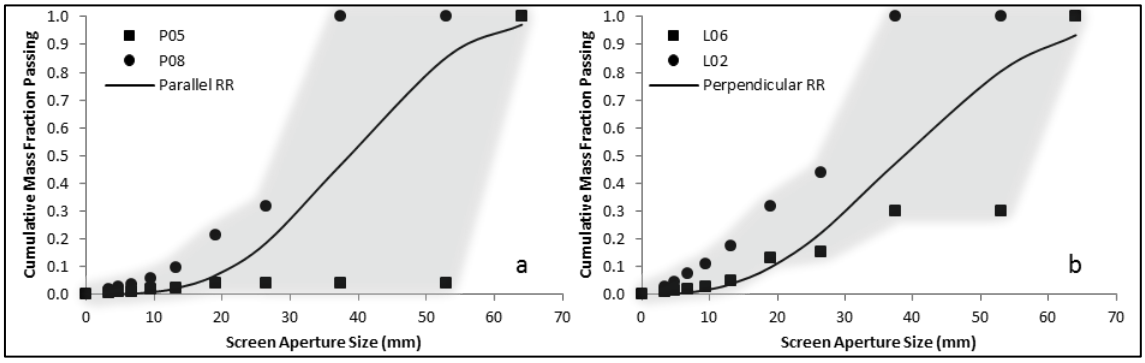

Figure 7.13: PSD comparison of the perpendicularly and parallelly impacted particles including the most extreme PSDs of individual particles for each orientation (P05, P08, L06, and L02)

The data of the combined PSDs were fitted to a Rosin-Rammler distribution and Figure 7.14 shows the comparison of the two distributions on a single figure; from Figure 7.14 it is clear that there is very little difference between the combined distributions for the different orientations. The d^* values for the Perpendicular RR and Parallel RR is 44.2 mm and 43.2 mm respectively, and the values for the distribution parameters (n) 2.7 and 3.2 respectively (See Equation 7.1).

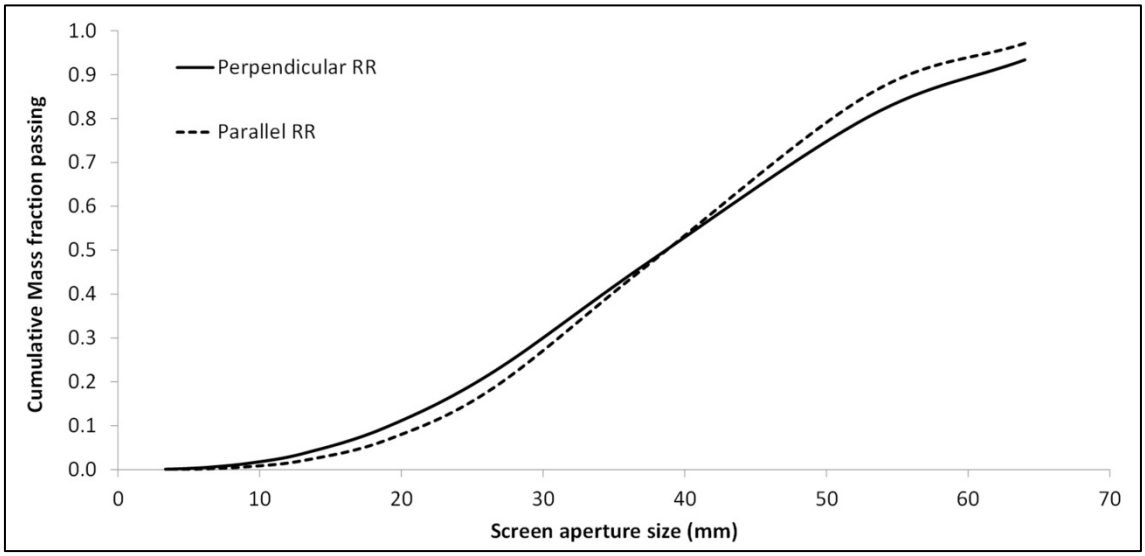

Figure 7.14: Comparison of the Rosin-Rammler models for the perpendicularly and parallelly impacted populations

Conclusions

The aim of this study was to determine the influence coal bedding plane orientation, pre-existing cracks, microlithotype boundaries as well as mineral boundaries has on the breakage characteristics of single coal particles during impact at low impact energies. A number of cubic coal particles were prepared and dropped from a height equivalent to 1 m onto a steel impact anvil. The particle size distributions of the products were determined and the changes to the internal structure were characterised using micro-focus computed tomography. This analysis showed that newly formed cracks either initiated or terminated at the pre-existing cracks, microlithotype boundaries, and mineral boundaries. Cracks also propagated along the microlithotype and mineral boundaries. The orientation of the coal bedding planes influenced the propagation of cracks vertically through the impacted particles, with the cracks propagating deeper into particles that were impacted with their bedding plane perpendicular to the impact surface when compared to the particles impacted with their bedding plane parallel to the impact surface; although neither the individual particles' PSD, nor the average PSD reflect this. This may be due to the fact that even though the development of new cracks can be observed in the tomograms, it does not necessarily mean that the cracks were fatal (caused the parent particle to break). Additionally it was found that, although all of the structures do influence the breakage characteristics of the coal, the contributions of the structures to an individual particle cannot be predicted yet. The aggregate contribution of all of the individual features can, however, be fitted using a Rosin-Rammler distribution; for the specific coal used during this study the size distribution parameters for the impacted particles was determined as $n = 2.97$ and $d^* = 43.66$ mm.

Chapter 7 - References

11. Teo, C., Waters, A. & Nicol, S. 1990. Quantification of the breakage of lump materials during handling operations. *International journal of mineral processing*, 30(3):159-184.

13. Sahoo, R.K. & Roach, D. 2005. Effect of different types of impact surface on coal degradation. *Chemical engineering and processing*, 44(2):253-261.

14. Menacho, J.M. 1986. Some solutions for the kinetics of combined fracture and abrasion breakage. *Powder technology*, 49(1):87-95.

15. Sahoo, R. 2007. Degradation characteristics of steel making materials during handling. *Powder technology*, 176(2):77-87.

16. Tavares, L.M. & de Carvalho, R.M. 2011. Modeling ore degradation during handling using continuum damage mechanics. *International journal of mineral processing*, 101(1–4):21-27.

17. Esterle, J., Kolatschek, Y. & O'Brien, G. 2002. Relationship between in situ coal stratigraphy and particle size and composition after breakage in bituminous coals. *International journal of coal geology*, 49(2):195-214.

18. Sahoo, R. & Roach, D. 2005. Degradation behaviour of weathered coal during handling for the COREX process of iron making. *Powder technology*, 152(1–3):1-8.

20. Sahoo, R. & Roach, D. 2005. Quantification of the lump coal breakage during handling operation at the gladstone port. *Chemical engineering and processing*, 44(7):797-804.

21. Sahoo, R., Weedon, D. & Roach, D. 2004. Degradation model of Gladstone Port Authority's coal using a twin-pendulum apparatus. *Advanced powder technology*, 15(4):459-475.

23. Sahoo, R. 2006. An investigation of single particle breakage tests for coal handling system of the gladstone port: a review. *Powder technology*, 161(2):158-167.

26. Chandramohan, R., Holtham, P.N. & Powell, M. 2010. The influence of particle shape in rock fracture. (*In* XXV International Mineral Processing Congress 2010 organised by Australasian Institute of Mining and Metallurgy, Brisbane: The Australasian Institute of Mining and Metallurgy. p. 3163-3171).

27. Shi, F. & Kojovic, T. 2007. Validation of a model for impact breakage incorporating particle size effect. *International journal of mineral processing*, 82(3):156-163.

37. Le Roux, M., Campbell, Q., Watermeyer, M. & de Oliveira, S. 2005. The optimization of an improved method of fine coal dewatering. *Minerals engineering*, 18(9):931-934.

46. Powell, M.S. & Morrison, R.D. 2007. The future of comminution modelling. *International journal of mineral processing*, 84(1–4):228-239.

47. Tavares, L. & King, R. 1998. Single-particle fracture under impact loading. *International journal of mineral processing*, 54(1):1-28.

48. Özer, C.E. & Whiten, W.J. 2012. A multi-component appearance function for the breakage of coal. *International journal of mineral processing*, 104-105:37-44.

50. Vogel, L. & Peukert, W. 2003. Breakage behaviour of different materials—construction of a mastercurve for the breakage probability. *Powder technology*, 129(1):101-110.

51. Kelly, E.G. & Spottiswood, D.J. 1982. Introduction to mineral processing. New York: John Wiley.

60. Austin, L.G. 2002. A treatment of impact breakage of particles. *Powder technology*, 126(1):85-90.

67. Viljoen, J., Campbell, Q.P., le Roux, M. & De Beer, F. 2015. An analysis of the slow compression breakage of coal using microfocus X-ray computed tomography. *International journal of coal preparation and utilization*, 35(1):1-13.

68. Campbell, Q.P. & Viljoen, J. 2011. Single particle impact breakage of coal. (*In* Morsi, B., *ed*. 28th Annual International Pittsburgh Coal Conference organised by University of Pittsburgh, S.S.o.E., Pittsburgh, PA: International Pittsburgh Coal Conference. p. 1-16).

74. Falcon, R.M. & Snyman, C. 1986. An introduction to coal petrography: atlas of petrographic constituents in the bituminous coals of South Africa. Johannesburg: Geological Society of South Africa.

83. Genc, O., Ergun, L. & Benzer, H. 2004. Single particle impact breakage characterization of materials by drop weight testing. *Fizykochemiczne problemy mineralurgii*, 38:241-255.

89. Vogel, L. & Peukert, W. 2004. Determination of material properties relevant to grinding by practicable labscale milling tests. *International journal of mineral processing*, 74:S329-S338.

100. Buzug, T.M. 2008. Computed tomography: from photon statistics to modern cone-beam CT. Berlin: Springer.

101. SABS. 2005. Non-destructive testing - radiation methods - computed tomography. Pretoria: South African Bereau of Standards (SABS).(South African National Standard (SANS) 15708-1:2005).

102. Hoffman, J.W. & De Beer, F. 2012. Characteristics of the Micro-Focus X-ray Tomography Facility (MIXRAD) at Necsa in South Africa. (*In* 18th World Conference on Nondestructive Testing, Durban: South African Institute for Non-Destructive Testing. p. 1-12).

103. Van Geet, M., Swennen, R. & David, P. 2001. Quantitative coal characterisation by means of microfocus X-ray computer tomography, colour image analysis and back-scattered scanning electron microscopy. *International journal of coal geology*, 46(1):11-25.

104. Simons, F.J., Verhelst, F. & Swennen, R. 1997. Quantitative characterization of coal by means of microfocal X-ray computed microtomography (CMT) and color image analysis (CIA). *International journal of coal geology*, 34(1–2):69-88.

107. Duliu, O.G. 1999. Computer axial tomography in geosciences: an overview. *Earth-science reviews*, 48(4):265-281.

112. Feldkamp, L.A., Davis, L.C. & Kress, J.W. 1984. Practical cone-beam algorithm. *Journal of the Optical Society of America*, 1(6):612-619.

126. Ketcham, R.A. & Carlson, W.D. 2001. Acquisition, optimization and interpretation of X-ray computed tomographic imagery: applications to the geosciences. *Computers & geosciences*, 27(4):381-400.

155. Pinheiro, H. 1999. A techno-economic and historical review of the South African coal Industry in the 19th and 20th centuries and analysis of coal product samples of South African Collieries 1998-1999. *(In* Bulletin 113. Pretoria: South African Bereau of Standards (SABS). p. 1-97).

Chapter 7 - Additional notes

In Chapter 7 it was shown that the features present in coal can influence the final crack network in one of four ways:

- The feature remains unchanged.
- A new crack can initiate at any feature.
- A new crack can terminate at any feature.
- A new crack can propagate along any feature.

Additionally, it was shown that the bedding plane orientation of a particle in relation to the impact surface influences the degradation of the particles: particles that impact with their bedding planes perpendicular to the impact surface (force applied along the bedding plane) generated more fines, more specific surface area, and new cracks propagate further into the particles. When particles impact with their bedding planes parallel to the impact surface (force applied across the bedding plane) new cracks do not propagate into the particle as far (see Figure 7.12). This was assumed to be due to the fact that the boundaries between microlithotypes can act to either halt the propagation of a crack, or the crack can propagate along the boundaries. If the bedding planes (and the boundaries between the layers) are perpendicular to the impact surface, the cracks propagate along the boundaries further into the particle, whereas if the bedding planes are parallel to the impact surface the boundaries between the layers prevent the cracks from propagating further into the particle.

In addition to the influence of the bedding plane orientation on the specific surface area, an increase in the impact energy also increased the specific surface area. It is however unclear if the dependence is due to impact energy, particle size, both impact energy and particle size, or some other property not considered during this study. Expanding the range of particle sizes and impact energies tested will enable future researchers to determine the dependence on either influence.

Although it was possible to fit the progeny PSD of a population of Waterberg coal particles, subjected to impact breakage, using a Rosin-Rammler distribution, the progeny PSD of a single particle could not be predicted. Every individual particle contains a large number of features that has the potential to contribute to the degradation of that particle, but only a relatively small number of these features actually contribute to that particle's degradation. During this study there was no indication what caused a specific feature to "activate" and contribute to the final crack network and progeny PSD. In order to accurately predict the progeny PSD of a single particle, whether or not a feature will contribute to particle

degradation, and the effect of that feature to particle degradation, needs to be accurately modelled.

The particle masses used to determine the particle size distributions of the impacted particles were indeed far less than that prescribed by the SABS.[156] Due to the fact that the study's focus is on single particles, however, all of the PSD results had to be generated from the single particles. Because a standard procedure could not be used to determine the PSDs all possible efforts were made to ensure that the PSD results are as accurate as possible and no secondary breakage occurred.

In the comparisons of the tomograms generated before and after impact (Figure 7.4, Figure 7.5, Figure 7.6, Figure 7.7, and Figure 7.8) it can be seen that there is a difference in the quality of the tomograms generated before and after impact. Although every effort was made to ensure that this dissimilarity in quality did not affect the data presented in the paper, it did complicate the analysis and comparison of the tomograms. The difference in quality was due to the setup of the tomograph used during the study being changed between the generation of the tomograms before impact and the generation of the tomograms after impact; specifically, the tungsten target in the X-ray tube was replaced. This resulted in an average improvement of 10% to all the resolutions obtained after impact compared to the resolutions obtained before impact.

Chapter 7 – Additional notes references

156. SABS. 1994. Hard coal - size analysis by sieving. Pretoria: Standards South Africa.(South African National Standard (SANS) 1953:1994).

Chapter 8 - Conclusions

In Chapter 2 through to Chapter 7 coal degradation and the influence of a coal particle's physical structures on its degradation was explored. Chapter 8 assimilates the conclusions drawn in the various chapters, suggests possible improvements to the experimental setups used, recommends possible directions for future research, and provides the contribution of this thesis to the study of coal degradation and the study of coal degradation using micro-focus X-ray computed tomography.

General conclusions

The overall aims of the thesis, as given in Chapter 1 (page 4), are to determine the effect that particle shape, coal microstructure, and bedding plane orientation has on the degradation characteristics of coal. A series of two review manuscripts, one peer-reviewed conference paper, two papers published in peer-reviewed journals, and one paper submitted for publication in a peer-reviewed journal are presented. From these publications the following conclusions were drawn:

- In Chapter 2 it was shown that various factors influence the degradation of coal including particle size, particle composition, weathering, and the impact surface. A particle's shape and the orientation with which it impacts also influences the degradation but very little research has been published on their influence on the degradation of South African coal.

- In Chapter 3 it was shown that the shape and the impact orientation of a single particle will influence the degradation characteristics of the particle. Slab-like particles (particles where one of the three orthogonal dimensions is significantly smaller than the other two) that impacted with a large contact area showed the highest production of fines, whilst blocky/cubic particles (particles where all three orthogonal dimensions are similar) that impacted onto an edge or a protrusion showed the least amount of fines production. This is due to the protrusion disintegrating and dissipating the energy imparted to the particle and preventing the rest of the particle from degrading.

- In Chapter 2 the t_{10} degradation model (JKMRC breakage model that allows for particle top size to be incorporated) was identified as a possible method to model coal degradation, and to predict the progeny particle size distribution after degradation. The data presented in Chapter 3, however, did not fit the t_{10} degradation model well and a simplified relation was proposed to predict the degradation of the specific South African Highveld coal used in this study. The reason the t_{10} degradation model could not accurately predict the degradation of coal is that coal is a brittle and bimodal rock type; and the t_{10} model cannot be applied to model the degradation of these ore types. The simplified relation used the t_{10} model as starting point and assumes that the low energy degradation of coal happens in the linear section of the model. Even though the t_{10} model could not predict the degradation of the coal used

in this study, the definition of t_{10} (see Chapter 2, Page 29) remains a convenient way to report the degradation of a particle as a single number.

- Chapter 4 introduces micro-focus X-ray computed tomography (µCT) and discusses its history, the process, the physics that govern the process, and the applications of µCT in the geosciences and coal science. Chapter 4 shows that µCT is a technology that is uniquely suited to identify the microstructures in coal that influence the degradation of coal, as well as possibly track the changes that occurs in and around these microstructures during degradation, although very few studies applied µCT to coal breakage, moreover no studies were found that applied µCT to coal degradation.

- The ability of µCT to identify the microstructure in coal was confirmed for slow compression breakage in Chapter 5 and, additionally, for impact breakage and thermal shock in Chapter 6. The microstructures that influenced the degradation of coal, and which can be identified and tracked using µCT are: pre-existing cracks and cleats, boundaries between coal microlithotypes and mineral inclusions, as well as the boundaries between coal microlithotypes of varying densities. In Chapter 5, Chapter 6, and Chapter 7 µCT is used to track the changes that occur in and around these microstructures.

- The microstructures present in coal influence the degradation of coal in one of four possible ways:
    - Either the features remain unchanged and do not contribute to the final crack network,
    - the features act as an initiation site for a new crack,
    - the features act to aid the propagation of a crack though the particle,
    - or the features act to terminate the propagation of a crack.

  Other than conjecture, it is impossible to determine whether a specific feature was an initiation point or a termination point for a new cracks using µCT.

- Chapter 5, Chapter 6, and Chapter 7 shows that, of all of the microstructures present in a coal particle, the pre-existing cracks and cleats shows the biggest influence on the final crack network.

- In Chapter 5 and Chapter 6 it was shown that heterogeneous coal particles compressed parallel to the bedding plane (the compressive force applied along the bedding plane) show the highest production of fines, while homogeneous particles compressed perpendicular to the bedding planes (the compressive force applied across the bedding plane) show the least fines production. A possible answer for this phenomenon was found in Chapter 7, where it was shown that the boundaries between the coal macerals could act to aid crack propagation if the applied force was along the bedding plane, but could also halt crack propagation if the force was applied across the bedding plane.

- When a particle is impacted with its bedding plane perpendicular to the impact surface (the force applied along the bedding plane) more degradation products are formed compared to particles impacted with the bedding plane parallel to the impact surface (the force applied across the bedding plane).

- In Chapter 7, analysis of the tomograms showed that the orientation of the particle bedding plane in relation to the impact surface influenced crack propagation within the particle. When a particle is impacted with the force applied along the bedding plane, cracks that propagate through the particle propagate along the boundaries between the microlithotypes; when a particle is impacted with the force applied across the bedding plane however, the propagating cracks terminate at the boundaries between microlithotypes. This resulted in more of the propagating cracks terminating closer to the top of the particle (further away from the impacted surface) if the particle is impacted with its bedding plane perpendicular to the impact surface, compared to a particle impacted with its bedding plane parallel to the impact surface.

- Lower density (vitrinite rich) microlithotypes shows a propensity towards higher fines production (as discussed in Chapter 5, Chapter 6, and Chapter 7), compared to the higher density microlithotypes.

- Although every particle has a large number of features that can possibly contribute to the degradation of coal, in this thesis no way of predicting whether a feature will activate and contribute to the final crack network of a particle could be established.

- Due to the many factors that influence the degradation of coal, and the fact that it is not possible to predict if a feature will contribute to the degradation of that particle, it is not currently possible to predict the progeny particle size distribution when a single particle degrades. The degraded particle size distribution of a population of particles, however, fits a Rosin-Rammler distribution function (Chapter 7).

Revised hypothesis

Taking into account the conclusions drawn above the hypothesis, given on page 6, can be improved and restated as follows:

> The shape of a coal particle, the orientation of a coal particle relative to the impact surface, the orientation of the coal particle's bedding plane relative to the applied force, and the microstructure (pre-existing cracks and cleats, boundaries between coal microlithotypes of varying density, and the boundaries between coal microlithotypes and mineral inclusions) of a loaded coal particle will all influence the breakage and degradation of the coal particle. If it can be predicted which of the features present in a coal particle will contribute to the degradation of that coal particle, and what the influence of those features are, the progeny size distribution of a single coal particle can be predicted; but the t_{10} degradation model cannot be used because the it is not applicable to heterogeneous and bimodal rock types such as the Highveld coal used in this study.

Thesis contribution

This thesis contributed the following to the study of coal degradation:

- The combined effect of a coal particle's shape and the orientation of the coal particle in the moments before impact on the degradation characteristics was shown, and a possible explanation for this influence given.

- Micro-focus X-ray computed tomography was successfully applied to identify and track the changes that occur around a number of the microstructures present in a coal particle subjected to single particle impact breakage.

- It was shown that the orientation of a coal particle's bedding plane relative to the impact surface (applied force) influences the distance that a propagating crack will travel in a particle. If the applied force is along the bedding plane the cracks travel along the boundaries separating different microlithotypes, while cracks are arrested at these boundaries if the applied force is cross the bedding planes; this results in cracks propagating for longer distances when the force is applied along the bedding plane.

Future research

To reliably predict the breakage of a single coal particle it is necessary to not only determine which microstructures contribute to coal degradation, and what the relative contributions are (this thesis addressed only those microstructures that could be observed using µCT). It will also be necessary to determine what causes a specific feature to contribute, predict when a feature will contribute, and what the relative contributions will be to the degradation of a single coal particle. In order to accomplish this, coal degradation research will benefit should future studies focus on determining:

- It is clear that the boundaries between the higher density microlithotypes and lower density microlithotypes contribute to the degradation and breakage of single coal particles. If this effect can be further elucidated and applied to coal comminution, high quality coal can be effectively liberated from lower quality coal using selective comminution.

- It is necessary to determine what causes a specific feature that is present in a coal particle to contribute to the degradation of a coal particle. This will allow modelling a single coal particle's breakage based on its microstructure. These models can then be applied to improve the comminution of coal, and also to reduce the degradation of coal by making changes to the processes used to beneficiate coal.

- The experiments in this thesis should be repeated using technology that will allow smaller resolutions to be achieved. There are many features which exist in coal, such as the porosity, that could not be observed using micro-focus X-ray computed tomography; these features may also contribute to the breakage and degradation characteristics of coal, but because these features could not be observed, their influence on coal degradation could not be determined.

- The experiments in this thesis should be repeated for different coal types and mines to determine whether the conclusions drawn here is true for all coal types.

- All of the experiments done for this study were conducted on single coal particles. The experiments should be extended to include particle

populations. Extending the study to particle populations should result in more statistically representative data and result in industrially applicable results.

- The assumption that the high density polyethylene cling wrap did not influence the breakage of the coal, nor influenced the tomogram quality of the scanned particles should be tested.

- Although every effort was made and care was taken to prevent breakage during the sieve size analyses, it is possible that the amount of fines produced during these analyses could influence the results obtained. During future experiments an alternative method to analyse the particle size distribution, that will ensure no secondary breakage occur, should be sought.

Thesis references

1. Chaline, E. 2012. Fifty minerals that changed the course of history. Cape Town: Struik Nature.

2. Osborne, D., *ed*. 2013. The Coal Handbook: towards cleaner production. Vol. 1: coal production. Cambridge: Woodhead. (Woodhead Publishing Series in Energy).

3. Höök, M. & Aleklett, K. 2010. A review on coal-to-liquid fuels and its coal consumption. *International journal of energy research*, 34(10):848-864.

4. Jeffrey, L. 2005. Characterization of the coal resources of South Africa. *Journal of the South African Institute of Mining and Metallurgy*, 105(2):95-102.

5. Mohale, S., Masetlana, T.R., Bonga, M., Ikaneng, M., Dlambula, N., Malebo, L. & Mwape, P. Department of Mineral Resources. 2015. South Africa's mineral industry 2013-2014. Pretoria.

6. Ansolabehere, S., Beer, J., Deutch, J., Ellerman, A., Friedmann, S., Herzog, H., Jacoby, H., Joskow, P., Mcrae, G. & Lester, R., *eds*. 2007. The future of coal: options for a carbon-constrained world. Cambridge, MA: Massachusetts Intitute of Technology.

7. Hancox, P.J. & Götz, A.E. 2014. South Africa's coalfields: a 2014 perspective. *International journal of coal geology*, 132:170-254.

8. Scholtz, J., Du Plessis, K., Roche, R., Cresswell, M., Toerien, L., Voges, J., Reddy, D., De Korte, J., Craddock, M., Lok, G., McMillan, K., Buthelezi, V., Darley, P., Jacobs, J., Campbell, Q.P. & Jacobs, J., *eds*. 2015. Coal preparation in Southern Africa. 5th ed. Witbank: Southern African Coal Processing Society.

9. SABS. 2004. South African guide to the systematic evaluation of coal resources and coal reserves. Pretoria: Standards South Africa.(South African National Standard (SANS) 10320:2004).

10. Anon. Department of Energy. 2001. National inventory discard and duff coal. Pretoria.

11. Teo, C., Waters, A. & Nicol, S. 1990. Quantification of the breakage of lump materials during handling operations. *International journal of mineral processing*, 30(3):159-184.

12. Tao, D., Groppo, J.G. & Parekh, B.K. 2000. Enhanced ultrafine coal dewatering using flocculation filtration processes. *Minerals engineering*, 13(2):163-171.

13. Sahoo, R.K. & Roach, D. 2005. Effect of different types of impact surface on coal degradation. *Chemical engineering and processing*, 44(2):253-261.

14. Menacho, J.M. 1986. Some solutions for the kinetics of combined fracture and abrasion breakage. *Powder technology*, 49(1):87-95.

15. Sahoo, R. 2007. Degradation characteristics of steel making materials during handling. *Powder technology*, 176(2):77-87.

16. Tavares, L.M. & de Carvalho, R.M. 2011. Modeling ore degradation during handling using continuum damage mechanics. *International journal of mineral processing*, 101(1–4):21-27.

17. Esterle, J., Kolatschek, Y. & O'Brien, G. 2002. Relationship between in situ coal stratigraphy and particle size and composition after breakage in bituminous coals. *International journal of coal geology*, 49(2):195-214.

18. Sahoo, R. & Roach, D. 2005. Degradation behaviour of weathered coal during handling for the COREX process of iron making. *Powder technology*, 152(1–3):1-8.

19. Sahoo, R., Weedon, D. & Roach, D. 2004. Single-particle breakage tests of Gladstone Port Authority's coal by a twin pendulum apparatus. *Advanced powder technology*, 15(2):263-280.

20. Sahoo, R. & Roach, D. 2005. Quantification of the lump coal breakage during handling operation at the gladstone port. *Chemical engineering and processing*, 44(7):797-804.

21. Sahoo, R., Weedon, D. & Roach, D. 2004. Degradation model of Gladstone Port Authority's coal using a twin-pendulum apparatus. *Advanced powder technology*, 15(4):459-475.

22. Broadbent, S. & Calcott, T. 1957. Coal breakage processes: the analysis of a coal transport system. *Journal of the institute of fuel*, 1957(30):13-25.

23. Sahoo, R. 2006. An investigation of single particle breakage tests for coal handling system of the gladstone port: a review. *Powder technology*, 161(2):158-167.

24. Esterle, J., O'Brien, G. & Kojovic, T. 1994. Influence of coal texture and rank on breakage energy and resulting size distributions in Australian coals. (*In* 6th Australian Coal Science Conference, Newcastle, NSW: Australian Institute of Energy. p. 175-181).

25. Pan, J., Meng, Z., Hou, Q., Ju, Y. & Cao, Y. 2013. Coal strength and Young's modulus related to coal rank, compressional velocity and maceral composition. *Journal of structural geology*, 54:129-135.

26. Chandramohan, R., Holtham, P.N. & Powell, M. 2010. The influence of particle shape in rock fracture. (*In* XXV International Mineral Processing Congress 2010 organised by Australasian Institute of Mining and Metallurgy, Brisbane: The Australasian Institute of Mining and Metallurgy. p. 3163-3171).

27. Shi, F. & Kojovic, T. 2007. Validation of a model for impact breakage incorporating particle size effect. *International journal of mineral processing*, 82(3):156-163.

28. Genç, Ö. & Benzer, A. 2009. Single particle impact breakage characteristics of clinkers related to mineral composition and grindability. *Minerals engineering*, 22(13):1160-1165.

29. Eswaraiah, C., Gupta, A., Nagarajan, R., Rajavel, M. & Nandakumar, K. 2008. Minimization of fines generation in size reduction of coals by impact crusher. *Fuel processing technology*, 89(7):704-714.

30. Bunt, J.R. & Waanders, F.B. 2008. An understanding of lump coal physical property behaviour (density and particle size effects) impacting on a commercial-scale Sasol-Lurgi FBDB gasifier. *Fuel*, 87(13–14):2856-2865.

31. Hlatshwayo, H.L., Pinetown, K.L. & Campbell, Q.P. 2007. Fundamental understanding of the influence of physical properties on the thermal fragmentation of coal. (*In* International Conference on Coal Science and Technology organised by The University of Nottingham, Nottingham).

32. Paprika, M.J., Komatina, M.S., Dakić, D.V. & Nemoda, S.Đ. 2013. Prediction of coal primary fragmentation and char particle size distribution in fluidized bed. *Energy & fuels*, 27(9):5488-5494.

33. van Dyk, J.C. 2001. Development of an alternative laboratory method to determine thermal fragmentation of coal sources during pyrolysis in the gasification process. *Fuel*, 80(2):245-249.

34. Keyser, M.J., Conradie, M., Coertzen, M. & Van Dyk, J.C. 2006. Effect of coal particle size distribution on packed bed pressure drop and gas flow distribution. *Fuel*, 85(10–11):1439-1445.

35. Oberholzer, V. & van der Walt, J. 2009. Investigation of factors influencing the attrition breakage of coal. *Journal of the South African Institute of Mining and Metallurgy*, 109(4):211-216.

36. Le Roux, M. & Campbell, Q. 2003. An investigation into an improved method of fine coal dewatering. *Minerals engineering*, 16(10):999-1003.

37. Le Roux, M., Campbell, Q., Watermeyer, M. & de Oliveira, S. 2005. The optimization of an improved method of fine coal dewatering. *Minerals engineering*, 18(9):931-934.

38. Le Roux, M. 2008. The effect of thermal drying on the mechanical strength of South African coals. *Journal of the South African Institute of Mining and Metallurgy*, 108(12):783-787.

39. Esterle, J., O'Brien, G., Sexty, G., Thornton, D., Kojovic, T., Djordjevic, N., Kolatschek, Y., Firth, B. & Clarkson, C. 1998. Assessing coal fines and their impact on plant performance. (*In* XIII International Coal Preparation Conference, Brisbane. p. 173-182).

40. Dacombe, P., Pourkashanian, M., Williams, A. & Yap, L. 1999. Combustion-induced fragmentation behavior of isolated coal particles. *Fuel*, 78(15):1847-1857.

41. Senneca, O., Allouis, C., Chirone, R. & Russo, S. 2010. Set up of an experimental apparatus for the study of fragmentation of solid fuels upon severe heating. *Experimental thermal and fluid science*, 34(3):366-372.

42. Senneca, O., Russo, S. & Chirone, R. 2009. Primary fragmentation of coal particles at high heating rate. *Chemical engineering transactions*, 18:569-574.

43. Senneca, O., Urciuolo, M. & Chirone, R. 2013. A semidetailed model of primary fragmentation of coal. *Fuel*, 104:253-261.

44. Senneca, O., Urciuolo, M., Chirone, R. & Cumbo, D. 2011. An experimental study of fragmentation of coals during fast pyrolysis at high temperature and pressure. *Fuel*, 90(9):2931-2938.

45. Zhang, H., Cen, K., Yan, J. & Ni, M. 2002. The fragmentation of coal particles during the coal combustion in a fluidized bed. *Fuel*, 81(14):1835-1840.

46. Powell, M.S. & Morrison, R.D. 2007. The future of comminution modelling. *International journal of mineral processing*, 84(1–4):228-239.

47. Tavares, L. & King, R. 1998. Single-particle fracture under impact loading. *International journal of mineral processing*, 54(1):1-28.

48. Özer, C.E. & Whiten, W.J. 2012. A multi-component appearance function for the breakage of coal. *International journal of mineral processing*, 104-105:37-44.

49. Han, T., Kalman, H. & Levy, A. 2003. Theoretical and experimental study of multi-compression particle breakage. *Advanced powder technology*, 14(5):605-620.

50. Vogel, L. & Peukert, W. 2003. Breakage behaviour of different materials—construction of a mastercurve for the breakage probability. *Powder technology*, 129(1):101-110.

51. Kelly, E.G. & Spottiswood, D.J. 1982. Introduction to mineral processing. New York: John Wiley.

52. Wills, B.A. & Napier-Munn, T. 2006. Wills' mineral processing technology: an introduction to the practical aspects of ore treatment and mineral recovery. 7th ed. Oxford: Elsevier.

53. Wang, E.Z. & Shrive, N.G. 1995. Brittle fracture in compression: mechanisms, models and criteria. *Engineering fracture mechanics*, 52(6):1107-1126.

54. Lindqvist, J.E., Åkesson, U. & Malaga, K. 2007. Microstructure and functional properties of rock materials. *Materials characterization*, 58(11–12):1183-1188.

55. Inglis, C. 1913. Stresses in a cracked plate due to the presence of cracks and sharp corners. *Transaction of Naval Architects*, 60:213.

56. Fischer-Cripps, A.C. 2007. Introduction to contact mechanics. 2nd ed. New York, NY: Springer. (Mechanical Engineering Series).

57. Gilvarry, J. 1961. Fracture of brittle solids: distribution function for fragment size in single fracture (theoretical). *Journal of applied physics*, 32(3):391-399.

58. Bruchmüller, J., van Wachem, B.G.M., Gu, S. & Luo, K.H. 2011. Modelling discrete fragmentation of brittle particles. *Powder technology*, 208(3):731-739.

59. Meier, M., John, E., Wieckhusen, D., Wirth, W. & Peukert, W. 2009. Generally applicable breakage functions derived from single particle comminution data. *Powder technology*, 194(1–2):33-41.

60. Austin, L.G. 2002. A treatment of impact breakage of particles. *Powder technology*, 126(1):85-90.

61. Zhong, S., Baitalow, F., Nikrityuk, P., Gutte, H. & Meyer, B. 2014. The effect of particle size on the strength parameters of German brown coal and its chars. *Fuel*, 125:200-205.

62. Shi, F. 2014. Coal breakage characterisation: part 2: multi-component breakage modelling. *Fuel*, 117:1156-1162.

63. Shi, F. & Zuo, W. 2014. Coal breakage characterisation: part 1: breakage testing with the JKFBC. *Fuel*, 117:1148-1155.

64. Poulsen, B.A. & Adhikary, D.P. 2013. A numerical study of the scale effect in coal strength. *International journal of rock mechanics and mining sciences*, 63:62-71.

65. Oka, Y. & Majima, H. 1970. A theory of size reduction involving fracture mechanics. *Canadian metallurgical quarterly*, 9(2):429-439.

66. Scholtès, L., Donzé, F.-V. & Khanal, M. 2011. Scale effects on strength of geomaterials, case study: coal. *Journal of the mechanics and physics of solids*, 59(5):1131-1146.

67. Viljoen, J., Campbell, Q.P., le Roux, M. & De Beer, F. 2015. An analysis of the slow compression breakage of coal using microfocus X-ray computed tomography. *International journal of coal preparation and utilization*, 35(1):1-13.

68. Campbell, Q.P. & Viljoen, J. 2011. Single particle impact breakage of coal. (*In* Morsi, B., *ed*. 28th Annual International Pittsburgh Coal Conference organised by University of Pittsburgh, S.S.o.E., Pittsburgh, PA: International Pittsburgh Coal Conference. p. 1-16).

69. Garcia, D., Lin, C. & Miller, J. 2009. Quantitative analysis of grain boundary fracture in the breakage of single multiphase particles using X-ray microtomography procedures. *Minerals engineering*, 22(3):236-243.

70. Nie, B., He, X., Li, X., Chen, W. & Hu, S. 2014. Meso-structures evolution rules of coal fracture with the computerized tomography scanning method. *Engineering failure analysis*, 41:81-88.

71. Ward, C.R. 2002. Analysis and significance of mineral matter in coal seams. *International journal of coal geology*, 50(1–4):135-168.

72. Man, C.K., Jacobs, J. & Gibbins, J.R. 1998. Selective maceral enrichment during grinding and effect of particle size on coal devolatilisation yields. *Fuel processing technology*, 56(3):215-227.

73. Falcon, R. 2013. Coal petrography. *(In* Osborne, D., *ed.* The coal handbook: towards cleaner production. Woodhead. p. 53-79).

74. Falcon, R.M. & Snyman, C. 1986. An introduction to coal petrography: atlas of petrographic constituents in the bituminous coals of South Africa. Johannesburg: Geological Society of South Africa.

75. Wang, G.X., Wang, Z.T., Rudolph, V., Massarotto, P. & Finley, R.J. 2007. An analytical model of the mechanical properties of bulk coal under confined stress. *Fuel*, 86(12–13):1873-1884.

76. Laubach, S.E., Marrett, R.A., Olson, J.E. & Scott, A.R. 1998. Characteristics and origins of coal cleat: a review. *International journal of coal geology*, 35(1–4):175-207.

77. Klawitter, M., Esterle, J. & Collins, S. 2015. A study of hardness and fracture propagation in coal. *International journal of rock mechanics and mining sciences*, 76:237-242.

78. Tavares, L.M. & das Neves, P.B. 2008. Microstructure of quarry rocks and relationships to particle breakage and crushing. *International journal of mineral processing*, 87(1–2):28-41.

79. Vuthaluru, H.B., Brooke, R.J., Zhang, D.K. & Yan, H.M. 2003. Effects of moisture and coal blending on Hardgrove Grindability Index of Western Australian coal. *Fuel processing technology*, 81(1):67-76.

80. Salman, Russell, A., Aman, S. & Tomas, J. 2015. Breakage probability of granules during repeated loading. *Powder technology*, 269:541-547.

81. Han, T., Petukhov, Y., Levy, A. & Kalman, H. 2006. Theoretical and experimental study of multi-impact breakage of particles. *Advanced powder technology*, 17(2):135-157.

82. Rozenblat, Y., Portnikov, D., Levy, A., Kalman, H., Aman, S. & Tomas, J. 2011. Strength distribution of particles under compression. *Powder technology*, 208(1):215-224.

83. Genc, O., Ergun, L. & Benzer, H. 2004. Single particle impact breakage characterization of materials by drop weight testing. *Fizykochemiczne problemy mineralurgii*, 38:241-255.

84. Bourgeois, F. & Banini, G. 2002. A portable load cell for in-situ ore impact breakage testing. *International journal of mineral processing*, 65(1):31-54.

85. Barrios, G., de Carvalho, R. & Tavares, L. 2011. Extending breakage characterisation to fine sizes by impact on particle beds. *Mineral processing and extractive metallurgy*, 120(1):37-44.

86. Jin, P., Wang, E., Liu, X., Huang, N. & Wang, S. 2013. Damage evolution law of coal-rock under uniaxial compression based on the electromagnetic radiation characteristics. *International journal of mining science and technology*, 23(2):213-219.

87. Salatino, P., Senneca, O. & Masi, S. 1999. Assessment of thermodeactivation during gasification of a bituminous coal char. *Energy & fuels*, 13(6):1154-1159.

88. Vogel, L. & Peukert, W. 2002. Characterisation of grinding-relevant particle properties by inverting a population balance model. *Particle & particle systems characterization*, 19(3):149-157.

89. Vogel, L. & Peukert, W. 2004. Determination of material properties relevant to grinding by practicable labscale milling tests. *International journal of mineral processing*, 74:S329-S338.

90. Aslan, N. & Cebeci, Y. 2007. Application of Box–Behnken design and response surface methodology for modeling of some Turkish coals. *Fuel*, 86(1–2):90-97.

91. Filippa, L., Trento, A. & Álvarez, A.M. 2012. Sauter mean diameter determination for the fine fraction of suspended sediments using a LISST-25X diffractometer. *Measurement*, 45(3):364-368.

92. Foord, D. 2008. The determination of single particle breaking characteristics of different coal samples. Potchefstroom: North-West University. (Mini-dissertation - B.Eng, Unpublished).

93. van der Merwe, W. 2008. Single particle impact-breakage tests on different South African coal sources. Potchefstroom: North-West University. (Mini-dissertation - B.Eng, Unpublished).

94. Button, R. 2007. The determination of single particle breaking characteristics of different coal sample. Potchefstroom: North-West University. (Mini-dissertation - B.Eng, Unpublished).

95. Powell, M., Hilden, M., Ballantyne, G., Liu, L. & Tavares, L.M. 2014. The appropriate and inappropriate application of the JKMRC t_{10} relationship. (*In* Yianatos, J., *ed*. XXVII International Mineral Processing Congress organised by Universidad de Chile, Santiago: Gecamin Digital Publications. p. 133-144).

96. Bushberg, J.T., Seibert, J.A., Leidholdt, E.M., Jr. & Boone, J.M. 2002. The essential physics of medical imaging. 2nd ed. Philadelphia, PA: Lippincott, Williams & Wilkins.

97. Cierniak, R. 2011. X-ray computed tomography in biomedical engineering. London: Springer.

98. Beckmann, E.C. 2006. CT scanning the early days. *The British journal of radiology*, 79(937):5-8.

99. Kruth, J.P., Bartscher, M., Carmignato, S., Schmitt, R., De Chiffre, L. & Weckenmann, A. 2011. Computed tomography for dimensional metrology. *CIRP annals - manufacturing technology*, 60(2):821-842.

100. Buzug, T.M. 2008. Computed tomography: from photon statistics to modern cone-beam CT. Berlin: Springer.

101. SABS. 2005. Non-destructive testing - radiation methods - computed tomography. Pretoria: South African Bereau of Standards (SABS).(South African National Standard (SANS) 15708-1:2005).

102. Hoffman, J.W. & De Beer, F. 2012. Characteristics of the Micro-Focus X-ray Tomography Facility (MIXRAD) at Necsa in South Africa. (*In* 18th World Conference on Nondestructive Testing, Durban: South African Institute for Non-Destructive Testing. p. 1-12).

103. Van Geet, M., Swennen, R. & David, P. 2001. Quantitative coal characterisation by means of microfocus X-ray computer tomography, colour image analysis and back-scattered scanning electron microscopy. *International journal of coal geology*, 46(1):11-25.

104. Simons, F.J., Verhelst, F. & Swennen, R. 1997. Quantitative characterization of coal by means of microfocal X-ray computed microtomography (CMT) and color image analysis (CIA). *International journal of coal geology*, 34(1–2):69-88.

105. Wikiradiography.net. 2012. Physics of the X-ray tube. http://www.wikiradiography.net/page/Physics+of+the+X-Ray+Tube Date of access: 13 April 2016.

106. Carmignato, S. 2012. Accuracy of industrial computed tomography measurements: experimental results from an international comparison. *CIRP annals - manufacturing technology*, 61(1):491-494.

107. Duliu, O.G. 1999. Computer axial tomography in geosciences: an overview. *Earth-science reviews*, 48(4):265-281.

108. Van Geet, M., Swennen, R. & Wevers, M. 2001. Towards 3-D petrography: application of microfocus computer tomography in geological science. *Computers & geosciences*, 27(9):1091-1099.

109. Akin, S. & Kovscek, A.R. 2003. Computed tomography in petroleum engineering research. *(In* Mees, F., Swennen, R., van Geet, M. & Jacobs, J., *eds.* Applications of X-ray computed tomography in the geosciences. London: Geological Society. p. 23-38).

110. Markoe, A. 2006. Analytic tomography. New York: Cambridge University Press. (Encyclopedia of mathematics and its applications).

111. Banhart, J., *ed*. 2008. Advanced tomographic methods in materials research and engineering. Oxford: Oxford University Press. (Monographs on the Physics and Chemistry of Materials).

112. Feldkamp, L.A., Davis, L.C. & Kress, J.W. 1984. Practical cone-beam algorithm. *Journal of the Optical Society of America*, 1(6):612-619.

113. Cunningham, J.A., Rahman, I.A., Lautenschlager, S., Rayfield, E.J. & Donoghue, P.C.J. 2014. A virtual world of paleontology. *Trends in ecology & evolution*, 29(6):347-357.

114. Krimmel, S., Stephan, J. & Baumann, J. 2005. 3D computed tomography using a microfocus X-ray source: analysis of artifact formation in the reconstructed images using simulated as well as experimental projection data. *Nuclear instruments and methods in physics research*, 542(1–3):399-407.

115. De Chiffre, L., Carmignato, S., Kruth, J.P., Schmitt, R. & Weckenmann, A. 2014. Industrial applications of computed tomography. *CIRP annals - manufacturing technology*, 63(2):655-677.

116. Cnudde, V., Masschaele, B., Dierick, M., Vlassenbroeck, J., Hoorebeke, L.V. & Jacobs, P. 2006. Recent progress in X-ray CT as a geosciences tool. *Applied geochemistry*, 21(5):826-832.

117. Barrett, J.F. & Keat, N. 2004. Artifacts in CT: recognition and avoidance. *RadioGraphics*, 24(6):1679-1691.

118. Remeysen, K. & Swennen, R. 2006. Beam hardening artifact reduction in microfocus computed tomography for improved quantitative coal characterization. *International journal of coal geology*, 67(1–2):101-111.

119. Kyle, J.R. & Ketcham, R.A. 2015. Application of high resolution X-ray computed tomography to mineral deposit origin, evaluation, and processing. *Ore geology reviews*, 65(4):821-839.

120. Van Geet, M. & Swennen, R. 2001. Quantitative 3D-fracture analysis by means of microfocus X-Ray computer tomography (μCT): an example from coal. *Geophysical research letters*, 28(17):3333-3336.

121. Mees, F., Swennen, R., Van Geet, M. & Jacobs, P. 2003. Applications of X-ray computed tomography in the geosciences. *(In* Mees, F., Swennen, R., van Geet, M. & Jacobs, J., *eds.* Applications of X-ray computed tomography in the geosciences. London: Geological Society. p. 1-6).

122. Ketcham, R.A. & Hanna, R.D. 2014. Beam hardening correction for X-ray computed tomography of heterogeneous natural materials. *Computers & geosciences*, 67:49-61.

123. Titarenko, S., Withers, P.J. & Yagola, A. 2010. An analytical formula for ring artefact suppression in X-ray tomography. *Applied mathematics letters*, 23(12):1489-1495.

124. Cnudde, V. & Boone, M.N. 2013. High-resolution X-ray computed tomography in geosciences: a review of the current technology and applications. *Earth-science reviews*, 123:1-17.

125. Fisher, D.C., Shirley, E.A., Whalen, C.D., Calamari, Z.T., Rountrey, A.N., Tikhonov, A.N., Buigues, B., Lacombat, F., Grigoriev, S. & Lazarev, P.A. 2014. X-ray computed tomography of two mammoth calf mummies. *Journal of paleontology*, 88(4):664-675.

126. Ketcham, R.A. & Carlson, W.D. 2001. Acquisition, optimization and interpretation of X-ray computed tomographic imagery: applications to the geosciences. *Computers & geosciences*, 27(4):381-400.

127. Lin, C. & Miller, J. 1996. Cone beam X-ray microtomography for three-dimensional liberation analysis in the 21st century. *International journal of mineral processing*, 47(1):61-73.

128. Gagarin, S. 2012. Study of coke structure by computerized X-ray tomography: a review. *Coke and chemistry*, 55(2):56-61.

129. Keller, A. 1998. High resolution, non-destructive measurement and characterization of fracture apertures. *International journal of rock mechanics and mining Sciences*, 35(8):1037-1050.

130. Ketcham, R.A., Slottke, D.T. & Sharp, J.M. 2010. Three-dimensional measurement of fractures in heterogeneous materials using high-resolution X-ray computed tomography. *Geosphere*, 6(5):499-514.

131. Lin, C. & Miller, J. 2005. 3D characterization and analysis of particle shape using X-ray microtomography (XMT). *Powder technology*, 154(1):61-69.

132. Miller, J. 2010. Characterisation, analysis and simulation of multiphase particulate systems using high resolution X-ray micro computed tomography (HRXMT). (*In* XXV Internation Mineral Processing Congress (IMPC), Brisbane, QLD, Australia).

133. Yao, Y., Liu, D., Che, Y., Tang, D., Tang, S. & Huang, W. 2009. Non-destructive characterization of coal samples from China using microfocus X-ray computed tomography. *International journal of coal geology*, 80(2):113-123.

134. Li, S., Tang, D., Xu, H. & Yang, Z. 2012. Advanced characterization of physical properties of coals with different coal structures by nuclear magnetic resonance and X-ray computed tomography. *Computers & geosciences*, 48:220-227.

135. Van Geet, M., David, P. & Swennen, R. 2000. Three dimensional coal characterisation (maceral, mineral and cleats) by means of X-ray microfocus computer tomography (µCT). (*In* Podemski, M. & Jureczka, J., *eds*. European Coal Conference IV, Warsaw, Poland: Polish Geological Institute. p. 263-270).

136. Verhelst, F., David, P., Fermont, W., Jegers, L. & Vervoort, A. 1996. Correlation of 3D-computerized tomographic scans and 2D-colour image analysis of Westphalian coal by means of multivariate statistics. *International journal of coal geology*, 29(1–3):1-21.

137. Mazumder, S., Wolf, K.-H., Elewaut, K. & Ephraim, R. 2006. Application of X-ray computed tomography for analyzing cleat spacing and cleat aperture in coal samples. *International journal of coal geology*, 68(3):205-222.

138. Stach, E. & Murchison, D.G. 1982. Stach's textbook of coal petrology. 3rd ed. Berlin: Gebrüder Borntraeger.

139. Naudé, G., Hoffman, J., Theron, S.J. & Coetzer, G. 2013. The use of X-ray computed tomography in the characterisation of coal and associated char reductants. *Minerals engineering*, 52:143-154.

140. Hoffman, J.W. 2012. Ionizing radiation as imaging tool for coal characterization and gasification research. Potchefstroom: North-West University. (Dissertation - M.Eng).

141. Pone, J.D.N., Hile, M., Halleck, P.M. & Mathews, J.P. 2009. Three-dimensional carbon dioxide-induced strain distribution within a confined bituminous coal. *International journal of coal geology*, 77(1):103-108.

142. Pone, J.D.N., Halleck, P.M. & Mathews, J.P. 2010. 3D characterization of coal strains induced by compression, carbon dioxide sorption, and desorption at in-situ stress conditions. *International journal of coal geology*, 82(3):262-268.

143. Karacan, C.Ö. & Mitchell, G.D. 2003. Behavior and effect of different coal microlithotypes during gas transport for carbon dioxide sequestration into coal seams. *International journal of coal geology*, 53(4):201-217.

144. Golab, A., Ward, C.R., Permana, A., Lennox, P. & Botha, P. 2013. High-resolution three-dimensional imaging of coal using microfocus X-ray computed tomography, with special reference to modes of mineral occurrence. *International journal of coal geology*, 113:97-108.

145. Natterer, F. 1982. The mathematics of computerized tomography. Philadelphia: Society for Industrial and Applied Mathematics. (Classics in applied mathematics).

146. Stock, S.R. 2008. Microcomputed tomography: methodology and applications. Boca Raton: Taylor & Francis.

147. Wagner, N.J. & Tlotleng, M.T. 2012. Distribution of selected trace elements in density fractionated Waterberg coals from South Africa. *International journal of coal geology*, 94:225-237.

148. Faure, K., Willis, J.P. & Claris Dreyer, J. 1996. The grootegeluk formation in the Waterberg coalfield, South Africa: facies, palaeoenvironment and thermal history — evidence from organic and clastic matter. *International journal of coal geology*, 29(1–3):147-186.

149. England, T., Hand, P.E., Michael, D.C., Falcon, L.M. & Yell, A.D., *eds*. 2002. Coal preparation in South Africa. 4th ed. Pietermaritzberg: The South African Coal Processing Society.

150. Bunt, J.R., Wagner, N.J. & Waanders, F.B. 2009. Carbon particle type characterization of the carbon behaviour impacting on a commercial-scale Sasol-Lurgi FBDB gasifier. *Fuel*, 88(5):771-779.

151. Dhillon, R.K., Singh, P., Gupta, S.K., Singh, S. & Kumar, R. 2013. Study of high energy (MeV) N^{6+} ion and gamma radiation induced modifications in low density polyethylene (LDPE) polymer. *Nuclear instruments and methods in physics research*, 301:12-16.

152. Coetzee, S., Neomagus, H.W.J.P., Bunt, J.R., Strydom, C.A. & Schobert, H.H. 2014. The transient swelling behaviour of large (−20 + 16 mm) South African coal particles during low-temperature devolatilisation. *Fuel*, 136:79-88.

153. Mathews, J.P., Pone, J.D.N., Mitchell, G.D. & Halleck, P. 2011. High-resolution X-ray computed tomography observations of the thermal drying of lump-sized subbituminous coal. *Fuel processing technology*, 92(1):58-64.

154. Coetzee, G. 2011. The influence of particle size on the steam gasification kinetics of coal. Potchefstroom: North-West University. (Dissertation).

155. Pinheiro, H. 1999. A techno-economic and historical review of the South African coal Industry in the 19th and 20th centuries and analysis of coal product samples of South African Collieries 1998-1999. *(In* Bulletin 113. Pretoria: South African Bereau of Standards (SABS). p. 1-97).

156. SABS. 1994. Hard coal - size analysis by sieving. Pretoria: Standards South Africa.(South African National Standard (SANS) 1953:1994).

eAppendix – High-resolution JPEG images

On the Compact Disc that accompanies this thesis there are high-resolution JPEG (Joint Photographic Expert Group) images used during the course of this study. The images are subdivided into four categories: (A) copies of all of the original images used in the thesis, (B) inverted copies of all original images used in the thesis, (C) centre slices from all of the tomograms generated during this study, and (D) comparisons used in Chapter 7 to determine the new crack counts. A list of all of the images included is given below:

Copies of original images used in the thesis

- Figure 1.2: Thesis flow
- Figure 2.2: Inglis crack
- Figure 2.6: Example load-extension curve output of a Mansanto tensometer
- Figure 3.2: Experimental setup
- Figure 3.3: A sequence of six individual frames taken from 12 µs worth of high speed video of sample 2/37/2/7
- Figure 3.4: A sequence of six frames taken from 8 µs worth of high speed video of sample 2/37/3/7
- Figure 3.5: A sequence of six frames taken from 26 µs worth of high speed video of sample 3/75/2/7
- Figure 3.6: A sequence of six frames taken from 7 µs worth of high speed video of sample 6/37/3/7
- Figure 3.7: A sequence of six frames taken from 15 µs worth of high speed video of sample 7/75/1/7
- Figure 3.8: Average PSD of all -37.5 mm parent particles dropped from 2 m, 5 m, and 7 m. The groupings correspond to the top size of the progeny particles
- Figure 3.9: Representation of the orientation factors
- Figure 3.10: Influence of the impact orientation factor on the t_{10} parameter
- Figure 3.11: t_{10} vs. x.E when samples are grouped by passing size and drop height
- Figure 4.2: Simplified principle of CT acquisition
- Figure 4.3: Schematic representation of an X-ray tube
- Figure 4.5: Visual representation of the linear attenuation coefficient

- Figure 7.12: Comparison of crack propagation through the height of a particle impacted perpendicularly (right) and parallelly (left) to the impact surface
- Figure 7.13: PSD comparison of the perpendicularly and parallelly impacted particles including the most extreme PSDs of individual particles for each orientation (P05, P08, L06, and L02)
- Figure 7.14: Comparison of the Rosin-Rammler models for the perpendicularly and parallelly impacted populations

Inverted copies of original images used in the thesis

- Figure 4.7(I): Examples of a metal- and ring artefact
- Figure 5.4(I): Centre slice of a heterogeneous particle with the load applied parallel to the bedding planes with (i) before and (ii) after application of the compressive force
- Figure 5.6(I): Centre slice of a homogeneous particle with the load applied perpendicular to the bedding planes with (i) before and (ii) after application of the compressive force
- Figure 5.7(I): Centre slice of a homogeneous particle with the load applied parallel to the bedding planes with (i) before and (ii) after application of the compressive force
- Figure 6.2(I): Comparison of a particle compressed perpendicular to the bedding plane
- Figure 6.3(I): Comparison of a particle compressed parallel to the bedding plane
- Figure 6.4(I): Comparison of a particle compressed incrementally perpendicular to the bedding plane
- Figure 6.5(I): Comparison of a particle compressed incrementally parallel to the bedding plane
- Figure 6.6(I): Comparison of a particle impacted with the bedding plane parallel to the anvil
- Figure 6.7(I): Comparison of a particle impacted with the bedding plane perpendicular to the anvil
- Figure 6.8(I): Comparison of a particle heated to 800ºC at a rate of 31ºC.s^{-1}
- Figure 6.9(I): Comparison of a particle heated to 700ºC at a rate of 51ºC.s^{-1}

Centre slices from tomograms generated during this study

- Figure A.1: Centre slice from a heterogeneous particle's tomogram generated before compression (JN1)
- Figure A.2: Centre slice from a heterogeneous particle's tomogram generated after compression (JN1)
- Figure A.3: Centre slice from a heterogeneous particle's tomogram generated before compression (JN2)
- Figure A.4: Centre slice from a heterogeneous particle's tomogram generated before compression (JN3)
- Figure A.5: Centre slice from a homogeneous particle's tomogram generated after compression (WB1)
- Figure A.6: Centre slice from a homogeneous particle's tomogram generated after compression (WB2)
- Figure A.7: Centre slice from a homogeneous particle's tomogram generated before compression (WB3)
- Figure A.8: Centre slice from a homogeneous particle's tomogram generated after compression (WB3)
- Figure A.9: Centre slice from the tomogram generated before the stepwise compression of a particle with the force applied along the bedding plane (CH1)
- Figure A.10: Centre slice from the tomogram generated during the stepwise compression of a particle with the force applied along the bedding plane (first force increase, CH1)
- Figure A.11: Centre slice from the tomogram generated during the stepwise compression of a particle with the force applied along the bedding plane (second force increase, CH1)
- Figure A.12: Centre slice from the tomogram generated before the stepwise compression of a particle with the force applied along the bedding plane (third force increase, CH1)
- Figure A.13: Centre slice from the tomogram generated after the stepwise compression of a particle with the force applied along the bedding plane (CH1)
- Figure A.14: Centre slice from the tomogram generated before the stepwise compression of a particle with the force applied across the bedding plane (CH2)

- Figure A.15: Centre slice from the tomogram generated during the stepwise compression of a particle with the force applied across the bedding plane (first force increase, CH2)
- Figure A.16: Centre slice from the tomogram generated after the stepwise compression of a particle with the force applied across the bedding plane (CH2)
- Figure A.17: Centre slice from the tomogram generated before the stepwise compression of a particle with the force applied across the bedding plane (CH3)
- Figure A.18: Centre slice from the tomogram generated after the stepwise compression of a particle with the force applied across the bedding plane (CH3)
- Figure A.19: Centre slice from a tomogram generated before thermal fragmentation (CB1)
- Figure A.20: Centre slice from a tomogram generated after thermal fragmentation (CB1)
- Figure A.21: Centre slice from a tomogram generated before thermal fragmentation (CB2)
- Figure A.22: Centre slice from a tomogram generated after thermal fragmentation (CB2)
- Figure A.23: Centre slice from a tomogram generated before thermal fragmentation (CB3)
- Figure A.24: Centre slice from a tomogram generated after thermal fragmentation (CB3)
- Figure A.25: Centre slice from a tomogram generated before thermal fragmentation (CB4)
- Figure A.26: Centre slice from a tomogram generated after thermal fragmentation (CB4)

Tomographic comparisons used in Chapter 7 to determine new crack counts

- Figure A.27: Comparison of three slices from tomograms generated before and after impact of a particle where the force application was along the bedding plane (JVL01)